



Impact of Energy Storage on the Stability and Transmission Efficiency of a Remote Grid

Mohd Fakhizan bin Romlie (M.Eng)

Thesis submitted to the University of Nottingham
for the degree of Doctor of Philosophy

July 2014

Abstract

This thesis addresses a remote grid fed by a weak transmission line and a local source of renewable generation. Energy Storage System (ESS) is installed at the remote grid. The thesis investigates the use of the Energy Storage System in improving the overall system efficiency and increasing the power system stability for the transmission line and remote grid system.

The Energy Storage System reduces transmission line losses and hence can improve the overall efficiency of the system. The key parameters that are significant to improving the overall system efficiency are derived and a simple mathematical analysis is undertaken to show the criteria for increased system efficiency. A PSCAD/EMTDC simulation is undertaken which is shown to be consistent with analysis both for simple and real wind profiles.

For the case of stability investigation, a large Constant Power Load (CPL) is connected at the remote grid. This thesis performs the mathematical modelling and stability analysis of the combined CPL, grid, wind farm and energy storage. It is shown that CPLs fed by active PWM rectifiers are fundamentally stable if operated below the transmission line load-ability limit, and those fed by diode bridge rectifier can be unstable depending on filter values. It is revealed that the instability can be improved by control of auxiliary units such as an energy storage units.

In order to reduce the simulation time required, a simplified model of a wind farm feeding a DFIG connected to a remote grid is proposed and compared with a detailed model using the PSCAD/EMTDC software.

Acknowledgements

I have a great many people to acknowledge for their contribution in completing this thesis. Firstly, my appreciations go to my supervisors, Professor Greg Asher and Associate Professor Christian Klumpner. This would never have been possible without their advice and guidance. I must thank Professor Greg Asher for his effort to review and proof reading drafts of the thesis. My thanks are also extended to Dr Mohamed Rashed whom acted as my informal teacher for the work in the thesis. I gratefully appreciate all of my friends, colleagues, lecturers and technicians for sharing and all kinds of support that have made this work possible. Thanks also to examiners: Professor Sarath B Tennakoon and Professor Jon Clare for the time and effort spent to evaluate the thesis.

I am greatly indebted to the Islamic Development Bank (IDB) for the scholarship under its Merit Scholarship Program for my PhD study. I would like to express my appreciation to all IDB staffs especially to Dr Malek Shah Mohd Yusoff and Abulmayeen M. Shaharuql Huq for their hard work to provide the best services to all the scholarship recipients. Not to forget, grateful thanks to Universiti Teknologi PETRONAS, my current employer, for the financial support and the paid study leave awarded to me.

My sincere gratitude to my beloved wife Erni Yenti Amir for her understanding, and wonderful words of soothing. I will not be able to pay for all the sacrifices she has done especially to take care of our children: Ammar, Aisyah, Adni and Izzah (a very newly born), whom have brought colours into my life. I also wish to thank my parents, Romlie Md Zain and Azizah Hashim and all others family members for their love, support, encouragement, prayer and the inspiration to my study. Thanks also to all my friends in UK especially in Nottingham for making my stay here like home.

Finally, the greatest thanks to the God for being very close to me all the time and surrounds me with wonderful family, friends, teachers and people.

Contents

Abstract	2
Acknowledgements	3
Contents	4
List of Figures	9
List of Tables	15
List of Abbreviations	16
List of Symbols	18
Chapter 1 Introduction	22
1.1 Background of Study and Research Objectives.....	22
1.2 Review of Storage Technologies.....	24
1.2.1 Comparison of Energy Storage.....	29
1.2.2 Role of energy Storage in Power System.....	32
1.3 Wind Turbine Systems.....	35
1.4 Constant Power Loads.....	37
1.5 Definition of a Weak Grid.....	39
1.6 Contributions of this Thesis.....	40
1.7 Thesis Structure.....	41

Chapter 2	Modeling and Simulation of Doubly-Fed Induction Generator	
Wind Turbine	43
2.1	Introduction.....	43
2.2	Wind Turbine Model.....	45
2.2.1	Aerodynamic Model in PSCAD.....	45
2.2.2	Mechanical Model.....	46
2.2.3	Control for Maximum Power Point Tracking.....	46
2.2.4	Pitch Angle Control.....	48
2.2.5	Wind Model.....	49
2.3	DFIG Modeling and Control.....	50
2.3.1	DFIG Modeling.....	50
2.3.2	Vector Control Scheme of DFIG converters.....	51
2.3.2.1	Vector control of rotor side PWM voltage source converter..	51
2.3.2.2	Vector control of grid side PWM voltage source converter...	56
2.3.3	System Parameters for Simulation.....	59
2.3.4	PSCAD Simulation Results and Discussion.....	61
2.4	Simplified DFIG for Wind Turbine under MPPT.....	65
2.5	Chapter Summary.....	77
Chapter 3	An Analysis of Efficiency Improvement with the Installation of	
Energy Storage in Power Systems	78
3.1	Introduction.....	78
3.2	Mathematical Analysis of Efficiency Improvement with Energy	
Storage.....		81
3.2.1	Loss Reduction in Transmission Line.....	81
3.2.2	Breakeven Point for Overall Efficiency Improvement.....	82
3.3	PSCAD Simulation.....	89
3.3.1	Simulation Parameters.....	91

3.3.2	Estimation of Supercapacitor Round Trip Efficiency.....	91
3.3.3	Simulation Procedures, Results and Discussions.....	92
3.3.3.1	Idealized Waveform Power Generation.....	92
3.3.3.2	Real Wind Power Profile.....	97
3.4	Discussion from a Practical Viewpoint.....	104
3.5	Chapter Summary.....	107
Chapter 4 Stability Analysis of a Microgrid with a Constant Power Load Fed by a Controlled Converter		108
4.1	Introduction.....	108
4.2	Control and Modeling.....	110
4.2.1	Dq-Transformation and the Phase Locked Loop.....	110
4.2.2	Modeling of the Grid and the Transmission Line.....	113
4.2.3	Control and Modeling of the CPL Fed by the PWM Converter.....	114
4.2.4	Control and Modeling of the Wind Farm.....	118
4.2.5	Control and Modeling of the Energy Storage System.....	120
4.2.5.1	Modeling the PWM converter.....	120
4.2.5.2	Modeling the DC/DC converter and Load Dynamics.....	121
4.2.5.3	Modeling the AC Side Dynamics of the Energy Storage System.....	123
4.2.5.4	Equations to a Complete Energy Storage System.....	123
4.2.6	The Complete Mathematical Model of the System Study.....	124
4.2.6.1	Linearized Model of the System.....	125
4.3	Small-signal Stability Analysis.....	126
4.3.1	Eigenvalues Analysis.....	126
4.3.2	Model Validation.....	127
4.3.2.1	System Parameters for the Study.....	127
4.3.2.2	Comparison of Mathematical Model and PSCAD System Model.....	128

4.3.3	Stability Analysis at Various Power Levels.....	130
4.3.3.1	Transmission Line Load ability Limit.....	135
4.4	Chapter Summary.....	137
Chapter 5 Stability Analysis and Control of a Large Constant Power Load fed by Diode Bridge Rectifier in a Local Grid.....		138
5.1	Introduction.....	138
5.2	System Modeling.....	140
5.2.1	Modeling of CPL fed via a Diode Bridge Rectifier.....	140
5.2.2	The Complete Mathematical Model of the System Studied.....	144
5.2.2.1	Linearized Mathematical Model.....	144
5.3	Small-signal Stability Analysis.....	145
5.4	The CPL Connected to Local Grid.....	149
5.4.1	The CPL DC Link Smoothing LC Filter and Stability Limit Characteristic.....	150
5.5	Control System to Improve Stability.....	154
5.5.1	Participation Factor Analysis.....	154
5.5.2	Control Structure.....	156
5.5.3	PSCAD Simulation Results.....	157
5.6	Chapter Summary.....	162
Chapter 6 Conclusion and Future Work		164
6.1	Conclusion.....	164
6.2	Future work.....	166
6.3	Publication.....	168
Appendix A	: Matlab code to obtain a new set of wind profile at a different wind perturbation.....	169
Appendix B	: Average model of PWM AC/DC converter	170

Appendix C	: Parameters of Front End Converters	172
Appendix D	: Parameters of Energy Storage System	174
Appendix E	: Matlab code for the energy calculations in Chapter 3..	176
Appendix F	: Matlab code to obtain a Jacobian matrices.....	177
Appendix G	: Matlab code to calculate participation factor	179
References	180

List of Figures

Figure 1.1: World energy consumption as given by International Energy Statistic, US Energy Information Administration [2]	22
Figure 1.2: Pumped Storage Plant [19]	25
Figure 1.3: CAES system [19]	26
Figure 1.4: Ragone plot showing the specific power vs. specific energy of electrochemical energy storage	29
Figure 1.5: Typical load demand pattern [46]	33
Figure 1.6: Different types of wind turbine generator systems (a) CSIG, (b) DFIG, (c) BGFC and (d) DDGS	36
Figure 1.7: An actuator drive system behaving as a CPL system with a rectifier at the front end connected to the AC power	37
Figure 1.8: Negative impedance characteristic of CPL	38
Figure 2.1: Overall block diagram of the weak grid-connected wind turbine system	44
Figure 2.2: Schematic diagram of DFIG for wind turbine simulated in PSCAD	44
Figure 2.3. Turbine power-shaft speed characteristic for wind speed of 6-13m/s in 1m/s increments for a wind turbine represented by (2.1)-(2.4)	47
Figure 2.4. Mechanical torque-shaft speed characteristic for wind speed of 6-13m/s in 1m/s increments for a wind turbine represented by (2.1)-(2.4)	47
Figure 2.5: Pitch angle control scheme used in this thesis	49
Figure 2.6: Real wind profile used in this thesis with average speed 13.65m/s and standard deviation 1.25m/s for 600s	49
Figure 2.7. Vector control structure of rotor- side PWM converter	55
Figure 2.8: Cascaded power and current controller of the rotor-side PWM converter	55
Figure 2.9: Schematic diagram of grid side voltage source converter connected to grid	56
Figure 2.10: Vector control structure of the grid-side PWM converter	58

Figure 2.11: Cascaded power and current controller of the grid-side PWM converter	59
Figure 2.12: DFIG output power versus wind speed	60
Figure 2.13: Power flow in a DFIG	62
Figure 2.14: Simulation result of the DFIG connected to grid for wind speed of 0.32-1.2pu with step increments of 0.08pu (a) wind speed (pu), V_w ; (b) active power (pu), P_{out} ; (c) output reactive power (pu), Q_{out} ; (d) voltage magnitude at PCC (pu), V_{pcc} ; (e) shaft speed (pu) ω_r ; and (f) pitch angle (degree) , β	63
Figure 2.15: Simulation result of the DFIG connected to grid with the real wind profile of average wind speed 0.864pu (a) wind speed (pu), V_w ; (b) active power (pu), P_{out} ; (c) output reactive power (pu), Q_{out} ; (d) voltage magnitude at PCC (pu), V_{pcc} ; (e) shaft speed (pu) ω_r ; and (f) pitch angle (degree) , β	64
Figure 2.16: Schematic diagram of the simplified model	66
Figure 2.17: Simulation results of the detailed and the simplified models with wind speed of 0.32 -1.2pu and step increments of 0.88 m/s (a) wind speed (pu), V_w ; (b) output active power (pu), P_{out} ; (c) output reactive power (pu), Q_{out} ; (d) voltage magnitude (pu), V_{pcc} ; (e) shaft speed (pu), ω_r ; and (f) pitch angle (degree), β	69
Figure 2.18: Zoomed of Figure 2.17 for simulation time between 59s to 70s (a) wind speed (pu), V_w ; (b) output active power (pu), P_{out} ; (c) output reactive power (pu), Q_{out} ; (d) voltage magnitude (pu), V_{pcc} ; (e) shaft speed (pu), ω_r ; and (f) pitch angle (degree), β	70
Figure 2.19: Zoomed of Figure 2.17 for simulation time between 109s to 120s (a) wind speed (pu), V_w ; (b) output active power (pu), P_{out} ; (c) output reactive power (pu), Q_{out} ; (d) voltage magnitude (pu), V_{pcc} ; (e) shaft speed (pu), ω_r ; and (f) pitch angle (degree), β	71
Figure 2.20: Simulation results of the detailed and simplified models with the real wind profile of average wind speed 0.864pu 120s (a) wind speed (pu), V_w ; (b) output active power (pu), P_{out} ; (c) output reactive power (pu), Q_{out} ; (d) voltage magnitude (pu), V_{pcc} ; (e) shaft speed (pu), ω_r ; and (f) pitch angle (degree), β	72
Figure 2.21: Zoomed of Figure 2.20 for simulation time between 70s to 90s (a) wind speed (pu), V_w ; (b) output active power (pu), P_{out} ; (c) output reactive power (pu), Q_{out} ; (d) voltage magnitude (pu), V_{pcc} ; (e) shaft speed (pu), ω_r ; and (f) pitch angle (degree), β	73
Figure 2.22: Step of reactive power at wind speed of 0.64pu (a) wind speed (pu), V_w ; (b) output active power (pu), P_{out} ; (c) output reactive power (pu), Q_{out} ; (d)	

voltage magnitude (pu), V_{pcc} ; (e) shaft speed (pu), ω_r ; and (f) pitch angle (degree), β 74

Figure 2.23: Step of reactive power at wind speed 0.8pu (a) wind speed (pu), V_w ; (b) output active power (pu), P_{out} ; (c) output reactive power (pu), Q_{out} ; (d) voltage magnitude (pu), V_{pcc} ; (e) shaft speed (pu), ω_r ; and (f) pitch angle (degree), β 75

Figure 2.24: Step of reactive power at wind speed of 1.04pu (a) wind speed (pu), V_w ; (b) output active power (pu), P_{out} ; (c) output reactive power (pu), Q_{out} ; (d) voltage magnitude (pu), V_{pcc} ; (e) shaft speed (pu), ω_r ; and (f) pitch angle (degree), β 76

Figure 3.1: Power system under study 80

Figure 3.2: RMS currents profile 80

Figure 3.3: Transmission line losses reduction by shifting the power transmitted 82

Figure 3.4: 3D plots of $\Delta I_{w,Brk}$, SCR and η_{rt} (a) various X/R, (b) various $I_{w,o}$, and (c) various D 87

Figure 3.5: $\Delta I_{w,Brk}$ versus η_{rt} (a) various SCR, (b) various X/R, (c) various $I_{w,o}$ and (d) various D 88

Figure 3.6: Block diagram of wind power system and its control structure 90

Figure 3.7: Block diagram of energy storage system and its control structure 90

Figure 3.8: Simulation results for a case with the square wave power generated (a) reference wind power generated (pu), P_w^* ; (b) wind current generated (pu), I_w ; (c) Power loss in transmission line (pu), $P_{t,loss}$ (d) power to/from energy storage(pu), P_{ess} ; (e) Energy storage voltage(pu), V_C 94

Figure 3.9: ΔE_{sl} as a function of η_{rt} 95

Figure 3.10: Plot of $\Delta I_{w,Brk}$ versus η_{rt} from mathematical and PSCAD simulation results (a) various SCR, (b) various X/R, (c) various $I_{w,o}$ 96

Figure 3.11: Frequency spectrum of (a) the transmission line current and (b) the transmission power losses ($\sigma_{Iw}=0.1pu$; $I_{w,o}=0.5pu$) when comparing the square-wave template with the real wind power data. 98

Figure 3.12: Simulation results for a case with the real wind power generated ($\sigma_{Iw}=0.1pu$; $I_{w,o}=0.5pu$) (a) Wind speed(pu), V_w ; (b) Power generated(pu), P_{gen} ; 98

(c)Transmission line current(pu), I_t ; (d) Power loss in transmission line (pu), $P_{t,loss}$;
 (e)Power to/from energy storage(pu), P_{ess} ; (f) Energy storage voltage(pu), V_C 101

Figure 3.13: Simulation results for a case with SCR=2 and X/R=2 without the ESS
 (a)Wind speed(pu), V_w ;(b) Power generated(pu), P_{gen} ; (c)Transmission line
 current(pu), I_t ; (d) Power loss in transmission line (pu), $P_{t,loss}$ 102

Figure 3.14: $\sigma_{Iw,Brk}$ versus η_{rt} (a) SCR=4 and 5; (b) X/R=2 and 3. 103

Figure 3.15: Breakeven lines for a practical range of $\sigma_{Iw,Brk}$ and η_{rt} (a) various SCR,
 (b) various X/R ratio and (c) various $I_{w,o}$ 106

Figure 4.1: Block diagram of the system under study 110

Figure 4.2: Phasor diagram for dq -transformation 111

Figure 4.3: Block diagram of a phase locked-loop 112

Figure 4.4: A CPL fed via a PWM converter and its control structure 115

Figure 4.5: Schematic of control structure for the CPL front end converter 116

Figure 4.6: Wind Power feeding local grid via a PWM converter and its control
 structure 119

Figure 4.7: Schematic of control structure for the wind farm front end converter 119

Figure 4.8: Block diagram of the energy storage system 120

Figure 4.9: Schematic of control structure for the energy storage front end converter 121

Figure 4.10: Schematic of control structure for the energy storage unit DC/DC
 converter 122

Figure 4.11: Response of V_{pcc} , $V_{dc,L}$ and $V_{dc,w}$ when CPL is stepped from 2MW to
 2.5MW 129

Figure 4.12: Response of V_{pcc} , $V_{dc,L}$ and $V_{dc,w}$ when CPL is stepped from 5MW to
 5.5MW 129

Figure 4.13: Response of V_{pcc} , $V_{dc,L}$ and $V_{dc,w}$ when CPL is stepped from 7MW to
 7.1MW 129

Figure 4.14: Eigenvalues trace for the Case 1 132

Figure 4.15: Zoomed area of interest from Figure 4.14 132

Figure 4.16: PSCAD simulation result for Case 1 132

Figure 4.17: Eigenvalues trace for the Case 2	133
Figure 4.18: Zoomed area of interest from Figure 4.17 (for P_{cpl} from 4MW to 11MW)	133
Figure 4.19: PSCAD simulation result for case 2	133
Figure 4.20: Eigenvalues trace for the Case 3	134
Figure 4.21: Zoomed area of interest from Figure 4.20	134
Figure 4.22: PSCAD simulation result for case 3	134
Figure 4.23: The transmission line equivalent circuit	135
Figure 5.1: Block diagram of the power system under study	139
Figure 5.2: A block diagram of CPL interfaced with Diode Bridge to a three-phase AC system	141
Figure 5.3: The equivalent diode-bridge rectifier in the dq frame	143
Figure 5.4: Equivalent circuit of the system in Figure 5.2	143
Figure 5.5: Eigenvalue plot when CPL varies from 0 to 0.5pu for three cases. (Legend: Case 1- Green diamond; Case 2-Blue circle; Case 3-Red star)	148
Figure 5.6: Zoomed for the area of interest from Figure 5.5 (Legend: Case 1- Green diamond; Case 2-Blue circle; Case 3-Red star)	148
Figure 5.7: PSCAD simulation result for the three cases (a) CPL stepped by 0.01pu from 0.3 to 0.35pu; (b) V_{pcc} (pu) for Case 1; (c) V_{pcc} (pu) for Case 2; (d) V_{pcc} (pu) for Case 3	148
Figure 5.8: A block diagram of DRF-CPL connected to a local grid	149
Figure 5.9: Simplified equivalent circuit of the system in Figure 5.8	150
Figure 5.10: DC link capacitance versus inductance curve for 80, 160 and 240Hz (shown by blue lines) and CPL stability limits of 0.2,0.4 and 0.6pu (shown by red lines)	152
Figure 5.11: Capacitance versus CPL stability limit for $L_{fl} = 0.05\text{mH}$, 0.1mH and 0.2mH	152
Figure 5.12: The original controller of ESS as described in section 4.2.5	158
Figure 5.13: The control scheme 1	158
Figure 5.14: The control scheme 2	158

Figure 5.15: The simulation result for the system in Figure 5.1 with the original ESS controller; (a) CPL, P_{cpl} (pu); (b) Voltage magnitude at PCC, V_{pcc} (pu); (c) Active current injected by ESS, $I_{d,ie}$ (pu); (d) Reactive power injected by ESS, $I_{q,ie}$ (pu); (e) DC link voltage of the DRF-CPL, $V_{dc,cpl}$ (pu); (f) Load current, $I_{dc,o}$ (pu); 159

Figure 5.16: The simulation result for the system in Figure 5.1 with the ESS controller scheme 1; (a) CPL, P_{cpl} (pu); (b) Voltage magnitude at PCC, V_{pcc} (pu); (c) Active current injected by ESS, $I_{d,ie}$ (pu); (d) Reactive power injected by ESS, $I_{q,ie}$ (pu); (e) DC link voltage of the DRF-CPL, $V_{dc,cpl}$ (pu); (f) Load current, $I_{dc,o}$ (pu); 160

Figure 5.17: The simulation result for the system in Figure 5.1 with the ESS controller scheme 1; (a) CPL, P_{cpl} (pu); (b) Voltage magnitude at PCC, V_{pcc} (pu); (c) Active current injected by ESS, $I_{d,ie}$ (pu); (d) Reactive power injected by ESS, $I_{q,ie}$ (pu); (e) DC link voltage of the DRF-CPL, $V_{dc,cpl}$ (pu); (f) Load current, $I_{dc,o}$ (pu); 161

List of Tables

Table 1.1: Energy Storage Technology Comparison [19], [21]–[23], [26]	31
Table 2.1.: Wind Turbine Parameters	59
Table 2.2: Wound Rotor Induction Machine Parameters	59
Table 2.3: PI controller parameters	61
Table 2.4: Total simulation time required for the simulations in Figure 2.17	68
Table 2.5: Total simulation time required for the simulations in Figure 2.20	68
Table 4.1: Parameters of the transmission line of the system in Figure 4.1	127
Table 5.1. Parameters of the transmission line in Figure 5.1	145
Table 5.2. Parameters of the DRF-CPL in Figure 5.2	146
Table 5.5: Participation factor of the unstable modes in states, p_{ki}	155
Table 5.6: Participation factor of states in the unstable modes, π_{ki}	155

List of Abbreviations

Acronyms : Definition

AC	: Alternating Current
AV	: Average Value
BGFC	: Brushless Generator with Gear and Full-Converter
CAES	: Compressed Air Energy Storage
CPL	: Constant Power Load
CSIG	: Constant Speed Squirrel-Cage Induction Generator
CPM	: Constant Power Mode
CTM	: Constant Torque Mode
DC	: Direct Current
DDGS	: Direct-Drive Generator System
DFIG	: Doubly-Fed Induction Generator
DG	: Distributed Generation
DRF-CPL	: Diode Rectifier Fed-Constant Power Load
DSFO	: Direct Stator Flux Orientation
ESS	: Energy Storage System
ISFO	: Indirect Stator Flux Orientation
KCL	: Kirchoff Current Law
KVL	: Kirchoff Voltage Law
LC	: Inductor-Capacitor
LCL	: Inductor-Capacitor-Inductor
MPPT	: Maximum Power Point Tracking

PCC	:	Point of Common Coupling
PI	:	Proportional-Integral
PLL	:	Phase Locked Loop
PSCAD	:	The Power System Software
PWM	:	Pulse Width Modulation
RC	:	Resistor - Capacitor
SCR	:	Short Circuit Ratio
SMES	:	Superconducting Magnetic Energy Storage
SSA	:	State-Space Averaging
STD	:	Standard Deviation
X/R	:	Ratio of Reactance to Resistance

List of Symbols

Symbols	: Definition
A	: Turbine blade area
α	: Control signals to the PWM converters
β	: Blade pitch angle
β_{cal}	: Pitch angle calculated
C_p	: Power coefficient
C_{sc}	: Supercapacitor capacitance
D	: Duty cycle
E_C	: Amount of energy charge
E_D	: Amount of energy discharge
$E_{es,in}$: Total energy stored in the energy storage system
$E_{es,loss}$: Energy loss in the energy storage system
ΔE_{sl}	: Energy saving or losses
$E_{t,loss}$: Energy loss in the transmission line without energy storage
$E_{t,loss}^{ES}$: Energy loss in the transmission line with the energy storage
$E_{t,saved}$: Energy loss reduction in the transmission line with the energy storage employment
G	: Gear ratio
I_{CPL}	: Current into the CPL
I_{iL}, I_{iw}, I_{ie}	: Input currents to the load, wind and energy storage
$I_{d,gen}$: d -axis of current generated by the wind farm (active current)
$I_{q,gen}$: q -axis of current generated by the wind (reactive current)
$I_{d,es}^*$: Active current demand reference of the energy storage
$I_{q,es}^*$: Reactive current demand reference of the energy storage
i_{ms}	: Magnetizing current of the generator
i_r	: Rotor current
i_{rd}	: Rotating d -axis rotor current

i_{rq}	: Rotating q-axis rotor current
$i_{s\alpha}$: Stationary α -axis stator current
$i_{s\beta}$: Stationary β -axis stator current
I_m	: Nominal values of rms current of the transmission line
$I_{t,max}$: Maximum rms currents in the transmission line
$I_{t,min}$: Minimum rms currents in the transmission line
$\Delta I_{t,pu\min}$: Minimum value of ΔI_t in per unit required to ensure that the energy storage installation increases overall system efficiency
$\Delta I_{t,pu}$: Amount of current shifted in per unit
$I_{to,pu}$: Average transmission line current in per unit
$I_{t,o}$: Average current carried by the transmission line
J	: Moment of inertia
K_{opt}	: Wind turbine constant for an optimal power capture
$K_{u,pL}, K_{u,pw}$: Voltage loop proportional gain
$K_{u,iL}, K_{u,iw}$: Voltage loop integral gain
$K_{d,pL}, K_{q,pL}, K_{d,pw}, K_{q,pw}$: Current loop proportional gain
$K_{d,iL}, K_{q,iL}, K_{d,iw}, K_{q,iw}$: Current loop integral gain
K_{pll}	: Phase Locked Loop Gain
$K_{d,pe}, K_{q,pe}$: Current loop proportional gain
$K_{d,ie}, K_{q,ie}$: Current loop integral gain
$K_{v,pe}$: Proportional gain for the voltage magnitude controller
$K_{v,ie}$: Integral gain for the voltage magnitude controller
$K_{s,p}$: DC/DC converter controller inner loop proportional gain
$K_{s,i}$: DC/DC converter controller inner loop integral gain
$K_{y,p}$: DC/DC converter controller outer loop proportional gain
$K_{y,i}$: DC/DC converter controller outer loop integral gain
L_s	: Stator leakage inductance
L_r	: Rotor leakage inductance
L_t	: Transmission line inductance
L_o	: Magnetizing inductance
N	: Sample number
η_{rt}	: Round trip efficiency of the energy storage
P_C	: Amount of power flow to the energy storage unit when charging
P_{CPL}	: CPL active power

$P_{CPL,o}$: P_{CPL} at an operating point
P_D	: Amount of power flow to the energy storage unit when discharging
P_{gen}	: Power generated
$P_{gen,max}$: Maximum power generated
$P_{gen,min}$: minimum power generated
P_{gen}^*	: Reference power generated coming from the wind farm
P_m	: Mechanical power
P_{opt}	: Maximum power captured
P_{rated}	: Rated output power of the DFIG
P_s	: Stator active power
P_s^*	: Reference stator active power
P_{out}	: Output power
ρ	: Air density
Q_s	: Stator reactive power
Q_s^*	: Reference stator reactive power
R_r	: Rotor resistance
R_s	: Stator resistance
R_{sc}	: Supercapacitor resistance
R_t	: Transmission line resistance
s	: Slip
Subscript d and q	: Direct and quadrature axes the respective quantity
Subscript L,w,cpl and e	: Represent load, wind, CPL and energy storage quantities, respectively.
S_{cr}	: the short circuit ratio (SCR) ,
S_r	: Rated apparent power
$S_{t,rated}$: Rated apparent power of the transmission line
σ	: Standard deviation
σ_n	: New standard deviation
σ_{I_t}	: Standard deviation of transmission line current
$\sigma_{I_t,min}$: Standard deviation of transmission line current in per unit required to ensure that the energy storage installation increases overall system efficiency
σ_w	: Standard deviation of the wind speed profile
T	: A duration of time for a to complete a cycle of charging and discharging the energy storage
T_e	: Electrical torque
T_L	: Load torque
T_m	: Mechanical torque
θ_r	: Rotor flux angular position
θ_s	: Stator flux angular position
θ_{slip}	: Slip angular position

U_t	: Grid voltage
u_r	: Rotor voltage
u_{rd}	: Rotating d-axis rotor voltage
u_{rq}	: Rotating q-axis rotor voltage
ψ_s	: Magnitude of the stator flux linkage
$\psi_{s\alpha}$: Stationary α -axis stator fluxes
$\psi_{s\beta}$: Stationary β -axis stator fluxes
$V_{C,max}$: Supercapacitor maximum voltage
$V_{C,min}$: Supercapacitor minimum voltage
V_{dc}	: DC link voltage
$V_{dc,o}$: V_{dc} at an operating point
V_n	: Nominal voltage
V_{pcc}	: Voltage at point of common coupling (PCC)
V_m	Nominal values of rms voltage of the transmission line
$v_{s\alpha}$: Stationary α -axis stator voltage
$v_{s\beta}$: Stationary β -axis stator voltage
V_w	: Wind speed
$\overline{V_w}$: Average value of the wind speed
V_{wi}	: i^{th} sample of the wind speed data
V_{win}	: i^{th} sample of the new wind profile
ω	: Fundamental frequency
ω_r	: Rotor or shaft speed
ω_e	: Electrical angular frequency of the stator voltage
ω_s	: Synchronous frequency or base angular frequency
ω_{slip}	: Slip frequency
X_t	: Transmission line reactance
X_{2R}	: Ratio of reactance to resistance
Y_{pu}	: Admittance at fundamental frequency in per unit
Z_{CPL}	: Incremental impedance
Z_{pu}	: Impedance in per unit
Z_t	: Transmission line impedance
λ	: Tip speed ratio

Chapter 1

Introduction

1.1 Background of Study and Research Objectives

The world energy consumption from 1980 to 2010 is growing as shown in Figure 1.1. The energy demands have been met by various energy sources mainly fossil fuel, nuclear and renewable energy. More than 80% of the energy is currently generated using fossil fuel such as oil, gas and coal. The power generation using these fossil fuels contribute to significant environmental problem due to CO₂ emission. As an effort to reduce the harmful climate impact, many countries have committed to increase the generation of energy from renewable energy sources such as wind, solar, hydro, biomass, ground source heat and tidal. For example, in the United Kingdom, the government has committed to increase renewable energy generation to at least 15% of the total energy demand by 2020. Over 30% of the renewable energy generation will be coming from wind energy generation [1]. An issue with renewable energy generation is their intermittency, which is typically solved with energy storage systems. Therefore, renewable energy generation will also increase the demand for energy storage in power systems.

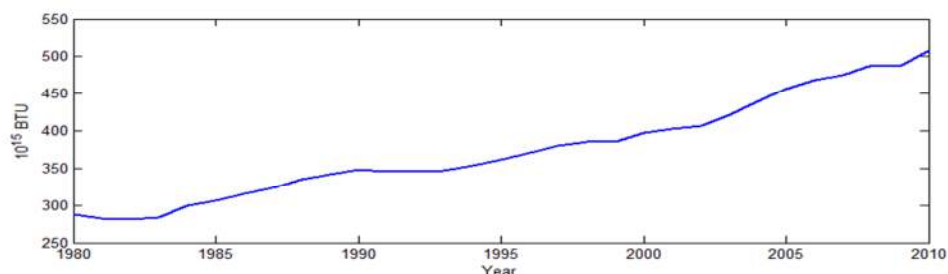


Figure 1.1: World energy consumption as given by International Energy Statistic, US Energy Information Administration [2]

The benefits of energy storage in power system are discussed and analysed in many publications, for example [3]–[6]. However, little attention has been paid to the study of energy storage installation to improve overall system efficiency. This is due to the fact that the installation of an energy storage is like adding another source of losses to the power system. Therefore, it will tend to reduce the overall system efficiency rather than improving it. However, there is a possibility of reducing the transmission line losses with the installation of energy storage. If the reduction of the transmission line losses is higher than the losses in the energy storage system, the overall system efficiency can be improved [7]. This issue is addressed in [3] but there is no systematic analysis of achieving the purpose. The analytical analysis in [7] focuses on load levelling application but not on the power generation smoothing with energy storage.

Another important issue in a power system is the possible system instability which may be caused by Constant Power Loads (CPLs) [8]–[11]. Many studies focus on stability analysis of CPLs in isolated AC or DC microgrids as can be found in [12]–[17]. The condition may become worse if the CPLs are connected to a local weak grid with renewable energy generation. This thesis will investigate a stability analysis of a CPL on a remote grid that has not been addressed. This thesis also aims to investigate the potential to make use of an added energy storage system to improve the system stability.

The above issues actually originated from a request of an industrial sponsor to investigate the benefits of grid applications of energy storage that were additional to those of peak shaving and the decoupling of demand with intermittent (renewable) supply. From this general aim, the studies focussed on remote grids in which the power transfer through a long weak connection is reduced through local generation and energy storage. These systems may become common in for example, mining industries that are necessarily sited in remote regions. The above two problems of overall efficiency gain and stability investigation were chosen for the study.

1. To analyse the benefit of energy storage for improving the overall power system efficiency.

2. To study the benefit of an energy storage system to increase power system stability in a system with a CPL.

In order to achieve these objectives, the following is also performed and discussed in this thesis:

1. Modelling of the power system for the studies. The system considered consists of a renewable energy generation, a CPL and an energy storage system connected to a local weak grid. Since the wind energy generation has received high attention as shown by annual growth of 30% [18], the wind energy generation will be modelled in this thesis. The system modelling is discussed throughout the thesis. The simulation model is developed in PSCAD/EMTDC software. However, the simulation model with a full DFIG system which was modelled takes a long time to run. Therefore, a simplified model is proposed.

2. To perform the stability analysis of the system. Small-signal stability analysis is employed. For that reason, the mathematical model of the system study is developed and presented in this thesis. This was originally undertaken for the case of loads interfaced with active front end PWM converters. However, as a result of the investigations, it was found that the tight DC-link voltage control of these converters suppressed instability. The study therefore was extended to conventional diode bridge rectifiers where instability is more likely.

3. Investigation of instability reduction through system control. The idea here is to investigate whether an active front-end control unit at the remote grid can be used for improving the system stability.

The remainder of this chapter will present a literature review of energy storage technologies, wind energy systems and constant power load instability. A definition of a weak grid will also be presented.

1.2 Review of Storage Technologies

The energy storage technologies reviewed in this section are: pumped hydro, compressed air energy storage, flywheel, superconducting magnetic energy storage and electrochemical energy storage. Also discussed are the energy storage

comparison and role of energy storage in power system. Given that the thesis will address the system efficiency, the round-trip efficiency of each type is particularly important. The characteristic, efficiencies and costs will be summarized in Table 1.1.

Pumped hydro

The energy is stored in the form of water kept in an uphill reservoir. This is done by pumping water from downhill to uphill using excess energy during low demand period. Electricity can then be generated when demand is high by the natural flow of water through turbine from upper to lower reservoir. A typical pumped hydro plant is illustrated in Figure 1.2. This is an economical method of energy storage for bulk energy storage. The technique has been widely used for decades. However, pump hydro is mainly limited by topographic and environmental constraints. To overcome the limitation, a new concept of underground pump hydro storage has been examined. However this increases the cost of excavation. The roundtrip efficiency of a pump hydro is approximately 70% to 85% [19]. Losses are due to evaporation, electric turbine or pump inefficiency, and mechanical friction. The system is discussed in [19]–[22]. There are many pumped-hydro projects operating around the world with total generating capacity of more than 100GW including the 1.88MW Dinorwig plant in North Wales [23], [24].

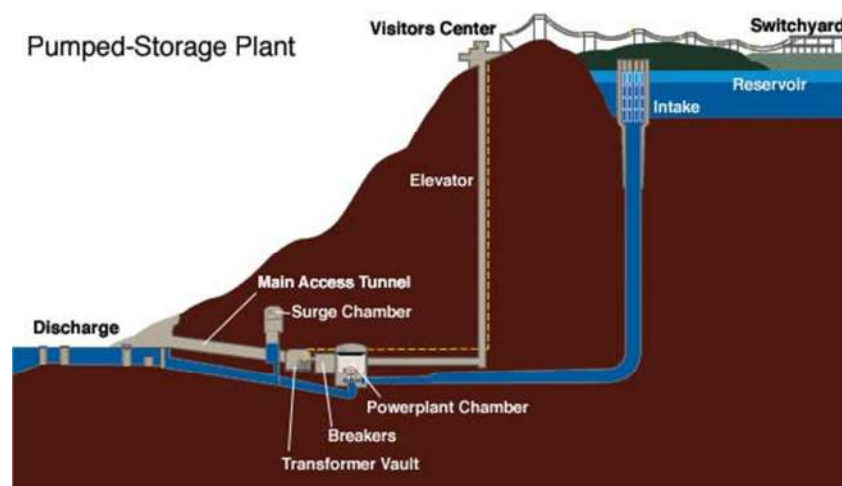


Figure 1.2: Pumped Storage Plant [19]

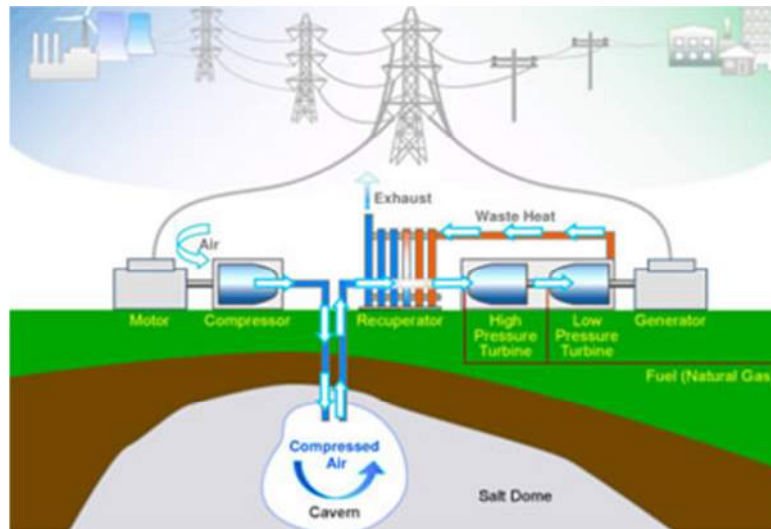


Figure 1.3: CAES system [19]

Compressed Air Energy Storage

Compressed Air Energy Storage (CAES) stores energy in the form of compressed air in a proper-designed underground cavern as seen in Figure 1.3. The compressed air will be used to feed a gas turbine to regenerate electricity when necessary. Although the method is economical and technically viable for bulk energy storage, the roundtrip efficiency is only about 75% to 80% mainly due to losses in its components to compress and regenerate the electricity; and losses in the cavern [22]. In addition, it is also difficult to find suitable locations for the CAES siting because of the geological requirement for air storage cavity. CAES systems are reviewed in [19], [20], [22]. Currently, only two CAES plants are commercially available in the world: in Huntorf, Germany (capable of supplying output power 330MW in 2 hours) and in McIntosh, Alabama, USA (capable of supplying 110MW output power in 26 hours) [23].

Flywheels

Storing electricity in the form of mechanical kinetic energy is the concept used in flywheels. Flywheels are rotated by electric motors and the spinning flywheel stores the kinetic energy. The energy is reconverted to electricity by the use of a 4-quadrant power converter. The application for storing energy is made economic for long

periods of time by the developments in material and bearing technology [21]. The technology has matured for short-term and small scale applications in transportation. The efficiency is about 85-90% [19], [22] . However, the efficiency drops significantly for storing for longer period of time. It is also constrained by safety. Mechanical failure may be catastrophic due to the high speeds and stresses involved. Commercially, flywheels have been used in uninterruptible power supply (UPS) applications with rating of up to some megawatts [20]. Further investigation of the flywheels energy storage system can be found in [19]–[22], [25].

Superconducting Magnetic Energy Storage

Superconducting Magnetic Energy Storage (SMES) stores energy in magnetic fields. A superconducting coil with high magnetic field is required. The superconducting winding is charged by connecting it to voltage source and thus builds up the magnetic field in it. This energy can be discharged as electric current by connecting it to the electrical load. This storage option is expensive because of the cost of superconducting winding itself and the supporting structure to contain the forces required. Although there are losses associated with the cooling system required, the efficiency greater than 95% can be obtained [26]. Nevertheless, superconductor winding research over the last 30 years has still not matured for commercial application [27]. This energy storage technique is also presented in [19], [26], [28].

Electrochemical Energy Storage

Energy is stored as chemical energy. Batteries, fuel-cells, supercapacitors and supercapatteries are technologies for electrochemical energy storage. Electrochemical energy storage has a high power density and low energy density technology relative to other type of energy storage. The Ragone plot in Figure 1.4 illustrates the specific power versus specific energy of various types of electrochemical energy storage technologies.

Batteries

There are many types of battery available in the market such as Lithium-ion (Li-ion), sodium sulphur (NaS) and the related zebra battery (Na-NiCl₂), nickel cadmium (NiCd), nickel metal hydride (Ni-MeH), and lead acid (Pb-acid) batteries. For power system application where large scale is required, the options available are NiCd, NaS and Li-ion. Efficiency of NiCd batteries varies from about 60% to 80% depending on the technology used in manufacturing process. NaS efficiency is about 89-92%. Li-ion is the most developed technology because it has the highest energy density (80 to 150Wh/kg) and efficiency of 98% [19]. Generally, a battery has low energy density due to the fact that the weight of battery is occupied by inert material such as water, separator, connector, terminal and the container itself. Further discussion about battery application in power system can be found in numerous papers [19], [20], [25], [29]–[34]. Examples of commercially available systems are: (1) Golden Valley Electric Association battery energy storage system project in Alaska [20]. The system employs four parallel strings of 3,440 NiCd pocket plate battery cells, type SBH920. The system was commission in 2003 can delivers up to 46MW power with a specified run time of 15 minutes; (2) 4MW NAS and 0.1MW Li-ion battery energy storage system installed with a photovoltaic plant in Miyoko Island, Japan [35].

Fuel-Cells

These are different from batteries owing to the external fuel storage. Fuel-cells can continuously interchange the chemical and electrical quite efficiently. The synthetic fuels that have been proposed are hydrogen, methanol, ammonia and methane. Focus has been given to hydrogen-oxygen fuel cells because of their good energy density, low pollution and high cell efficiency. The efficiency is 40-60%. However, if waste heat is captured and reused in cogeneration process, the efficiency can be improved of up to 80%. Publications related to fuel-cell are [21], [25], [36]–[39].

Supercapacitors

The supercapacitor is a high power density energy storage device. It has higher power density but lower energy density compared to the battery. Thus, the charge and the discharge rates of supercapacitors are higher than those of batteries.

Supercapacitors efficiencies can be greater than 95%. A number of papers discuss supercapacitors used to complement batteries in power system applications, especially because the supercapacitors have very high lifecycle compared to batteries. This energy storage element is discussed in [19], [26], [30], [37], [40].

Hybrid Supercapacitor-Battery

The devices are being researched to have higher energy density than supercapacitors and higher power density compared to batteries as illustrated in Figure 1.4. The aim is to bridge the gap between battery and supercapacitor. An example is the “Supercapattery” which is a type of hybrid supercapacitor-battery and is under research at the University of Nottingham [27], [41]. The Supercapattery efficiency has achieved 90% and can to be further improved.

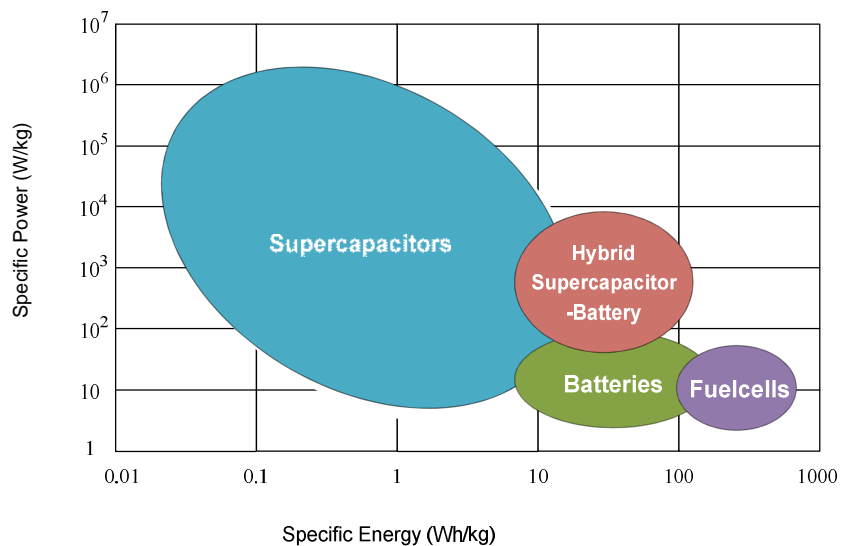


Figure 1.4: Ragone plot showing the specific power vs. specific energy of electrochemical energy storage

1.2.1 Comparison of Energy Storage

The different types of energy storage technologies use different physical principles, storage mediums and often different power conversion systems and power conversion control systems. Consequently, direct comparison between the technologies is challenging. Common characteristic of energy storage technology are identified to make a relevant comparison. The characteristics that are commonly used to compare energy storage technology are:

- Charge/discharge time: Time required to charge/discharge the storage element to its capacity
- Reverse time: Time required to regenerate electricity from the storage element
- Energy density: Amount of energy stored per unit volume.
- Power density: Amount of power stored per unit volume.
- Rated power: The amount of power that the energy storage unit produces under maximum continuous operation.
- Life cycle: Indicates how many charge/discharge cycles can be expected in the life of the device
- Round-trip Efficiency: The ratio of output energy to input energy over a charge/discharge cycle.
- Environmental impact: The impact to the environment can be due to construction, installation, waste produce etc.
- Capital cost: Initial cost required to install the energy storage per unit power.
- Cost per cycle: Cost to generate electricity per cycle of operation.
- Sitting suggestion and requirement: Best location of installation based on the energy storage requirement and operating principle.

A summary of comparisons between energy storage technologies are given in Table 1.1. The information in the table cannot be used for accurate assessment but is suitable for relative evaluation of energy storage technologies. It is noticeable that the battery has a wider range in all aspects of comparison. This is because there are many types of battery available in the market. Likewise, each energy storage technology can be optimized for a different purpose and application. Thus, the comparison of energy storage also needs to consider every aspect of purpose and application.

Table 1.1: Energy Storage Technology Comparison [19], [21]–[23], [26]

Characteristic \ Energy Storage	Supercapacitor	Battery	Flywheel	SMES	Fuel Cell	Pumped Hydro	CAES
Charge Time	1~30 s	0.3 ~ 5 h	0.5 ~ 2h	0.1 ~ 2 h	0.3 ~ 5 h	10 ~ 50 h	1 ~ 50 h
Reverse Time (s)	0.01	0.01	0.1	0.01	360	10	360
Energy Density (Wh/Kg)	1~10	30 ~ 130	5 ~ 50	10 ~ 50	20~30	0.2 ~ 0.7	20 ~ 50
Power Density (W/kg)	$10^3 \sim 10^5$	$10 \sim 10^2$	$10^2 \sim 10^4$	$10^3 \sim 10^4$	$10^2 \sim 10^3$	Not relevant	Not relevant
Rated Power (MW)	0.01 ~ 5	0.01 ~ 90	0.1 ~ 10	1 ~ 50	0.01 ~ 90	500 ~ 5000	100 ~ 1000
Life Cycle	$>10^6$ times	10^3 times	$10^4 \sim 10^6$ times	$> 10^6$ times	10^3	$10^4 \sim 10^6$ times	$10^4 \sim 10^5$ times
Efficiency	$>95\%$	60 ~ 95%	85~90%	$> 95 \%$	40-60%	70 ~ 85 %	75 ~ 80 %
Capital Cost (£/kW)	300 ~ 500	300 ~ 3000	3000 ~ 5000	700 ~ 3000	700 ~ 3000	700 ~ 2000	700 ~ 1500
Cost per Cycle (C/kWh - output)	2 ~ 20	9 ~ 100	3 ~ 20	6 ~ 100	6 ~ 100	0.1 ~ 1.5	2 ~ 5
Sitting suggestion / Requirement	Close to load terminal	Close to load terminal	Close to load terminal	Substations, generator terminal	Close to load terminal	Geological consideration	Geological Consideration

1.2.2 Role of energy Storage in Power System

Applications can be categorized into three major functions according to the duration of energy charge/discharge [23]:

- **Energy management** – For this function the energy storage is required to serve for longest duration with respect to other functions. Typically, from minutes up to a few hours. Generally, they are used for load leveling or peak load shaving. Large amount of energy may be handled for this purpose which can be up to 10kWH.
- **Power bridging** – For this purpose, the energy storage required is between seconds to minutes to ensure continuous supply of electricity. This is known as spinning reserve.
- **Power quality improvement** – For this application, energy storage is needed over the millisecond range. Hence, energy storage with higher power density is preferred. It needs to be able to discharge rapidly in order to increase the power quality in terms of voltage, current and frequency.

Storage for Energy Management

Load demand is not always constant. It depends on many factors and hence varies with respect to time. Numerous studies focusing on load forecasting have been undertaken in the last decades [42]–[44]. The typical total load profile curve for 24 hours is shown in Figure 1.5. The load demand increases until it reaches a certain peak and then decreases to a lower value. Then it climbs again to another peak and reduces to another lower value. In general, there are several peaks in a 24 hour period. The load demand reaches peaks only once or twice in a day. However, the electricity supplier has to size the total generation capacity to meet the peak plus operating reserve. Some generators may have to be run continuously but some are only running when the load peaks. Most of the time, the generators are running below their rated power because the demand is less than the generators rated value. It is estimated that 20% of generation are required to only meet the peak demand [45].

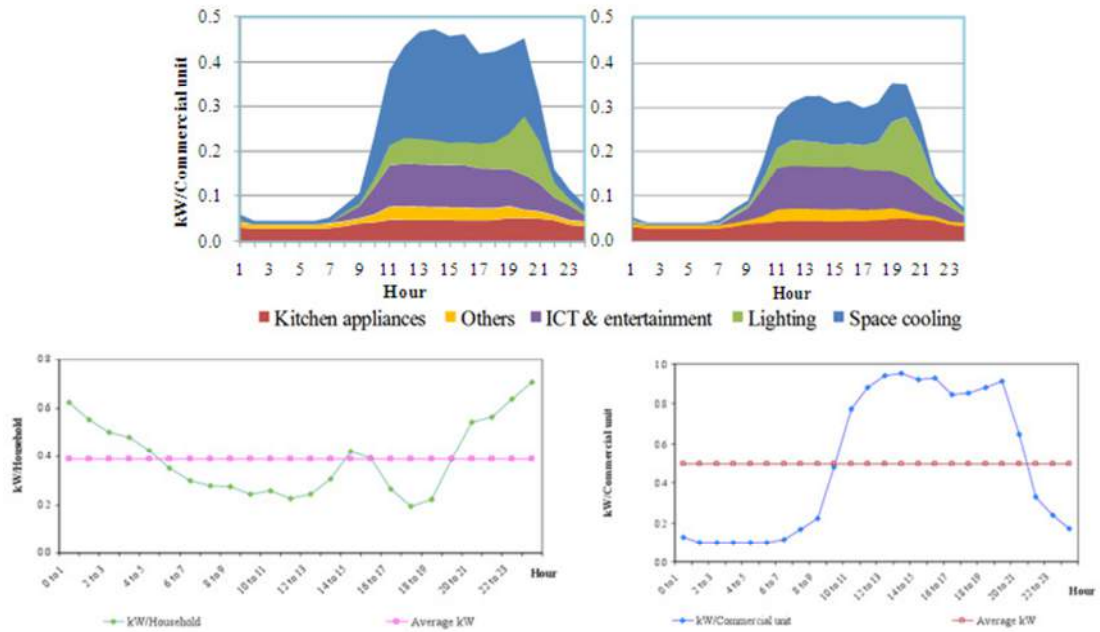


Figure 1.5: Typical load demand pattern [46]

An option to tackle the problem of varying demand is to have energy storage. The electricity can be stored when the demand is low to be used when the demand is high. This is referred to as load leveling or peak load shaving [47], [48]. The advantage of having energy storage for this function is that the generator can always be operated close to their rated value for greater efficiency even if the load is less than the total generated value. The stored energy can be used when the load is peaks and thus, no additional generator is required to supply peak load.

It is then possible to have generation supplying only average power. This will reduce the need for additional generators and also optimize the generators available in the system. It will also help to reduce the carbon footprint because all generators can be operated efficiently and many of the energy storage technologies are environmentally friendly compared to the typical fossil power plant such as coal and gas. Moreover, the overall capital and operating cost are also significantly reduced.

In addition, the energy storage is also employed to handle the intermittency of renewable energy systems to smooth the output from the energy sources. Example of papers discussing this concept are [49], [50].

Energy Storage to Bridge Power

The energy storage can be used to bridge power or also known as spinning reserve. It supplies energy for contingency for short intervals of time in order to meet demand in case of sudden increase in load or disruption in the power system. Spinning reserve are reserves that are already connected to grid and can come on-line between a few seconds to 30 minutes. After this time, backup generators can be started and expected to be online after the spinning reserve has been consumed. Conventionally, this spinning reserve is realized by increasing the output from an already connected generator. To make this possible, some generators may be running at less than their rated power. Spinning reserve can also be achieved by energy storage system, for instance as discussed in [51], [52]. An advantage of using energy storage as spinning reserve is that the generators supplying less than peak power can be operated at optimum rated value and thus will contribute to lower CO₂ emissions.

Achieving High Power Quality by Energy Storage

Power quality is a term used to represent the voltage and current quality. The concern is the deviation of voltage and current from ideal conditions. This includes magnitude, phase angle and frequency variation. The interest in power quality has increased due to an increase of equipment sensitivity to voltage disturbances and the fact that power quality is now measurable. Conventionally, power quality is achieved by shunt resistor brakes, static var compensator (SVC), boiler governor control and steam reserve in a fossil-fuel plant [53]. Energy storage can also plays a role to improve power quality in power system grid through voltage sag mitigation [38], [54]–[56], frequency regulation [28], [56], [57], harmonic compensation [55], [58] and unbalanced load control [58], [59].

1.3 Wind Turbine Systems

This section presents an overview of wind turbine systems widely used. There are four types of wind turbine generator technologies most commonly installed: (a) Constant Speed Squirrel-Cage Induction Generator (CSIG), (b) Doubly Fed Induction Generator (DFIG), (c) Brushless Generator with Gear and Full-Converter (BGFC), and (d) Direct-Drive Generator System (DDGS) [60]. The block diagrams of the wind turbine systems are shown in Figure 1.6.

Despite the fact that the CSIG is cheap, due to the simple components used, the constant speed causes significant power quality problems. This is because being fixed speed, there is no inertial smoothing effect of the transmitted power so that all wind power variations are immediately fed to the grid. This causes voltage fluctuation due to the grid impedance. The constant speed also reduces the power extracted relative to the wind power available. The DFIG, BGFC and DDGS are variable speed wind turbine systems employing power converters. These are capable of delivering better power quality; they can capture higher energy and produce less noise. Of all the variable wind turbine systems, the DFIG system is the cheapest. The DFIG can be controlled using a power converter in the rotor circuit. If the speed variation is restricted to a limited slip about synchronization speed, as is the case for wind generator applications, the rotor power is only a fraction of the stator power (and hence the total power generated) so that the power converter is of reduced rating and so, cheaper. The DFIG does have the disadvantage of a direct grid connection so that voltage dips on the grid can cause significant flux transients and high rotor current to flow. This requires protective measures e.g. a rotor crow bar circuit [61], [62]. However, even with this extra protection circuit, the DFIG is still the cheapest option and moreover, uses traditional and hence reliable technology. Therefore, the DFIG wind turbine system is chosen to be modelled in this thesis as seen in Chapter 2.

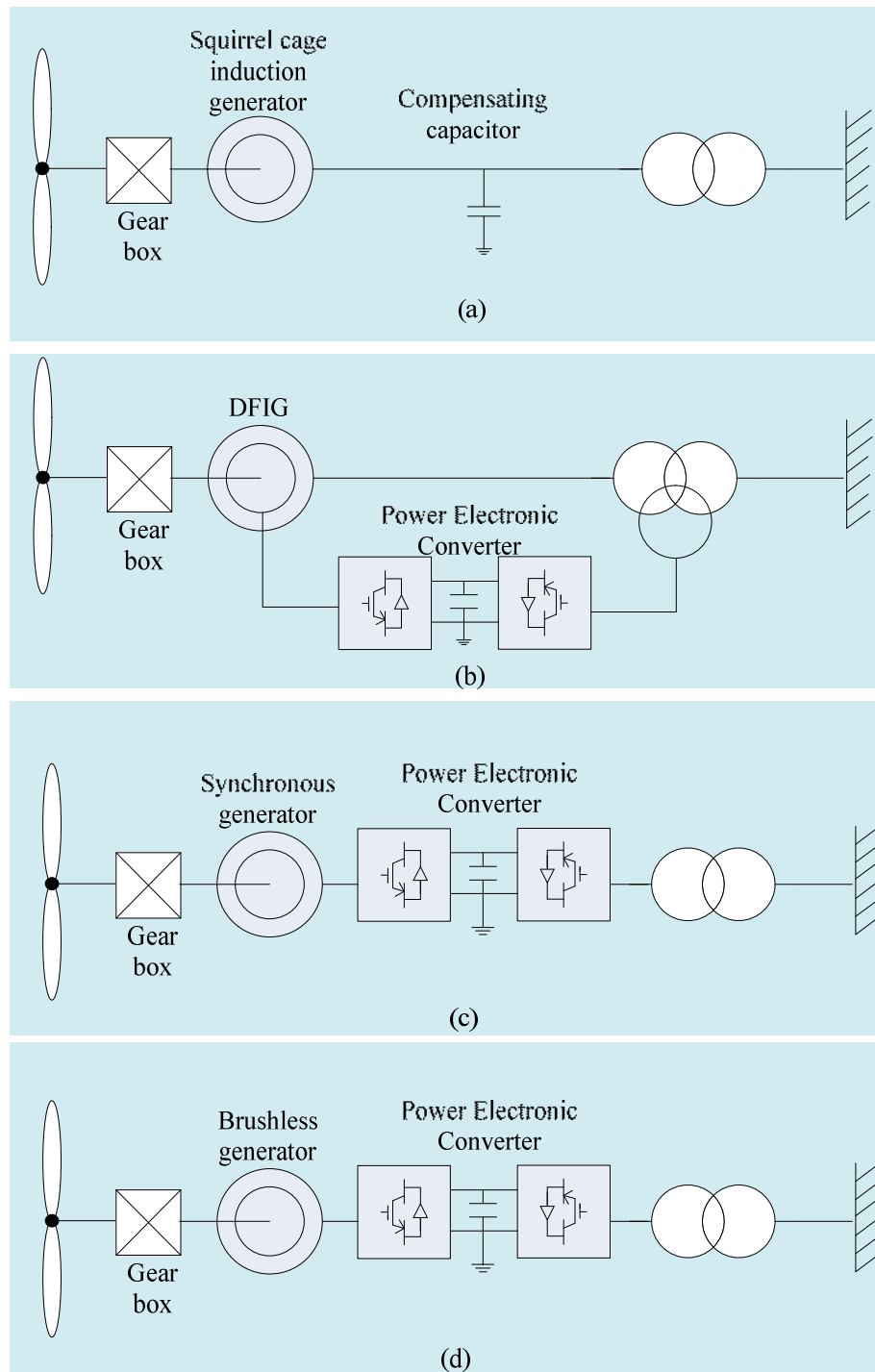


Figure 1.6: Different types of wind turbine generator systems (a) CSIG, (b) DFIG, (c) BGFC and (d) DDGS

1.4 Constant Power Loads

Nowadays, power electronics converter loads are extensively used in power system. Many applications involving power electronic control draw or deliver constant power or a power that is slowly changing so can be considered constant over short time period. Examples are renewable energy generation in which deliver a constant power over short periods (seconds). Energy storage systems also have power demand control. Tightly regulated power electronic converters behave as CPLs. As will be shown, a common example of a CPL is a DC/AC inverter feeding a motor under tight current and speed control as shown in Figure 1.7. The CPL is connected to the AC power via a DC link filter and a controlled or uncontrolled rectifier at the front end.

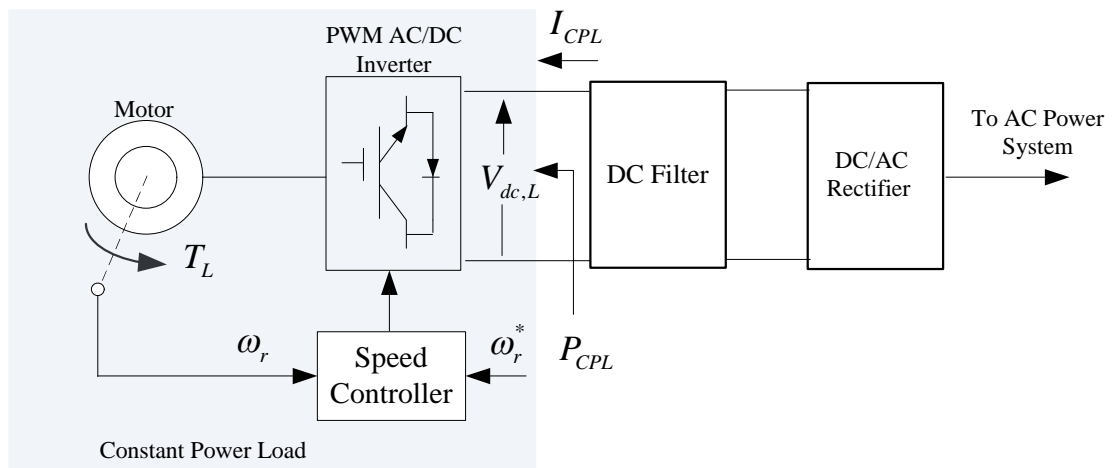


Figure 1.7: An actuator drive system behaving as a CPL system with a rectifier at the front end connected to the AC power

Since the speed, ω_r is regulated, it is almost constant in steady state. Over a short period of time, the load torque, T_L maybe considered constant. Therefore, the output power, P_{out} can also be considered constant because $P_{out} = T_L \omega_r$. Assuming the losses are negligible, the power to the AC/DC inverter, P_{CPL} is therefore also constant. Hence, the inverter feeding a regulated drive looks like a CPL to the AC power system. The current into the CPL can be defined as:

$$I_{CPL} = \frac{P_{CPL}}{V_{dc,L}} \quad (1.1)$$

where $V_{dc,L}$ is the DC voltage across the CPL. The partial differential of (1.1) is:

$$\partial I_{CPL} = -\frac{P_{CPL,o}}{V_{dc,Lo}^2} \partial V_{dc,L} + \frac{1}{V_{dc,o}} \partial P_{CPL} \quad (1.2)$$

where $P_{CPL,o}$ and $V_{dc,Lo}$ are P_{CPL} and $V_{dc,L}$ at an operating point, respectively. At each operating point the P_{CPL} is constant. Hence, $\partial P_{CPL} = 0$, thus:

$$\frac{\partial V_{dc,L}}{\partial I_{CPL}} = -\frac{V_{dc,Lo}^2}{P_{CPL,o}} \quad (1.3)$$

As shown in Figure 1.8, when $V_{dc,L}$ decreases, I_{CPL} increases so that P_{CPL} is kept constant. Therefore, the incremental impedance, Z_{CPL} is negative as given in (1.3). Thus, the CPL has a negative impedance behaviour which influences the small-signal stability of the power system [63], [64].

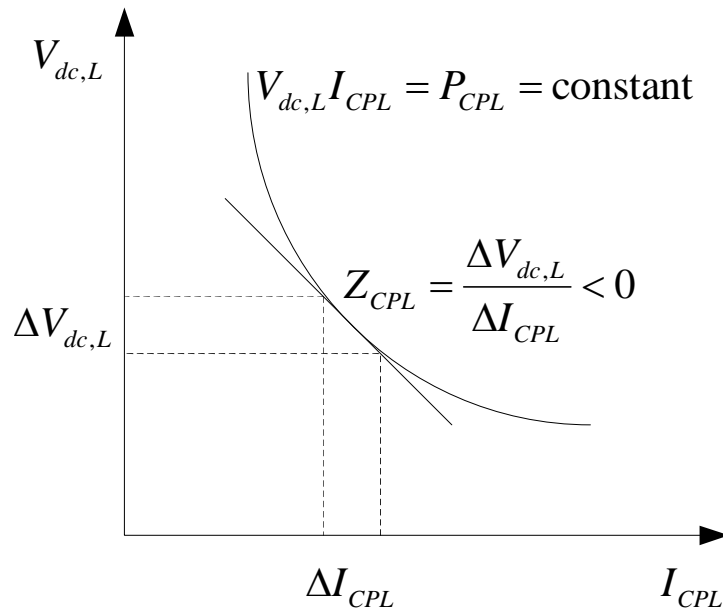


Figure 1.8: Negative impedance characteristic of CPL

For the stability analysis of the system with the AC power system with CPL, the system has to be modelled. Three possible methods of modelling are: State-Space

Averaging (SSA) [65], Average-Value (AV) [66] and dq -transformation [67], [68]. The SSA method requires high-order mathematical models. Meanwhile, the AV method does not provide information on the AC side. Both SSA and AV methods are difficult for power systems with vector-controlled converters. However, the dq -transformation modelling method produces a lower order model and can also be used for modelling the power system with vector-controlled converters. The analysis with multiple-converters also is easier with the dq -transformation method [68]. Therefore, the dq -modelling method is chosen to be used in this thesis. The power systems modelled using this technique is presented in chapter 4 and chapter 5 for the CPL with a controlled PWM rectifier and an uncontrolled diode-bridge rectifier, respectively.

1.5 Definition of a Weak Grid

The term ‘weak grid’ is used to describe a transmission line when voltage level to the user varies significantly with load. The grid impedance in a weak grid is relatively high thus causing the voltage to significantly vary. It is normally found in remote places where the feeders are long and is operated at a medium voltage level. When the load is high, the voltage level will drop significantly due to the high impedance.

For simplicity, a transmission line and a grid is modelled by an impedance, $Z_t = R_t + j\omega L_t$, where R_t and L_t are the resistance and inductance, respectively. The impedance is connected to an AC voltage source. The grid can be characterized by Short Circuit Capacity (SCC) that is the amount of power flowing at a given point in case of a short circuit. The SCC depends on the rated voltage and the absolute value of grid impedance which can be determined at a particular point. The grid strength can be quantified by the Short Circuit Ratio (SCR). The SCR can be defined as:

$$SCR = \frac{SCC}{S_r} = \frac{V_n^2}{Z_g S_r} \quad (1.4)$$

where, S_r is rated apparent power of the load or generator connected to the grid, V_n is the nominal voltage and Z_g is the grid impedance. Lower SCR means weaker grid.

Referring to [69], the following SCR value is used to classify the strength of AC/DC system:

1. Stiff system has SCR value more than 3
2. Weak system has SCR between 2 and 3
3. Very weak system has SCR lower than 2

The SCR is the value of admittance at fundamental frequency in per unit, Y_{pu} at a rated apparent power, S_r and a nominal voltage, V_n . Thus:

$$Z_{pu} = \frac{1}{SCR} = \frac{1}{Y_{pu}} \quad (1.5)$$

where, Z_{pu} is the impedance in per unit. Hence, the grid impedance in ohm, Z_g is:

$$Z_g = \frac{Z_{pu} V_n^2}{S_r} \quad (1.6)$$

Assuming the grid impedance is dominated by the transmission line reactance, then $L_t = Z_t / \omega$, at the fundamental frequency, ω . Thus, L_t can be calculated using (1.6). Meanwhile, R_t can be calculated if the ratio between reactance and resistance (X/R ratio) is known and the reactance, $X_t = \omega L_t$ has been determined. Note that, the range of X/R ratio of a transmission line is between 2 to 16 with typical a value of 5. However, a weak grid has an ohmic characteristic with lower X/R ratio [70].

1.6 Contributions of this Thesis

The research work proposes a simplified model of DFIG wind turbine under maximum power point tracking. The thesis compared the simplified model with the detail model. The simplified model reduces the simulation times required in the detailed model with an acceptable accuracy for certain applications such as analyses of efficiency and stability found later in the thesis.

Another contribution of this thesis is to analyse the potential benefit of energy storage system to improve overall system efficiency of a remote grid fed by a transmission line and a local fluctuating renewable power generation. The parameters that influence the efficiency gain are identified. For real renewable power fluctuations an algorithm for deriving the system parameters for efficiency gain is derived. Such an algorithm has not been derived before.

Another contribution is that of a stability analysis of the above remote grid feeding a constant power load (CPL). It will be shown that a CPL is fed by an active PWM rectifier is very stable whilst a CPL fed by diode bridge rectifier can be unstable. It is shown that instability can be overcome by the control of an auxiliary unit such as an energy storage unit. The stability analysis and the control method proposed in this thesis has not been reported before.

1.7 Thesis Structure

The thesis is structured as follow:

Chapter 1: As presented, this chapter has given the background and motivation towards the research work in this thesis. Also included are the problem statement and objectives to be achieved. A review of energy storage technologies, wind turbine systems, constant power loads and the definition of a weak grid have been given. The contributions of this thesis are also presented.

Chapter 2: This chapter discusses the modeling, control and simulation of a wind turbine feeding a DFIG using the PSCAD/EMTDC software. The wind turbine modeling includes the wind model, the aerodynamic model and the mechanical model. The control design of the wind turbine for maximum power point tracking and the pitch angle controller are also described. The DFIG mathematical modeling is briefly described and the vector control scheme is explained. A simplified model is then proposed in an effort to reduce simulation time for later complex system studies. The PSCAD simulation results and discussion are presented.

Chapter 3: In this chapter, the benefit of energy storage to improve the system efficiency in a system with fluctuating renewable power generation (specifically wind energy generation) is analysed. In this chapter, a simple mathematical analysis consistent with PSCAD simulation is undertaken to investigate the potential of energy storage to improve the system overall efficiency. Simulations with real wind profile are also performed and presented and compared with the simple analytical case.

Chapter 4: The stability of the power system consisting of a CPL connected via a controlled PWM rectifier is modelled and investigated with respect to system stability when power system also contains a wind farm and connected to a grid. This chapter will derive the dynamic equations for the system. The dq -modelling approach is employed for the mathematical modeling. The small-signal stability analysis based on eigenvalues is also discussed. The analysis is verified through PSCAD simulation.

Chapter 5: In this chapter, a CPL (e.g. a large motor drive load) is connected to the system by an uncontrolled diode-bridge rectifier. The chapter first proposes a relevant system formed by a weak transmission grid connection of a low SCR, a large multi-pulse diode bridge fed CPL, a large wind generator, and an energy storage system with active front end capability. The stability analysis is performed based on the mathematical derivation of the system. In this chapter, the system modeling is described. The eigenvalues analysis approach is used to perform the stability study. The method of participation factor analysis is employed to determine the influence of the unstable modes on the states and vice versa. Then, a proposed controller augmented in the energy storage converter feed is proposed to improve the system stability. The methodology is based on mathematical analysis, stability analysis through MATLAB and verification through PSCAD simulation.

Chapter 6: This chapter concludes and summarizes the research work and findings of this thesis. Also given are useful suggestions for future researches to be continued from this project.

Chapter 2

Modeling and Simulation of Doubly-Fed Induction Generator Wind Turbine

2.1 Introduction

This chapter discusses the modeling, control and simulation of a wind turbine feeding a doubly-fed induction generator (DFIG) using the PSCAD/EMTDC software. The wind turbine modeling includes the wind model, the aerodynamic model and the mechanical model. The control of the wind turbine for maximum power tracking and the pitch angle control are also described. The DFIG mathematical modeling is briefly described and the vector control scheme used is explained. The system parameter selection, PSCAD simulation results and discussion are also described.

The system consists of a wind turbine which is connected to the DFIG and its electrical components through the mechanical drive train. The aerodynamic model uses the inputs wind speed, V_w , rotor speed, ω_r and blade pitch angle, β to produce an output mechanical torque, T_m . The mechanical drive train receives T_m and electrical torque, T_e from the DFIG and electrical system. Its output is ω_r . The DFIG and its electrical system are connected to a weak grid with voltage, U_t and current, I_t . The control system block plays an important role to ensure the system is operated at the particular settings and requirements. It provides β to the aerodynamic model and control signals to the PWM converters, α . The overall

block diagram and schematic diagram of the system are shown in Figure 2.1 and Figure 2.2, respectively.

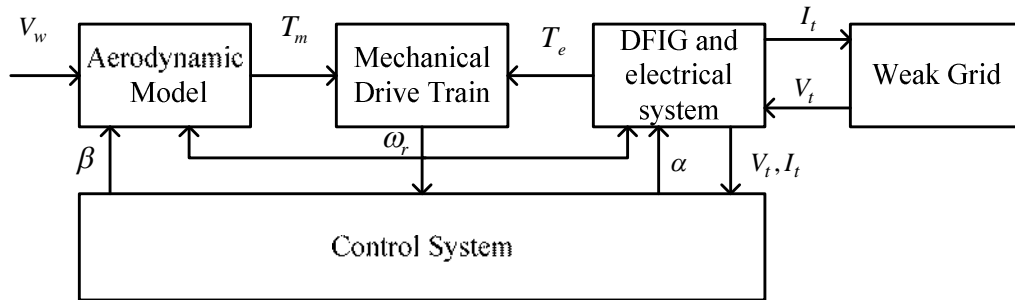


Figure 2.1: Overall block diagram of the weak grid-connected wind turbine system

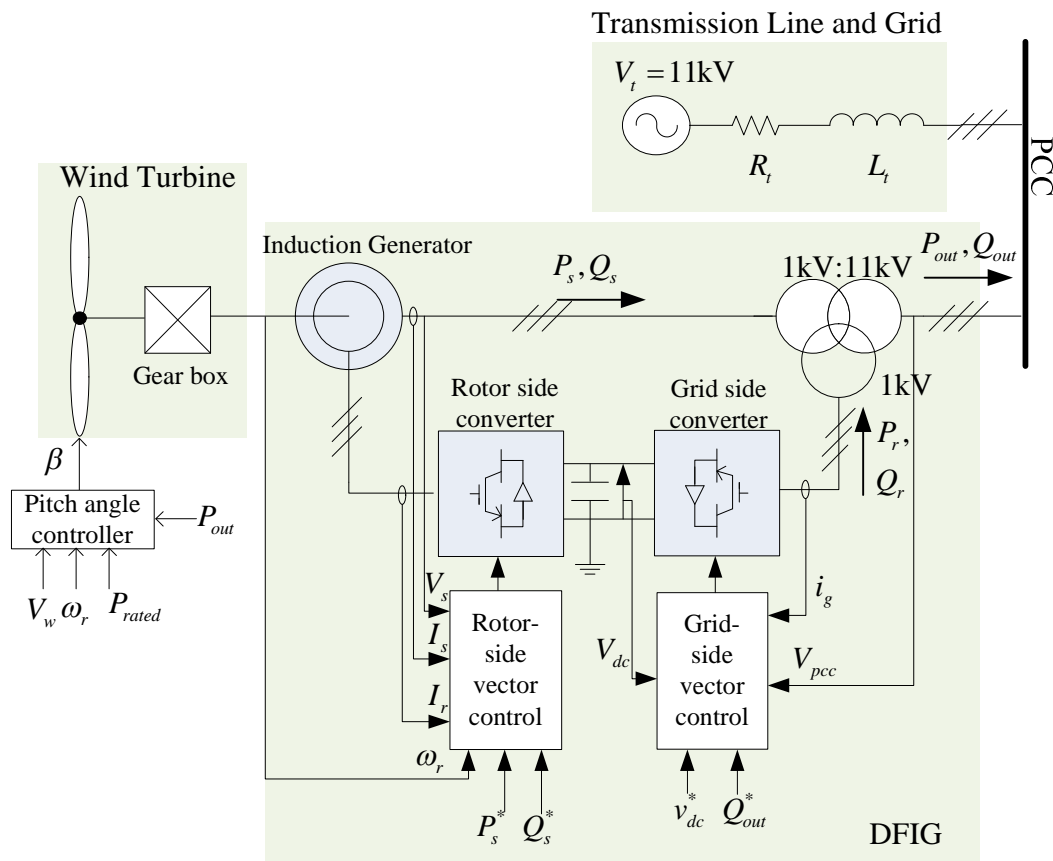


Figure 2.2: Schematic diagram of DFIG for wind turbine simulated in PSCAD

The wind turbine model will be discussed in section 2.2. A model of the system which is referred to as a detail model is elaborated in section 2.3. Then, a simplified model is discussed in section 2.3. The simplified model is proposed in order to reduce the simulation times required in the detail model. Finally, the summary of the chapter is given in section 2.5.

2.2 Wind Turbine Model

The aim of this section is to describe the wind turbine model that is used in this thesis. The PSCAD package has two classes of wind turbine model: MOD-2 and MOD-5 for a 3-bladed and a 2-bladed rotor system, respectively. The term MOD referring to the wind turbines model classification according to NASA standard [71]. Since the 3-bladed (MOD-2) wind turbine is more common, this model is selected for this thesis.

2.2.1 Aerodynamic Model in PSCAD

The aerodynamic model also known as the blade dynamic model in PSCAD is used in this thesis. The mechanical power and torque of the wind turbine are represented by:

$$P_m = 0.5\rho AC_p V_w^3 \quad (2.1)$$

$$T_m = \frac{P_m}{\omega_r} \quad (2.2)$$

where

$$C_p = 0.5(\lambda - 0.022\beta^2 - 5.6)e^{-0.17\lambda} \quad (2.3)$$

$$\lambda = \frac{2.237GV_w}{\omega_r} \quad (2.4)$$

The following notations are used:

P_m =mechanical power, W

T_m =mechanical torque, Nm

ρ = air density, kg/m³

A = turbine blade area, m²

V_w = wind speed, m/s

β = pitch angle, degrees

ω_r = rotor or shaft speed, rad/s

G = gear ratio

C_p = power coefficient

λ = tip speed ratio

The mechanical power is a function of power coefficient, blade area and cubic of wind speed. The power coefficient given by (2.3), is a function of tip speed ratio and pitch angle [72]. The equation (2.1) - (2.4) are embedded in the aerodynamic model block of Figure 2.1.

2.2.2 Mechanical Model

To keep the model simple, all mechanical components are lumped and modeled as a single rotating mass system which is expressed as a differential equation:

$$J \frac{d\omega_r}{dt} = T_m - T_e \quad (2.5)$$

where T_e and J are the electrical torque [Nm] and moment of inertia [s], respectively [73]. In this model, the mechanical friction and losses are neglected. The mechanical model block in PSCAD implements equation (2.5). It is contained in the mechanical drive block of Figure 2.1. T_m is obtained from wind turbine block and T_e is obtained from DFIG model of PSCAD. The shaft speed is an output from the mechanical drive train.

2.2.3 Control for Maximum Power Point Tracking

Three methods of controlling wind turbine are: constant torque mode (CTM), constant power mode (CPM) and maximum power point tracking (MPPT) [50]. Of the three methods, the MPPT receives highest attention because it captures the most electrical power from the wind turbine [74]–[77]. In addition, the MPPT is always stable for all shaft speeds when compared to the CTM or the CPM as detailed in [50]. Therefore, the MPPT is used throughout this thesis.

For the wind turbine represented by (2.1)–(2.4), the turbine mechanical power versus shaft speed characteristic and the mechanical torque versus shaft speed characteristic are illustrated in Figure 2.3 and Figure 2.4, respectively. From the Figure 2.3, to extract maximum power from the wind, the shaft speed has to be at an optimum value for a given wind speed. This is achieved if the electrical torque, T_e , is controlled as:

$$T_e = K_{opt} \omega_r^2 \quad (2.6)$$

as shown in Figure 2.4. The notation K_{opt} is a known constant for a wind turbine. By controlling the electrical torque, the shaft speed is driven to the optimum speed and thus captured maximum power, P_{opt} for a particular wind speed. This is given by:

$$P_{opt} = K_{opt} \omega_r^3 \quad (2.7)$$

The curves shown in Figure 2.3 are for pitch angle, $\beta = 0$. If $\beta \neq 0$, the MPPT curves are reduced.

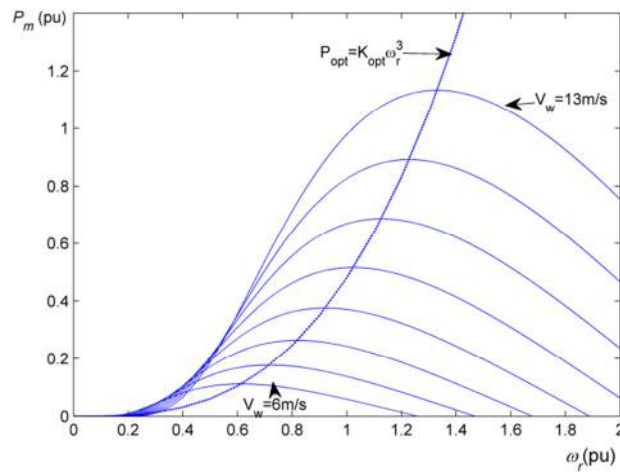


Figure 2.3. Turbine power-shaft speed characteristic for wind speed of 6-13m/s in 1m/s increments for a wind turbine represented by (2.1)-(2.4)

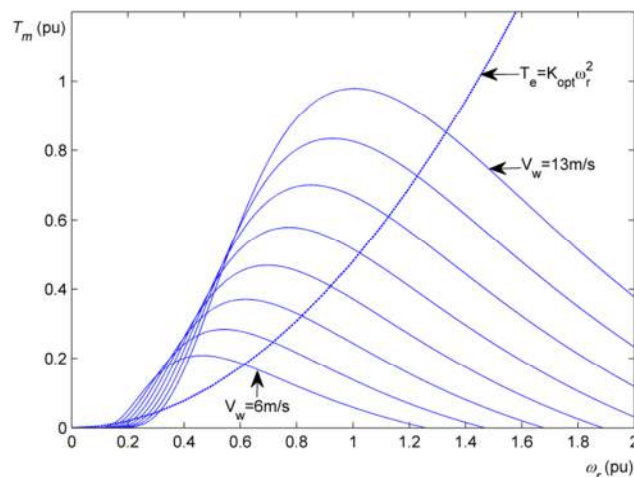


Figure 2.4. Mechanical torque-shaft speed characteristic for wind speed of 6-13m/s in 1m/s increments for a wind turbine represented by (2.1)-(2.4)

2.2.4 Pitch Angle Control

Various control schemes have been developed for the purpose of controlling the pitch angle for optimum power and to limit the power captured from wind turbine when the wind speed reaches certain limits, for example as reported in [77]–[80].

In this thesis only a simple controller is adopted to perform the duty. Figure 2.5 shows the block diagram of pitch controller used in this thesis. Rearranging(2.3), the pitch angle calculated, β_{cal} at a particular wind speed, V_w , shaft speed, ω_r and a rated output power of the DFIG, P_{rated} can be calculated by:

$$\beta_{cal} = \sqrt{45.45 \left(\lambda - 5.6 - \frac{2C_p}{e^{-0.17\lambda}} \right)} \quad (2.8)$$

where λ is given by (2.4) and

$$C_p = \frac{P_{rated}}{0.5\rho AV_w^3} \quad (2.9)$$

which is obtained by rearranging (2.1) at $P_m = P_{rated}$. The wind speed and shaft speed are instantaneous values measured. The calculated pitch angle is passed through rate limiter to limit the rate of change. The limiter is set to 5 degrees per second. This causes some time delay which is reflects in the actual pitch angle controller in a real implementation. The resulting pitch angle, β_{rl} is only supplied to the wind turbine model when the rated power is reached. The pitch angle is kept at zero when the measured DFIG output power, P_{out} (as shown in Figure 2.2) is less than the rated value in order to achieve the MPPT.

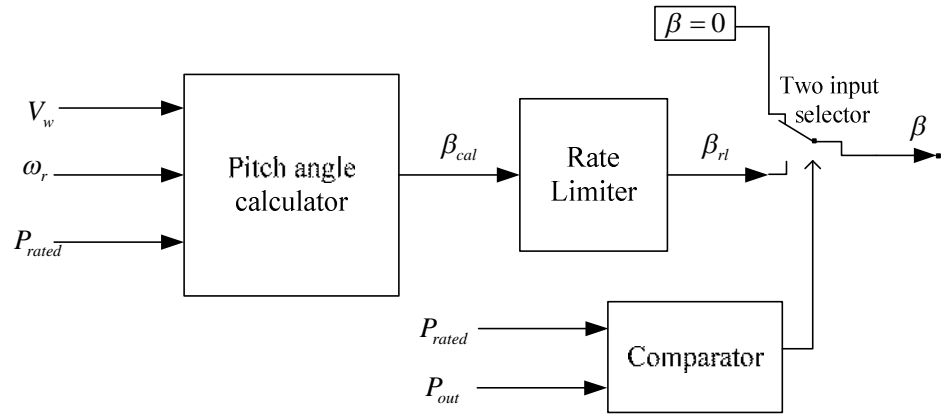


Figure 2.5: Pitch angle control scheme used in this thesis

2.2.5 Wind Model

Wind blows in a very random pattern. A wind model that can emulate the wind profile considering the ramp, gust, turbulence and noise components can be modeled as discussed in [72], [81]. The wind model is important to support numerous studies with regard to wind power generation and interconnection system.

In this thesis, a real or measured wind speed of 600s (10minutes) which is sampled at every second is used as plotted in Figure 2.6. The profile was obtained from a Chilean research group collaborating with the University of Nottingham [77].

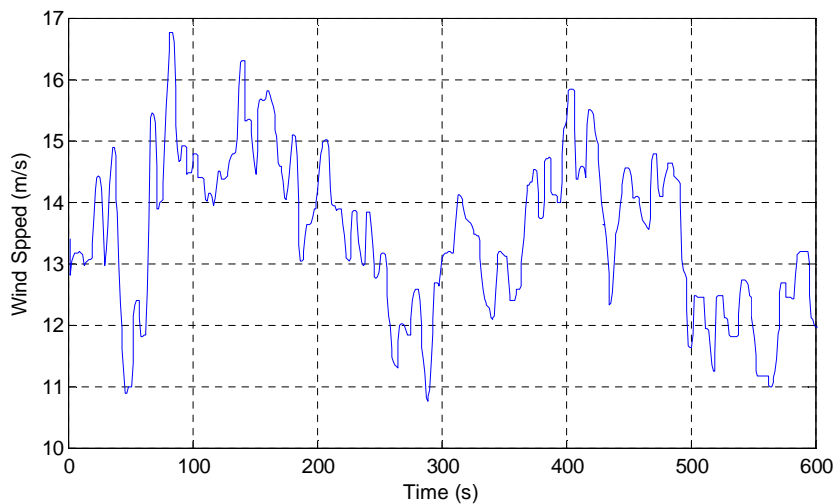


Figure 2.6: Real wind profile used in this thesis with average speed 13.65m/s and standard deviation 1.25m/s for 600s

The average wind speed of the wind profile can be varied by adding a value to the sampled data. The perturbation of the wind profile can be defined by its standard deviation [77]:

$$\sigma = \sqrt{\frac{\sum_{i=1}^N (V_{wi} - \overline{V_w})^2}{N}} \quad (2.10)$$

where N is the sample number, V_{wi} is the i^{th} sample of the data and $\overline{V_w}$ is the average value of the wind speed. The perturbation can also be varied by varying the standard deviation while keeping the average wind speed at the same value. If the perturbation is scaled by a constant, k , the new standard deviation, σ_n is:

$$\sigma_n = k\sigma \quad (2.11)$$

and the i^{th} sample of the new wind profile is:

$$V_{win} = k(V_{wi} - \overline{V_w}) + \overline{V_w} \quad (2.12)$$

In this way a profile of programmable average and mean variation can be used for investigations. The Matlab code written to obtain a new set of wind speed data at different wind averages perturbations is given in Appendix A. In some cases a step of wind speed or constant wind speed are used to investigate a particular situation.

2.3 DFIG Modeling and Control

2.3.1 DFIG Modeling

The DFIG is a wound rotor induction motor connected to the system by a power electronics converter. The stator winding is directly connected to the mains while the rotor winding is connected by a power electronics converter to the system as shown in Figure 2.2. Further details of the mathematical model of the DFIG is discussed in [80]. In this thesis, the model of wound rotor induction machines is obtained from the PSCAD library. An average model of the PWM voltage source converter is used

in this thesis. The average model is a non-switching model that effectively defines the dynamic input and output characteristics of the input and output voltages and currents considering only the AC fundamental quantities. It is used to reduce simulation time since this study is not focusing on the converter switching and harmonics. It is modelled in PSCAD and added to the PSCAD library. The detail is given in Appendix B. The converter is controlled based on the vector control scheme which is described in the section 2.3.2. The grid is modelled by resistance and inductance and a voltage source. The grid strength can be determined by its SCR as discussed in the section 1.5.

2.3.2 Vector Control Scheme of DFIG converters

There are two converters in the system. The converter connected directly to the rotor winding of the induction machine is called the rotor side converter while the converter connected to the grid side is called the grid side converter. The vector control scheme of the rotor converter and the grid side converter are discussed in the section 2.3.2.1 and 2.3.2.2, respectively.

2.3.2.1 Vector control of rotor side PWM voltage source converter

The rotor side converter control objective is to control the stator active power, P_s and stator reactive power, Q_s . The reference stator active power, P_s^* is derived from the maximum power tracking. However, the maximum power tracking gives the overall output power of the DFIG, P_{opt} . Neglecting losses, $P_{opt} = P_s(1-s)$, where s is the slip given by $s = (\omega_s - \omega_r) / \omega_s$ and ω_s is the synchronous frequency. Therefore, $P_s^* = P_{opt} / (1-s)$. The reference stator reactive power, Q_s^* is dependent on the system requirement.

For the purpose of vector control, the stator flux angular position needs to be determined. Two possible methods of determining the stator flux are direct stator flux orientation (DSFO) or indirect stator flux orientation (ISFO) [82], [83]. In DSFO, the stator flux is derived from the grid voltage. In ISFO, the stator flux is controlled by the rotor excitation and this ISFO is normally used in a stand-alone system when there is no voltage source. In this thesis, the DSFO is employed

because the voltage source is obtainable from the grid. The induction generator is controlled in a synchronously rotating dq -axis frame. The d -axis is oriented along the stator-flux vector position. Therefore, a decoupled control of stator side active power and reactive power is achieved.

The DFIG equations are now derived. These are used in the PSCAD DFIG model and are discussed here to provide the basis of controller design.

By measuring the stator current and voltage, the stator flux angular position, θ_s can be calculated by:

$$\begin{aligned}\psi_{s\alpha} &= \int (v_{s\alpha} - R_s i_{s\alpha}) dt \\ \psi_{s\beta} &= \int (v_{s\beta} - R_s i_{s\beta}) dt \\ \theta_s &= \int \omega_s dt = \tan^{-1} \left(\frac{\psi_{s\beta}}{\psi_{s\alpha}} \right)\end{aligned}\quad (2.13)$$

where $\psi_{s\alpha}$, $\psi_{s\beta}$, $v_{s\alpha}$, $v_{s\beta}$, $i_{s\alpha}$ and $i_{s\beta}$ are the stationary α and β -axis stator fluxes, voltages and currents, respectively. ω_s is the electrical angular velocity of the stator flux. Aligning the d -axis of the reference frame along the stator flux vector position results in $\psi_{sq} = 0$. Assuming that the stator resistance is small, the stator flux can be considered constant. The DFIG equation with the state variables i_{rd} and i_{rq} can be written as:

$$\begin{aligned}u_{sd} &= 0 \\ u_s &= u_{sq} = \omega_s \psi_{sd} \\ u_{rd} &= R_r i_{rd} + \sigma L_r \frac{di_{rd}}{dt} - \omega_{slip} \sigma L_r i_{rq} \\ u_{rq} &= R_r i_{rq} + \sigma L_r \frac{di_{rq}}{dt} + \omega_{slip} (L_{mm} i_{ms} + \sigma L_r i_{rd}) \\ \psi_{sd} &= \psi_s = L_o i_{ms} = L_s i_{sd} + L_o i_{rd} \\ \psi_{sq} &= 0 = L_s i_{sq} + L_o i_{rq} \\ \psi_{rd} &= \frac{L_o^2}{L_s} i_{ms} + \sigma L_r i_{rd} \\ \psi_{rq} &= \sigma L_r i_{rq}\end{aligned}\quad (2.14)$$

where:

$$\begin{aligned}
\omega_s &= \omega_e \\
\omega_{slip} &= \omega_s - \omega_r \\
\sigma &= 1 - \frac{L_o^2}{L_s L_r} \\
L_{mm} &= \frac{L_o^2}{L_s}
\end{aligned} \tag{2.15}$$

where u_s is the magnitude of the stator phase voltage, ω_e is the electrical angular velocity of the stator voltage, ψ_s is the magnitude of the stator flux linkage and i_{ms} is the magnetizing current of the generator [80]. The subscript d and q represent the rotating d and q - axis component value of the respective quantity.

Defining:

$$\begin{aligned}
\dot{u}'_{rd} &= u_{rd} + \omega_{slip} \sigma L_r i_{rq} \\
\dot{u}'_{rq} &= u_{rq} + \omega_{slip} (L_{mm} i_{ms} + \sigma L_r i_{rd})
\end{aligned} \tag{2.16}$$

the transfer functions between u'_r and i_r can be written as in (2.17).

$$\frac{\dot{i}_{rd}(s)}{\dot{u}'_{rd}(s)} = \frac{\dot{i}_{rq}(s)}{\dot{u}'_{rq}(s)} = \frac{1}{\sigma L_r s + R_r} \tag{2.17}$$

If we apply the voltage compensation terms as in Figure 2.7, i.e.:

$$\begin{aligned}
u_{rdcomp} &= \omega_{slip} \sigma L_r i_{rq} \\
u_{rqcomp} &= \omega_{slip} (L_{mm} i_{ms} + \sigma L_r i_{rd})
\end{aligned} \tag{2.18}$$

then, the PI controller sees a linear plant given by (2.17). This shows that the rotor current can be regulated by regulating rotor voltage and that (2.17) is used for current loop control design.

The stator active and reactive powers are given by:

$$\begin{aligned}
 P_s &= \frac{3}{2} (u_{sd} i_{sd} + u_{sq} i_{sq}) \approx -\frac{3}{2} \frac{L_o}{L_s} u_s i_{rq} \text{ for } R_s \approx 0 \\
 Q_s &= \frac{3}{2} (u_{sq} i_{sd} - u_{sd} i_{sq}) = \frac{3}{2} u_s \left(\frac{u_s}{\omega_s L_s} - \frac{L_o}{L_s} i_{rd} \right)
 \end{aligned} \tag{2.19}$$

Assuming that the stator voltage is constant, the stator active and reactive power can thus be regulated by current i_{rq} and i_{rd} , respectively.

Figure 2.7 shows the block diagram for the vector control scheme of rotor side PWM voltage source converter. The stator voltage and current are measured and transformed to its alpha and beta components and used to calculate the stator flux angle by implementing equation(2.13). Then, stator current and stator voltage are transformed to their dq -components aligned along the stator flux vector position. The dq -components of stator current and voltage are used to calculate the stator active and reactive power using the equation(2.19). The slip angular position, $\theta_{slip} = \theta_s - \theta_r$ is calculated where θ_r is the rotor angular position. The rotor current, i_r is transformed to the dq -components oriented along the slip angular position. A cascade control is utilized in this system. The outer loop control stator active and reactive power, while the inner loop control the i_{rq} and i_{rd} . The u_{rabc}^* is the three phase reference value of the rotor side converter voltage obtained from the reference values of the rotor voltage in d-and q –axis (u_{rd} and u_{rq}) oriented at θ_{slip} .

2.3.2.2 Vector control of grid side PWM voltage source converter

The grid side converter aims to regulate the DC link voltage and the reactive current injection to the grid (assuming that the reactive power from the DFIG stator is zero). This reactive power can be set to zero to maintain zero reactive power exchange between the grid and the grid side converter. The schematic diagram of the grid side converter is shown in Figure 2.9.

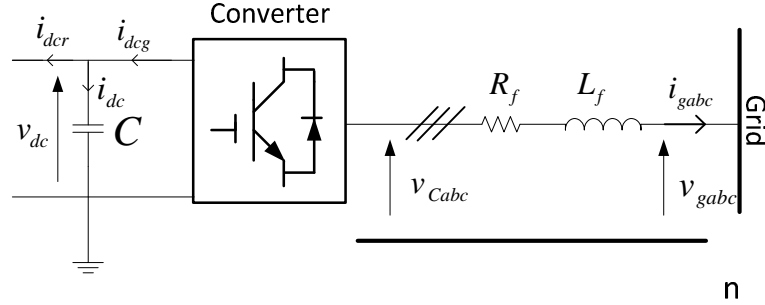


Figure 2.9: Schematic diagram of grid side voltage source converter connected to grid

Using Kirchoff voltage law we have (2.20).

$$v_{Cabc} - v_{gabc} = R_f i_{gabc} + L_f \frac{di_{gabc}}{dt} \quad (2.20)$$

The equation (2.20) can be written in dq -rotating frame with a frequency ω_e as shown in (2.21).

$$\begin{aligned} v_{gd} &= R_f i_{gd} + L_f \frac{di_{gd}}{dt} - \omega_e L_f i_{gq} + v_{Cd} \\ v_{gq} &= R_f i_{gq} + L_f \frac{di_{gq}}{dt} + \omega_e L_f i_{gd} + v_{Cq} \end{aligned} \quad (2.21)$$

Since the d -axis of the rotating frame is oriented on the grid voltage vector, $v_{gq} = 0$ and $v_{gd} = v_g$. Meanwhile, the active and reactive power flow between the grid and converter are given by (2.22).

$$\begin{aligned} P_g &= \frac{3}{2} (v_{gd} i_{gd} + v_{gq} i_{gq}) = \frac{3}{2} v_{gd} i_{gd} \\ Q_g &= \frac{3}{2} (v_{gq} i_{gd} - v_{gd} i_{gq}) = -\frac{3}{2} v_{gd} i_{gq} \end{aligned} \quad (2.22)$$

Defining (2.23):

$$\begin{aligned} v_{gd}' &= v_{Cd} - v_{gd} + w_e L_f i_{gq}' \\ v_{gq}' &= v_{Cq} - v_{gq} - w_e L_f i_{gd}' \end{aligned} \quad (2.23)$$

means that, the transfer function between current and voltage is:

$$\frac{i_{gd}'(s)}{u_{gd}'(s)} = \frac{i_{gq}'(s)}{u_{gq}'(s)} = \frac{1}{L_f s + R_f} \quad (2.24)$$

Hence the addition of the compensation terms of (2.23) – see Figure 2.10 – means the PI controllers see a linear plant defined by (2.24).

Neglecting harmonics and losses, we have (2.25),

$$\begin{aligned} v_{dc} i_{dcg} &= \frac{3}{2} v_{gd} i_{gd} \\ v_{gd} &= \frac{m}{2} v_{dc} \\ i_{dcg} &= \frac{3}{4} m i_{gd} \\ C \frac{dv_{dc}}{dt} &= i_{dcg} - i_{dcr} \end{aligned} \quad (2.25)$$

where m is the modulation index of the grid side PWM converter.

The DC link voltage controller design can be carried out in the continuous domain. The inner loop i_{gd} assumes the idea case and $i_{dcr} = 0$. Therefore, from (2.25), the effective transfer function of the plant is given by:

$$\frac{v_{dc}(s)}{i_{gd}(s)} = \frac{3m}{4Cs} \quad (2.26)$$

The block diagram for vector control scheme of grid side converter is illustrated in Figure 2.10. The grid voltage angle is calculated and used for the transformation of voltage and current to their respective d - and q -components. The outer loop controls the DC voltage via the d -axis grid converter current, i_{gd} . The output reactive power, Q_{out} is regulated by the q -axis grid converter current, i_{gq} . Typically, the reactive

power is set to zero for unity power factor. The inner loop controls the currents, i_{gd} and i_{gq} via the voltages, v_{gd} and v_{gq} , respectively.

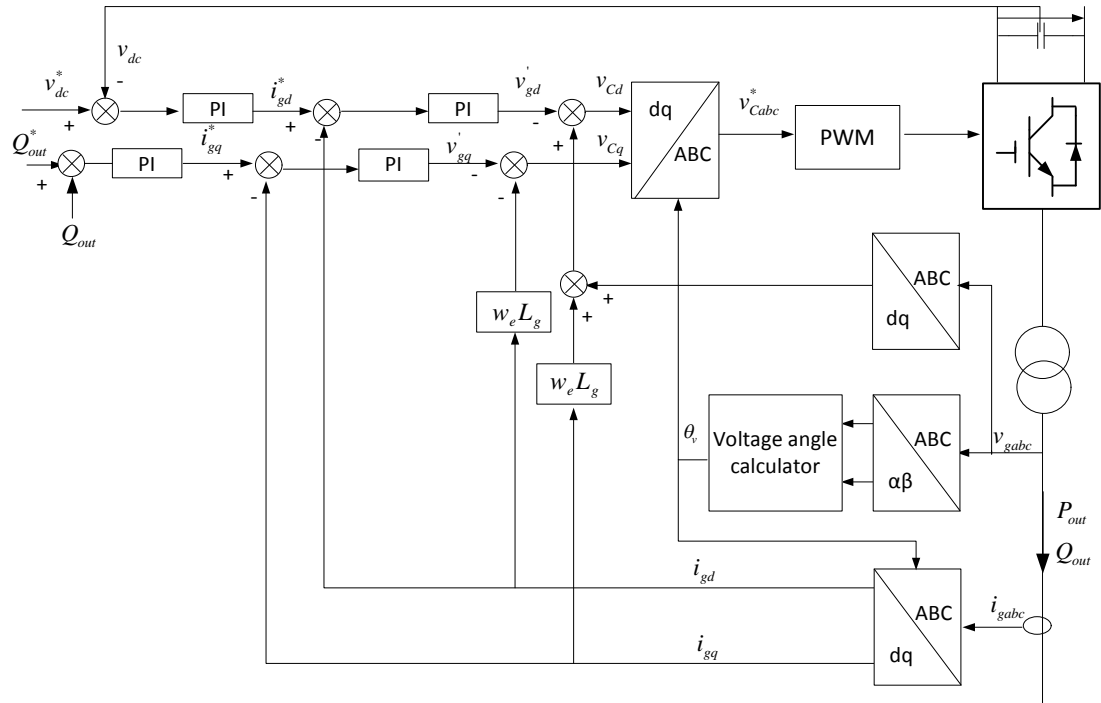


Figure 2.10: Vector control structure of the grid-side PWM converter

The schematic diagram for the cascaded power and current control loops of the grid side converter can be illustrated in Figure 2.11 making use of (2.24) and (2.26). Thus, the controller parameters can be designed by standard controller design methods. In this thesis, the Matlab *pidtool* function is employed in obtaining the controller parameters.

The control scheme of Figure 2.10 and Figure 2.11 are used in all grid connected connection of this thesis.

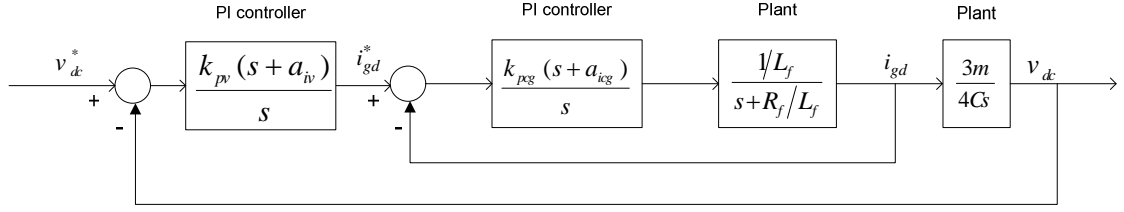


Figure 2.11: Cascaded power and current controller of the grid-side PWM converter

2.3.3 System Parameters for Simulation

In this thesis, the small wind farm is simulated by an equivalent aggregated 10-MVA DFIG [62], [84]. The wind turbine parameters and induction machine parameters employed are shown in Table 2.1 and Table 2.2 respectively. The data is obtained from [77]. The data is based on a database of typical wind turbines installed. Per unit values are based on the rated power and rated voltage of 10MVA and 1kV, respectively. The system frequency is 50 Hz. The DFIG is connected to 11kV transmission line via a 3 winding transformer of 1kV/1kV/11kV with leakage reactance of 0.12pu. The transformer model is available in PSCAD library.

Table 2.1.: Wind Turbine Parameters

Parameter	Value
Rated Power	10MVA
Rated angular mechanical speed	1000rpm
Turbine blade area, (A)	20111m ²
Air density (ρ)	1.225kg/m ³
Gear Ratio	55

Table 2.2: Wound Rotor Induction Machine Parameters

Parameters	Value
Rated power	10MVA
Rated voltage at stator	1kV
Base angular frequency (ω_s)	314.16rad/s
Stator/rotor turns ratio (n)	1
Angular moment of inertia (J)	2s
Stator resistance (R_s)	0.0066pu
Rotor resistance (R_r)	0.0044pu
Stator leakage inductance (L_s)	0.07pu
Rotor leakage inductance (L_r)	0.15pu
Magnetizing inductance (L_o)	3.07pu

For the above parameters, the wind turbine power characteristic versus wind speed is shown in Figure 2.12. The cut in speed is 0.24pu and cut-off speed is 2pu. Note that the base wind speed for the per unit calculation 12.5m/s which is producing 1pu of power. Therefore, the output power of the wind turbine hits the rated power at wind speed of 1pu that is at 12.5m/s. (The base wind speed for the per unit calculation, $V_{w,base} = 12.5\text{m/s}$). When the rated power is reached the pitch angle increases accordingly to maintain the output power to the rated value. The characteristics provide maximum power tracking for the wind turbine.

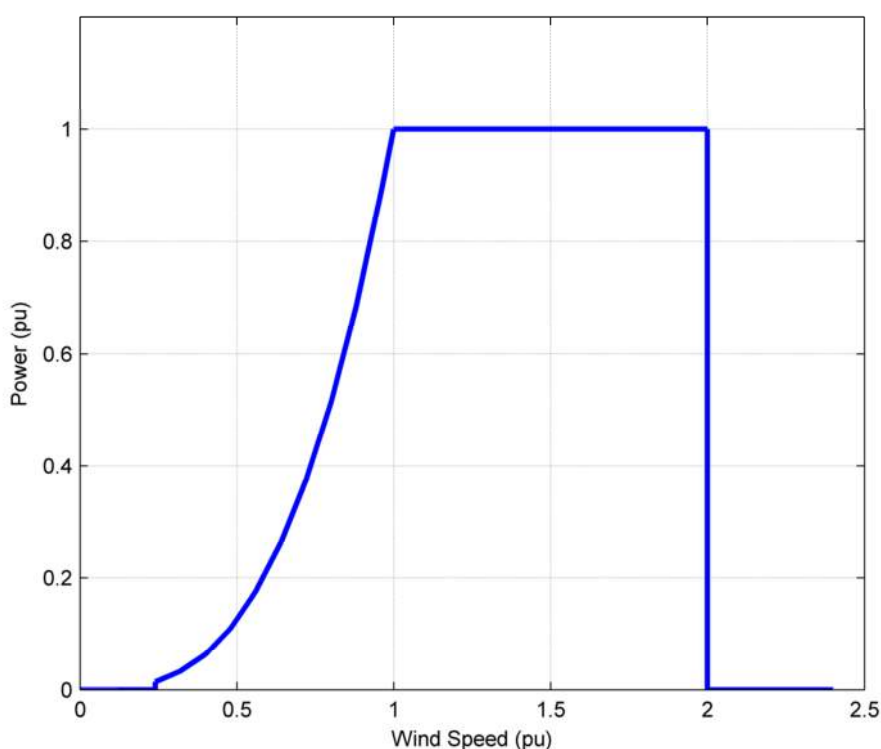


Figure 2.12: DFIG output power versus wind speed

The transmission line is represented by its impedance, $Z_t = R_t + j\omega L_t$. As discussed in section 1.5, the grid strength can be defined by its SCR. For example in this chapter, the transmission line parameters for SCR=3 and X/R=3 at the transmission line rated voltage 11kV (line-to-line) and rated power of 10 MVA are $R_t = 1.3444\ \Omega$ and $L_t = 0.012838\text{H}$. The grid voltage source is 11kV.

The PI controller parameters of the current loops and power loop at a particular bandwidth and damping ratio of 0.9 is determined using Matlab *pidtoolbox* is given in Table 2.3.

Table 2.3: PI controller parameters

Control Loop	Proportional Gain	Integral Gain	Bandwidth (Hz)
Rotor side current loop	0.1049	1.5071	200
Rotor side power loop	0.0682	0.0097	20
Grid side current loop	0.1440	0.5305	200
DC link voltage loop control	7.5398	0.0011	20

2.3.4 PSCAD Simulation Results and Discussion

This section shows the PSCAD simulation results of the DFIG connected to the grid as illustrated in Figure 2.2. The simulation results with step changes in wind speed and with the wind speed profile in Figure 2.6 are discussed.

The simulation result for step changes in wind speed from 0.32pu to 1.2pu with step increments of 0.08pu (equivalent to 1m/s) is shown in Figure 2.14. The active output power, P_{out} as shown in Figure 2.14(b) increases as the wind speed changes. For example, when the wind speed stepped from 0.88pu to 0.96pu, the power increases from 0.682pu to 0.886pu in about 4s. This is due to the fact that the energy captured from the wind turbine is used to overcome the machine inertia. The output power of the DFIG at a particular instant is the sum of the stator power, P_s and the rotor power, P_r . P_r is negative when the shaft speed is lower than 1pu as can be seen in Figure 2.14 (b) and (c) for $t < 70$ s. This is when the DFIG is operating in sub-synchronous generation. When the shaft speed is greater than 1pu, the DFIG is operating in super-synchronous generation and the rotor power is positive as seen for $t > 70$ s. The power flow in DFIG is shown in Figure 2.13, where s refers to the slip is given by:

$$s = \frac{\omega_s - \omega_r}{\omega_s} \quad (2.27)$$

where ω_s and ω_r are the synchronous frequency and rotor frequency, respectively. The slip is positive in the sub-synchronous generation and negative in super-synchronous generation.

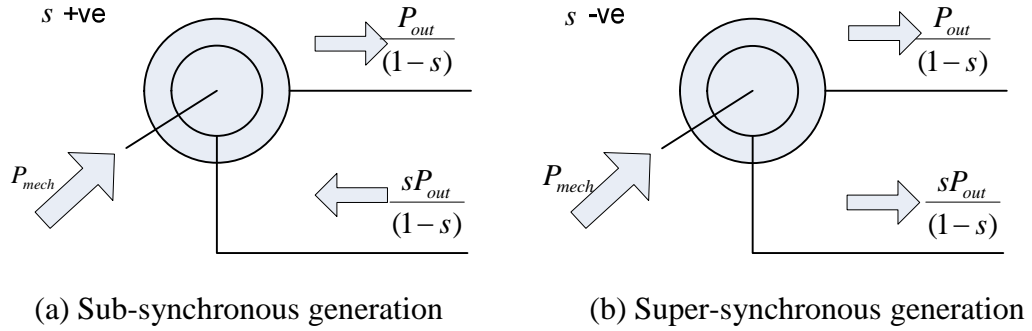


Figure 2.13: Power flow in a DFIG

The rated power of DFIG is reached at the wind speed of 1pu as shown in Figure 2.12. In Figure 2.14(b), when the wind speed is stepped from 0.96pu to 1.04pu at 100s, P_{out} is capped to its rated value of 1pu. This is because the pitch angle is now increased as seen in Figure 2.14(f). Below the rated power of the DFIG, the pitch angle is zero. A glitch in P_{out} is noticed when the wind speed increase from 1.04pu to 1.12pu etc. This is due to the time delay in the pitch angle controller as discussed in section 2.2.4. The output reactive power, Q_{out} is well-regulated at zero as shown in Figure 2.14(c). The voltage magnitude at PCC, V_{pcc} increases as wind power increases because the power transmitted to the grid increases.

The simulation result with a real wind profile for 600s, average wind speed of 0.864pu and standard deviation of 0.104pu is shown in Figure 2.15. The output power extracted from the wind turbine varies according to the wind speed, taking into account the inertia of the machine. The pitch angle controller limits the output power at a rated power of 1pu when the wind speed increases above 1pu.

The simulation time taken for the simulation of 600s wind profile to produce the result shown in Figure 2.15 is 7185s, which is almost 2 hours. That is simulated with time step of $10\mu\text{s}$ and plot step of $5000\mu\text{s}$ in PSCAD. Therefore, it is a good idea if the model could be simplified in order to reduce the simulation time. The simplified model of DFIG wind turbine model is discussed in the following section.

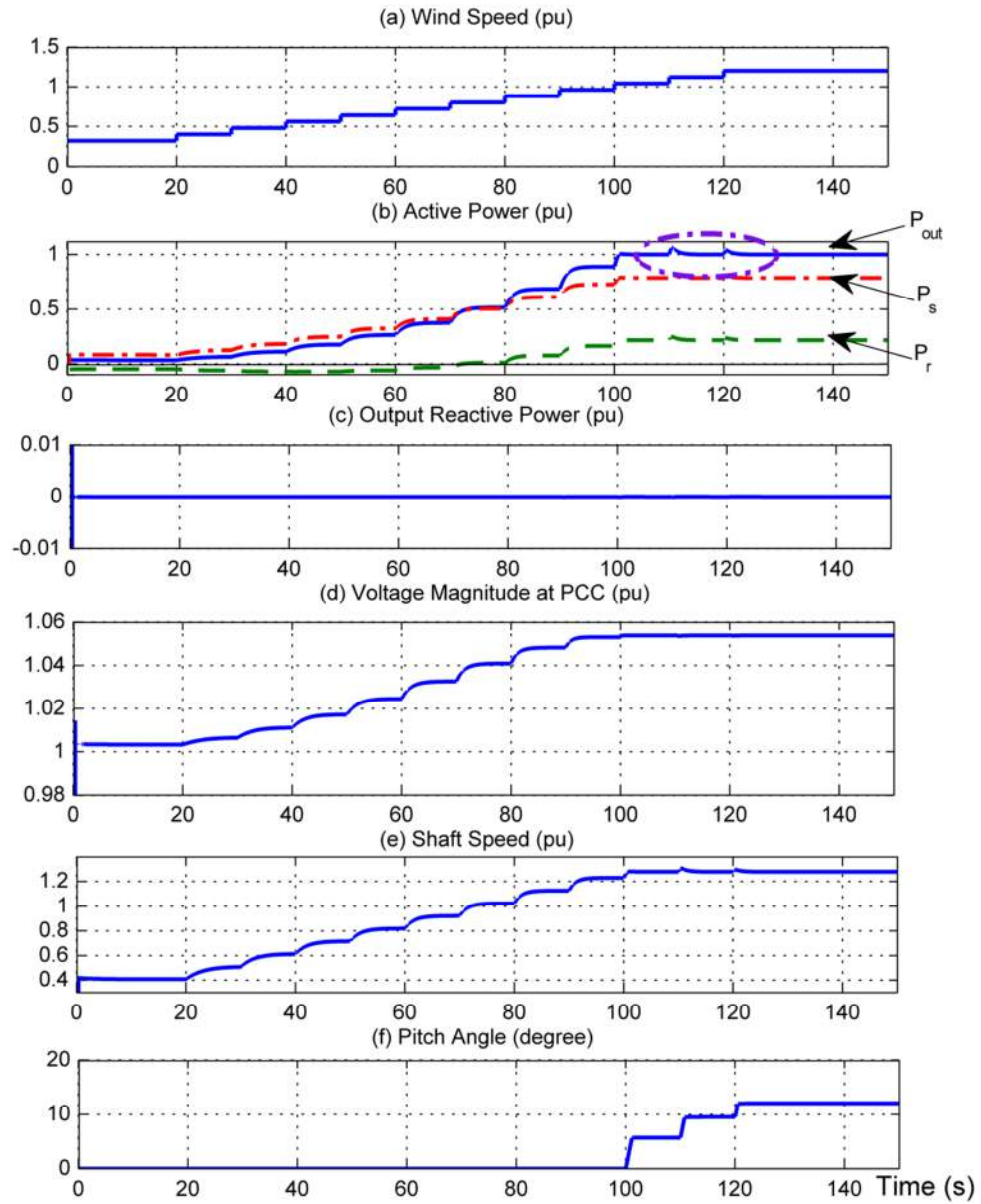


Figure 2.14: Simulation result of the DFIG connected to grid for wind speed of 0.32-1.2pu with step increments of 0.08pu (a) wind speed (pu), V_w ; (b) active power (pu), P_{out} ; (c) output reactive power (pu), Q_{out} ; (d) voltage magnitude at PCC (pu), V_{pcc} ; (e) shaft speed (pu) ω_r ; and (f) pitch angle (degree) , β

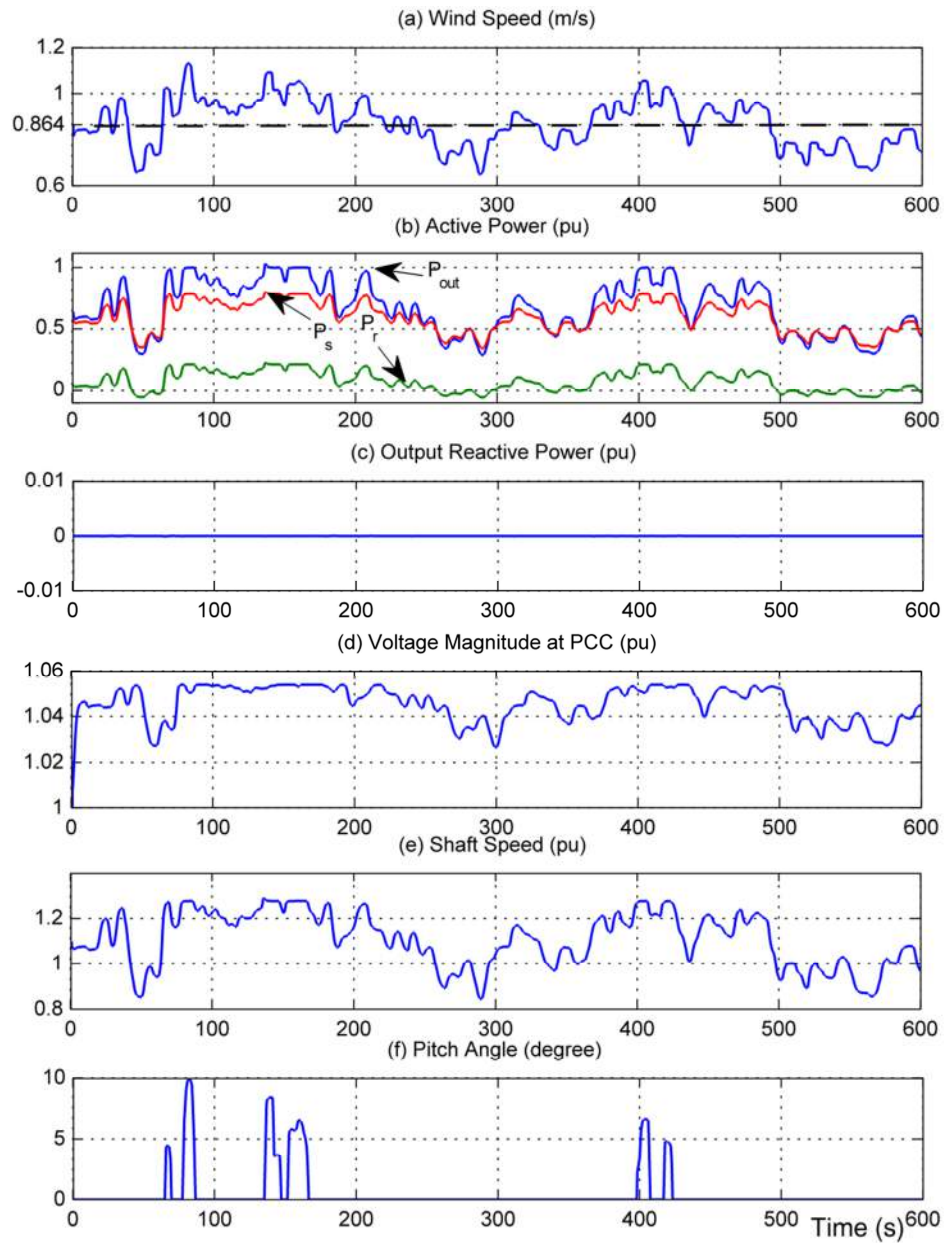


Figure 2.15: Simulation result of the DFIG connected to grid with the real wind profile of average wind speed 0.864pu (a) wind speed (pu), V_w ; (b) active power (pu), P_{out} ; (c) output reactive power (pu), Q_{out} ; (d) voltage magnitude at PCC (pu), V_{pcc} ; (e) shaft speed (pu) ω_r ; and (f) pitch angle (degree) , β

2.4 Simplified DFIG for Wind Turbine under MPPT

The PSCAD model of the DFIG wind system as discussed in the previous section will be referred to as the detailed model. As mentioned, it takes a long time to simulate. This may cause inconvenience for simulating different scenarios which may require several repetitions. Therefore, a simplified model is proposed. The simplified model reduces the complexity of the detailed model in order to achieve fast simulations times, while keeping an acceptable level of accuracy. The acceptable level in the context of this thesis refers to the ability of the model to characterize the output active power and reactive power response from the DFIG. The simplification is possible by neglecting fast phenomena whose bandwidth is much larger than the wind power variations. Assuming that the grid voltage is constant one can assume the machine flux is also constant. Since the current loops are very fast then it is possible to neglect the machine dynamics completely.

The schematic diagram of the simplified model is shown in Figure 2.16. The simplified model keeps the full model of the wind turbine, pitch angle controller and mechanical drive train as used in the detail model. An optimal power calculator block implements equations (2.6) and (2.7) to calculate electrical torque, T_e and optimal power, P_{opt} , respectively.

For the DFIG system equipped with voltage dip ride through facility, its behavior very similar to that of a full converter system [85], [86]. Therefore, the simplified model proposed here assumes that the grid side converter is directly connected to the point of common coupling (PCC) similar to that of the full converter. Thus, the simplified model the electrical component is represented by an AC/DC converter connected to the grid. A current source is connected in parallel with the DC link capacitor. The input signal of the current source is:

$$I_w = \frac{P_{opt}}{V_{dc}} \quad (2.28)$$

where V_{dc} is the DC link voltage of the converter. The converter control structure is the same as that of the grid side converter as discussed in 2.3.2.2.

It is assumed that the reactive power for magnetizing the DFIG is supplied by the stator from the grid. The DC link capacitor, C_r in Figure 2.16 is chosen in conjunction with the DC-link voltage current controllers to make a voltage control bandwidth very much higher than the wind power variation bandwidth. The control bandwidth is in the region of 20Hz. If one wanted to mimic the DFIG stator dynamics delay and the delay due to the DC link DFIG converter voltage control, then one would need to emulate the exact dynamics with the grid converter of the DFIG simplified system. This would mean the grid P_{out} and Q_{out} being obtained as a function of wind power and rotor side current, i_{rd} demand (that sets the DFIG stator reactive power). These dynamic functions would be part of a dynamic emulator model. However, the bandwidth of these P_{out} and Q_{out} controller dynamics are also much higher than the P_{opt} (wind power generation) bandwidth itself. Thus, it is not sufficiently significant to be modelled. This has been verified since the system stability simulations have used both the full DFIG model and the simplified model with very similar results.

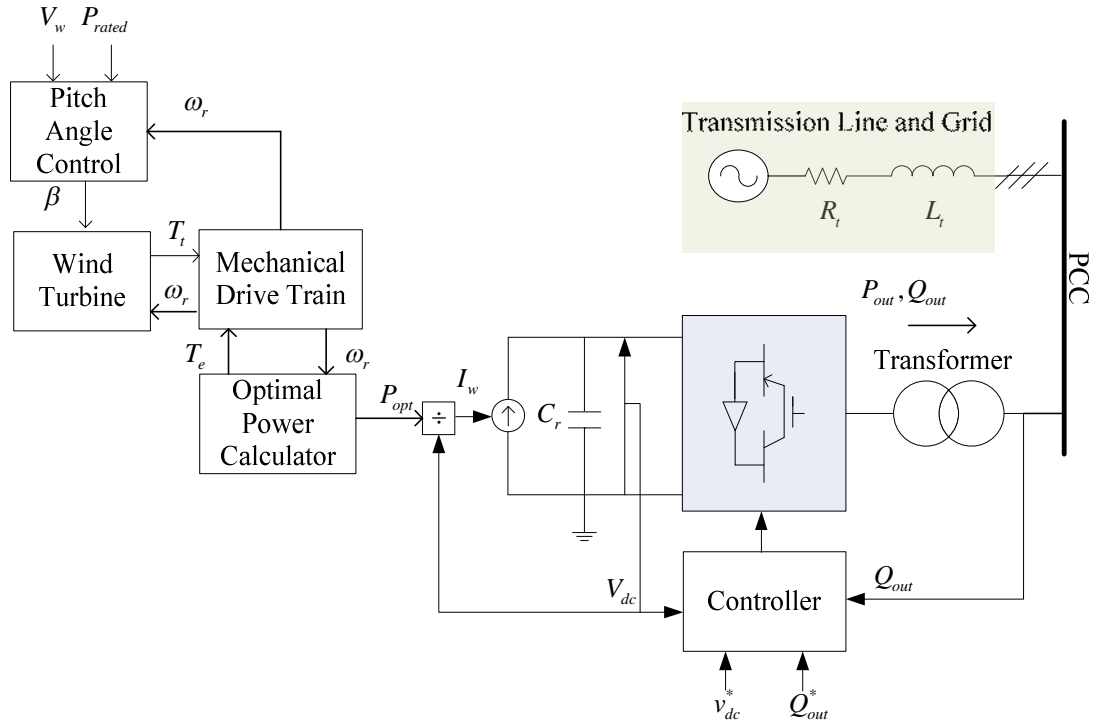


Figure 2.16: Schematic diagram of the simplified model

In [50], [87], it was shown that the stability margin of the DFIG generator itself is wider than that of the wind turbine, and for the MPPT the wind turbine is always stable. Therefore, the stable region of the simplified model is the same as that the detailed model because both models used the same wind turbine.

The simulation results of the simplified model are compared with the detailed model as shown in Figure 2.17 in which the wind speed is stepped from 0.32-1.2pu in increments of 0.08pu (1m/s). For the range of wind speed, the results for the simplified model have very good agreement with the detail model. As seen in Figure 2.18, for the simulation time range of 59s to 70s, where the wind speed is stepped from 0.64pu to 0.72pu, the simplified model can closely duplicate the detailed model simulation result. Simulation results for the step change of wind speed from 1.04pu to 1.12pu are illustrated in Figure 2.19. In this case, the P_{out} is kept at 1pu (rated power) but the pitch angle increases from 5.7° to 9.5° . As seen in the figure, Q_{out} during transient is slightly differing with very small values but the value is negligible. V_{pcc} of the simplified model is also slightly different from the detailed model. The difference in V_{pcc} is because there are actually also small differences in P_{out} and Q_{out} (cannot be seen in the figure) due to the component reduction in the simplified model. However, the difference in the voltage is only 4×10^{-4} pu which is insignificant.

Figure 2.20 shows the case of a real wind profile with an average wind speed of 0.864pu. A closer look at the results is seen in Figure 2.21 for the simulation time between 70s to 90s. Deviations of Q_{out} can be noticed of the two models but is considered negligible since the value is very small. Therefore, the simplified model is matching with the detailed model.

The total simulation time required to perform the simulations are given in Table 2.4 and Table 2.5 for the stepped and real wind speed profile, respectively. For both cases, the simplified model is takes only 20% of the time required to perform the same simulation by the detail model. Therefore, is has been shown that the simplified model is able to provide acceptable results 5 times faster than the detail model.

Table 2.4: Total simulation time required for the simulations in Figure 2.17

Model	Total Simulation Time
Detail Model	1897206 millisecond (31.62 minutes)
Simplified Model	412982 millisecond (6.88 minutes)

Table 2.5: Total simulation time required for the simulations in Figure 2.20

Model	Total Simulation Time
Detail Model	7451435 millisecond (124.19 minutes)
Simplified Model	1600929 millisecond (26.68 minutes)

Output Reactive Power Transient Response

Since Q_{out} of the two models deviations are noticed, step changes of reactive power are simulated. The simulation results are shown in Figure 2.22, Figure 2.23 and Figure 2.24 at the wind speed of 0.64pu, 0.8pu and 1.04pu, respectively. Three wind speeds are selected to represents three scenarios: sub-synchronous generation ($V_w=0.64pu$), super-synchronous generation ($V_w=0.68pu$), and operation at rated power ($V_w=1.04pu$). In all cases, the reference Q_{out} is stepped from 0 to 0.1pu at 1s. As seen in all cases, both models take about 0.065s to settle at a new steady state of P_{out} , Q_{out} and V_{pcc} following the change in output reactive power reference. However, more oscillations of P_{out} can be seen in the detailed model. The simplified model is not able to show this due to the circuit simplification.

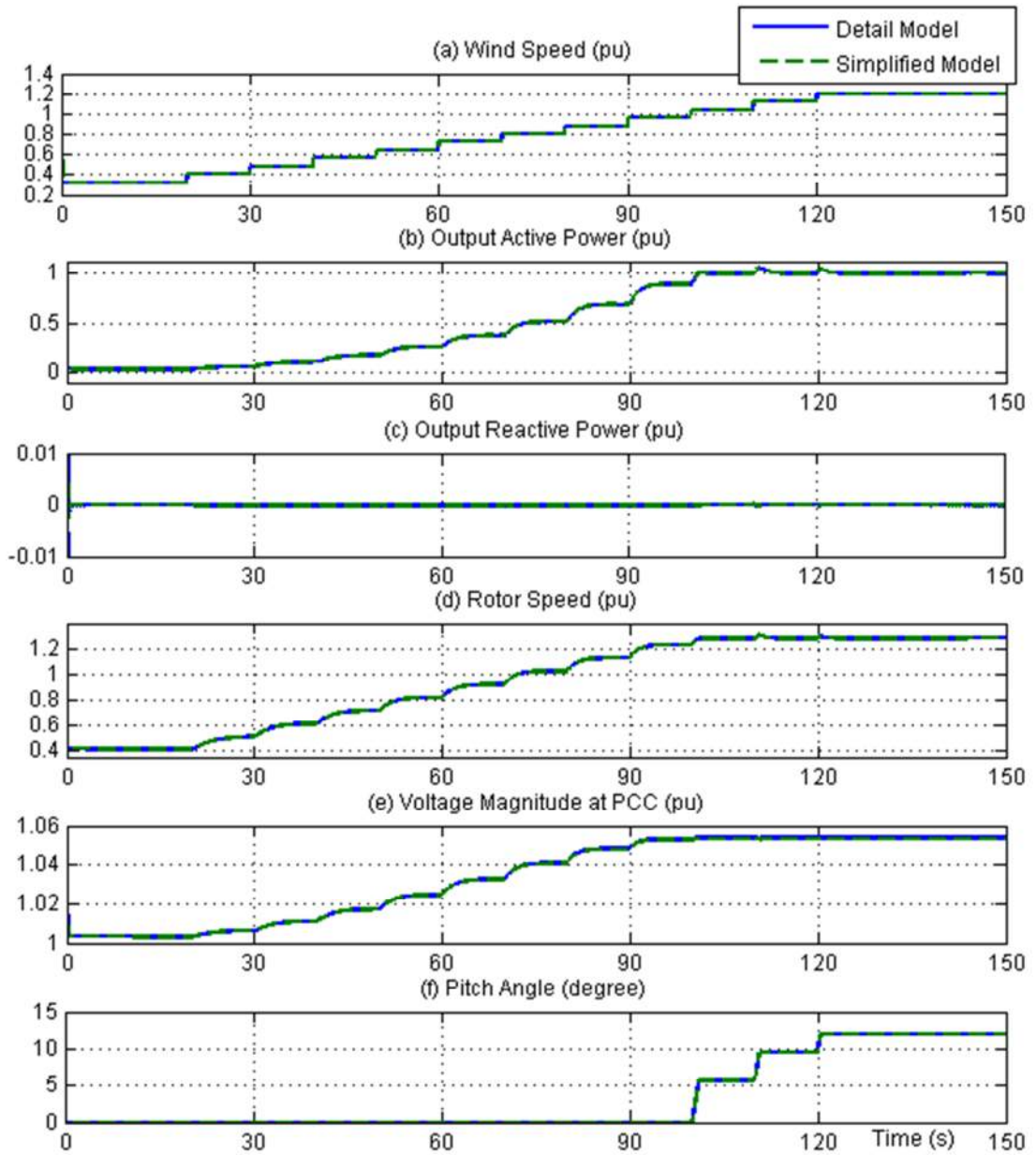


Figure 2.17: Simulation results of the detailed and the simplified models with wind speed of 0.32 -1.2pu and step increments of 0.88 m/s (a) wind speed (pu), V_w ; (b) output active power (pu), P_{out} ; (c) output reactive power (pu), Q_{out} ; (d) voltage magnitude (pu), V_{pcc} ; (e) shaft speed (pu), ω_r ; and (f) pitch angle (degree), β

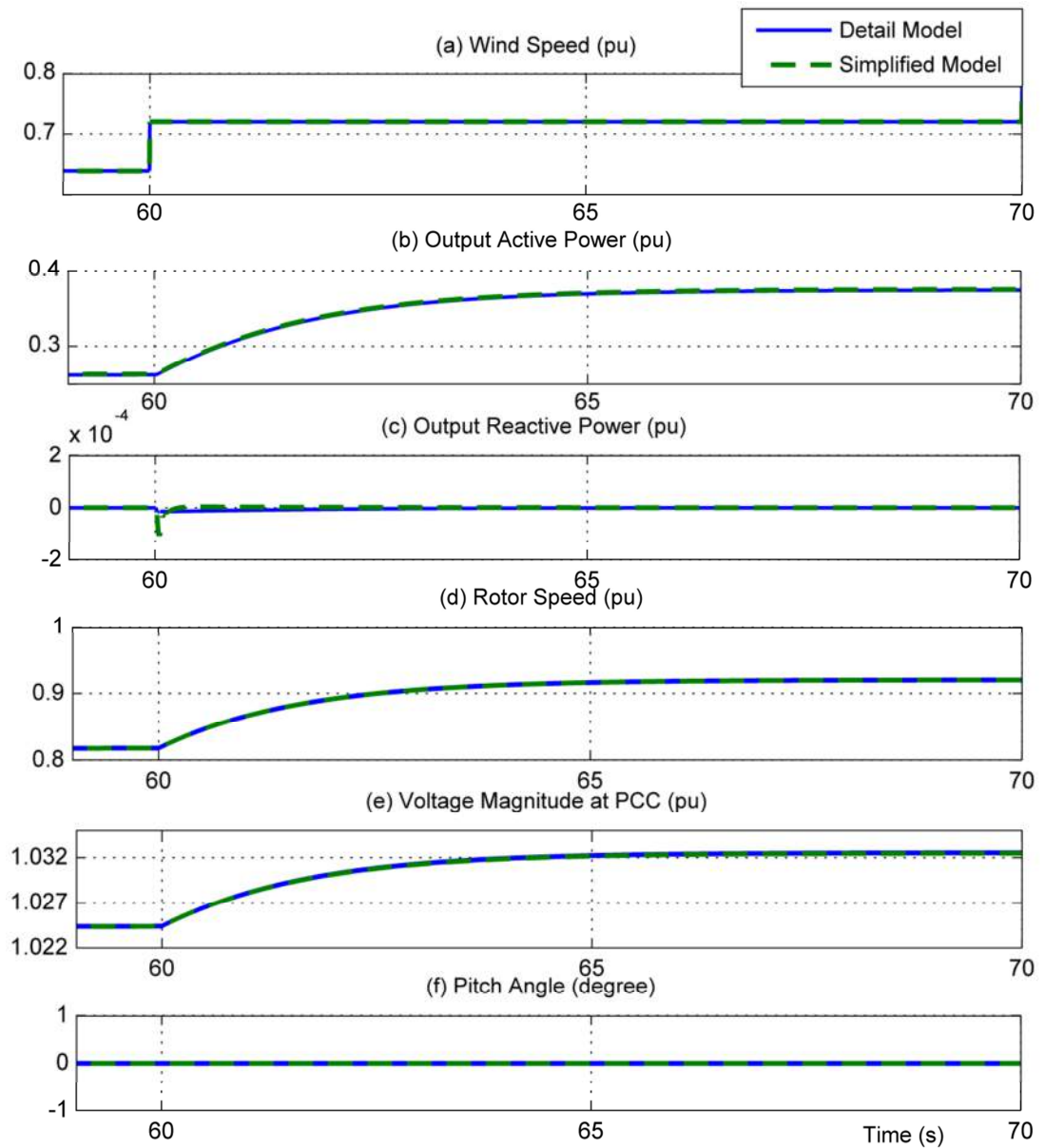


Figure 2.18: Zoomed of Figure 2.17 for simulation time between 59s to 70s (a) wind speed (pu), V_w ; (b) output active power (pu), P_{out} ; (c) output reactive power (pu), Q_{out} ; (d) voltage magnitude (pu), V_{pcc} ; (e) shaft speed (pu), ω_r ; and (f) pitch angle (degree), β

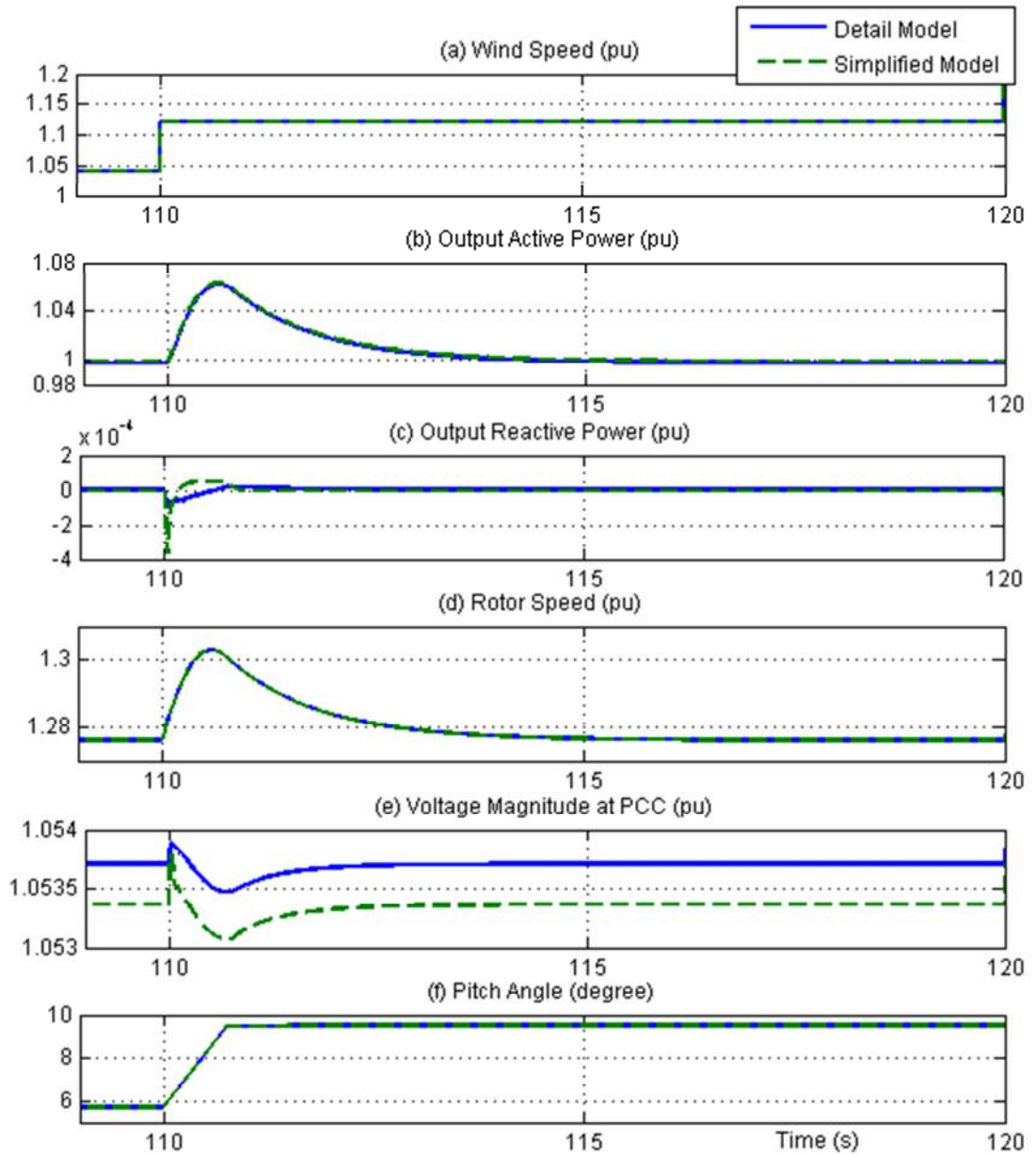


Figure 2.19: Zoomed of Figure 2.17 for simulation time between 109s to 120s (a) wind speed (pu), V_w ; (b) output active power (pu), P_{out} ; (c) output reactive power (pu), Q_{out} ; (d) voltage magnitude (pu), V_{pcc} ; (e) shaft speed (pu), ω_r ; and (f) pitch angle (degree), β

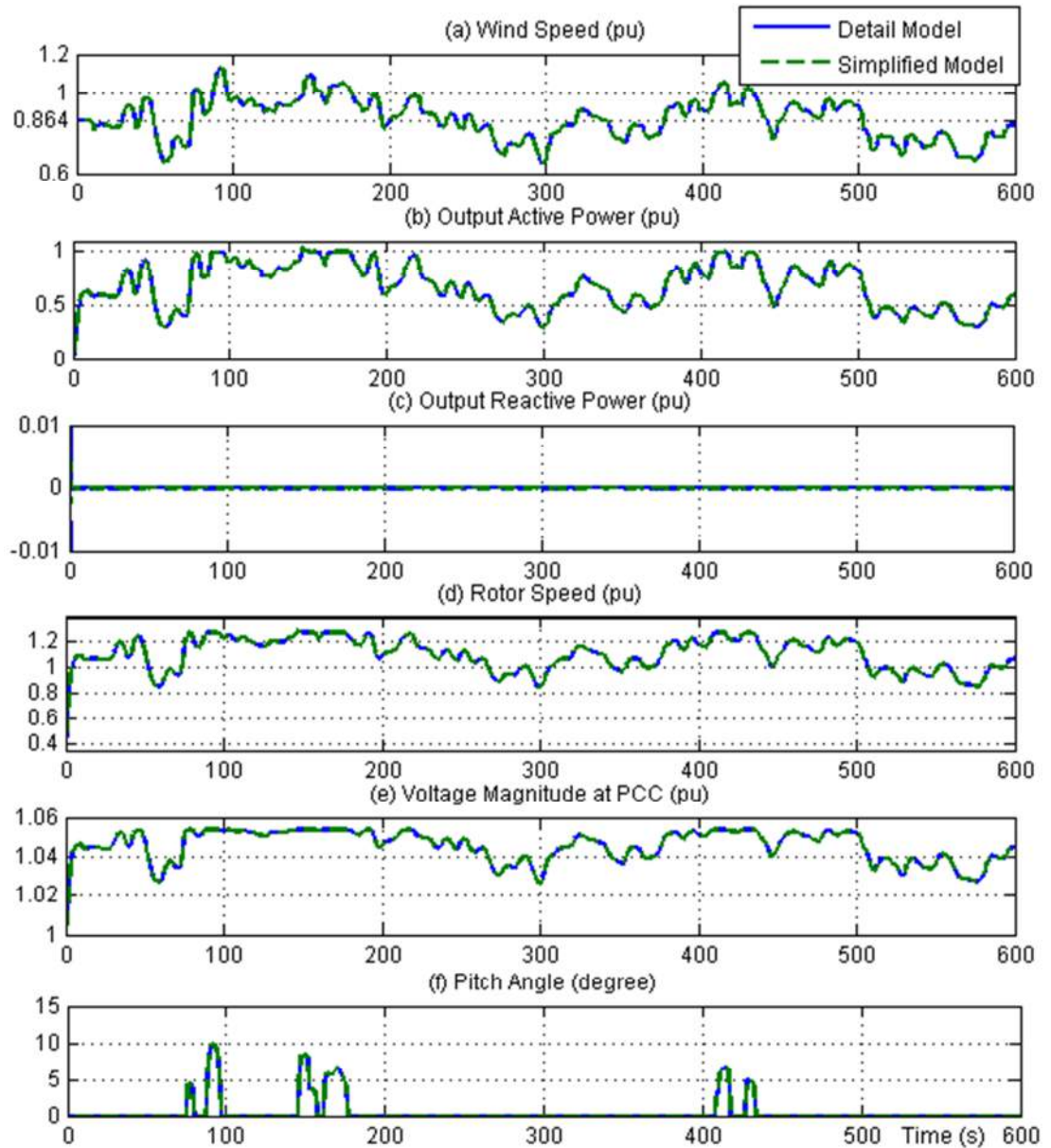


Figure 2.20: Simulation results of the detailed and simplified models with the real wind profile of average wind speed 0.864pu 120s (a) wind speed (pu), V_w ; (b) output active power (pu), P_{out} ; (c) output reactive power (pu), Q_{out} ; (d) voltage magnitude (pu), V_{pcc} ; (e) shaft speed (pu), ω_r ; and (f) pitch angle (degree), β

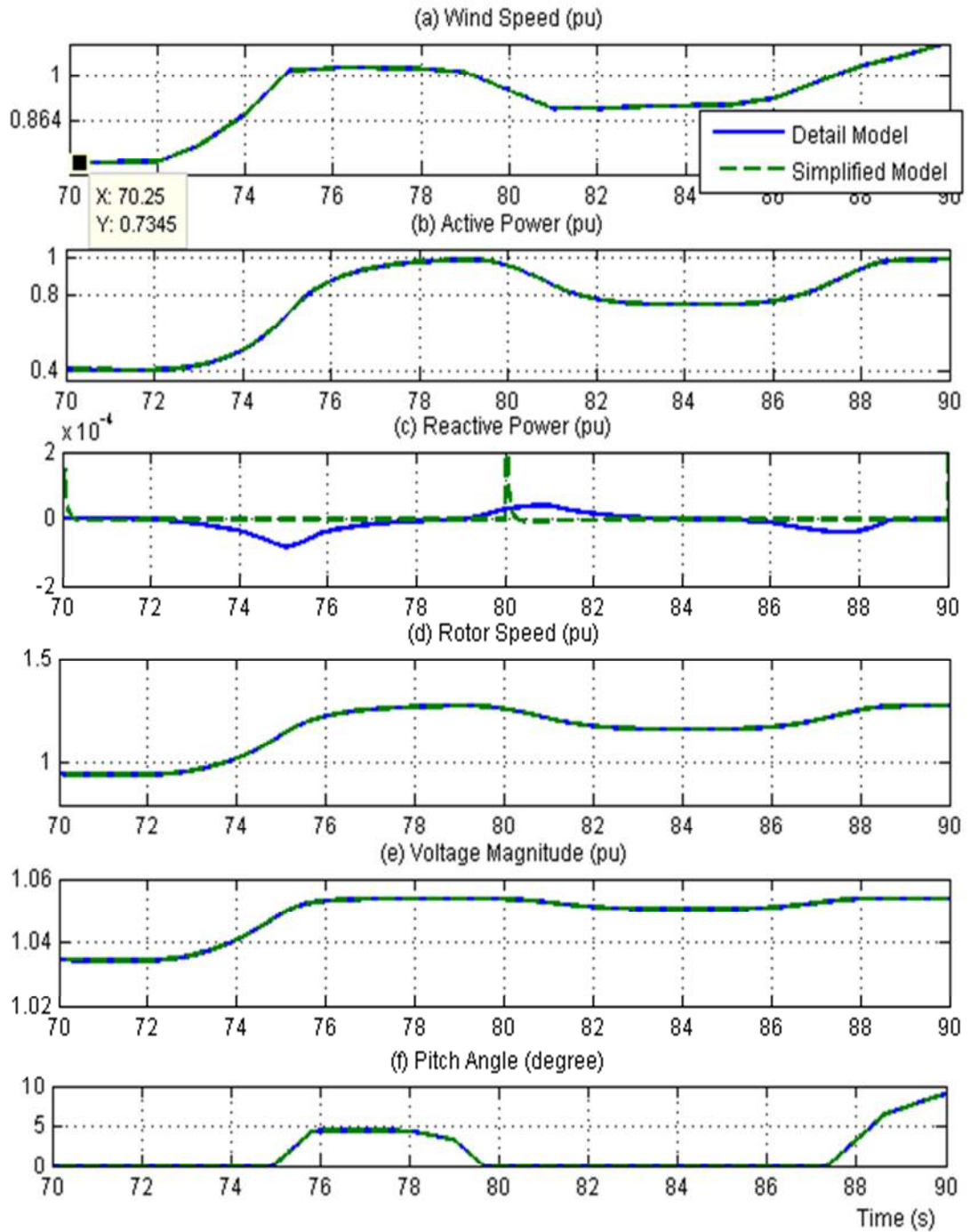


Figure 2.21: Zoomed of Figure 2.20 for simulation time between 70s to 90s (a) wind speed (pu), V_w ; (b) output active power (pu), P_{out} ; (c) output reactive power (pu), Q_{out} ; (d) voltage magnitude (pu), V_{pcc} ; (e) shaft speed (pu), ω_r ; and (f) pitch angle (degree), β

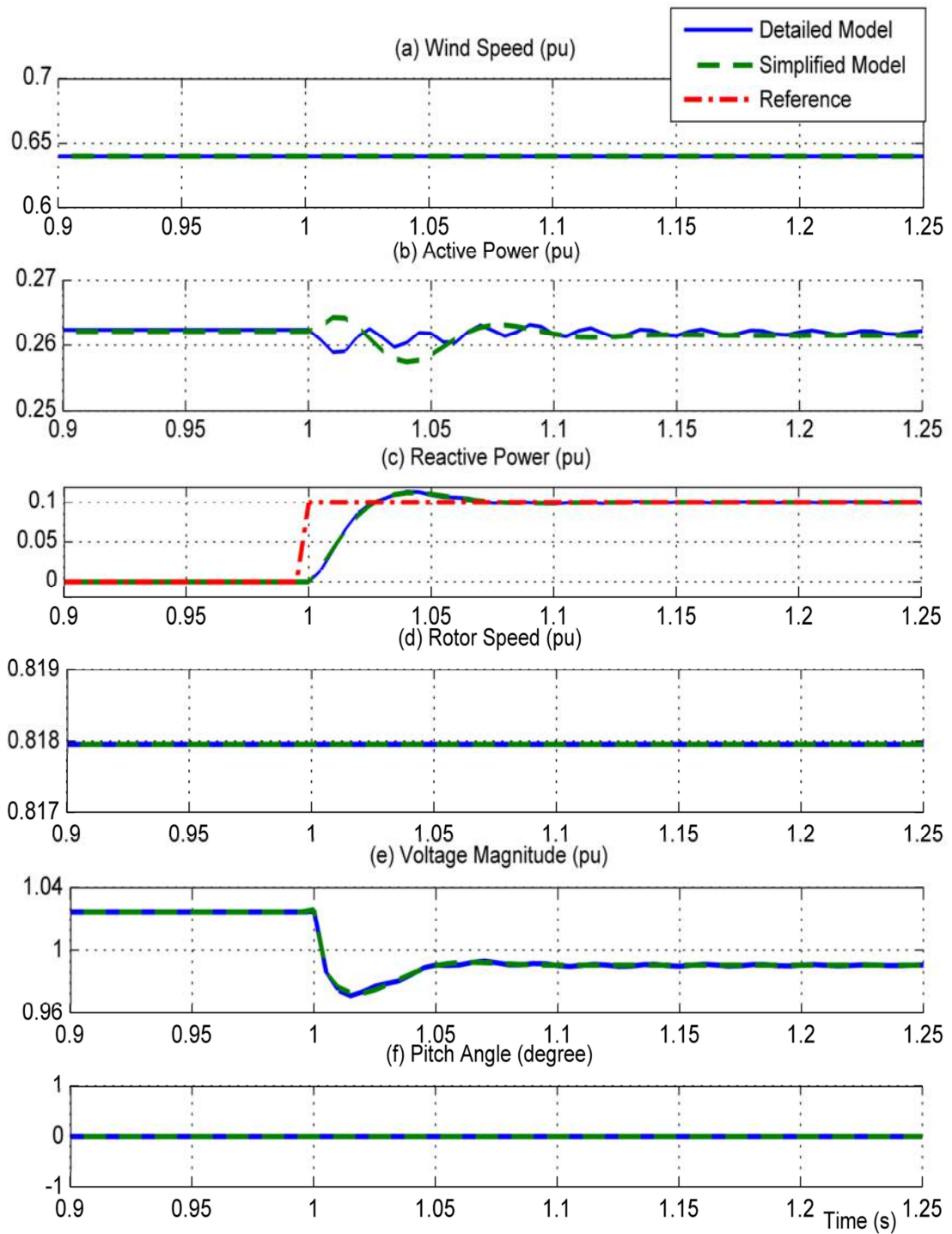


Figure 2.22: Step of reactive power at wind speed of 0.64pu (a) wind speed (pu), V_w ; (b) output active power (pu), P_{out} ; (c) output reactive power (pu), Q_{out} ; (d) voltage magnitude (pu), V_{pcc} ; (e) shaft speed (pu), ω_r ; and (f) pitch angle (degree), β

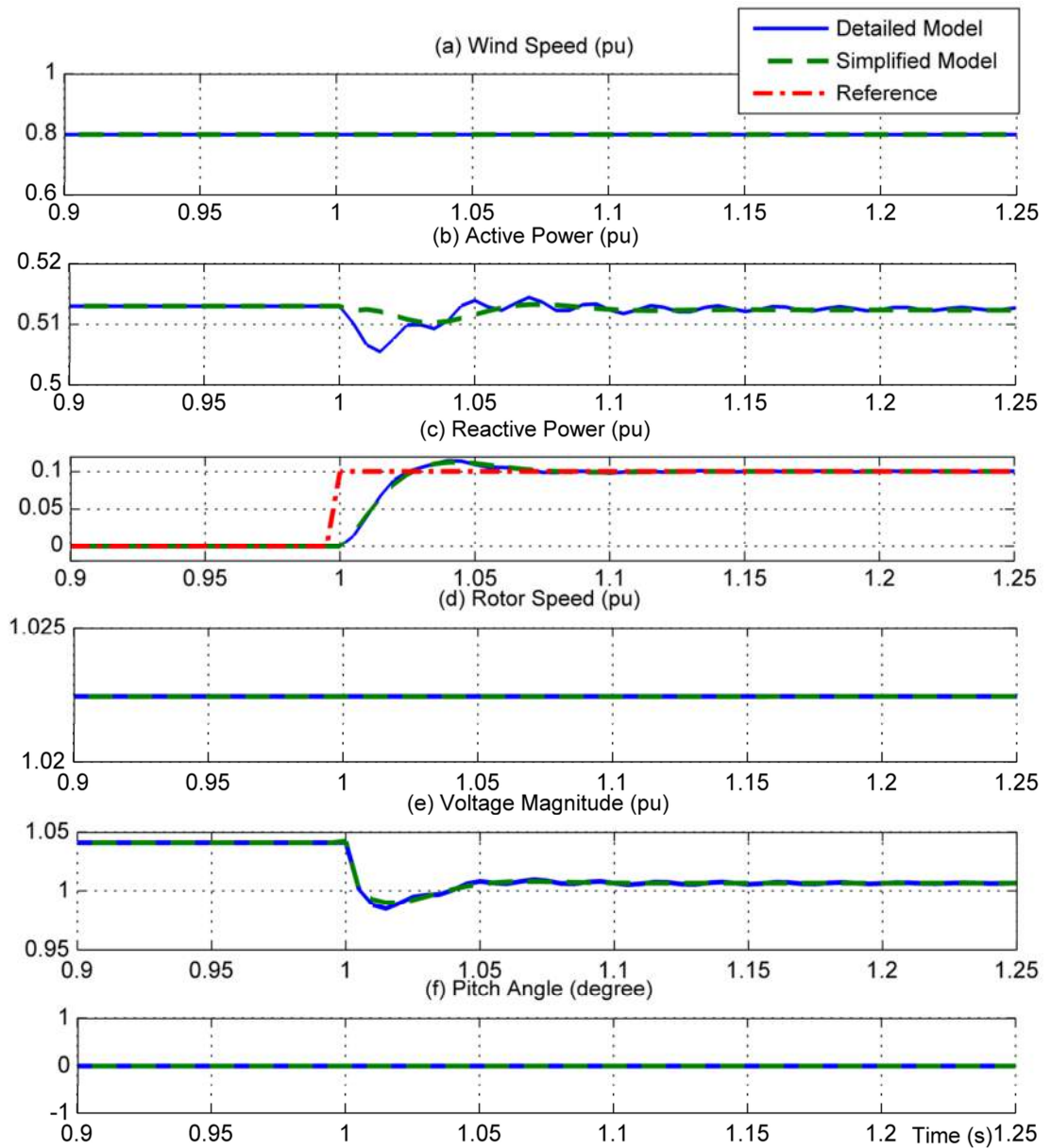


Figure 2.23: Step of reactive power at wind speed 0.8pu (a) wind speed (pu), V_w ;
 (b) output active power (pu), P_{out} ; (c) output reactive power (pu), Q_{out} ;
 (d) voltage magnitude (pu), V_{pcc} ; (e) shaft speed (pu), ω_r ; and (f) pitch angle (degree), β

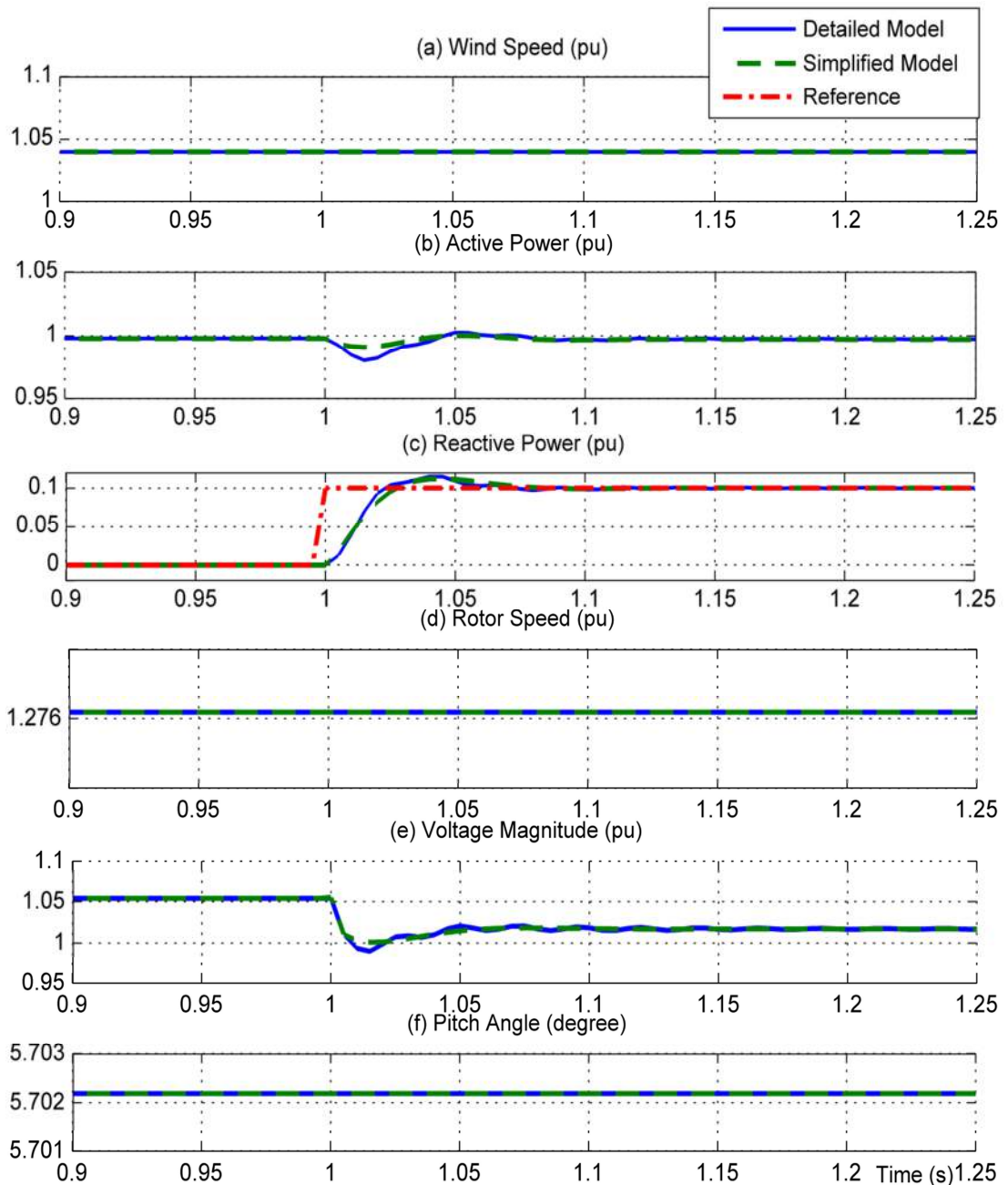


Figure 2.24: Step of reactive power at wind speed of 1.04pu (a) wind speed (pu), V_w ;
 (b) output active power (pu), P_{out} ; (c) output reactive power (pu), Q_{out} ;
 (d) voltage magnitude (pu), V_{pcc} ; (e) shaft speed (pu), ω_r ; and (f) pitch angle (degree), β

2.5 Chapter Summary

This chapter has discussed the PSCAD/EMTDC model of the DFIG wind turbine connected to a grid via a transmission line. The grid can be a weak grid depending on the selection of the transmission line parameters. The wind turbine is controlled using an MPPT algorithm with a pitch angle controller to limit the output power at rated value. The DFIG detailed model and the control system are presented and simulated in PSCAD. The results show that the detail model provides satisfactory results for the MPPT of the wind power system. However, the detail model takes a long time for the simulation. Therefore, a simplified model is proposed. In the simplified model, some components have been removed in order to reduce the complexity and thus the simulation time by 5 times. The simplified model gives acceptable results for low bandwidth of wind speed changes. The step change in output reactive power of the simplified model can also give a good agreement with the detailed model.

Chapter 3

An Analysis of Efficiency Improvement with the Installation of Energy Storage in Power Systems

3.1 Introduction

Energy storage devices are now commercially available and can be used in power systems for various reasons such as load levelling, power smoothing and power quality improvement. The roles of energy storage in power system are discussed and analysed in many publications, for example [3]–[6]. However, little attention has been paid to the study of energy storage installation to improve overall system efficiency. This is due to the fact that the installation of an energy storage is like adding another source of losses to the power system. Therefore, it tends to reduce the overall system efficiency rather than improving it. However, there is a possibility of reducing the transmission line losses with the installation of energy storage. If the reduction of the transmission line losses is higher than the losses in the energy storage system, the overall system efficiency can be improved [7]. This issue is addressed in [3] but there is no systematic analysis of achieving the improvement. The analytical analysis in [7] focus on load levelling application but not on the power generation smoothing with energy storage.

In this chapter, the benefit of energy storage to improve the system efficiency in a system with fluctuating renewable power generation is analysed. The aim of this chapter is to clarify the parameters that can be considered to improve the system efficiency with the installation of energy storage in a power system. In order to

perform the analysis, the system model in Figure 3.1 is employed. This system consists of a wind farm and an energy storage system connected to the grid by a transmission line. The energy storage unit is typically used in such a system for power smoothing since the wind power generation is fluctuating [5], [49], [88]. In this chapter, a simple mathematical analysis verified by PSCAD simulation is performed to investigate the potential of energy storage to improve the system overall efficiency.

The losses in a transmission line are proportional to the square of the current flow. If the excess peak power is stored in the energy storage system located in the proximity of the generation, less RMS current is carried by the transmission line. The loss reduction which is proportional to the square of current can be significant. However, the energy storage itself contributes towards overall system losses that have to be taken into account. The loss due the energy storage, (for example supercapacitor) is taken into account in this analysis. Typical round trip efficiency, η_r of an energy storage system is 70% to 95%, and may also be dependent on power.

A low Short Circuit Ratio (SCR) indicates a weaker grid. It is very weak if <2 . Since the transmission line is represented by a series impedance ($Z_t = R_t + j\omega L_t$), the ratio of reactance to resistance, X/R ratio can be calculated. Typical range of the transmission line X/R is between 2 to 10 [70].

To investigate basic feasibility, a wind power waveform producing an idealized current transmission waveform as shown in Figure 3.2 is assumed. In this case, the problem is analytic. A mathematical analysis to quantify the benefit from energy storage in terms of the system loss reduction is presented. This is followed by PSCAD simulation results that support the analytical analysis. Then, simulation studies undertaken with real wind velocity waveforms are presented. The summary of the findings are given in the last section of this chapter.

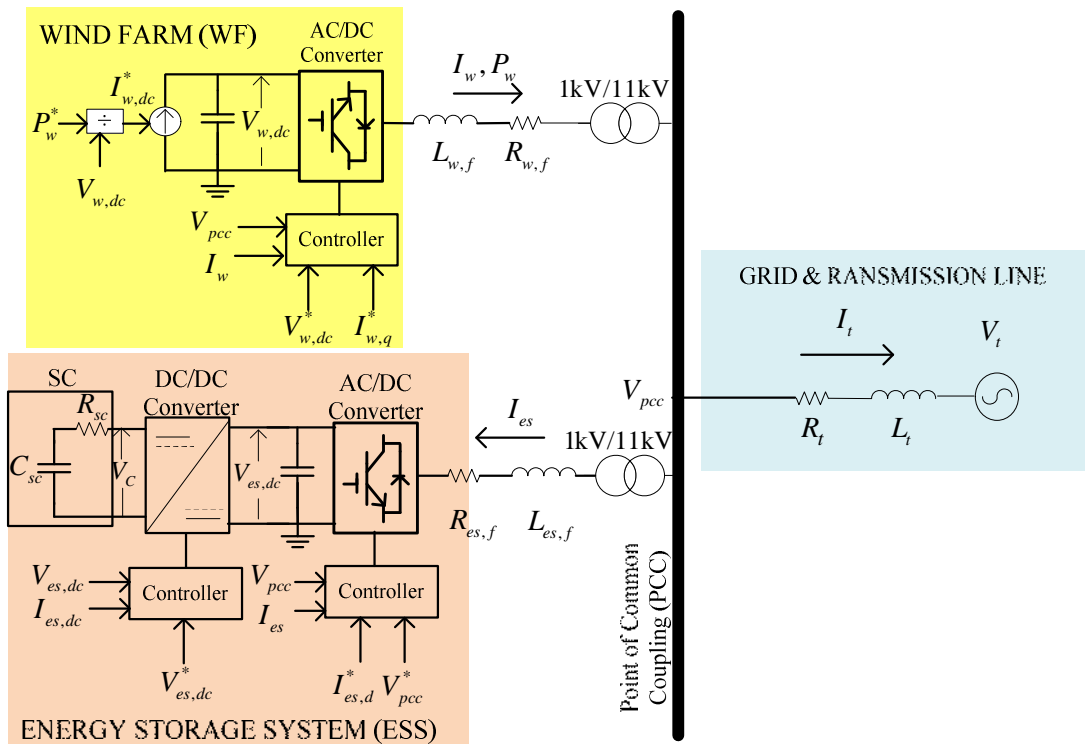


Figure 3.1: Power system under study

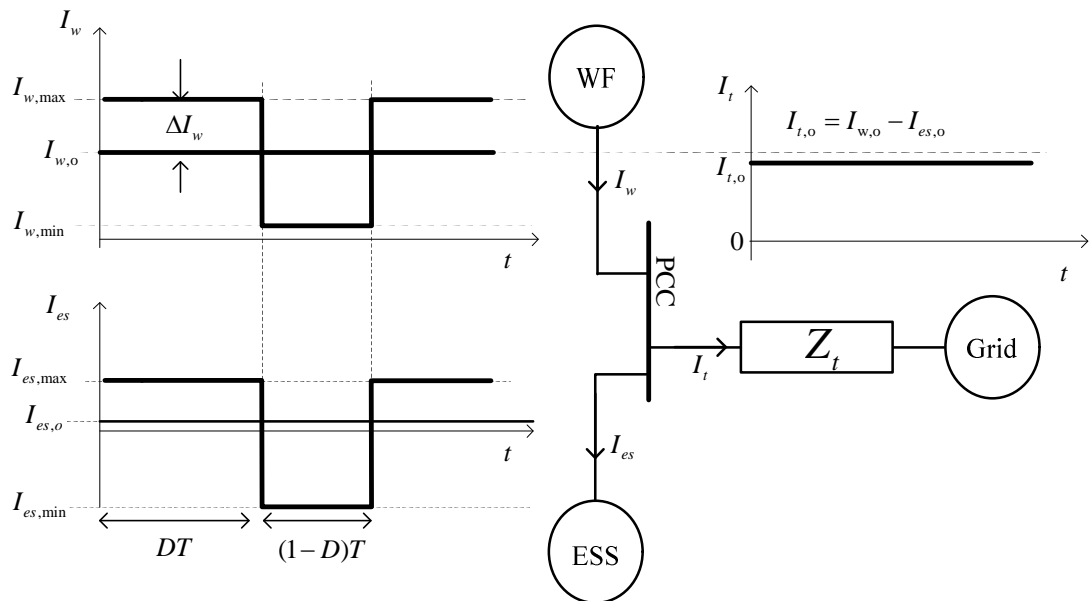


Figure 3.2: RMS currents profile

3.2 Mathematical Analysis of Efficiency Improvement with Energy Storage

3.2.1 Loss Reduction in Transmission Line

For the system as shown in Figure 3.1, the power generated is transmitted to the grid via a transmission line. The power is generated from renewable energy such as wind or solar panels and then transmitted to the grid. This power may be highly fluctuating. Energy storage installed close to the generation system may be used to smooth the power transmitted to the grid. In this section, a mathematical analysis is performed to investigate the possibility of improving the overall system efficiency with the installed energy storage. The main parameters contributing to this benefit will be determined.

It is known that the losses in the transmission line are proportional to the square of the current flow. If peak power is stored in the energy storage located close to the generation source, less RMS current is carried by the transmission line. The loss reduction which is proportional to the square of current may be large. The power stored in energy storage can be transmitted later when the power generation is low at lower current. Thus, there will be reduction in power loss due to the shifting of power transmitted. The RMS current profiles are illustrated in Figure 3.3. The current from the WF represents energy generated and current to the ESS represents energy being stored. The ESS is used to keep the transmission line current constant. In addition, the resistance of the transmission line is also higher at high current due to the increase in temperature. The higher resistance contributes towards higher loss at higher power transmission. However, this is not taken into account in the analysis of this thesis.

Therefore, shifting the transmission of power could improve the system efficiency due to the transmission line loss reduction. However, the energy storage itself contributes towards overall system losses that have to be taken into account. This is evaluated in the next section.

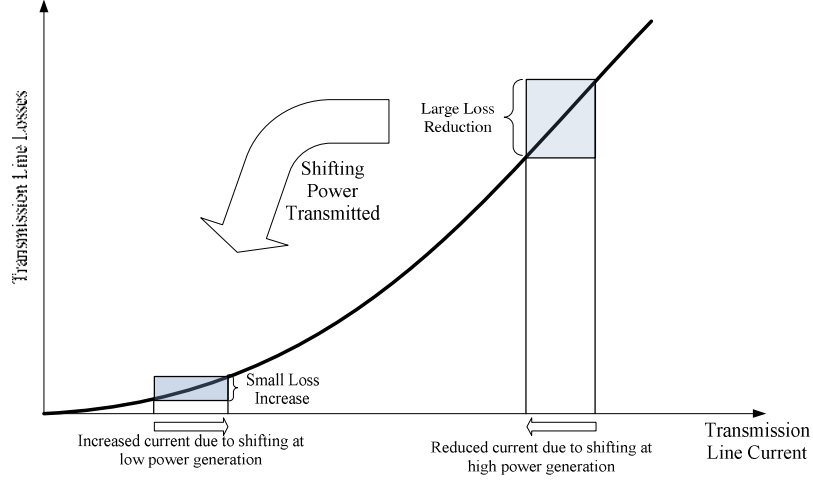


Figure 3.3: Transmission line losses reduction by shifting the power transmitted

3.2.2 Breakeven Point for Overall Efficiency Improvement

To simplify the analysis, the power generated is assumed to be in an idealized RMS current profile as shown in Figure 3.2. $I_{w,max}$ is the maximum generated current and $I_{w,min}$ is the minimum generated current by the wind farm (WF).

Without the energy storage system, the power generated by the wind turbine, P_w is sent to the grid instantaneously. Therefore, the energy loss in the transmission line with series impedance of $Z_t = R_t + j\omega L_t$ without an energy storage system, $E_{t,loss}$, can be calculated by:

$$E_{t,loss} = [I_{w,max}^2 D + I_{w,min}^2 (1 - D)] R_t T \quad (3.1)$$

where, D is the duty cycle and T is a time duration (see Figure 3.2).

In this analysis, the energy storage is used to keep the transmission line RMS current constant at an average current, $I_{t,o}$ given by:

$$I_{t,o} = I_{w,o} - I_{es,o} \quad (3.2)$$

Where $I_{w,o}$ and $I_{es,o}$ is the average wind current and average energy storage current, respectively. The energy storage is charged when $I_w > I_{w,o}$, and discharged when $I_w < I_{w,o}$. $I_{w,o}$ can be expressed as:

$$I_{w,o} = I_{w,max}D + (1-D)I_{w,min} \quad (3.3)$$

Taking into account the energy storage round trip efficiency, η_{rt} , the energy storage average current, $I_{es,o}$ is given by:

$$I_{es,o} = (1-\eta_{rt})(I_{w,max} - I_{t,o})D \quad (3.4)$$

Therefore, $I_{es,o}$ represents losses in the energy storage system.

Substituting (3.2) into (3.4) and rearranging, yields:

$$I_{t,o} = [I_{w,o} - (1-\eta_{rt})I_{w,max}D] / [1 - (1-\eta_{rt})D] \quad (3.5)$$

Then, the energy loss in the transmission line with the energy storage is given by:

$$E_{t,loss}^{ES} = I_{t,o}^2 R_t T \quad (3.6)$$

Hence, the energy loss reduction in the transmission line with the energy storage employed, $E_{t,saved}$ is the difference between (3.1) and (3.6):

$$E_{t,saved} = [I_{w,max}^2 D + I_{w,min}^2 (1-D) - I_{t,o}^2] R_t T \quad (3.7)$$

Assuming nominal voltage, V_n at the PCC, energy loss in the energy storage system, $E_{es,loss}$ can be obtained by:

$$E_{es,loss} = I_{es,o} V_n T \quad (3.8)$$

The breakeven point to achieve overall efficiency improvement is obtained when $E_{t,saved} = E_{es,loss}$. By equating (3.7) and (3.8) and rearranging it, produces:

$$[I_{w,\max}^2 D + I_{w,\min}^2 (1-D) - I_{t,o}^2] R_t T - I_{es,o} V_n T = 0 \quad (3.9)$$

The short circuit ratio (SCR), S_{cr} is given by the per unit admittance of the transmission line. Therefore:

$$Z_t = (1/S_{cr})(V_n/I_n) \approx X_t \quad (3.10)$$

where, I_n is the nominal value of the transmission line current. The ratio of the reactance to the resistance is:

$$X_{2R} = X_t / R_t \quad (3.11)$$

Substituting (3.11) into (3.10), yields:

$$R_t = V_n / (S_{cr} X_{2R} I_n) \quad (3.12)$$

Substituting (3.4), (3.5) and (3.12) into (3.9) and rearranging, gives:

$$A I_{w,\max}^2 + B I_{w,\max} + C = 0 \quad (3.13)$$

where:

$$A = D + D^2 / (1-D) - D^2 (1-\eta_{rt})^2 / (1-D(1-\eta_{rt}))^2 \quad (3.14)$$

$$B = \frac{-2D I_{w,o}}{(1-D)} + \frac{2D(1-\eta_{rt}) I_{w,o}}{(1-D(1-\eta_{rt}))^2} - \frac{D(1-\eta_{rt}) S_{cr} X_{2R} I_n}{(1-D(1-\eta_{rt}))} \quad (3.15)$$

$$C = \frac{I_{w,o}^2}{(1-D)} - \frac{I_{w,o}^2}{(1-D(1-\eta_{rt}))^2} + \frac{D(1-\eta_{rt}) I_{w,o} S_{cr} X_{2R} I_n}{1-D(1-\eta_{rt})} \quad (3.16)$$

A practical solution for (3.13) gives the value of $I_{w,\max}$ for energy loss breakeven situation:

$$I_{w,\max_Brk} = (-B + \sqrt{B^2 - 4AC}) / 2A \quad (3.17)$$

Defining:

$$\Delta I_{w,Brk} = I_{w,max_Brk} - I_{w,o} \quad (3.18)$$

Then,

$$\Delta I_{w,Brk} = (-B + \sqrt{B^2 - 4AC}) / 2A - I_{w,o} \quad (3.19)$$

where, $\Delta I_{w,Brk}$ is the difference between the maximum and the average wind current required to achieve the breakeven point for the overall system efficiency.

Therefore, from the relationship in (3.19), the parameters that can influence the overall energy gain with an ESS in the system are $\Delta I_{w,Brk}$, $I_{w,o}$, η_{rt} , D , SCR and X/R.

The 3D plots of $\Delta I_{w,Brk}$, SCR and η_{rt} at various D , $I_{w,o}$ and X/R are shown in Figure 3.4. The plots of $\Delta I_{w,Brk}$ versus η_{rt} for various SCR, X/R, D and $I_{w,o}$ are given in Figure 3.5. From the plots, it is observed that the break-even point, where the power savings in the transmission equals the added energy storage losses, moves towards smaller power peaks as the efficiency of the energy storage increases. Also, for higher value of SCR, which means that in a stronger system, very efficient energy storage systems are needed to achieve the break-even point. Therefore, higher peak power is needed to be levelled when the transmission grid has a larger value of SCR to offset the energy storage losses at the same η_{rt} . At $\eta_{rt} = 90\%$ for instance, the system with SCR=2 requires $\Delta I_{w,Brk}$ to be greater than 0.1582pu, while for SCR=3,4 and 5 (at X/R ratio of 2) $\Delta I_{w,Brk}$ greater than 0.263pu, 0.368pu and 0.474pu respectively is required. Hence, a transmission line with lower SCR value has higher chance of benefiting from the energy storage to increase the overall efficiency. Moreover, it is preferable to have smaller values of $\Delta I_{w,Brk}$ because the current is proportional to the power rating of the energy storage. Higher $\Delta I_{w,Brk}$ means a higher power rating is required for the energy storage system.

Varying $I_{w,o}$ also influences $\Delta I_{w,Brk}$ to meet the condition in (3.19). Less $\Delta I_{w,Brk}$ is required to achieve the break-even point at a higher value of $I_{w,o}$. The variation of $I_{w,o}$ will be more significant at lower η_{rt} . For example, at 80% of η_{rt} , the $\Delta I_{w,Brk}$ required are 0.3799 and 0.333 for $I_{w,o}$ of 0.3pu and 0.5pu, respectively, i.e. a 30% difference in $I_{w,o}$ contributes to 0.047pu difference in $\Delta I_{w,Brk}$. Meanwhile, at $\eta_{rt} = 70\%$, the difference in $\Delta I_{w,Brk}$ increases to 0.078pu. Thus, for overall efficiency improvement, it is better at higher $I_{w,o}$. Similar trend also seen with variation of the D .

If the X/R ratio is to be varied at a constant SCR, the trend will be the same as varying SCR. This is because a greater value of X/R ratio means a smaller resistance and thus lesser transmission line losses. Thus, a greater $\Delta I_{w,Brk}$ is required.

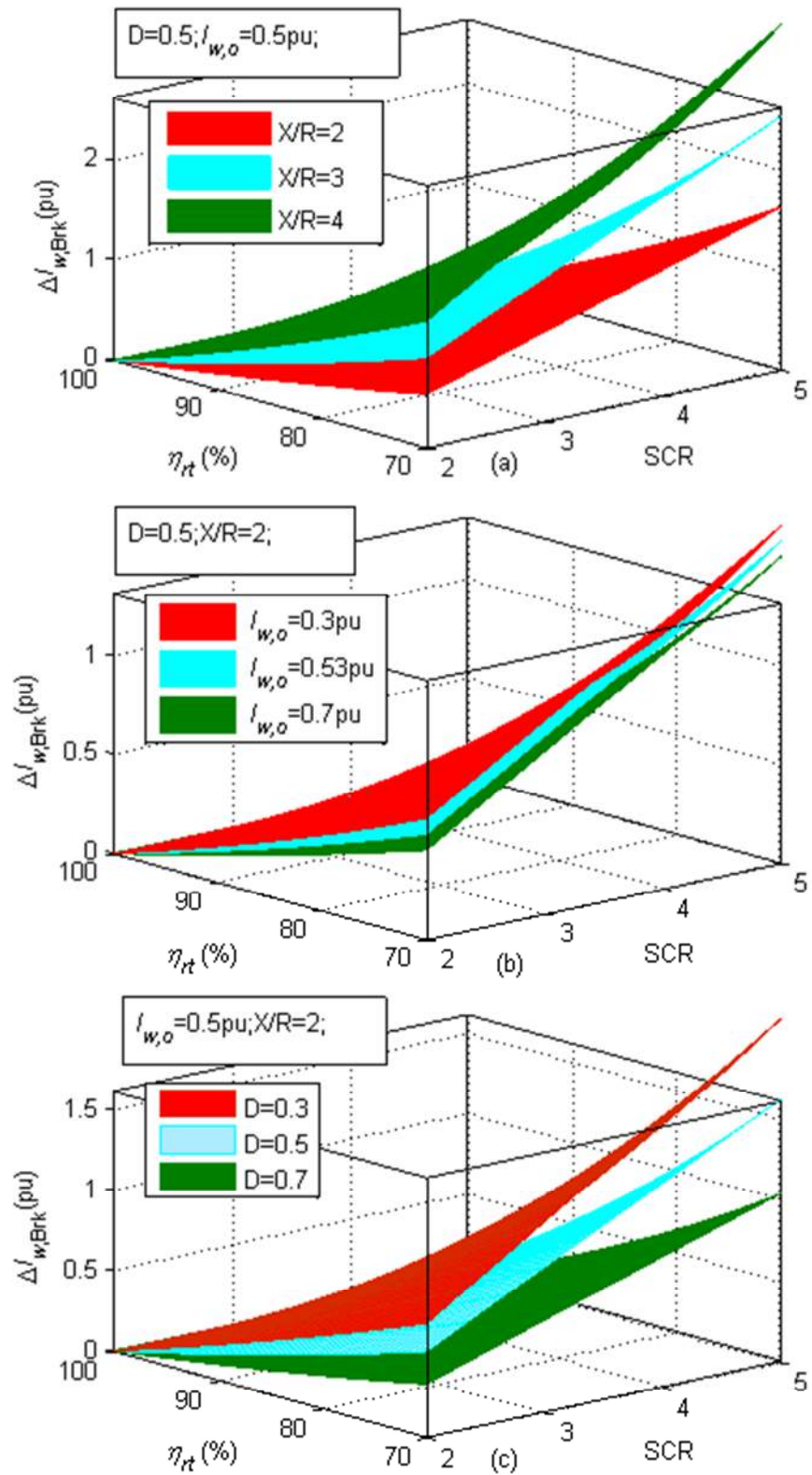


Figure 3.4: 3D plots of $\Delta'_{w,Brk}$, SCR and η_{rt} (a) various X/R, (b) various $I_{w,o}$, and (c) various D

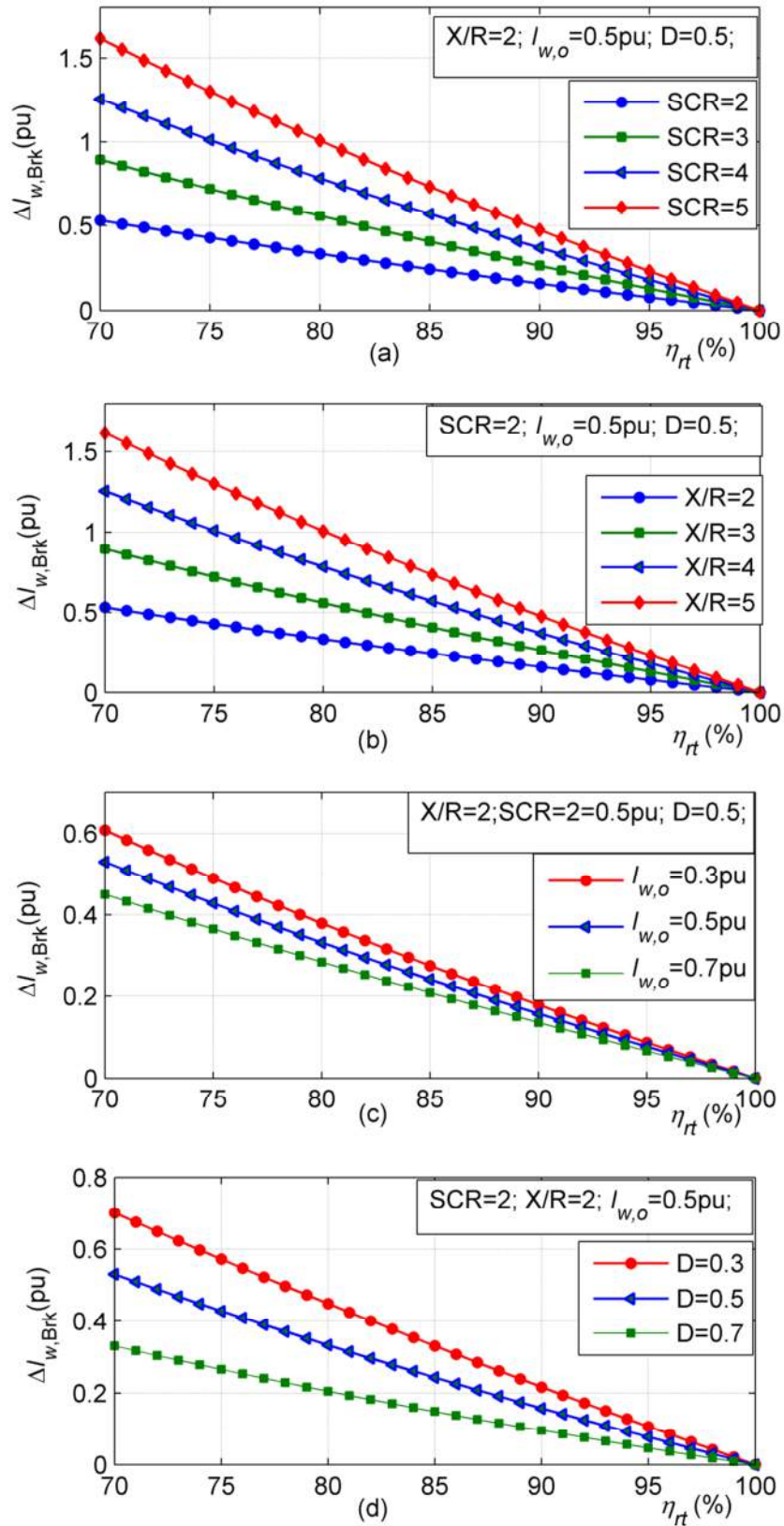


Figure 3.5: $\Delta I_{w,Brk}$ versus η_{rt} (a) various SCR, (b) various X/R, (c) various $I_{w,o}$ and (d) various D

3.3 PSCAD Simulation

The PSCAD simulation is done to investigate efficiency improvement for a more complex case with real wind profiles. A PSCAD simulation of the system in Figure 3.1 has been set up. The wind farm is connected to the PCC by a PWM converter. The system is similar to that described in the previous chapter. For convenience it is repeated in this section. Its vector control structure is shown in Figure 3.6. The voltages and currents are transformed to its equivalent dq -components. The d -axis of the dq -rotating frame is oriented on the voltage at PCC. The outer loop PI controller, controls the dc link voltage, $V_{w,dc}$ via the d -axis of input current, $I_{w,d}$. This PI controller provides the reference current. The inner current loop controls the active current, and reactive current, $I_{w,q}$, via the converter voltage. The power generated from the wind farm is modelled as current source in the DC link and given by:

$$I_{w,dc}^* = P_w^* / V_{w,dc} \quad (3.20)$$

where P_w^* is the reference power generated.

The block diagram of the energy storage system and its control structure is shown in Figure 3.7. The energy storage unit used is a supercapacitor. An ideal simplified RC circuit is used to model the supercapacitor. It is interfaced to the AC system via a DC/DC converter and an AC/DC converter. The AC/DC converter presents a current source to the grid through fast acting current loops. The voltages and currents measured are transformed to its equivalent dq -components. The d -axis of the dq -rotating frame is oriented on the voltage at the PCC. In this case, the converter is also used to control the voltage at the PCC. Thus, the reactive current demand, $I_{es,q}^*$ is obtained from the PCC voltage controller. The energy storage is charged or discharged depending on the active current reference, $I_{es,d}^*$. For the analysis in this chapter, $I_{es,d}^*$ is calculated to maintain a constant current transmitted to the grid by the transmission line. This requires the measurement of current from the wind, $I_{w,d}$ and the average computation of the current. The DC link voltage is kept constant by the DC/DC converter controller.

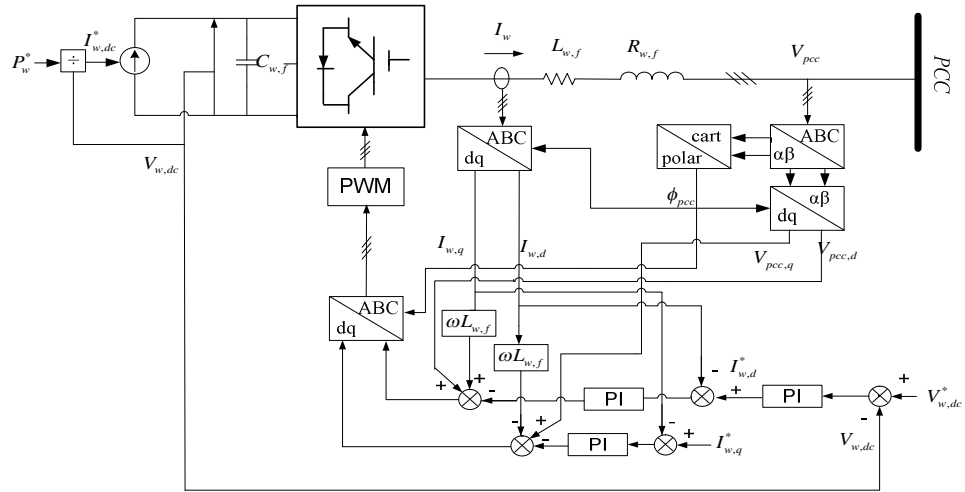


Figure 3.6: Block diagram of wind power system and its control structure

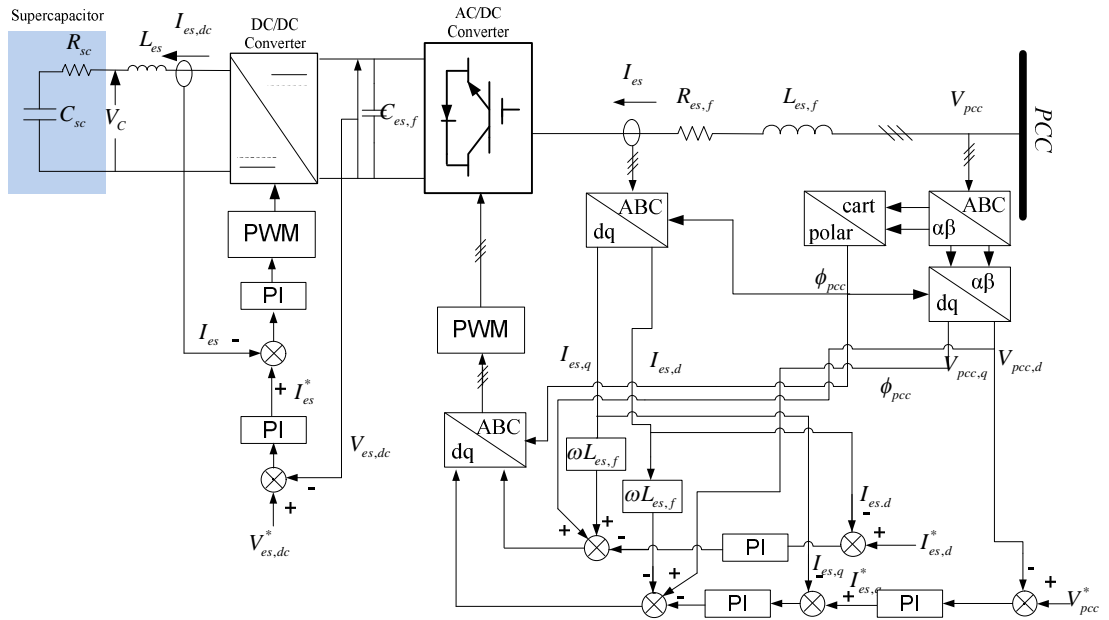


Figure 3.7: Block diagram of energy storage system and its control structure

3.3.1 Simulation Parameters

Transmission Line

The transmission line as shown in Figure 3.1 is represented by a series impedance, $Z_t = R_t + j\omega L_t$. The nominal voltage, $V_{t,n}$ is 11kV, system frequency is 50Hz and rated power of the transmission line, $S_{t, rated}$ is 10MVA. The resistance, R_t and inductance, L_t is calculated for a particular SCR and X/R ratio to represent the grid strength as described in section 1.2.1.

Wind Farm

The wind farm is connected to PCC via a 1kV, 10MVA front end converter. The parameters are given in Appendix C.

Energy Storage System

The ESS is connected to the PCC via a 1kV, 1MVA front end converter and a 2kV, 1MVA DC/DC converter. The parameters are given in Appendix C and Appendix D.

3.3.2 Estimation of Supercapacitor Round Trip Efficiency

For the analysis of overall system efficiency, the round trip efficiency of the supercapacitor has to be quantified. The estimation of round trip efficiency of the supercapacitor is complicated because it depends on the equivalent resistance of the supercapacitor, power level, supercapacitor voltage and current variation during the charge-discharge cycle. In order to estimate the round trip efficiency of the energy storage system, the losses in the AC/DC converter and DC/DC converters are neglected. All resistances in the energy storage system components are set to zero except R_{sc} which is varied depending on η_{rt} . The resistance is reduced to increase the efficiency. η_{rt} is calculated when a complete cycle is observed based on the supercapacitor voltage level (i.e: the voltage increases from $V_{C, min}$ to $V_{C, max}$ when charging and drops back to $V_{C, min}$ when discharging) [51]. This can be calculated by:

$$\eta_{rt} = -\frac{E_D}{E_C} \quad (3.21)$$

where, E_D and E_C is the amount of energy discharge and charge, respectively. In this chapter, the energy charged and discharge is calculated from the measured power flow into the supercapacitor. The measurement in the PSCAD simulation is exported to Matlab. In Matlab, the function *trapz*, which computes the integral of the power measured via a trapezoidal method, is used to determine the energy for the period of time specified. The PSCAD simulation is repeated many times and results are exported to Matlab for analysis to obtain the relationship between $\Delta I_{w,Brk}$ in pu versus η_{rt} for breakeven situation.

3.3.3 Simulation Procedures, Results and Discussions

First the simulation is done with the square wave power generation (i.e: $D=0.5$) and then the simulation is done with the real wind power generation.

3.3.3.1 Idealized Waveform Power Generation

The system in Figure 3.1 is modeled in PSCAD. The simulations procedures performed are as follows:

Step 1: The simulation in PSCAD is performed for the case with and without energy storage. The P_w^* applied is a square wave. The PSCAD simulation results are saved in a text file and exported to Matlab for analysis. The SCR, X/R ratio and ΔI_w are set to a particular value.

Without energy storage all power generated is transferred to the grid instantaneously. With the energy storage, a constant power at average value is exported to the grid. The energy is stored when power generated higher than the average value and released to the grid when power generated is less than the average value. For example, the PSCAD simulation result for a case is plotted in Figure 3.8. In this case, the maximum power generated is 0.6pu and minimum power is 0.4pu. The average power is 0.5pu. Both the SCR and X/R ratio are 2. As shown in Figure 3.8(b),

without energy storage, the transmission line is carrying 0.6pu current from 0.5s to 1.5s and 0.4pu current from 1.5s to 2.5s. With energy storage, the current transmitted in the transmission line is kept constant at 0.5pu. Thus, ΔI_w is 0.1pu. The power loss associated with this condition is seen in Figure 3.8(c). Without energy storage, the maximum power loss is about 5% between 0.5s to 1.5s and the minimum power loss is 2.5% between 1.5s to 2.5s. With energy storage, the power loss is constant at about 3.5%. In Figure 3.8(d), the power flow to and from the energy storage is shown. A negative value indicates that the power is flowing to the energy storage and a positive value means the energy storage is discharging. The energy storage voltage is shown in Figure 3.8(e). When charging from 0.5s to 1.5s, the voltage increases from 0.6pu to 0.95pu and when discharging, the voltage drops back to 0.6pu at 2.415s. Thus, a complete cycle of charging and discharging is from 0.5s to 2.415s.

Step 2: The quantities η_{rt} , $E_{es,loss}$, $E_{t,saved}$ and ΔE_{sl} are calculated. E_C and E_D for a complete cycle of charging and discharging are calculated from the power flow to the energy storage unit (Figure 3.8 (d)) using function *trapz* in Matlab. For the example case in Figure 3.8, E_C is calculated from 0.5s to 1.5s and E_D is calculated from 1.5s to 2.415s. $E_{es,loss} = E_C - E_D$. η_{rt} is calculated using (3.21). The energy losses in the transmission line with and without ESS, $E_{loss,w}$ and $E_{loss,wo}$, respectively are calculated from the measured power loss in the transmission line (Figure 3.12(d)) also using function *trapz* in Matlab. $E_{t,saved} = E_{loss,w} - E_{loss,wo}$. $\Delta E_{sl} = E_{t,saved} - E_{es,loss}$. The Matlab code to perform these calculations is given in Appendix C.

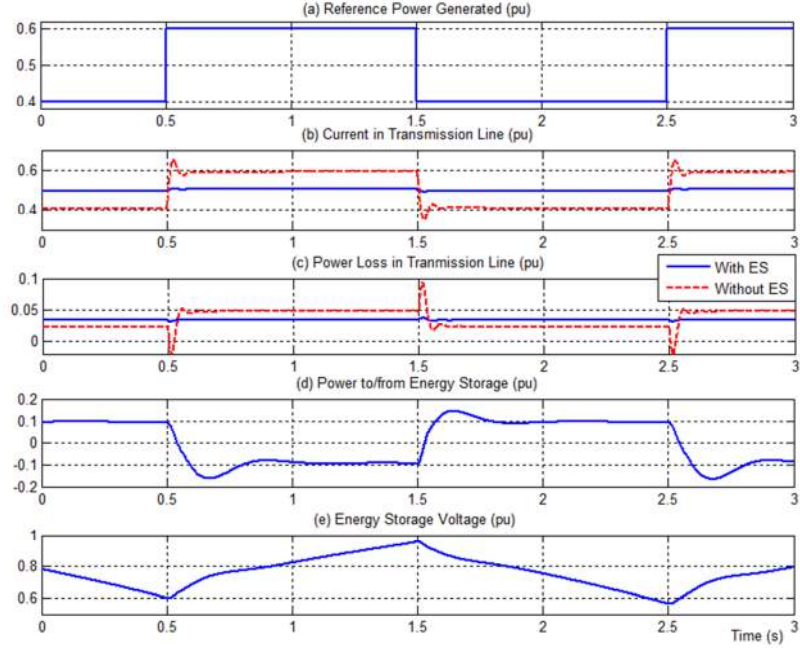


Figure 3.8: Simulation results for a case with the square wave power generated
(a) reference wind power generated (pu), P_w^* ; (b) wind current generated (pu), I_w ;
(c) Power loss in transmission line (pu), $P_{t,loss}$ (d) power to/from energy storage(pu), P_{ess} ;
(e) Energy storage voltage(pu), V_C

Step 3: R_{SC} is varied and steps 1 and 2 are repeated. The resistance is varied to obtain a different value of η_{rt} of the ESS. This step is repeated several times to attain the relationship between η_{rt} and ΔE_{sl} .

Step 4: Steps 1, 2 and 3 are repeated for different values of ΔI_w .

Step 5: η_{rt} versus ΔE_{sl} are plotted. The plots of η_{rt} versus ΔE_{sl} for the case with SCR 2 and X/R ratio of 2 and ΔI_t of 0.05pu, 0.1pu and 0.15pu are shown in Figure 3.9. From the figure, η_{rt} to achieve the condition where $E_{t,saved} = E_{es,loss}$ can be obtained for different values of ΔI_w . In this case, the η_{rt} are 97%, 94.9% and 90.9% for the ΔI_t of 0.05pu, 0.1pu and 0.15pu, respectively. Thus, the plot of $\Delta I_{w,Brk}$ versus η_{rt} can be established.

Step 6: The SCR is varied and steps 1 to 5 are repeated.

Step 7: $\Delta I_{w,Brk}$ versus η_{rt} are plotted.

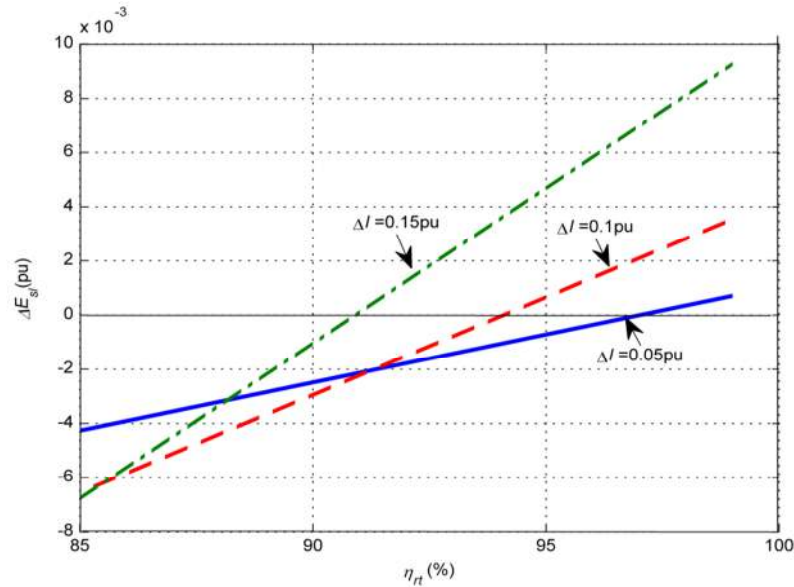


Figure 3.9: ΔE_{sl} as a function of η_{rt}

Step 8: The X/R ratio is varied and steps 1 to 7 are repeated.

Step 9: $I_{w,o}$ is varied and steps 1 to 7 are repeated.

The graphs of $\Delta I_{w,Brk}$ in pu versus η_{rt} are shown in Figure 3.10 for the cases when SCR, X/R ratio and $I_{w,o}$ are varied. $\Delta I_{w,Brk}$ is the minimum value of current variation that result in overall efficiency saving. In these graphs, the mathematical analysis and PSCAD simulation results are shown. It is seen that mathematical analysis closely matches the simulation results. Small deviations between PSCAD simulation results and mathematical analysis may be due to accumulation of errors in steps taken to get the relationship between $\Delta I_{w,Brk}$ and η_{rt} of the simulation results. Note that the simulations are only done for ΔI_w of 0.05pu, 0.1pu and 0.15pu. The curves are plotted assuming a linear relationship and extrapolation can also contribute to the deviations. Another possible cause of deviations is because in the mathematical analysis a perfect square wave current is used, but in simulation the current is not a perfect square wave due to delays caused by the controller action as seen in Figure 3.9 (c). However, the mathematical analysis and the PSCAD simulation results are consistent.

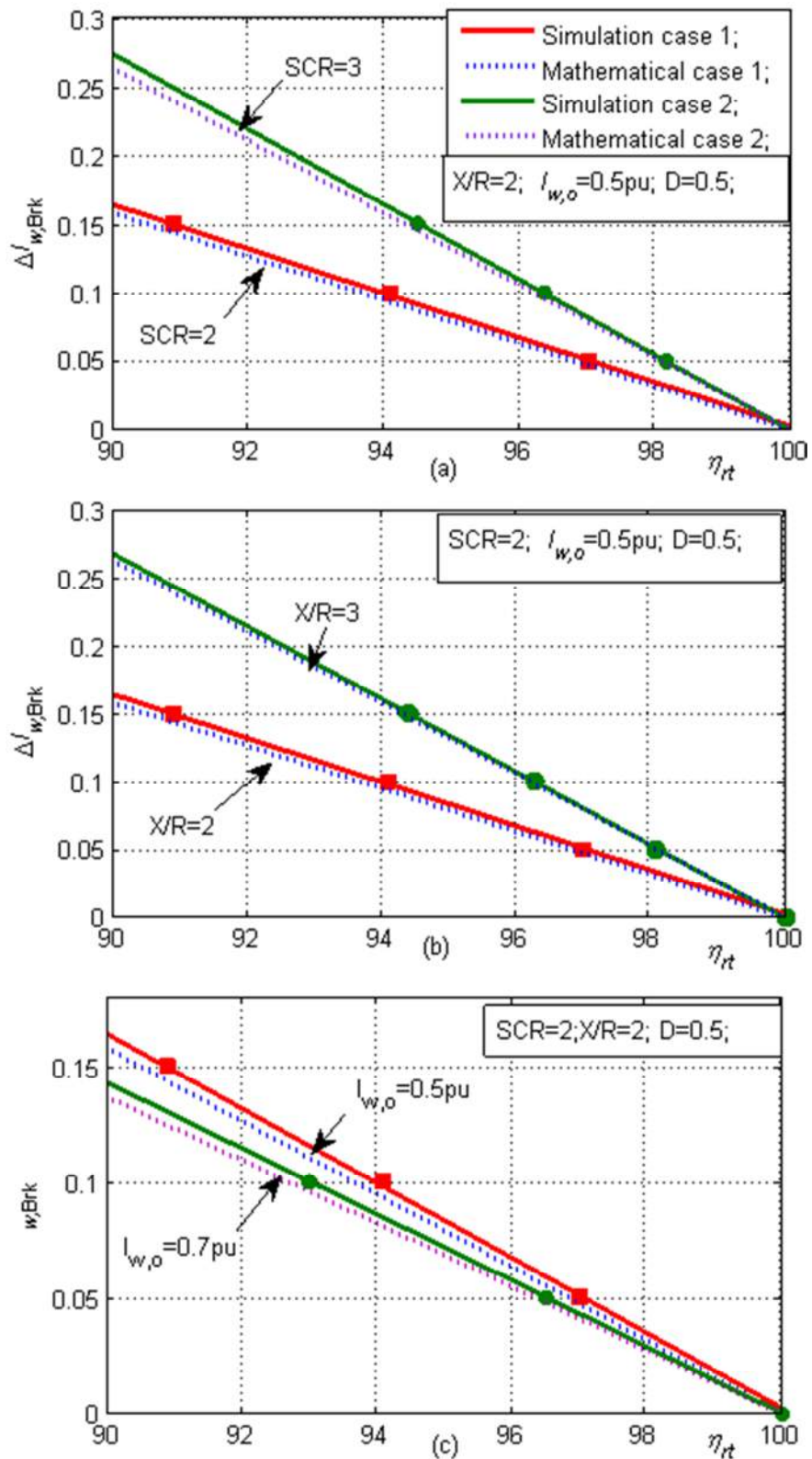


Figure 3.10: Plot of $\Delta I_{w,Brk}$ versus η_{rt} from mathematical and PSCAD simulation results
 (a) various SCR, (b) various X/R, (c) various $I_{w,o}$

3.3.3.2 Real Wind Power Profile

In the previous section, we have seen that the PSCAD simulation results are consistent with the mathematical analysis for the case where the power generation is a square wave form. If the power generation is coming from the wind farm that is extracting maximum power from the wind, the power generated will be fluctuating depending on the wind profile.

In this section, the simplified wind DFIG for wind turbine under MPPT as modelled in section 2.4 is used. The real wind speed as given in section 2.2.5 is employed for the analysis. Therefore, a perturbation of the wind power/current generated, σ_{I_w} and $I_{w,o}$ can be obtained for a particular wind profile. The σ_{I_w} is represented by its standard deviation. Figure 3.11 shows the frequency spectrum of transmission line current (top) and the associated power losses (bottom) caused by the idealized square-wave power profile and the one for the real wind speed data under the assumption that the DC and the 1st harmonic components are the same. As seen in the figure, the difference in average of sums square (equivalent to rms of power loss) is below 10% when the real wind power is approximated by a square-wave profile, which means very small differences in terms of power loss in the transmission line. Therefore, the approximation using the square-wave profile to replace real wind data may be a valid approach when assessing the benefits of employing energy storage and this will be verified next. Then we can consider $\Delta I_{w,Brk} = \sigma_{I_w,Brk}$ for the analysis with real wind data.

Setting the σ_{I_w} and $I_{w,o}$ to a particular value that is for a particular wind profile, the relationship between σ_{I_w} and η_{rt} can be obtained from PSCAD simulation results.

Step 1: The simulation in PSCAD is performed for the case with and without energy storage unit. The P_w^* is fluctuating corresponding to the wind profile with MPPT. The PSCAD simulation results are saved in a text file and exported to Matlab for analysis. The SCR, X/R ratio, σ_{I_w} and $I_{w,o}$ are set to a particular value.

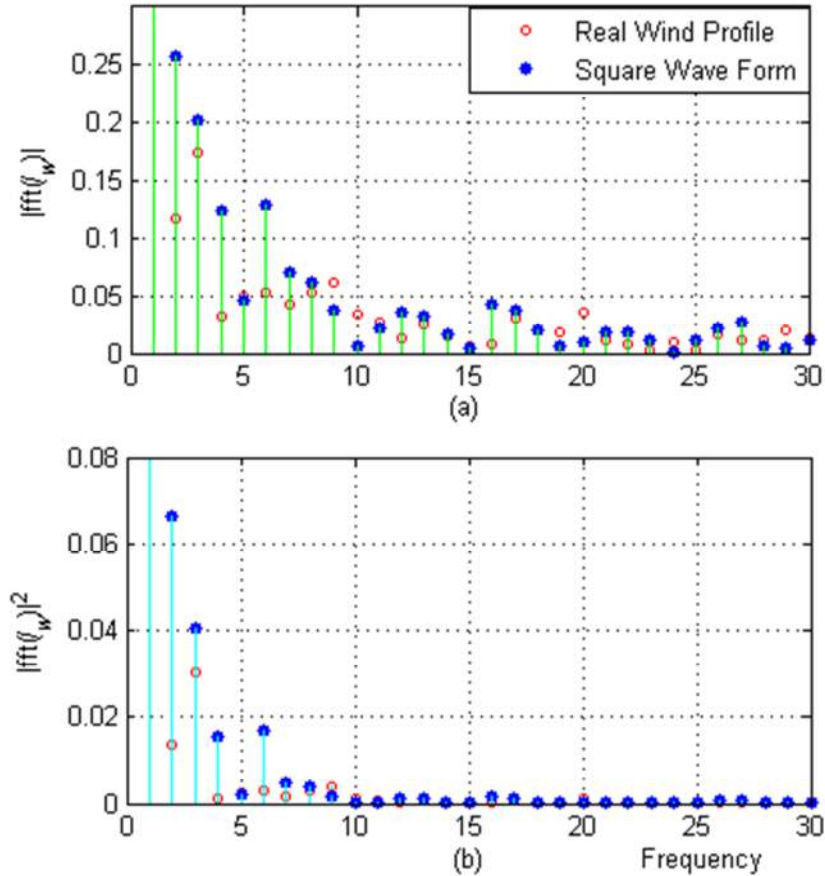


Figure 3.11: Frequency spectrum of (a) the transmission line current and (b) the transmission power losses ($\sigma_{I_w} = 0.1\text{pu}$; $I_{w,o} = 0.5\text{pu}$) when comparing the square-wave template with the real wind power data.

For example, the PSCAD simulation result for a case is plotted in Figure 3.12. The wind speed is fluctuating with average speed of 0.8pu and standard deviation of 0.1pu (Figure 3.12(a)). The power generated has the average power generated of 0.5pu as shown in Figure 3.12(b). As shown in Figure 3.12(c), without energy storage, the current generated is fluctuating corresponding to the power generated.

$I_{w,o}$ and σ_{I_w} are calculated as 0.5pu and 0.16294pu , respectively. With energy storage, the current transmitted in the transmission line is kept constant at 0.5pu . The power loss associated with this condition is seen in Figure 3.12(d). With energy storage, the power loss in the transmission line is constant. In Figure 3.12(e), the power flow to and from the energy storage is shown. A negative value indicates that the power is flowing to the energy storage and a positive value means the energy storage is discharging. The energy storage voltage is shown in Figure 3.12(f). When charging the voltage increases and when discharging the voltage drops.

Step 2: The values of η_{rt} , $E_{es,loss}$, $E_{t,saved}$ and ΔE_{sl} are calculated. The E_C and E_D in a complete cycle is calculated from the power flow to the energy storage unit (Figure 3.12(e)) using the *trapz* function in Matlab. For the example case, a complete cycle of charging and discharging of the supercapacitor can be taken from 66.23s to 577.6s. This is when the voltage increases from 0.7279pu at 66.23s and it drops back to the same value at 577.6s as seen in Figure 3.12(f). E_C from 66.23s to 577.6s is calculated using the *trapz* function in Matlab when the power flow to the energy storage (Figure 3.12(e)) is negative. The value of E_D is calculated when the power flow is positive. $E_{es,loss} = E_C - E_D$. η_{rt} is calculated using (3.21). The energy losses in the transmission line with and without ESS, $E_{loss,w}$ and $E_{loss,wo}$, respectively are calculated from the measured power loss in the transmission line (Figure 3.12(d)) also using function *trapz* in Matlab. $E_{t,saved} = E_{loss,w} - E_{loss,wo}$. $\Delta E_{sl} = E_{t,saved} - E_{es,loss}$. The Matlab code written to perform these calculations is similar to that given in Appendix C.

Step 3: R_{SC} is varied. Then, steps 1 and 2 are repeated. The resistance is varied to obtain a different value of η_{rt} . This step is repeated only 3 times to attain the relationship between η_{rt} and ΔE_{sl} . It is assumed that the relationship is linear in order to reduce the need to repeat the simulations too many times.

Step 4: Steps 1, 2 and 3 are repeated with a different set of wind profile with a new σ_{Iw} keeping the same $I_{w,o}$. The simulations are done with σ_{Iw} values of 0.126pu, 0.968pu and 0.052pu, respectively.

Step 5: ΔE_{sl} versus η_{rt} is plotted. From this plot, η_{rt} to achieve the condition where $E_{t,saved} = E_{es,loss}$ can be obtained for different values of σ_{Iw} . Thus, the plot of $\sigma_{Iw,Brk}$ versus η_{rt} can be established.

Step 6: Steps 1 to 5 are repeated for the cases: (1) SCR=4 and X/R=2; (2) SCR=5 and X/R=2; (3) SCR=4 and X/R=3. Simulations are performed with SCR of 4 and 5.

These relatively high SCRs were simulated because at lower SCR's the transmission line has a lower transmission line capability. An example of the simulation results for the case with SCR=2 and X/R=2 is shown in Figure 3.13. The variation of wind power includes high power where the system becomes oscillatory and underdamped when simulating without the ESS. This makes the energy loss processing of the simulation results difficult. If the transmission instantaneous power exceeds the transmission line limit, instability can result. The investigation of the oscillation of instability is investigated in Chapter 4.

Figure 3.14 shows the graphs of the simulation result compared with the mathematical results obtained using (3.19) for the square wave with $\sigma_{I_w,Brk} = \Delta I_{w,Brk}$. In Figure 3.14(a) graphs for cases with SCR=4 and SCR=5 are shown for X/R=2. In Figure 3.14(b), graphs for X/R=2 and X/R=3 are shown for SCR=4. For all cases shown, the simulated results closely match the mathematical ones. The small deviations are because of the accumulation of errors in the numerical data processing in the steps taken for the simulation result. Equation (3.19) can also be applied to the real wind speed profile where $\Delta I_{w,Brk} = \sigma_{I_w,Brk}$, yielding:

$$\sigma_{I_w,Brk} = (-B + \sqrt{B^2 - 4AC}) / 2A - I_{w,o} \quad (3.22)$$

As seen in Figure 3.14, the simulation results are given for $\sigma_{I_w} = 0.2$ pu corresponding to $\eta_{rt} > 95\%$. Again, this is due to the occurrence of peak wind power values that cause oscillation due to the line transmission limit being exceeded when the ESS is not used. Obviously, the presence of the ESS allows an increase in average transmitted power when $\sigma_{I_w} > 0.2$ pu. An increase in overall efficiency with $\sigma_{I_w} < 0.2$ pu implies that the ESS needs a minimum round trip efficiency of $\eta_{rt} > 95\%$. This can be achieved with some energy storage technologies such as batteries and supercapacitor as discussed in section 1.2. It is also apparent that at a lower SCR and X/R value the minimum η_{rt} required for overall efficiency is lower. Despite any arguments, the relationship in (3.22) can be used to evaluate a similar power system for an estimation to improve overall efficiency with an energy storage.

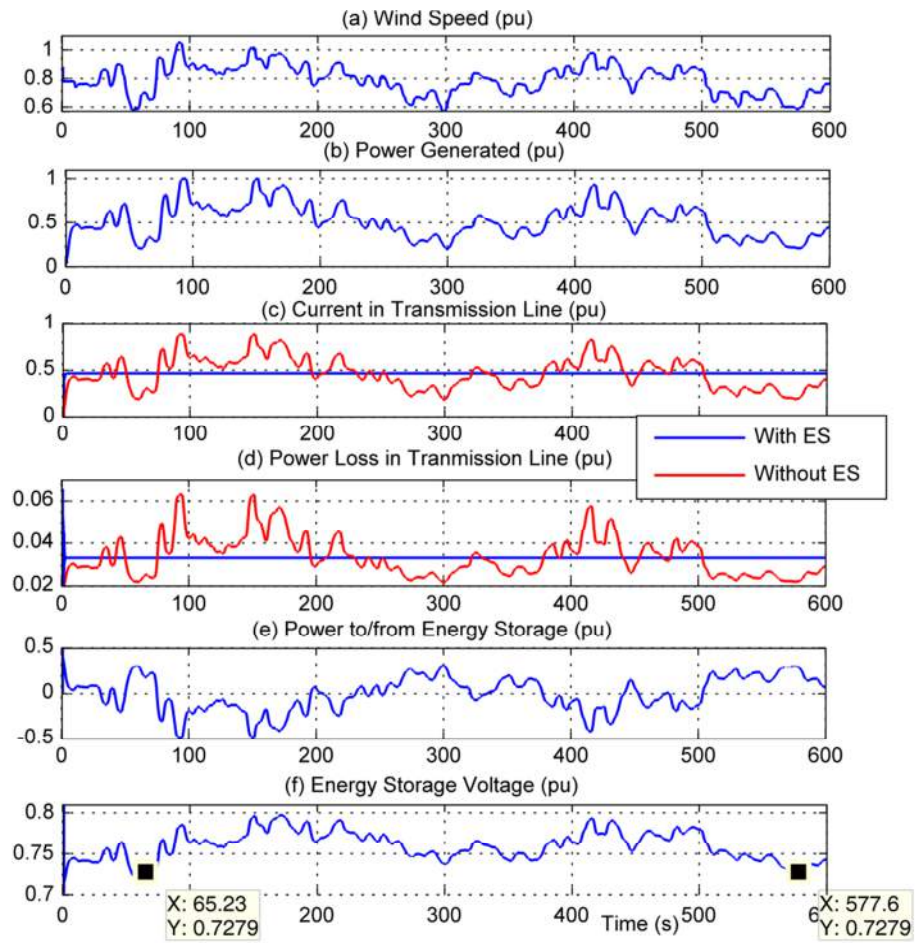


Figure 3.12: Simulation results for a case with the real wind power generated ($\sigma_{I_w} = 0.1$ pu; $I_{w,o} = 0.5$ pu) (a) Wind speed(pu), V_w ; (b) Power generated(pu), P_{gen} ; (c)Transmission line current(pu), I_t ; (d) Power loss in transmission line (pu), $P_{t,loss}$; (e)Power to/from energy storage(pu), P_{ess} ; (f) Energy storage voltage(pu), V_C

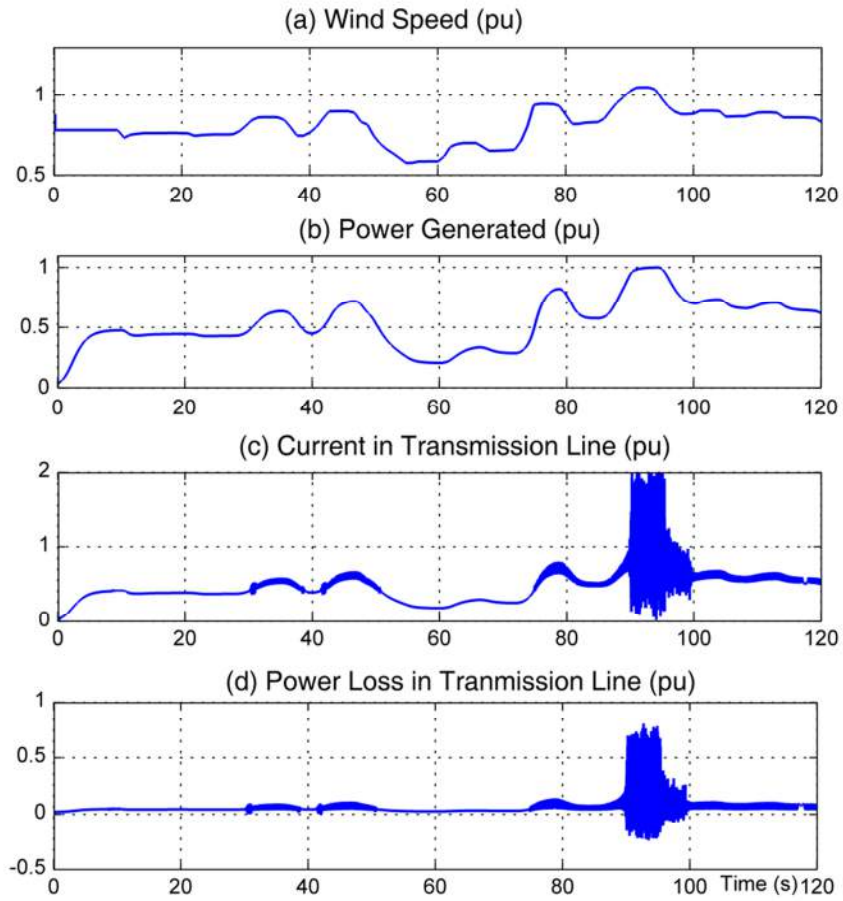


Figure 3.13: Simulation results for a case with SCR=2 and X/R=2 without the ESS
(a) Wind speed(pu), V_w ;(b) Power generated(pu), P_{gen} ; (c)Transmission line current(pu), I_t ;
(d) Power loss in transmission line (pu), $P_{t,loss}$

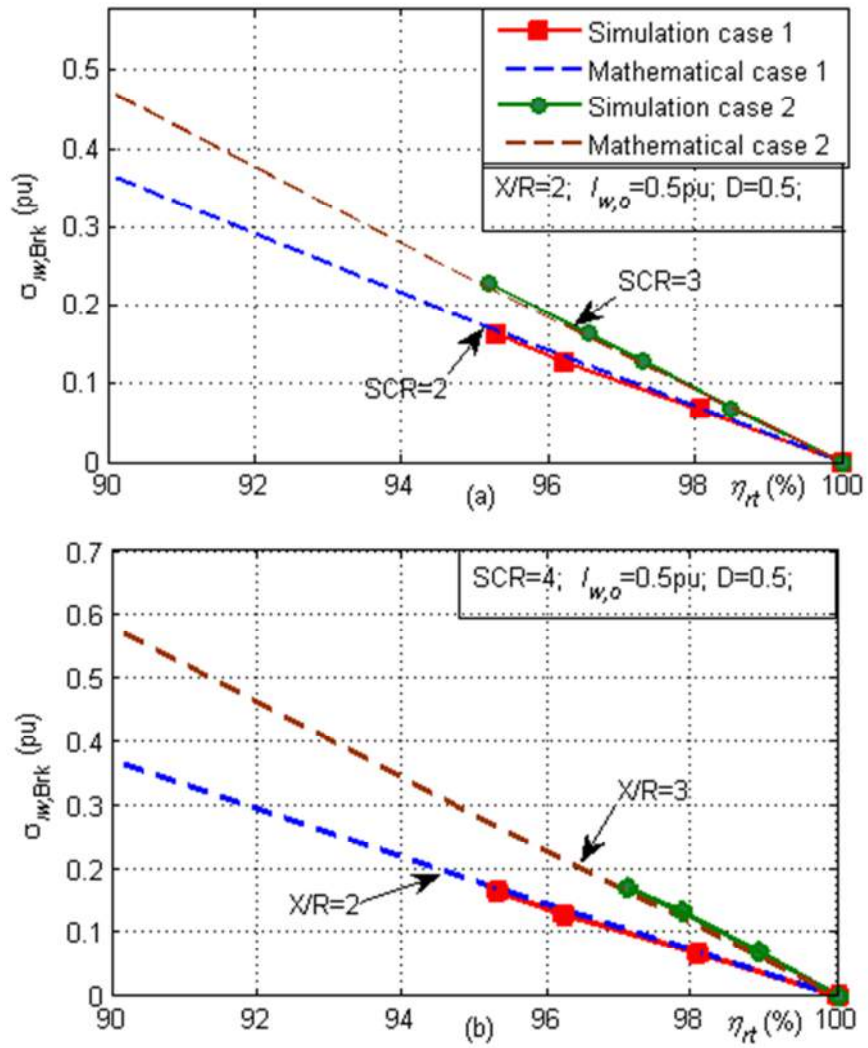


Figure 3.14: $\sigma_{Iw,Brk}$ versus η_{rt} (a) SCR=4 and 5; (b) X/R=2 and 3.

3.4 Discussion from a Practical Viewpoint

The analysis has suggested that the wind power ripple (represented by $\Delta I_{w,Brk} = \sigma_{I_{w,Brk}}$), the average wind power (represented by $I_{w,o}$), the ESS round trip efficiency (η_{rt}), the duty cycle (D) and the grid SCR and X/R ratio are the important parameters when assessing the benefit of installing energy storage for overall system efficiency improvement. The analysis can give a fair suggestion of the overall efficiency improvement when installing an energy storage system for a given practical application.

The typical range of wind power ripple is between 0 to 0.1pu. The maximum wind power ripple of 0.1pu corresponds to typical rating of the ESS itself. The average wind power generated may vary from 0 to 1pu depending on the time frame and the wind profile considered. The duty cycle D also depends on the wind profile. As seen previously, D has the least impact on the break-even condition. Therefore, for convenience, we can assume that D is 0.5. As discussed in section 1, η_{rt} depends on the type of ESS itself. With current technology η_{rt} of up to 95% is realistic.

As seen, low SCR values and low X/R ratios can increase the potential of overall energy saving with an ESS. A grid with SCR between 1 and 2 is referred to as a very weak grid [70]. It is common that a wind farm is located in a remote area and thus could be interfaced to a very weak grid. A very low X/R ratio indicates that the grid is very resistive. The X/R ratio range from 2 to 15 with typical value of 5 but a very weak grid may have lower X/R ratio due to more resistive components [70]. As discussed in section 1.5, the SCR is the value of admittance at fundamental frequency in per unit, Y_{pu} at a rated apparent power, S_r and a nominal voltage, V_n . Therefore, a low SCR value indicates that the system has a high impedance. This may be due to a very long transmission line of more than 100km. On top of that, the load in the system also may contribute toward a high impedance grid. A subject of future research that could be interesting is to derive the SCR and X/R as a function of the transmission line length and power rating.

Considering the practical values of all the parameters, breakeven lines are drawn as shown in Figure 3.15. The plots show only the η_{rt} up to 95% and the $\sigma_{I_{w,Brk}}$ up to 0.1pu. Figure 3.15 (a) shows the breakeven lines for the system with SCR=1 and SCR=2; while X/R=2, $I_{w,o}=0.5$ and $D=0.5$. If the rating of ESS installed is 0.1pu and the ESS having η_{rt} of greater than 81%, we gain some energy saving with the ESS installed for SCR=1. For example at a particular point where η_{rt} is 90% and the wind power ripple is 0.06pu, we are above the breakeven line for the SCR=1. If the system has SCR=2 with power ripple of 0.06pu we do not achieve energy saving even with $\eta_{rt}=95\%$. However, if the wind power ripple is 0.1pu, we gain energy saving with $\eta_{rt} > 93.5\%$ and SCR=2. At $\eta_{rt} > 95\%$ we save if the power ripple is greater than 0.078pu at SCR=2.

Figure 3.15 (b) show breakeven lines for a system with SCR=1, $I_{w,o}=0.5$ and $D=0.5$, when X/R is 2 or 3. When X/R ratio is higher, the break-even line shifts to higher value of $\sigma_{I_{w,Brk}}$ and η_{rt} . This indicates that the increase in X/R ratio will decrease the potential energy saving. However, for SCR=1 and X/R=3, we still gain energy saving for $\eta_{rt} > 91\%$ and a power ripple of 0.1pu. If the power ripple is 0.05pu, η_{rt} needs to be greater than 95% for overall efficiency gain.

Figure 3.15 (c) show break-even lines for a system with SCR=1, X/R=2 and $D=0.5$, when $I_{w,o}$ is 0.6pu or 0.4pu. When $I_{w,o}$ is lower, the break-even line shifts to higher value of $\sigma_{I_{w,Brk}}$ and η_{rt} . This means that higher values of $I_{w,o}$ (corresponding to higher average power generated) is preferable for an overall energy saving. From Figure 3.15 (c), it is observed that when power ripple is 0.1pu, the η_{rt} required to breakeven is only 73% with $I_{w,o}=0.6pu$ instead of 84% with $I_{w,o}=0.4pu$. With $\eta_{rt}=95\%$, we will already gain energy saving when power ripple is $>0.02pu$ at $I_{w,o}=0.6pu$ instead of $>0.05pu$ with $I_{w,o}=0.4pu$.

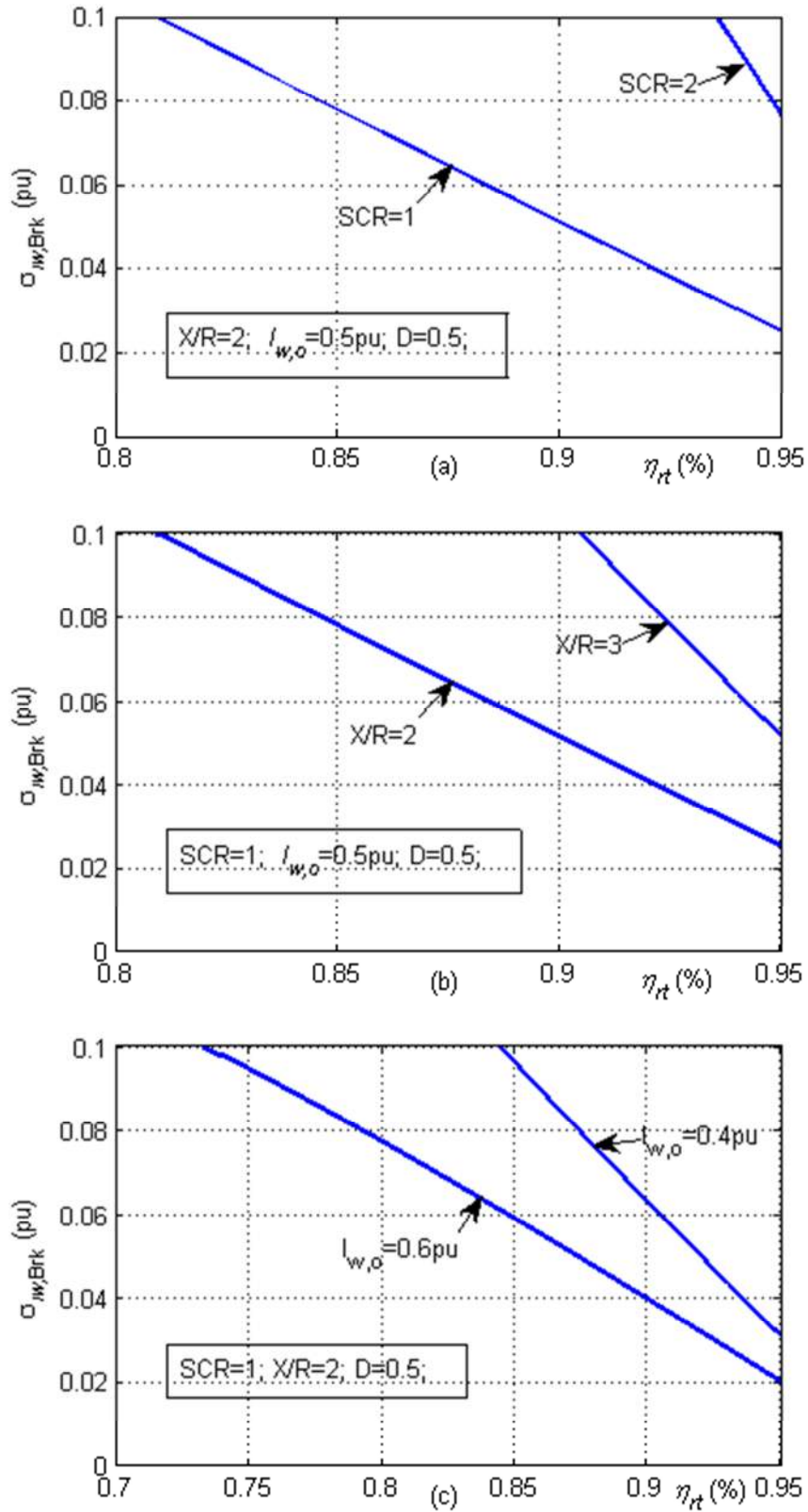


Figure 3.15: Breakeven lines for a practical range of $\sigma_{w,Brk}$ and η_{rt} (a) various SCR, (b) various X/R ratio and (c) various $I_{w,o}$

3.5 Chapter Summary

The key parameters that are significant to improving the overall efficiency of a wind power system employing energy storage have been identified and a simple analytical relationship has been derived to show the criteria for increased system efficiency. The analysis has suggested that the wind power ripple (represented by $\Delta I_{w,Brk}$), the average wind power (represented by $I_{w,o}$), the ESS round trip efficiency (η_{rt}), the duty cycle (D) and the transmission line SCR and X/R ratio are the important parameters when assessing the benefit of installing energy storage for overall system efficiency improvement. The analytical relationship derived in (3.19) can be used in the selection of the energy storage technology via its characteristic round trip efficiency η_{rt} , and to result in smaller energy storage losses than the savings achieved in the transmission system characterized by $I_{w,o}$, D , SCR and X/R ratio. From the simulation with real wind speed data, it is shown that the relationship in (3.19) with $D=0.5$ is consistent with $\Delta I_{w,Brk} = \sigma_{I_{w,Brk}}$ - the minimum value of the standard deviation of wind power/current generated to achieve the breakeven point for the overall system efficiency and an analysis based on FFT of the disturbance explains why this is the case.

In practice where the rating of energy storage is typically less than 0.1pu and η_{rt} is less than 95%, the analysis will be significant for a system with $SCR < 2$ and $X/R < 3$ which representing a very weak grid and a highly resistive system. A subject of future research that could be interesting is to derive the SCR and X/R as a function of the transmission line length and power rating.

Chapter 4

Stability Analysis of a Microgrid with a Constant Power Load Fed by a Controlled Converter

4.1 Introduction

Distributed generation technology has the potential to become widely available since renewable energy resources such as wind turbines and solar panels are available at small power and economically appropriate at local and even domestic level. The distributed generation will be connected to the network by power electronics converters [89], [90]. This is so to provide controllability and ability to maintain high power quality. In this chapter, the wind farm is assumed to be an intermittent, renewable source implemented at a local or distributed level. It is aggregated into a single unit feeding the network by a controlled Pulse Width Modulation (PWM) converter as shown in Figure 4.1. It is also noted that a wind power source is a quasi-constant power source that can influence the small-signal stability of the power system as discussed in section 1.3 [91].

In addition, the local grid may feed loads that are predominately constant power load (CPL): examples may be energy storage schemes, hydrogen production, and controlled variable speed drives. The possibility of instability caused by constant power loads is well known [8]–[11]. The combination of both constant power sources and loads is expected to increase the small-signal instability of the system.

The weak grid may make the stability issue become more significant. In [92], a voltage source rectifier interfaced load connected to a weak grid is research through

experiment. It is reported that the system becomes unstable when the load is increased suddenly. Thus, it is predicted that, the CPL connected to a weak grid may also cause instability in the system.

In this chapter, the stability of the system in Figure 4.1 is investigated. The power system consists of a wind farm (representing an intermittent, DG source) and a large constant power load, connected via a bus which has a grid connection. The transmission line parameters are chosen to create a weak grid. A third feed, an energy storage unit, is also connected to the point of common coupling (PCC). The voltage magnitude at PCC is regulated by reactive power injection from one or more of the converters. Here the voltage regulation is assigned to the energy storage unit [93]. Typically, LCL filter connected between a converter and PCC. The LCL filter causes oscillations at higher resonant frequencies. For a PWM converter, the resonant frequencies are significantly high. Therefore, to simplify the system modeling only filter inductance and resistance is connected between a PWM converter and PCC.

This chapter will derive the dynamic equations for the system. This is presented in section 4.2. The common dq -modelling approach as published in [67], [94], is employed for the mathematical modeling represented as a set of state space equations. The eigenvalues which can be calculated from the system matrix are used to analyze the small-signal stability. The small-signal stability analysis of the system is discussed in section 4.3. The stability analysis through mathematical model is verified through PSCAD simulation.

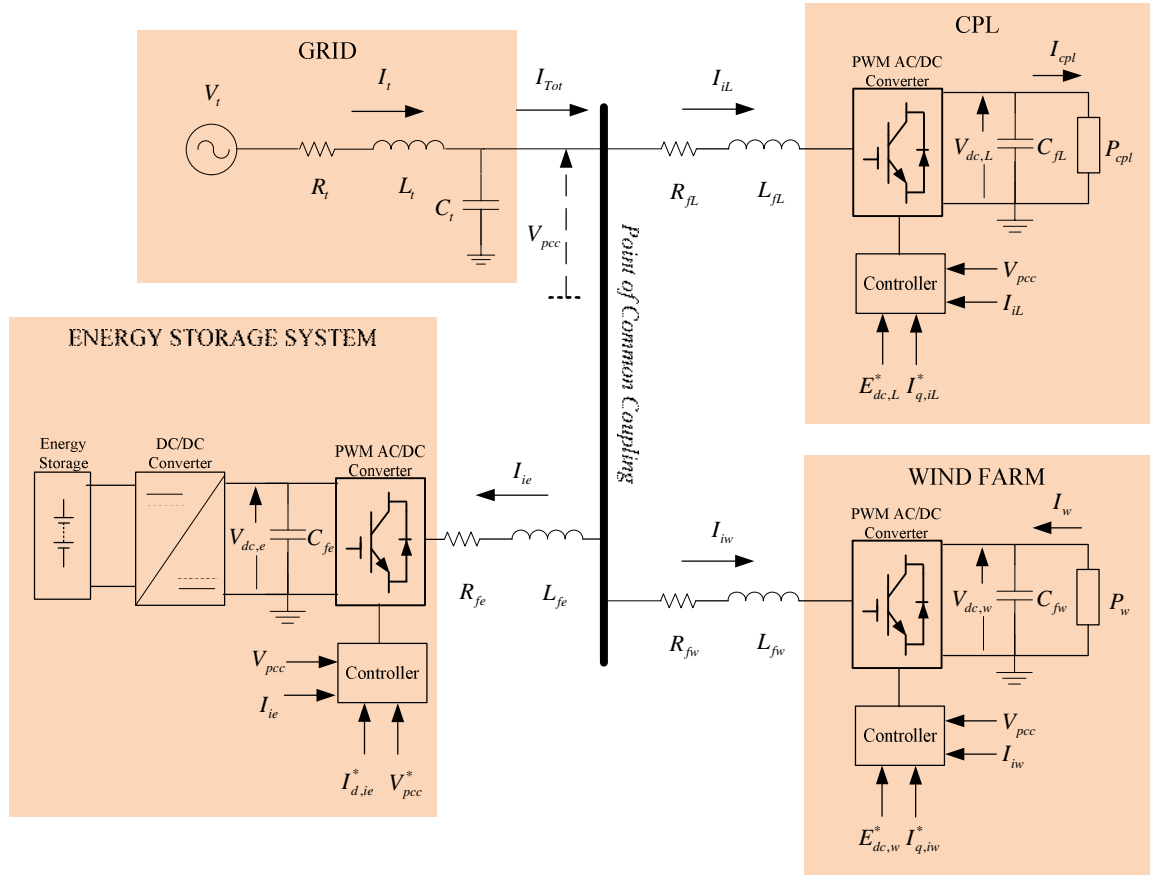


Figure 4.1: Block diagram of the system under study

4.2 Control and Modeling

This section presents the control and development of the mathematical model for the system in Figure 4.1. For clarity, the system is divided into four parts: the grid, the CPL, the wind farm and the energy storage system. These are described in section 4.2.2 - 4.2.5, respectively. The complete dynamic state-space equation is discussed in section 4.2.6, followed by its linearization in section 4.2.6.1.

4.2.1 Dq-Transformation and the Phase Locked Loop

The mathematical modeling is performed using dq -modeling approach. Thus, three phase quantities are transformed into a two axis frame (dq -frame), rotating at an instantaneous speed (system frequency), ω_e . The dq -transformation is done by

multiplying the three phase quantities with a transformation matrix T such that

$$\begin{bmatrix} x_d & x_q \end{bmatrix}^t = T \begin{bmatrix} x_a & x_b & x_c \end{bmatrix}^t \text{ and}$$

$$T = \sqrt{\frac{2}{3}} \begin{bmatrix} \cos(\omega_e t) & \cos(\omega_e t - \frac{2\pi}{3}) & \cos(\omega_e t + \frac{2\pi}{3}) \\ -\sin(\omega_e t) & -\sin(\omega_e t - \frac{2\pi}{3}) & -\sin(\omega_e t + \frac{2\pi}{3}) \end{bmatrix} \quad (4.1)$$

Similarly, the inverse transformation can be obtained by multiplying the dq -quantities with an inverse transformation matrix:

$$T^{-1} = \sqrt{\frac{2}{3}} \begin{bmatrix} \cos(\omega_e t) & -\sin(\omega_e t) \\ \cos(\omega_e t - \frac{2\pi}{3}) & -\sin(\omega_e t - \frac{2\pi}{3}) \\ \cos(\omega_e t + \frac{2\pi}{3}) & -\sin(\omega_e t + \frac{2\pi}{3}) \end{bmatrix} \quad (4.2)$$

The dq -transformation vector diagram is shown in Figure 4.2. In this chapter, the d -axis is fixed to the voltage at the PCC bus. Therefore:

$$\phi_{pcc} = \phi, V_{d,pcc} = |V_{pcc}| \text{ and } V_{q,pcc} = 0 \quad (4.3)$$

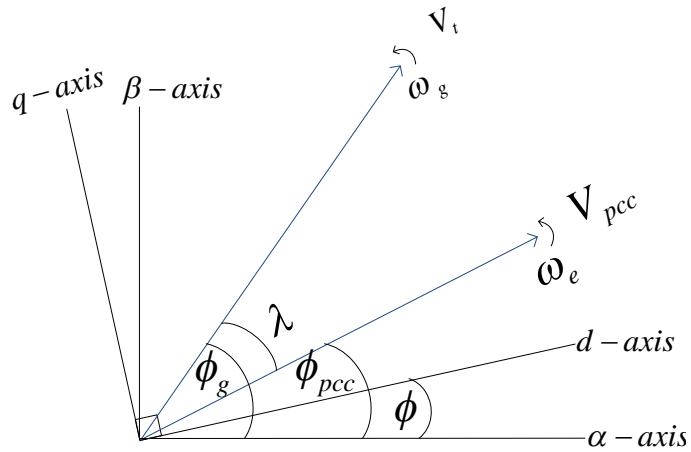


Figure 4.2: Phasor diagram for dq -transformation

All PWM converters in the system studied in Figure 4.1 are vector controlled oriented on the voltage at PCC. Thus, for convenient only one phase locked loop (PLL) is used to service all front end PWM converters in the system. The PLL provides the reference angle for the vector control. The block diagram of the PLL is shown in Figure 4.3. The output voltage is transformed to the rotating dq -reference frame, and the frequency (and hence phase) is controlled to make the q -component zero. The corresponding transformation matrices are given in (4.1). The PI controller can be used for the PLL but it will give another state variable and thus increase the order of overall system. To reduce the number of states, a proportional controller with proportional gain K_{pll} is used. The system electrical frequency, ω_e is variable during a transient. However, at steady state it is assumed to be able to track the voltage source frequency, ω_g without error. ω_g set is constant at 50Hz. The relationship between ω_e and is given by:

$$\omega_e = \omega_g + K_{pll}V_{q,pcc} \quad (4.4)$$

During steady state with $\omega_e = \omega_g$, $V_{q,pcc}$ is zero. The rate of change of the angle between V_g and V_{pcc} , λ is given by:

$$\frac{d\lambda}{dt} = \omega_g - \omega_e \quad (4.5)$$

which is the state equation to model the dynamics of the PLL.

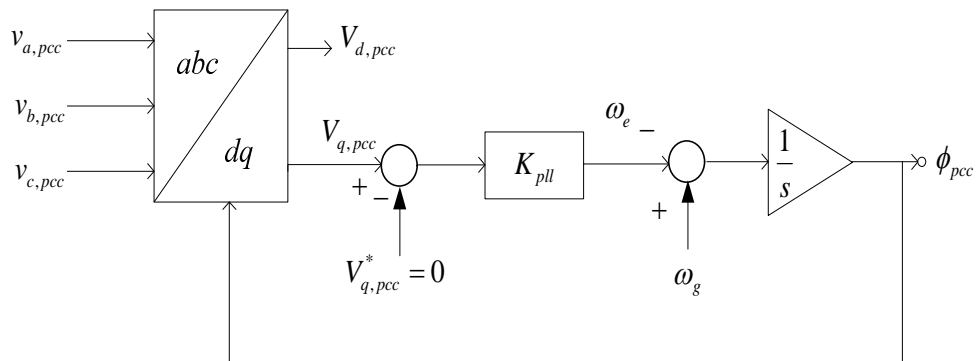


Figure 4.3: Block diagram of a phase locked-loop

In fact, the modelling could be performed without the PLL. This can be done by calculating the angle of voltage at PCC and used the angle for orientation of all PWM converters. However, using that method, a pair of eigenvalues at frequency of 0.7MHz is seen to move to the right hand plane. Since the frequency is very high, it is outside the area of interest. This is then addressed by the PLL. For simplicity, the K_{pll} was tuned using trial and error method to shift this high frequency oscillation to the left hand plane.

4.2.2 Modeling of the Grid and the Transmission Line

As seen in Figure 4.1, the grid is represented by a balanced three phase voltage source, V_t , its equivalent resistance, R_t , inductance, L_t , and capacitance, C_t . In this case, C_t is set to be a small value (2nF). It is included for modelling convenience.

Applying Kirchoff Current Law (KCL), Kirchoff Voltage Law (KVL) and the dq -transformation (defined in section 4.2.1), to the transmission line results in:

$$\begin{aligned}
\frac{dI_{d,t}}{dt} &= -\frac{R_t}{L_t} I_{d,t} + \omega_e I_{q,t} - \frac{1}{L_t} V_{d,pcc} + \frac{1}{L_t} V_t \cos \lambda \\
\frac{dI_{q,t}}{dt} &= -\frac{R_t}{L_t} I_{q,t} + \omega_e I_{d,t} - \frac{1}{L_t} V_{q,pcc} + \frac{1}{L_t} V_t \sin \lambda \\
\frac{dV_{d,pcc}}{dt} &= \frac{1}{C_t} I_{d,t} + \omega_e V_{q,pcc} - \frac{1}{C_t} I_{d,Tot} \\
\frac{dV_{q,pcc}}{dt} &= \frac{1}{C_t} I_{q,t} - \omega_e V_{d,pcc} - \frac{1}{C_t} I_{q,Tot}
\end{aligned} \tag{4.6}$$

where λ is the phase shift between V_t and the voltage at the PCC, V_{pcc} . The three phase currents, I_t and I_{Tot} are shown in Figure 4.1. The subscript d and q represent direct and quadrature axes of the voltage and current following the dq -transformation, respectively. The d and q components of the current I_{Tot} are $I_{d,Tot}$ and $I_{q,Tot}$, respectively, given by:

$$\begin{aligned}
I_{d,Tot} &= I_{d,iL} + I_{d,iw} + I_{d,ie} \\
I_{q,Tot} &= I_{q,iL} + I_{q,iw} + I_{q,ie}
\end{aligned} \tag{4.7}$$

where $I_{d,Tot}$ and $I_{q,Tot}$ are the sum of input currents to the load (I_{iL}), wind (I_{iw}) and energy storage (I_{ie}) in the d axis and q axis respectively.

4.2.3 Control and Modeling of the CPL Fed by the PWM Converter

The CPL connected to the PCC via a PWM converter is shown in Figure 4.4. The vector control schematic for the PWM converter is also shown. The voltages and currents are transformed to its equivalent dq -components as defined in section 4.2.1. The d -axis of the dq -rotating frame is oriented on the voltage at the PCC. The PLL is discussed in section 4.2.1. The outer loop PI controller, controls the dc link voltage via the d -axis of input current, $I_{d,iL}$. This PI controller provides the reference current $I_{d,iL}^*$. The inner current loops control the active current, $I_{d,iL}$, and reactive current, $I_{q,iL}$, via the converter voltages $V_{d,cL}$ and $V_{q,cL}$, respectively. A vector controlled motor drive can behave like a CPL as described in section 1.4. Rather than modeling the motor drive, the CPL can be approximated as a current source where the currents are given by (1.1).

It has been shown in [63] that, approximately, a speed controlled motor drive by given (1.1) results in a conservative estimate of instability i.e. it will tend to produce the on-set of instability at a lower power than a motor drive. This also has been discussed in section 1.4. Hence, the approximation of (1.1) is a good practical approach since it slightly under estimate the stability margin at a given power.

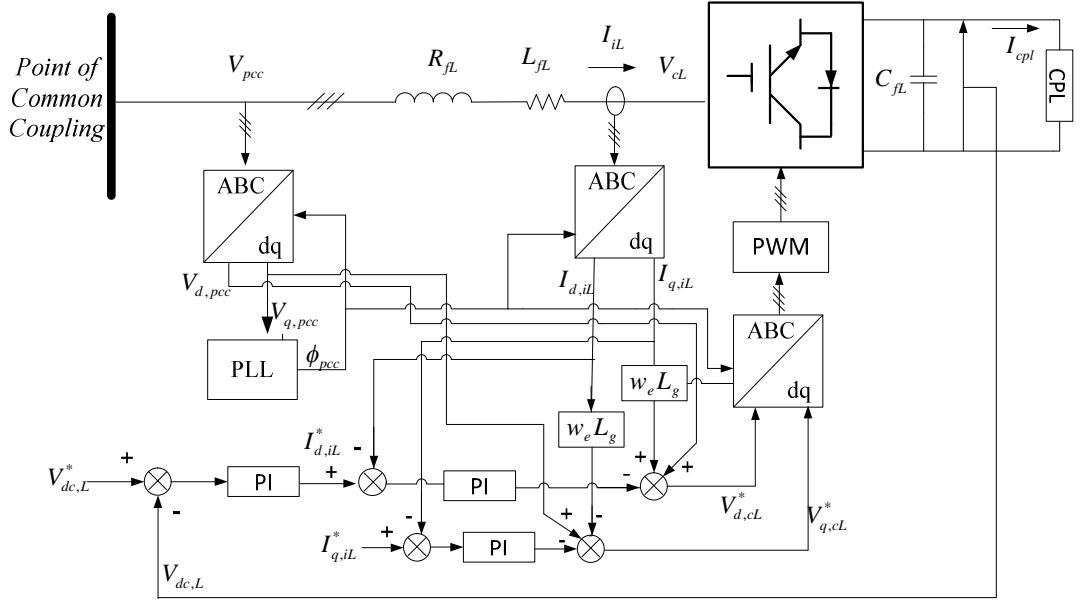


Figure 4.4: A CPL fed via a PWM converter and its control structure

Using KVL and dq -transformation at the AC side of the system in Figure 4.4 gives:

$$\begin{aligned} \frac{dI_{d,iL}}{dt} &= -\frac{R_{fL}I_{d,iL}}{L_{fL}} + \frac{\omega L_{fL}I_{q,iL}}{L_{fL}} + \frac{V_{d,pcc}}{L_{fL}} - \frac{V_{d,cL}}{L_{fL}} \\ \frac{dI_{q,iL}}{dt} &= -\frac{R_{fL}I_{q,iL}}{L_{fL}} - \frac{\omega L_{fL}I_{d,iL}}{L_{fL}} - \frac{V_{q,cL}}{L_{fL}} \end{aligned} \quad (4.8)$$

where the three phase input current to the converter, I_{iL} , and the converter three phase voltage, V_{cL} , are labeled in the diagram. The superscripts d and q represent direct and quadrature axes of the voltage and current following the dq -transformation, respectively.

The AC/DC PWM converter uses typical proportional-integral (PI) closed-loop control [67], [82]. The schematic diagram of the converter control structure is shown in Figure 4.5. On the direct axis, the controller aims to keep the DC link voltage constant and the quadrature axis is used to regulate the reactive power. In this case, the reactive current component, $I_{q,iL}^*$ is set to zero to maintain unity power factor at the PCC.

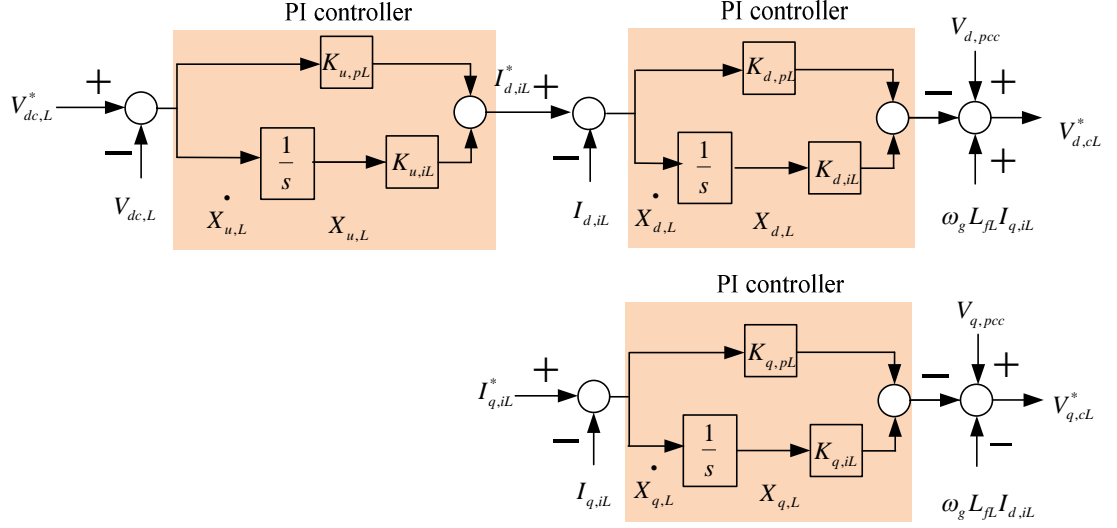


Figure 4.5: Schematic of control structure for the CPL front end converter

Introducing the state variables $X_{u,L}$, $X_{d,L}$ and $X_{q,L}$ as shown in Figure 4.5, we have:

$$\begin{aligned}
 \frac{dX_{u,L}}{dt} &= -V_{dc,L} + V_{dc,L}^* \\
 \frac{dX_{d,L}}{dt} &= -I_{d,iL} - K_{u,pL}V_{dc,L} + K_{u,pL}E_{dc,L}^* + K_{u,iL}X_{u,L} \\
 \frac{dX_{q,L}}{dt} &= -I_{q,iL} + I_{q,iL}^*
 \end{aligned} \tag{4.9}$$

$V_{d,cL}^*$ and $V_{q,cL}^*$ which are used in (4.8) are:

$$\begin{aligned}
 V_{d,cL}^* &= V_{d,pcc} - K_{u,pL}K_{d,pL}V_{dc,L}^* + K_{u,pL}K_{d,pL}V_{dc,L} - K_{u,iL}K_{d,pL}X_{u,L} + K_{d,pL}I_{d,iL} - K_{d,iL}X_{d,L} + \omega L_{fL}I_{q,iL} \\
 V_{q,cL}^* &= V_{q,pcc} - K_{q,pL}I_{q,iL}^* + K_{q,pL}I_{q,iL} - K_{q,iL}X_{q,L} - \omega L_{fL}I_{d,iL}
 \end{aligned} \tag{4.10}$$

The voltages of (4.10) are derived from the converter control structure and the state variables $X_{u,L}$, $X_{d,L}$ and $X_{q,L}$ as seen in Figure 4.5.

Finally, we also need a state equation for the state $V_{dc,L}$. This can be derived from the power equation. The power at the DC side of the converter, $P_{dc,L}$, and the power at the AC side of the converter, $P_{ac,L}$, are:

$$P_{dc,L} = \frac{2}{3} C_{fL} V_{dc,L} \frac{dV_{dc,L}}{dt} + \frac{2}{3} P_{cpl} \quad (4.11)$$

$$P_{ac,L} = V_{d,cL} I_{d,iL} + V_{q,cL} I_{q,iL} \quad (4.12)$$

Assuming no power loss in the converter, the power at the DC side of the converter, $P_{dc,L}$, is equal to the power at the AC side of the converter, $P_{ac,L}$. Thus:

$$\frac{2}{3} C_{fL} V_{dc,L} \frac{dV_{dc,L}}{dt} + \frac{2}{3} P_{cpl} = V_{d,cL} I_{d,iL} + V_{q,cL} I_{q,iL} \quad (4.13)$$

Rearranging (4.13), produces the differential equation:

$$\frac{dV_{dc,L}}{dt} = \frac{3}{2C_{fL}V_{dc,L}} (V_{d,cL}I_{d,iL} + V_{q,cL}I_{q,iL}) - \frac{P_{cpl}}{C_{fL}V_{dc,L}} \quad (4.14)$$

Therefore, the CPL fed by the PWM converter as seen in Figure 4.4, can be represented by the differential equations:

$$\begin{aligned} \frac{dI_{d,iL}}{dt} &= -\frac{R_{fL}I_{d,iL}}{L_{fL}} + \frac{\omega L_{fL}I_{q,iL}}{L_{fL}} + \frac{V_{d,pcL}}{L_{fL}} - \frac{V_{d,cL}}{L_{fL}} \\ \frac{dI_{q,iL}}{dt} &= -\frac{R_{fL}I_{q,iL}}{L_{fL}} - \frac{\omega L_{fL}I_{d,iL}}{L_{fL}} - \frac{V_{q,cL}}{L_{fL}} \\ \frac{dX_{u,L}}{dt} &= -V_{dc,L} + V_{dc,L}^* \\ \frac{dX_{d,L}}{dt} &= -I_{d,iL} - K_{u,pL}V_{dc,L} + K_{u,pL}V_{dc,L}^* + K_{u,iL}X_{u,L} \\ \frac{dX_{q,L}}{dt} &= -I_{q,iL} + I_{q,iL}^* \\ \frac{dV_{dc,L}}{dt} &= \frac{3}{2C_{fL}V_{dc,L}} (V_{d,cL}I_{d,iL} + V_{q,cL}I_{q,iL}) - \frac{P_{cpl}}{C_{fL}V_{dc,L}} \end{aligned} \quad (4.15)$$

We assume that $V_{d,cL}^* = V_{d,cL}$ and $V_{q,cL}^* = V_{q,cL}$; $V_{d,cL}$ and $V_{q,cL}$ in (4.15) are given by (4.10).

4.2.4 Control and Modeling of the Wind Farm

The wind power connected to the PCC by a PWM converter and its control structure is shown in Figure 4.6. The wind power is known to behave like a quasi-constant power source as discussed in section 1.3. The constant power element is modeled as current source in the DC link and given by:

$$I_w = \frac{P_{wind}}{E_w^{dc}} \quad (4.16)$$

The wind farm model and the control structure are similar to that of the CPL fed by a PWM converter as discussed in section 4.2.3. Therefore, the wind farm can be represented by the differential equations in (4.15) taking into account that the current I_w is in the opposite direction to I_{cpl} . Hence, the set of differential equations that represent the wind farm in Figure 4.6, with the schematic diagram of the control structure shown in Figure 4.7, is given by:

$$\begin{aligned} \frac{dI_{d,iw}}{dt} &= -\frac{R_{fw}I_{d,iw}}{L_{fw}} + \frac{\omega L_{fw}I_{q,iw}}{L_{fw}} + \frac{V_{d,pcc}}{L_{fw}} - \frac{V_{d,cw}}{L_{fw}} \\ \frac{dI_{q,iw}}{dt} &= -\frac{R_{fw}I_{q,iw}}{L_{fw}} - \frac{\omega L_{fw}I_{d,iw}}{L_{fw}} - \frac{V_{q,cw}}{L_{fw}} \\ \frac{dX_{u,w}}{dt} &= -V_{dc,w} + V_{d,cw}^* \\ \frac{dX_{d,w}}{dt} &= -I_{d,iL} - K_{u,pL}V_{dc,L} + K_{u,pL}V_{dc,L}^* + K_{u,iL}X_{u,L} \\ \frac{dX_{q,w}}{dt} &= -I_{q,iw} + I_{q,iw}^* \\ \frac{dV_{dc,w}}{dt} &= \frac{3}{2C_{fw}V_{dc,w}}(V_{d,cw}I_{d,cw} + V_{q,cw}I_{q,cw}) + \frac{P_{wind}}{C_{fw}V_{dc,w}} \end{aligned} \quad (4.17)$$

where $V_{d,cw}$ and $V_{q,cw}$ in (4.17) are given by:

$$\begin{aligned}
 V_{d,cw} &= V_{d,pcc} - K_{u,pw} K_{d,pw} V_{dc,w}^* + K_{u,pw} K_{d,pw} V_{dc,w} - K_{u,iw} K_{d,pw} X_{u,w} + K_{d,pw} I_{d,iw} - K_{d,iw} X_{d,w} + \omega L_{fw} I_{q,iw} \\
 V_{q,cw} &= V_{q,pcc} - K_{q,pw} I_{q,iw}^* + K_{q,pw} I_{q,iw} - K_{q,iw} X_{q,w} - \omega L_{fw} I_{d,iw}
 \end{aligned}
 \tag{4.18}$$

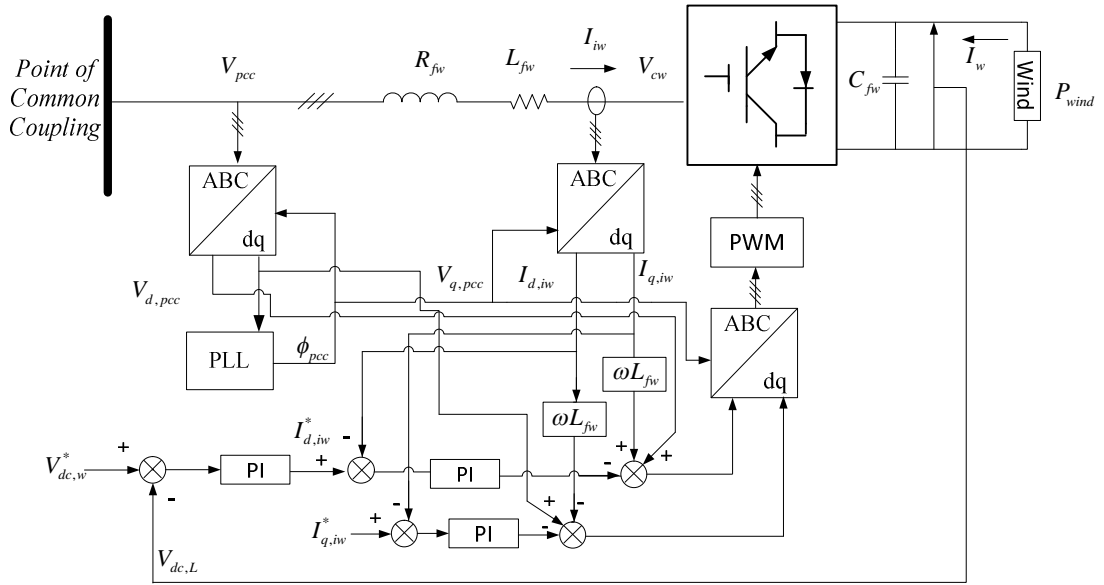


Figure 4.6: Wind Power feeding local grid via a PWM converter and its control structure

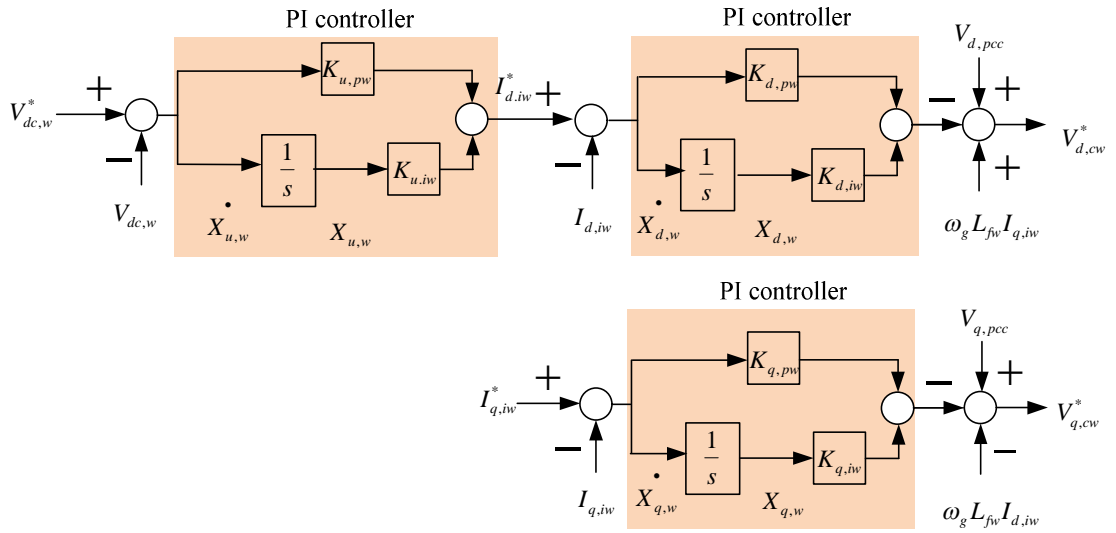


Figure 4.7: Schematic of control structure for the wind farm front end converter

4.2.5 Control and Modeling of the Energy Storage System

The energy storage is connected to the PCC via a PWM converter and a DC/DC converter as shown in Figure 4.8. The control structure of the converters of the energy storage unit system is also shown in Figure 4.8.

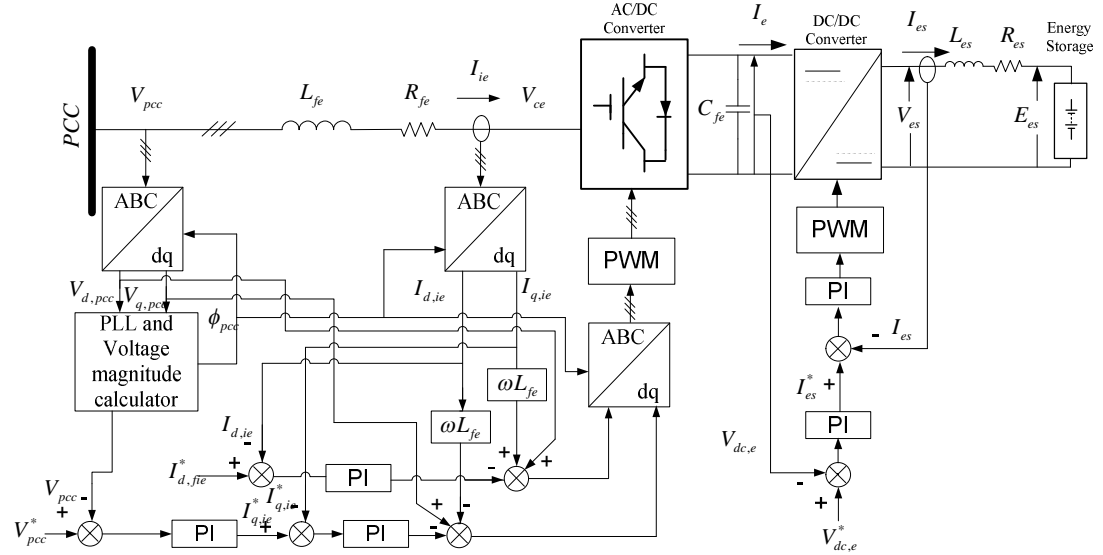


Figure 4.8: Block diagram of the energy storage system

The reactive current demand, $I_{q, ie}^*$ is obtained from a PCC voltage controller. The energy storage is charged or discharged depending on the active current reference, $I_{d, fie}^*$ which can be quantified based on the feed-forward current measurement from the AC side. Therefore, the active power is transferred to/from the energy storage unit depending on the value of $I_{d, fie}^*$. For the stability study in this chapter, $I_{d, fie}^*$ is set to zero. This indicates that the system is not handling active power, and thus behaves like a STATCOM. The DC link voltage is kept constant by the DC/DC converter controller.

4.2.5.1 Modeling the PWM converter

The schematic diagram of the control structure for the AC/DC PWM converter in Figure 4.8 is seen in Figure 4.9.

The state equations of Figure 4.9 are:

$$\begin{aligned}
\frac{dX_{d,e}}{dt} &= -I_{d,ie} + I_{d,ie}^* \\
\frac{dX_{v,e}}{dt} &= -V_{pcc} + V_{pcc}^* \\
\frac{dX_{q,e}}{dt} &= -I_{q,ie} + K_{v,pe} V_{pcc}^* - K_{v,pe} V_{pcc} + K_{v,ie} X_{v,e}
\end{aligned} \tag{4.19}$$

where:

$$\begin{aligned}
V_{ce}^{d*} &= V_{pcc}^d - K_{pe}^d I_{ie}^{d*} + K_{pe}^d I_{ie}^d - K_{ie}^d X_e^d + \omega L_{fe} I_{ie}^q \\
V_{ce}^{q*} &= V_{pcc}^q - K_{pe}^v K_{pe}^q V_{pcc}^* + K_{pe}^v K_{pe}^q V_{pcc} - K_{ie}^v K_{pe}^q X_e^v + K_{pe}^q I_{ie}^q - K_{ie}^q X_e^q - \omega L_{fe} I_{ie}^d
\end{aligned} \tag{4.20}$$

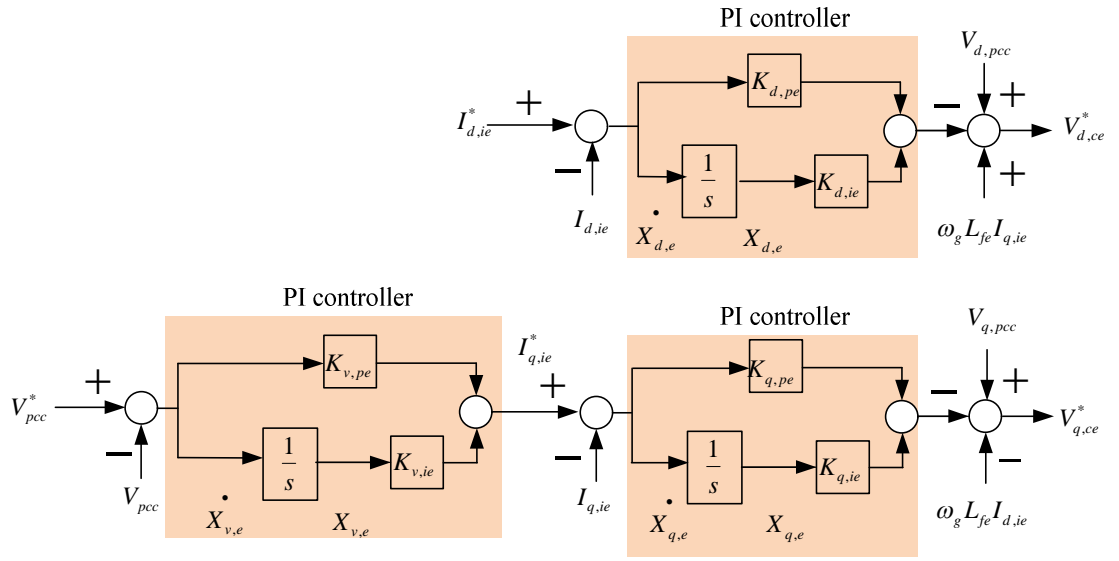


Figure 4.9: Schematic of control structure for the energy storage front end converter

4.2.5.2 Modeling the DC/DC converter and Load Dynamics

The schematic diagram of the DC/DC converter control structure is seen in Figure 4.10. The controller is designed to regulate the DC link voltage, $V_{dc,e}$. By regulating the DC link voltage, the energy storage is charge or discharge. The PI controller acts on the $V_{dc,e}$ error to set the charging and discharging current, I_{es}^* .

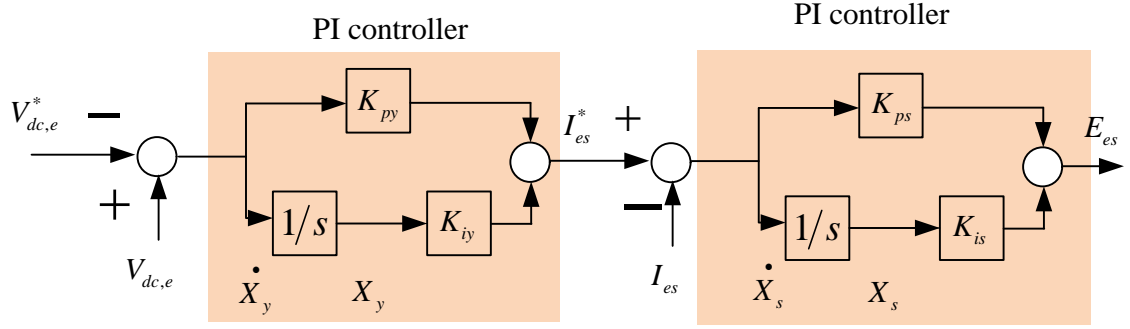


Figure 4.10: Schematic of control structure for the energy storage unit DC/DC converter

From the Figure 4.10, we can define the following state equations:

$$\begin{aligned} \frac{dX_s}{dt} &= -I_{es} - K_{py}V_{dc,e}^* + K_{py}V_{dc,e} + K_{iy}X_y \\ \frac{dX_y}{dt} &= -V_{dc,e}^* + V_{dc,e} \end{aligned} \quad (4.21)$$

In modeling the DC/DC converter, we note that we can define a duty cycle, D :

$$D = \frac{V_{es}}{V_{dc,e}} = \frac{I_e}{I_{es}} \quad (4.22)$$

where:

$$V_{es} = -K_{ps}K_{py}V_{dc,e}^* + K_{ps}K_{py}V_{dc,e} + K_{ps}K_{iy}X_y - K_{ps}I_{es} + K_{is}X_s \quad (4.23)$$

obtained from Figure 4.10.

Neclecting the power loss in the AC/DC converter, we assume:

$$P_{ac,e} = P_{dc,e} \quad (4.24)$$

Where the $P_{ac,e}$ and $P_{dc,e}$ are given by:

$$P_{ac,e} = V_{d,ce}^* I_{d,ie} + V_{q,ce}^* I_{q,ie} \quad (4.25)$$

$$P_{dc,e} = \frac{2}{3} C_{fe} V_{dc,e} \frac{dV_{dc,e}}{dt} + I_e V_{dc,e} \quad (4.26)$$

Equating (4.25) and (4.26), and rearranging we get:

$$\frac{dV_{dc,e}}{dt} = \frac{3}{2C_{fe}V_{dc,e}} \left(V_{d,ce}^* I_{d,ie} + V_{q,ce}^* I_{q,ie} \right) - \frac{3I_e}{2C_{fe}} \quad (4.27)$$

At the secondary side (energy storage side) of the DC/DC converter, by applying KVL, we set:

$$\frac{dI_{es}}{dt} = \frac{V_{es}}{L_{es}} - \frac{E_{es}}{L_{es}} - \frac{R_{es} I_{es}}{L_{es}} \quad (4.28)$$

In this case, the energy storage voltage, E_{es} is assumed to be a constant.

4.2.5.3 Modeling the AC Side Dynamics of the Energy Storage System

The mathematical model at the AC side of the system in Figure 4.8 is obtained using KVL and the dq -transformation and is given by:

$$\begin{aligned} \frac{dI_{d,ie}}{dt} &= -\frac{R_{fe} I_{d,ie}}{L_{fe}} + \frac{\omega L_{fe} I_{q,ie}}{L_{fe}} + \frac{V_{d,pcc}}{L_{fe}} - \frac{V_{d,ce}}{L_{fe}} \\ \frac{dI_{q,ie}}{dt} &= -\frac{R_{fe} I_{q,ie}}{L_{fe}} - \frac{\omega L_{fe} I_{d,ie}}{L_{fe}} - \frac{V_{q,ce}}{L_{fe}} \end{aligned} \quad (4.29)$$

4.2.5.4 Equations to a Complete Energy Storage System

Finally, the energy storage system in Figure 4.8 can be represented by gathering together equations (4.19), (4.21), (4.27), (4.28) and (4.29). The result is:

$$\begin{aligned}
\frac{dI_{d,ie}}{dt} &= -\frac{R_{fe}I_{d,ie}}{L_{fe}} + \frac{\omega L_{fe}I_{q,ie}}{L_{fe}} + \frac{V_{d,pcc}}{L_{fe}} - \frac{V_{d,ce}}{L_{fe}} \\
\frac{dI_{q,ie}}{dt} &= -\frac{R_{fe}I_{q,ie}}{L_{fe}} - \frac{\omega L_{fe}I_{d,ie}}{L_{fe}} - \frac{V_{q,ce}}{L_{fe}} \\
\frac{dX_{d,e}}{dt} &= -I_{d,ie} + I_{d,ie}^* \\
\frac{dX_{v,e}}{dt} &= -V_{pcc} + V_{pcc}^* \\
\frac{dX_{q,e}}{dt} &= -I_{q,ie} + K_{v,pe}V_{pcc}^* - K_{v,pe}V_{pcc} + K_{v,ie}X_{v,e} \\
\frac{dV_{dc,e}}{dt} &= \frac{3}{2C_{fe}V_{dc,e}}(V_{d,ce}^*I_{d,ie} + V_{q,ce}^*I_{q,ie}) - \frac{3I_e}{2C_{fe}} \\
\frac{dX_s}{dt} &= -I_{es} - K_{py}V_{dc,e}^* + K_{py}V_{dc,e} + K_{iy}X_y \\
\frac{dX_y}{dt} &= -V_{dc,e}^* + V_{dc,e} \\
\frac{dI_{es}}{dt} &= \frac{V_{es}}{L_{es}} - \frac{E_{es}}{L_{es}} - \frac{R_{es}I_{es}}{L_{es}}
\end{aligned} \tag{4.30}$$

We assume $V_{d,ce}^* = V_{d,ce}$ and $V_{q,ce}^* = V_{q,ce}$. Thus, $V_{q,ce}$ and $V_{d,ce}$ in (4.30) is given in (4.20).

4.2.6 The Complete Mathematical Model of the System Study

The complete mathematical model of the system in Figure 4.1 can be represented by combining together the mathematical representation of each component as described in sections 4.2.1, 4.2.2, 4.2.3, 4.2.4 and 4.2.5.

A set of differential equation that represent the system in Figure 4.1 is combination of differential equations in (4.5), (4.6), (4.15), (4.17) and (4.30). They are in the form:

$$\begin{aligned}
\dot{x} &= f(x, u, y) \\
y &= g(x, u)
\end{aligned} \tag{4.31}$$

where the state variables, x input u and output vector y are:

$$\begin{aligned}
x &= \langle I_{d,t}, I_{q,t}, V_{d,pcc}, V_{q,pcc}, I_{d,iL}, I_{q,iL}, X_{u,L}, X_{d,L}, X_{q,L}, V_{dc,L}, I_{q,iw}, I_{q,iw}, \\
&X_{u,w}, X_{d,w}, X_{q,w}, V_{dc,w}, I_{d,ie}, I_{q,ie}, X_{v,e}, X_{d,e}, X_{q,e}, V_{dc,e}, X_s, X_y, I_{es}, \lambda \rangle \\
u &= \langle V_{dc,L}^*, I_{q,iL}^*, P_{cpl}, V_{dc,w}^*, I_{q,iw}^*, P_w, V_{pcc}^*, I_{d,fi e}^*, V_{dc,e}^* \rangle \\
y &= \langle V_{pcc}, V_{dc,L}, V_{dc,w} \rangle
\end{aligned} \tag{4.32}$$

4.2.6.1 Linearized Model of the System

The set of differential equations that mathematically model the system as described in section 4.2.6 is a nonlinear system since it consists of nonlinear differential equations. To analyze the stability, the model can be linearized at an operating point. The linear model is derived using first order Taylor series expansions. The model can be written in the following linear state space form:

$$\begin{aligned}
\dot{\delta x} &= \mathbf{A}(x_0, u_0) \delta x + \mathbf{B}(x_0, u_0) \delta u \\
\delta y &= \mathbf{C}(x_0, u_0) \delta x + \mathbf{D}(x_0, u_0) \delta u
\end{aligned} \tag{4.33}$$

where

$$\begin{aligned}
\delta x &= [\delta I_{d,t}, \delta I_{q,t}, \delta V_{d,pcc}, \delta V_{q,pcc}, \delta I_{d,iL}, \delta I_{q,iL}, \delta X_{u,L}, \delta X_{d,L}, \delta X_{q,L}, \delta V_{dc,L}, \delta I_{d,iw}, \delta I_{q,iw}, \delta X_{u,w}, \\
&\delta X_{d,w}, \delta X_{q,w}, \delta V_{dc,w}, \delta I_{d,ie}, \delta I_{q,ie}, \delta X_{u,e}, \delta X_{v,e}, \delta X_{d,e}, \delta X_{q,e}, \delta V_{dc,e}, \delta X_s, \delta X_y, \delta I_{es}, \delta \lambda,]^T \\
\delta u &= [\delta V_{dc,L}^*, \delta I_{q,iL}^*, \delta P_{cpl}, \delta V_{dc,w}^*, \delta I_{q,iw}^*, \delta P_w, \delta V_{pcc}^*, \delta I_{d,fi e}^*, \delta V_{dc,e}^*]^T \\
\delta y &= [\delta V_{pcc}, \delta V_{dc,L}, \delta V_{dc,w}]
\end{aligned} \tag{4.33}$$

The matrices $\mathbf{A}(x_0, u_0)$, $\mathbf{B}(x_0, u_0)$, $\mathbf{C}(x_0, u_0)$ and $\mathbf{D}(x_0, u_0)$ are $N \times N$, $N \times M$, $P \times N$ and $P \times M$ matrix, respectively. M , N and P are total number of inputs, states and outputs, respectively. The matrices elements, a_{ij} , b_{ij} , c_{ij} and d_{ij} for the matrices $\mathbf{A}(x_0, u_0)$, $\mathbf{B}(x_0, u_0)$, $\mathbf{C}(x_0, u_0)$ and $\mathbf{D}(x_0, u_0)$, respectively, can be determined by:

$$\begin{aligned}
a_{ij}(x_o, u_o) &= \left. \frac{\partial}{\partial x_j} f_i(x, u, y) \right|_{x=x_o} \\
b_{ij}(x_o, u_o) &= \left. \frac{\partial}{\partial u_j} f_i(x, u, y) \right|_{x=x_o} \\
c_{ij}(x_o, u_o) &= \left. \frac{\partial}{\partial x_j} y_i(x, u) \right|_{x=x_o} \\
d_{ij}(x_o, u_o) &= \left. \frac{\partial}{\partial u_j} y_i(x, u) \right|_{x=x_o}
\end{aligned} \tag{4.33}$$

In this thesis, Matlab symbolic toolbox is used to obtain the matrices $\mathbf{A}(x_o, u_o)$, $\mathbf{B}(x_o, u_o)$, $\mathbf{C}(x_o, u_o)$ and $\mathbf{D}(x_o, u_o)$ for a given system operating point. The Matlab code is given in Appendix D. x_o and u_o is the solution to $f(x, u, y) = 0$ and $y = g(x, u)$.

4.3 Small-signal Stability Analysis

Eigenvalue analysis is used to investigate the small-signal stability of the system. The eigenvalues from the system matrix, calculated at an equilibrium point, are used for the stability analysis. The steady state values are determined by using Matlab *fsolve* function to solve the equation $\dot{x} = f(x, u, y) = 0$.

4.3.1 Eigenvalues Analysis

The eigenvalue theory has been widely used to evaluate the power system small-signal stability [11], [13], [63], [95]. The eigenvalues, λ can be determined using:

$$\det(\mathbf{A} - \lambda \mathbf{I}) = 0 \tag{4.34}$$

where $\lambda = \sigma \pm j\omega$. In this thesis, the Matlab function *eig* is used to calculate the eigenvalues. Real eigenvalues represents a non-oscillatory mode. A negative real eigenvalues shows decaying mode. Larger magnitude means faster decay. A positive real eigenvalues represent aperiodic instability. Complex eigenvalues occur in conjugate pairs and each pair corresponds to an oscillatory mode. The real

component of a complex conjugate eigenvalues gives the damping and the imaginary component gives the frequency of oscillation, as defined by $\lambda = \sigma \pm j\omega$. The frequency of oscillation is $f = \omega / (2\pi)$ in Hz and the damping ratio is $\zeta = -\sigma / \sqrt{\sigma^2 + \omega^2}$. A negative real part represents a damped oscillation whereas a positive real part represents oscillation of increasing amplitude. For a stable system, $\text{real}(\lambda) < 0$.

4.3.2 Model Validation

4.3.2.1 System Parameters for the Study

The common grid voltages are 11kV or 33 kV. In this thesis, all AC voltages are referred to an appropriate transformer side giving a single AC voltage for the system. The parameters are referred to the 1 kV voltage level. Resistance, R_t and inductance, L_t is chosen to represent a weak grid with SCR=1. The ratio between reactance and resistance (X/R) is chosen to be 5. Typical X/R ratio for a transmission line is between 2 to 16 [70]. The transmission line parameters are given in Table 4.1. The wind farm and the CPL are connected to the PCC via 1kV, 10MVA front end converter. The parameters are given in Appendix C. The ESS is connected to the PCC via a 1kV, 1MVA front end converter and a 2kV, 1MVA DC/DC converter. The parameters are given in Appendix C and Appendix D.

Table 4.1: Parameters of the transmission line of the system in Figure 4.1

Parameter	Value	Description
$S_{rated,t}$	10 MVA	Rated apparent power of transmission line
V_t	1 kV	Rated voltage (line-to-line)
ω_g	$2\pi \times 50$ rad/s	Grid voltage frequency
R_t	0.02 Ω	Transmission line resistance
L_t	0.32 mH	Transmission line inductance
C_t	30 nF	Transmission line capacitance

4.3.2.2 Comparison of Mathematical Model and PSCAD System Model

The responses from the mathematical model developed as discussed in section 4.2, is compared with a PSCAD software model results for the set of parameters given in Table 4.1, Appendix C and Appendix D.

Using the linearized mathematical model in (4.33), responses of V_{pcc} , $V_{dc,L}$ and $V_{dc,w}$ to a small step in CPL are obtained using Matlab function *step*. The small-signal response mathematical model is compared against the PSCAD simulation results at CPL power levels of 2MW, 5MW and 7MW with a wind power of 1MW. The results are shown in Figure 4.11, Figure 4.12 and Figure 4.13, respectively. From the plots, the linearized mathematical model has a very good agreement with the PSCAD simulation model. Note that, the mathematical model is a linearized model. Thus, it is more accurate for a smaller step changes. However, the linearized mathematical model can be considered validated, and can be used for the small-signal stability analysis.

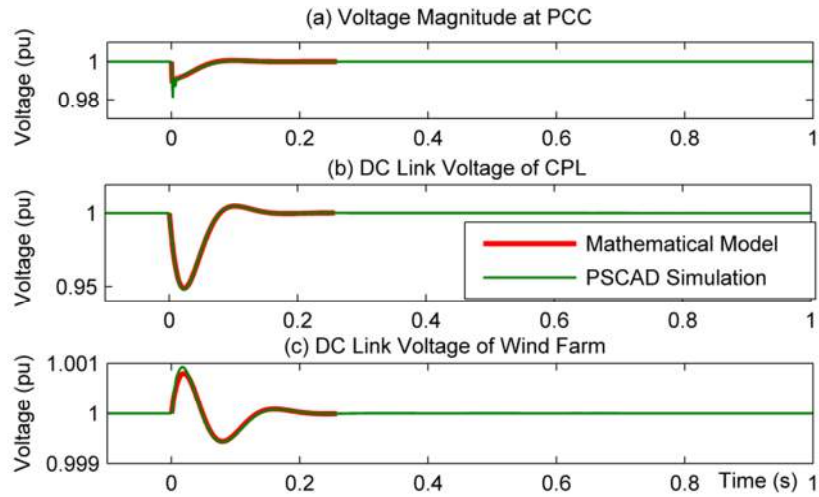


Figure 4.11: Response of V_{pcc} , $V_{dc,L}$ and $V_{dc,w}$ when CPL is stepped from 2MW to 2.5MW

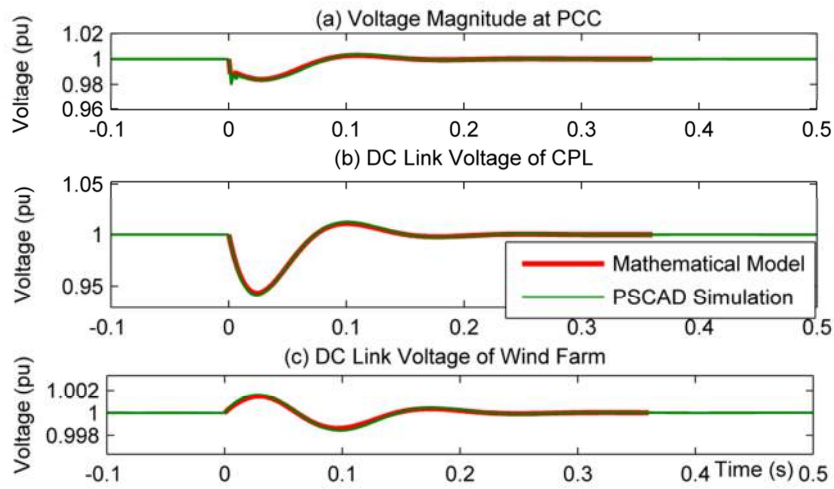


Figure 4.12: Response of V_{pcc} , $V_{dc,L}$ and $V_{dc,w}$ when CPL is stepped from 5MW to 5.5MW

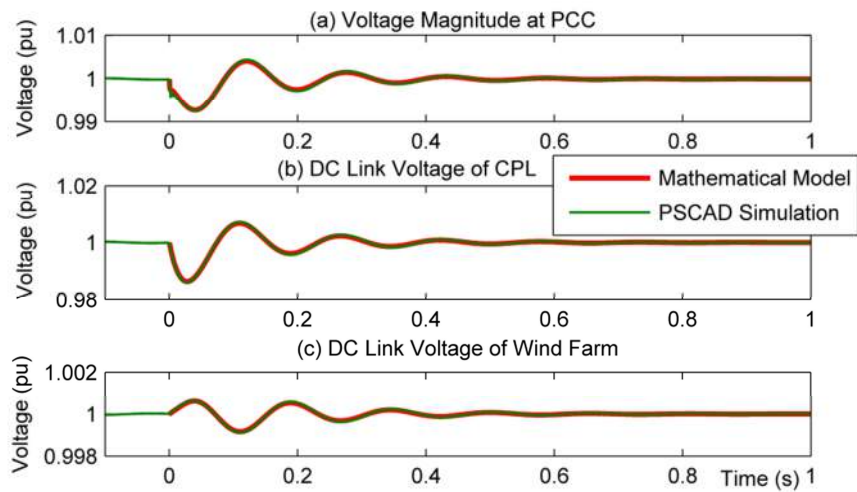


Figure 4.13: Response of V_{pcc} , $V_{dc,L}$ and $V_{dc,w}$ when CPL is stepped from 7MW to 7.1MW

4.3.3 Stability Analysis at Various Power Levels

For the analysis of system stability at various power levels, three cases are presented in this thesis:

- Case 1: The P_w is fixed at 1MW and P_{cpl} is varied from 1MW to 8MW.
- Case 2: The P_w is fixed at 4MW and P_{cpl} is varied from 1MW to 11MW.
- Case 3: The P_{cpl} is fixed at 1MW and P_w is varied from 1MW to 11MW.

Case 1 and 3 represent large power flows from and to the grid respectively. Case 2 is an intermediate case where the power flows from and then to the grid as the load power is increased. The reason that the power level is limited to 8MW in case 1 and 11MW in cases 2 and 3, is because the eigenvalues will cross to the right hand plane at these power levels. This indicates that the system become unstable above the power level. Further analysis is carried out to explain this instability.

The eigenvalues traces for case 1 are shown in Figure 4.14 and zoomed to the area of interest in Figure 4.15. There are eigenvalues crossing to the right hand plane indicating that the system is becoming unstable above P_{cpl} of 7.7MW. The PSCAD simulation validates this as shown in Figure 4.16 when P_{cpl} is stepped from 7.6MW to 7.7MW. In this case, the amount of power taken from the grid is higher than 6.7MW when the system becomes unstable. Note that, the wind farm is supplying 1MW power to the load.

In case 2, P_{cpl} is increased from 1MW to 11MW and P_w fixed at 4MW. The eigenvalues trace is shown in Figure 4.17. The system becomes unstable when the CPL is higher than 10.7MW as shown in Figure 4.18. The amount of power received from the grid is again 6.7MW while 4MW is generated by the wind farm. The PSCAD simulation result also agrees with this eigenvalues analysis as shown in Figure 4.19.

Also in case 2, a trend in dominant eigenvalues is observed. The dominant eigenvalues are those eigenvalues that cross to the right hand plane when CPL is increased. Figure 4.18 shows the eigenvalues move to the left when power is

increased from 1MW to 4MW. However, when the power is increased further, the eigenvalues moved towards the right. The wind farm is supplying 4MW of power. So when the CPL is less than 4MW, the difference is transmitted to the grid. Meanwhile, when the CPL is more than 4MW, the grid has to supply the additional required power to meet the demand. Therefore, the dominant eigenvalues are sensitive to the amount of power carried by the transmission line. The eigenvalues will move to the right when more power is carried by the line in any direction. This trend is further seen in case 3 of Figure 4.20 where CPL is fixed at 1MW. In this case, the power supplied by the wind farm is increased from 1MW to 11MW with an increasing transmission to grid. The CPL is fixed at 1MW. The system becomes unstable when wind power generation is higher than 10.5MW. The PSCAD simulation result also shows that the system becomes unstable when the power is stepped from 10.4MW to 10.5MW as seen in Figure 4.22. From the PSCAD simulation, the power received at the V_g side is measured to be 7.4MW when the system becomes unstable. Although the power generated is 10.5MW and the power consumed by the load is 1MW, the grid only received 7.4MW due to losses in transmission line and other resistive components.

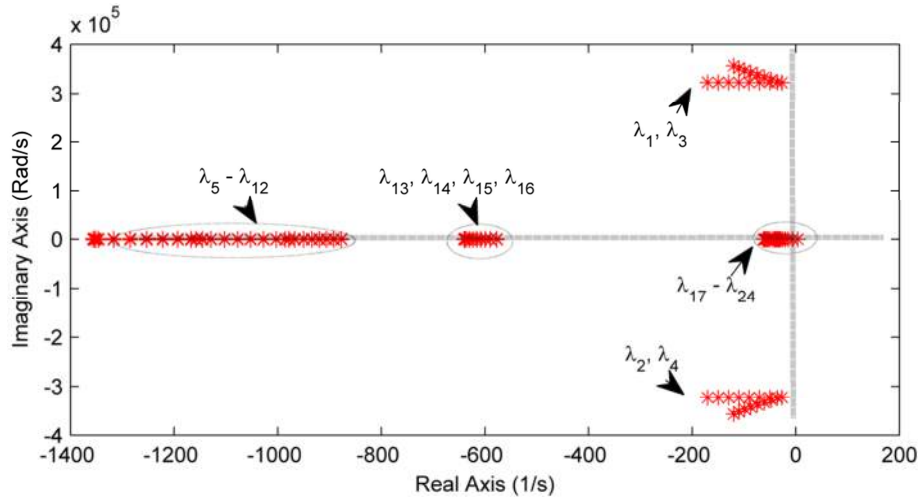


Figure 4.14: Eigenvalues trace for the Case 1

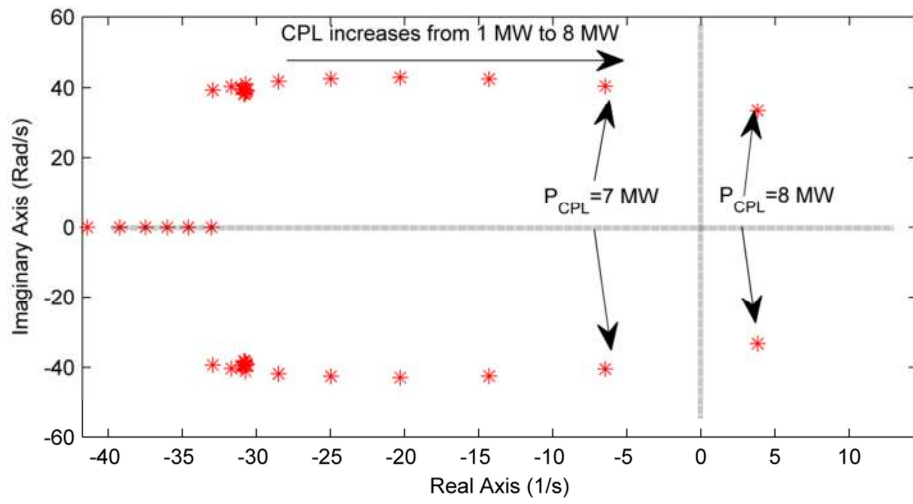


Figure 4.15: Zoomed area of interest from Figure 4.14

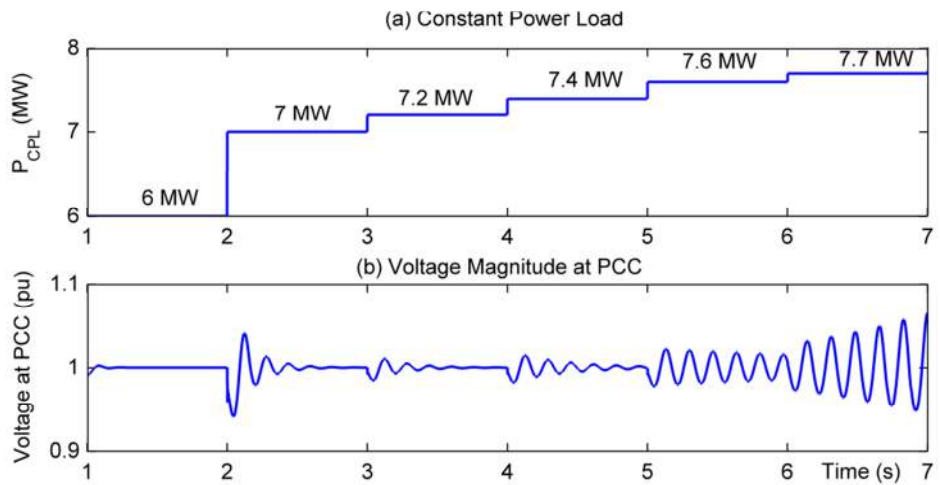


Figure 4.16: PSCAD simulation result for Case 1

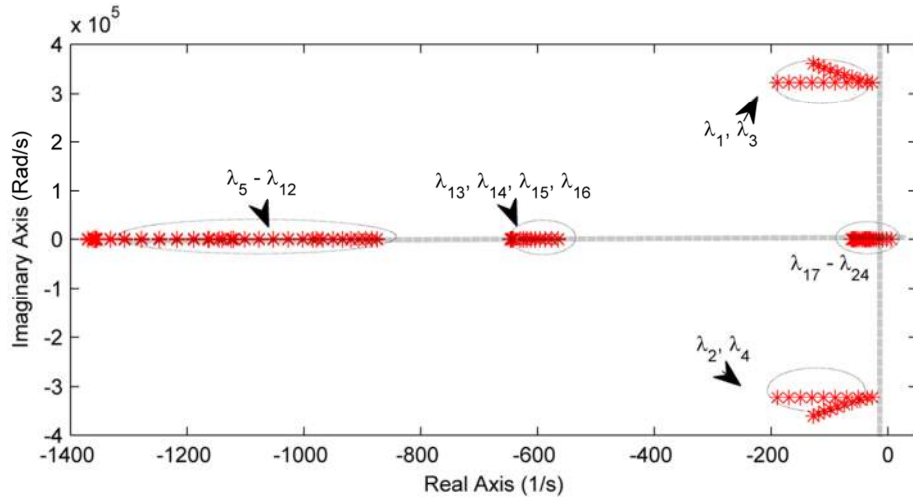


Figure 4.17: Eigenvalues trace for the Case 2

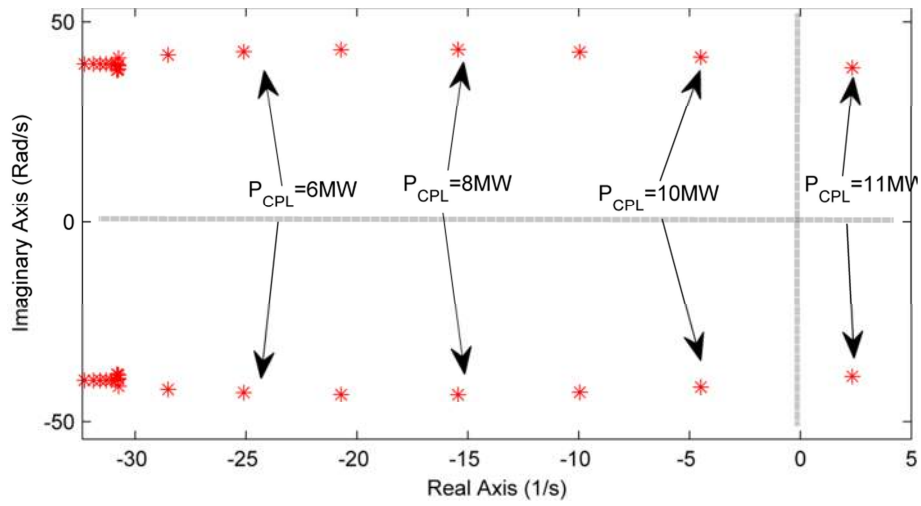


Figure 4.18: Zoomed area of interest from Figure 4.17 (for P_{cpl} from 4MW to 11MW)

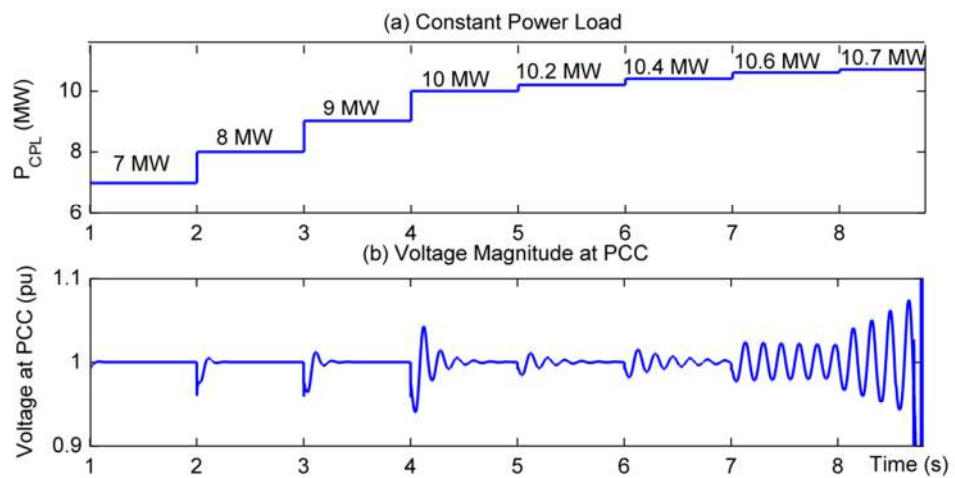


Figure 4.19: PSCAD simulation result for case 2

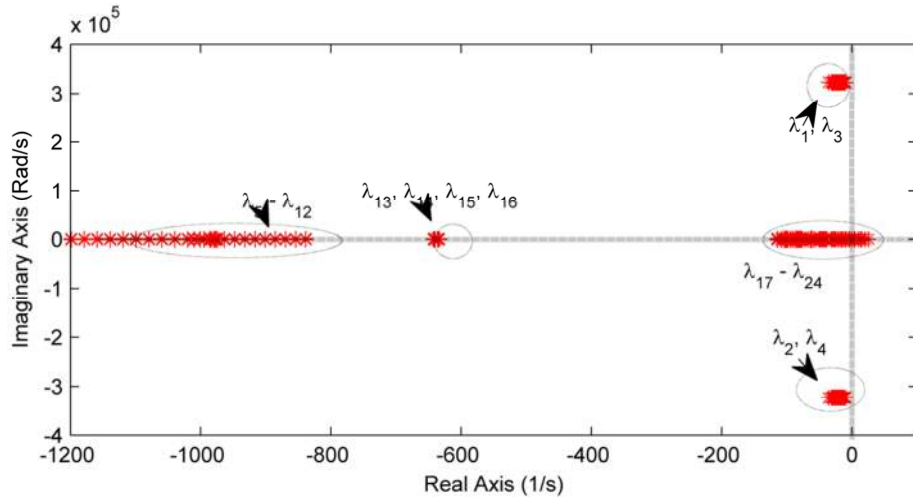


Figure 4.20: Eigenvalues trace for the Case 3

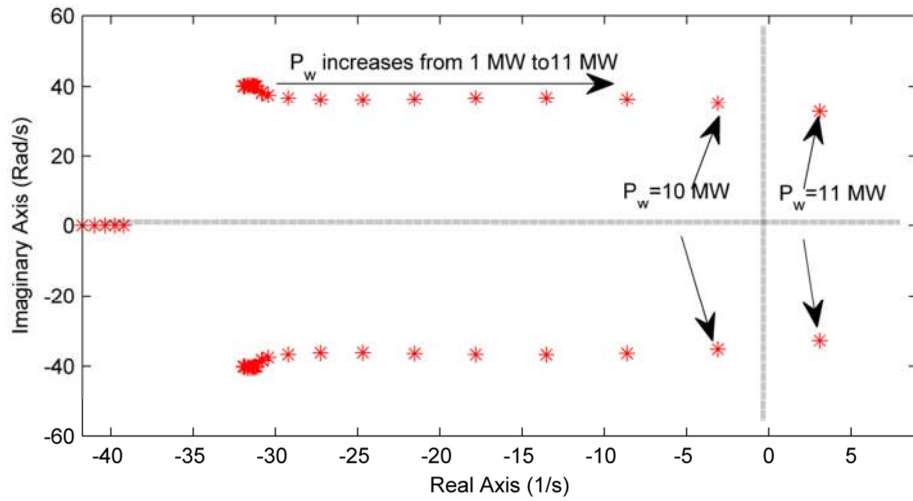


Figure 4.21: Zoomed area of interest from Figure 4.20

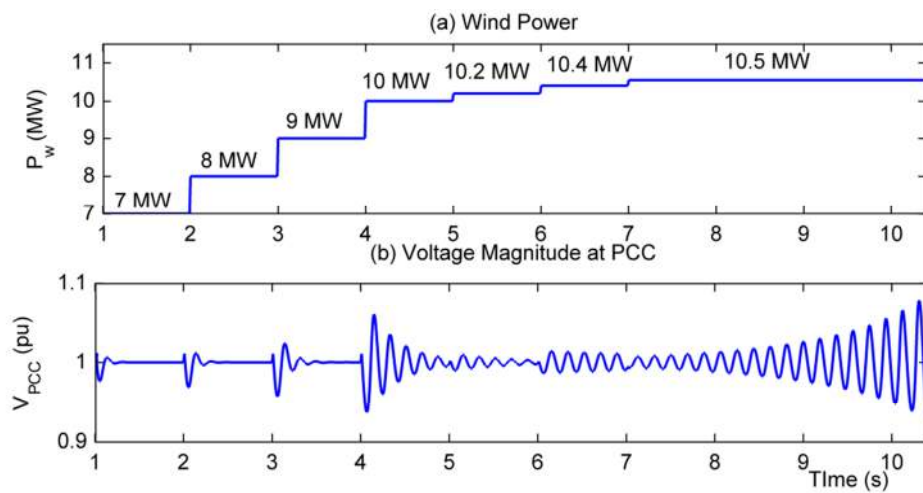


Figure 4.22: PSCAD simulation result for case 3

4.3.3.1 Transmission Line Load ability Limit

From all the three cases presented above, it seems that the system become unstable when the transmission line is carrying power above certain amount. Therefore, the transmission line load-ability limit is evaluated. The transmission line load-ability has been reported in many publications, for example [96]–[98].

The transmission line equivalent circuit can be illustrated in Figure 4.23. The transmission line is represented by its series impedance:

$$Z_t = R_t + j\omega L_t = Z_t \angle \theta_z \quad (4.35)$$

In this case the transmission line capacitance is assumed negligible.

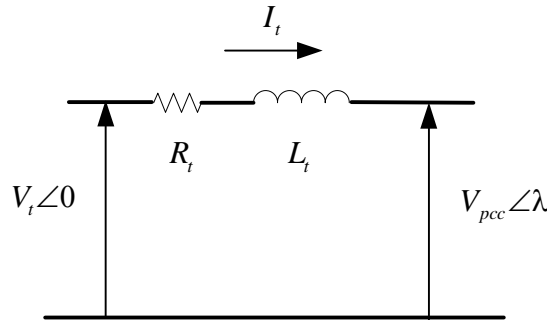


Figure 4.23: The transmission line equivalent circuit

As given in [98], the transmission line load-ability limit taking into account the line losses can be calculated using:

$$P_{R_{\max}} = \frac{V_t V_{pcc}}{Z_t} (\theta_z - \lambda) - \frac{V_t}{Z_t} \cos(\theta_z) \quad (4.36)$$

For the steady state stability margin of 30% that is normally used in practice, the corresponding load angle, λ is 44° [98]. For the parameters in Table 4.1 and $\lambda = 44^\circ$, the transmission line load-ability limit is 6.113 MW for the stability margin of 30%. This is calculated using (4.36). This indicates that if the transmission line is carrying power above 6.113MW, the system is operated above the transmission line load-ability limit itself. In case 1 and 2 as presented above, the stability issue is occurring when the transmission line is carrying power of 6.7MW. In case 3, the

instability occurs at power of 7.4MW. The difference in power in case 1 and 2 as compared to case 3 is perhaps due to the power direction. However, no further investigation has been done in this thesis. However, in all cases, the power is higher than 6.113MW (the load-ability limit). Therefore, the instability issues arising is mainly due to the fact that the transmission line is loaded above its load-ability limit rather than the CPL itself. In general, the system is stable if operated below the transmission line load-ability limit.

However, from the eigenvalues analysis, as well as the PSCAD simulation, it is seen that the amount of power transmitted by the transmission line is increased, the system damping reduces. Hence, the oscillation is higher when the power carried by the line is higher.

Other than the three cases presented, the author also has performed analysis for cases with various transmission line SCR and X/R (varying transmission line resistance and inductance), controller bandwidth, DC link capacitance and power combinations. It is found that, the results are consistent as for the three cases presented.

The results and discussion in this section lead to the following conclusions:

- The system is stable when operating within the transmission line load-ability limit.
- The damping decreases when active power transmitted in the transmission line increases. Thus, the oscillation increases with the increase in the amount of power carried by the line.
- If the transmission line inductance decreases (which means that the grid is stronger), more power can be transferred and thus the system is more stable with better damping at the same power level.

4.4 Chapter Summary

This chapter has developed a mathematical model of a system consisting of a wind farm, a large CPL and an energy storage unit connected to a weak grid. Each of the CPL, wind power and energy storage units is connected to the AC side via a PWM AC/DC converter. The mathematical model is validated by PSCAD simulation model. The combination of CPL and wind farm is expected to cause instability problem especially in a weak grid. Therefore, the eigenvalues analysis is used to perform the system small-signal stability study. From the stability study, it is concluded that the system is generally stable if operated below the transmission line load-ability limit. However, the damping decreases as the transmission line has to carry more power. Therefore, more oscillation is observed when there is a sudden change in load at higher power carried by the line than that at lower power. The model is able to analyze the stability of the system for changes in the DC-link voltage controller values, the dq -current controller values and the V_{pcc} controller values. In practice, it is found that the system is stable under a range of controller bandwidths and that the main influence on stability arises always from the power capacity of transmission line. This is a consequence of the controlled nature of the PWM interface rectifier. It will be shown that where a CPL is supplied by a diode-bridge rectifier, the situation is different. This is the subject of the next chapter. In the next chapter, a small-signal analysis is performed for the case where the CPL is fed by an uncontrolled diode bridge rectifier.

Chapter 5

Stability Analysis and Control of a Large Constant Power Load fed by Diode Bridge Rectifier in a Local Grid

5.1 Introduction

In chapter 5, the CPL is connected to the system by a controlled PWM converter. It has been shown that the system can remain in a stable condition, if it is operated below the transmission line load-ability limit. In other words, the existence of the CPL does not add significantly to the system instability when it is interfaced by a controlled PWM rectifier to the grid. In this chapter, the CPL is connected to the system by an uncontrolled diode-bridge rectifier.

One variable speed drive issue which has not been generally discussed is the stability of operating a large motor drive where the DC links is fed by a multi-pulse diode rectifier. The use of a multi-pulse rectifier improves the DC link voltage ripple allowing the DC link smoothing LC filters to be reduced. Using smaller electrolytic smoothing capacitor at the expense of larger inductor in the LC filter would improve the overall system reliability and the drive life time [99]. However it may also reduce the system stability margin. The chapter addresses the trade-off between the filter value and stability.

The chapter first proposes a relevant system formed by a weak transmission grid connection of a low SCR, a large multi-pulse diode bridge fed CPL and a large wind generator and an energy storage system with active front end capability as shown in

Figure 5.1. The ESS is responsible for the V_{pcc} control as described in section 4.2.5. There is no reactive power (or reactive current) demand for the wind farm front end converter. The stability analysis is performed based on the mathematical derivation of the system. In this chapter, the system modeling is described. The eigenvalues analysis approach is used to perform the stability study. The method of participation factor analysis is employed to determine the influence of the unstable modes on the states and vice versa. Then, a proposed controller to improve stability is discussed and validated. The methodology is based on mathematical analysis, stability analysis through MATLAB and verification through PSCAD simulation.

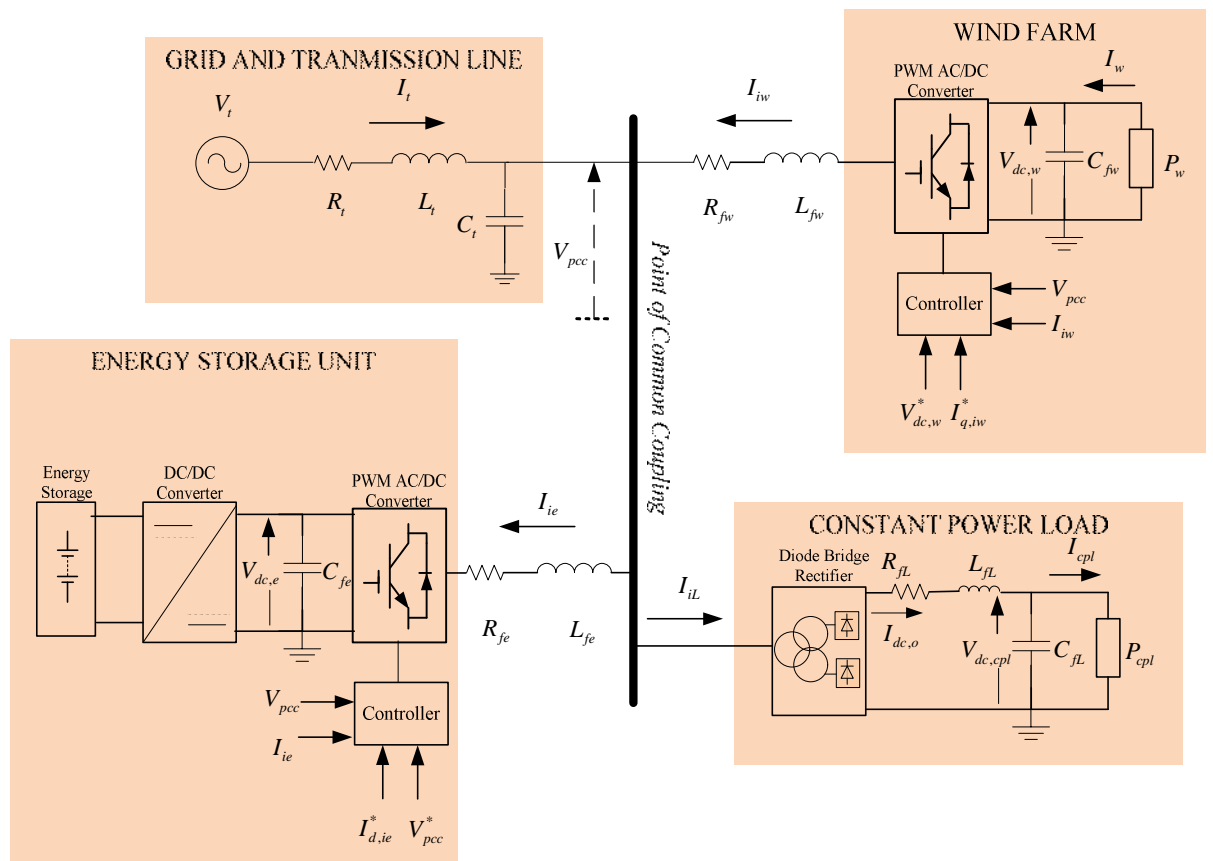


Figure 5.1: Block diagram of the power system under study

5.2 System Modeling

In chapter 5, the CPL is fed via a PWM controlled converter. However, in this chapter, the CPL is fed via an uncontrolled diode bridge rectifier. The diode bridge rectifier modeling feeding the CPL is discussed in this chapter. The modeling of grid, wind farm and energy storage unit is the same as that in chapter 5.

5.2.1 Modeling of CPL fed via a Diode Bridge Rectifier

A CPL fed via a three-phase diode bridge rectifier is illustrated in Figure 5.2. The three-phase diode bridge rectifier uses uncontrolled devices and converts AC power to DC power with the time instant determined by the circuit condition. For simplicity, a six-pulse diode rectifier is used for analysis in this thesis. However, higher pulse rectifiers can be implemented based on the six-pulse rectifier analysis; this is due to the symmetric property of the diode bridge rectifier [63], [100]. The DC-link LC filter represented by L_{fL} and C_{fL} in Figure 5.2, and used in the DC side to filter the DC voltage and current ripples. The CPL is model as a voltage-dependent current source as discussed in section 1.4 which currents are given by (1.1).

As reported in [63], this CPL modeled by (1.1) represents the worst case condition since the CPL actuator dynamics which are ignored can increase the stability of the system.

In practice LCL filter is connected between a converter and a PCC. The LCL filter causes oscillations at higher resonant frequencies. It is assumed that the line current smoothing has been undertaken by the DC-link filter. Therefore, the AC line current can also be assumed as sinusoidal in order to simplify the analysis.

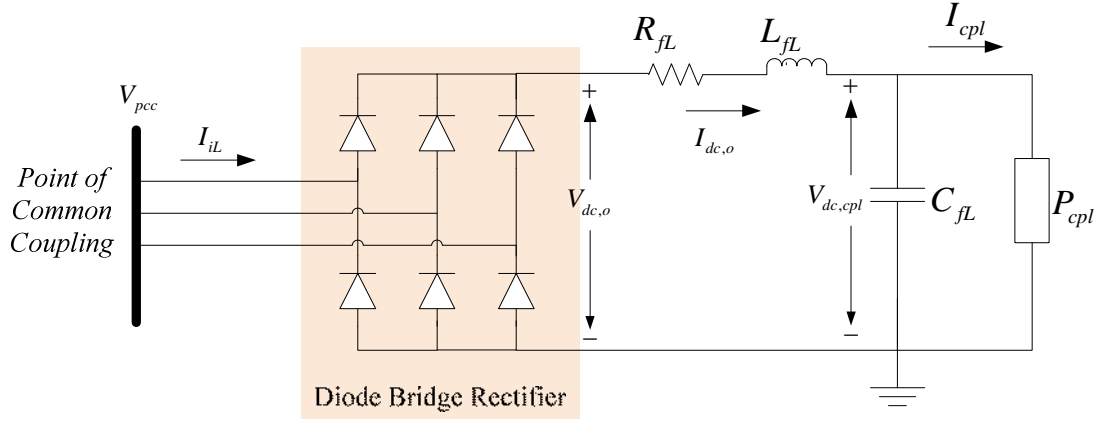


Figure 5.2: A block diagram of CPL interfaced with Diode Bridge to a three-phase AC system

The dq modeling approach of the Diode Bridge rectifier is employed for the stability analysis and control design strategy. This method is developed and validated in [63], [100]. An advantage of this method is that it can be easily combined with a power system comprising of other vector-controlled converters connected to the PCC.

Assuming the AC line current is sinusoidal and in balance condition, the three-phase AC voltage at PCC, V_{pcc} can be written as:

$$V_{pcc} = \begin{bmatrix} V_{a,pcc} \\ V_{b,pcc} \\ V_{c,pcc} \end{bmatrix} = V_{pcc} \begin{bmatrix} \sin(\omega t) \\ \sin(\omega t - 2\pi / 3) \\ \sin(\omega t + 2\pi / 3) \end{bmatrix} \quad (5.1)$$

where the V_{pcc} is the voltage magnitude at the PCC and ω is the angular frequency.

Thus, the fundamental component of switching function, S_{abc} can be given by:

$$S_{abc} = \begin{bmatrix} S_a \\ S_b \\ S_c \end{bmatrix} = \frac{2\sqrt{3}}{\pi} \begin{bmatrix} \sin(\omega t) \\ \sin(\omega t - 2\pi / 3) \\ \sin(\omega t + 2\pi / 3) \end{bmatrix} \quad (5.2)$$

From (5.1) and (5.2), it is known that the voltage and the fundamental component of switching function, and thus input terminal current, are in phase with each other.

Neglecting AC line filters, the relationship between input and output terminal of rectifier can be expressed as given by:

$$I_{iL} = S_{abc} I_{dc,o} \quad (5.3)$$

$$V_{dc,o} = S_{abc}^T V_{pcc} \quad (5.4)$$

The three-phase variables can then be transformed into dq rotating frame at angular frequency ω using the transformation matrix:

$$\mathbf{T} = \sqrt{\frac{2}{3}} \begin{bmatrix} \cos \theta & \cos(\theta - 2\pi/3) & \cos(\theta + 2\pi/3) \\ -\sin \theta & -\sin(\theta - 2\pi/3) & -\sin(\theta + 2\pi/3) \end{bmatrix} \quad (5.5)$$

By aligning the d -axis to the voltage at PCC, $V_{q,pcc}$ can be assumed as zero. Therefore, the q components are negligible. Then, the voltages and currents at the DC and AC side of the rectifier are related by:

$$V_{dc,o} = S_d V_{d,pcc} \quad (5.6)$$

$$I_{d,iL} = S_d I_{dc,o} \quad (5.7)$$

$$S_d = 6 / \pi \sqrt{2} \quad (5.8)$$

The commutation effect of the diode bridge is taken into account and modelled as:

$$r_\mu = 6 f_s L_{eq} \quad (5.9)$$

to represent voltage drop at the DC side as explained in [101]. L_{eq} is the total equivalent inductance at the AC side of the rectifier and f_s is the system frequency in Hz. The equivalent circuit of the diode bridge rectifier in dq frame is displayed in Figure 5.3.

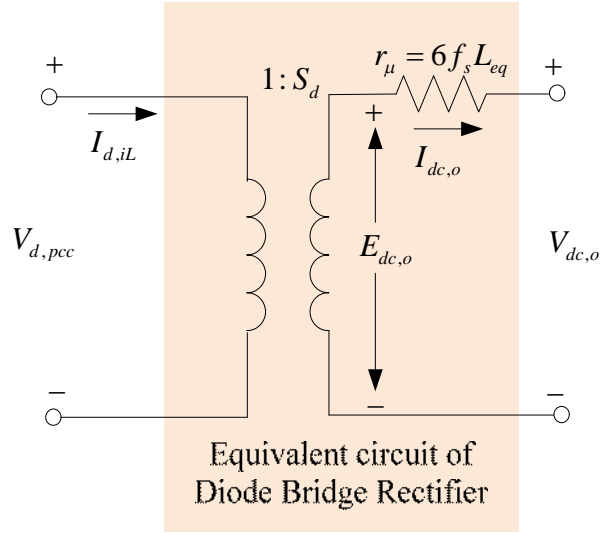


Figure 5.3: The equivalent diode-bridge rectifier in the dq frame

The system in Figure 5.2 can therefore be transformed into dq -frame and simplified as shown in Figure 5.4. Note that, the d -axis is aligned to the voltage at the PCC for the dq -transformation, thus making the q -components small.

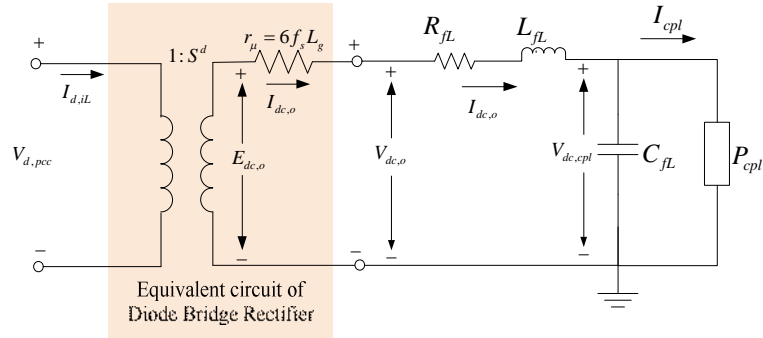


Figure 5.4: Equivalent circuit of the system in Figure 5.2

Using KVL and KCL for the circuit in Figure 5.4, the non-linear differential equations are derived to represent the system as:

$$\begin{aligned} \frac{dI_{d,o}}{dt} &= S_d V_{d,pcc} - \left(\frac{R_{fL}}{L_{fL}} + \frac{r_{\mu}}{L_{fL}} \right) I_{dc,o} - \frac{1}{L_{fL}} V_{dc,cpl} \\ \frac{dV_{dc,cpl}}{dt} &= \frac{1}{C_{fL}} I_{dc,o} - \frac{1}{C_{fL}} \frac{P_{cpl}}{V_{dc,cpl}} \end{aligned} \quad (5.10)$$

5.2.2 The Complete Mathematical Model of the System Studied

The complete mathematical model of the system in Figure 5.1 can be represented by combining the mathematical representation of all components as described in sections 4.2.1, 4.2.2, 4.2.4, 4.2.5 and 5.2.1. A set of differential equation that represent the system in Figure 5.1 is the combination of the differential equations in (4.5), (4.6), (4.17), (4.30) and (5.10). They are in the form as given in (4.31), with the state variables, x , input, u , and output vector, y , are:

$$\begin{aligned}
 x &= \langle I_{d,t}, I_{q,t}, V_{d,pcc}, V_{q,pcc}, I_{d,o}, V_{dc,cpl}, I_{d,iw}, I_{q,iw}, X_{u,w}, X_{d,w}, \\
 &X_{q,w}, V_{dc,w}, I_{d,ie}, I_{q,ie}, X_{v,e}, X_{d,e}, X_{q,e}, V_{dc,e}, X_s, X_y, I_{es}, \lambda \rangle \\
 u &= \langle P_{cpl}, V_{dc,w}^*, I_{q,iw}^*, P_w, V_{pcc}^*, I_{d,fi e}^*, V_{dc,e}^* \rangle \\
 y &= \langle V_{pcc}, V_{dc,cpl}, V_{dc,w} \rangle
 \end{aligned} \tag{5.11}$$

5.2.2.1 Linearized Mathematical Model

The set of differential equations that mathematically model the system given by (4.31) is a nonlinear system since it consists of nonlinear differential equations. The model can be linearized at an operating point. The linear model is derived using first order Taylor series expansions. The model can be written in the following linear state space form of (4.33), where

$$\begin{aligned}
 \delta x &= [\delta I_{d,t}, \delta I_{q,t}, \delta V_{d,pcc}, \delta V_{q,pcc}, \delta I_{d,o}, \delta V_{dc,cpl}, \delta I_{d,iw}, \delta I_{q,iw}, \delta X_{u,w}, \delta X_{d,w}, \delta X_{q,w}, \\
 &\delta V_{dc,w}, \delta I_{d,ie}, \delta I_{q,ie}, \delta X_{u,e}, \delta X_{v,e}, \delta X_{d,e}, \delta X_{q,e}, \delta V_{dc,e}, \delta X_s, \delta X_y, \delta I_{es}, \delta \lambda,]^T \\
 \delta u &= [\delta P_{cpl}, \delta V_{dc,w}^*, \delta I_{q,iw}^*, \delta P_w, \delta V_{pcc}^*, \delta I_{d,fi e}^*, \delta V_{dc,e}^*]^T \\
 \delta y &= [\delta V_{pcc}, \delta V_{dc,cpl}, \delta V_{dc,w}]
 \end{aligned} \tag{5.12}$$

The matrices $\mathbf{A}(x_0, u_0)$, $\mathbf{B}(x_0, u_0)$, $\mathbf{C}(x_0, u_0)$ and $\mathbf{D}(x_0, u_0)$ is $N \times N$, $N \times M$, $P \times N$ and $P \times M$ matrix, respectively. M , N and P is total number of inputs, states and outputs, respectively. The matrices elements, a_{ij} , b_{ij} , c_{ij} and d_{ij} for the matrices $\mathbf{A}(x_0, u_0)$, $\mathbf{B}(x_0, u_0)$, $\mathbf{C}(x_0, u_0)$ and $\mathbf{D}(x_0, u_0)$, respectively, can be determined by:

$$\begin{aligned}
a_{ij}(x_o, u_o) &= \left. \frac{\partial}{\partial x_j} f_i(x, u, y) \right|_{x=x_o} \\
b_{ij}(x_o, u_o) &= \left. \frac{\partial}{\partial u_j} f_i(x, u, y) \right|_{x=x_o} \\
c_{ij}(x_o, u_o) &= \left. \frac{\partial}{\partial x_j} y_i(x, u) \right|_{x=x_o} \\
d_{ij}(x_o, u_o) &= \left. \frac{\partial}{\partial u_j} y_i(x, u) \right|_{x=x_o}
\end{aligned} \tag{5.13}$$

In this thesis, Matlab symbolic toolbox is used to obtain the matrices, $\mathbf{A}(x_o, u_o)$, $\mathbf{B}(x_o, u_o)$, $\mathbf{C}(x_o, u_o)$ and $\mathbf{D}(x_o, u_o)$. The Matlab code is similar to that given in Appendix D. x_o and u_o is the solution to $f(x, u, y) = 0$ and $y = g(x, u)$. The steady state values are determined by using Matlab *fsolve* function to solve the equation $\dot{x} = f(x, u, y) = 0$.

5.3 Small-signal Stability Analysis

System Parameters

The transmission line and DRF-CPL parameters are given in Table 5.1 and Table 5.2, respectively. The wind farm is connected to the PCC via 1kV, 10MVA front end converter. The parameters are given in Appendix C. The ESS is connected to the PCC via a 1kV, 1MVA front end converter and a 2kV, 1MVA DC/DC converter. The parameters are given in Appendix C and Appendix D.

Table 5.1. Parameters of the transmission line in Figure 5.1

Parameter	Value	Description
$S_{rated,L}$	10MVA	Rated power of transmission line
V_t	1kV	Rated voltage (line-to-line)
ω	$2\pi \times 50$ rad/s	System frequency
R_t	6m Ω	Transmission line resistance
L_t	0.1mH	Transmission line inductance
C_t	20nF	Transmission line capacitance

Table 5.2. Parameters of the DRF-CPL in Figure 5.2

Parameter	Value	Description
$S_{rated,L}$	5MVA	Rated power of CPL
V_{Lr}	1kV	Rated voltage
$V_{dc,rL}^*$	2kV	DC link nominal voltage
C_{fL}	0.02F	DC link capacitance
R_{fL}	0 Ω	DC filter resistance
L_{fL}	0.2mH	DC filter inductance
f_{res}	80Hz	Resonant frequency

Eigenvalues Analysis

The eigenvalues of the system studied can be calculated from the system matrix ($A(x_0, u_0)$) in (4.33) for the small-signal stability analysis. Eigenvalues plot when the CPL varies from 0 to 0.5pu is shown in Figure 5.5 and zoomed for the area of interest in Figure 5.6, for three cases as follow:

Case 1 - The system with only the diode rectifier fed-CPL (DRF-CPL) and the transmission line connected to the grid. There is no wind farm and the voltage at PCC is not regulated. The eigenvalues are shown by the green diamond in the Figure 5.5 and Figure 5.6.

Case 2 - As in case 1 above but with voltage support at PCC from the ES interface converter. The detail of the controller is as describe in section 4.2.5. The ES only regulates the voltage at PCC with its reactive power without any active power exchange. The eigenvalues are shown by the blue circle in the Figure 5.5 and Figure 5.6

Case 3- As in case 2 above but with the wind farm. The wind power is 0.5pu. The eigenvalues are shown by the red dot in Figure 5.5 and Figure 5.6.

In Figure 5.6 the dominant eigenvalues that move towards the right hand plane causing instability. These dominant eigenvalues exist for all the three cases. The dominant eigenvalues are coming from the DRF-CPL since they are still there in the plot for case 1 where the wind farm and ESS are removed. Therefore, the main cause of instability is from the DRF-CPL. It is noted that the wind farm and the ESS also

decreases the overall system stability as seen in the eigenvalues traces (Figure 5.6) where the dominant eigenvalues are shifting to the right in cases 2 and 3. In all cases, the instability will be seen when CPL is higher than 0.32pu.

The PSCAD simulation results for the three cases are shown in Figure 5.7. The voltage magnitude at PCC, V_{pcc} is shown in Figure 5.7(b), Figure 5.7(c) and Figure 5.7(d) for case 1, 2 and 3, respectively. For case 1, V_{pcc} is oscillating when CPL is stepped from 0.33pu to 0.34pu. For case 2 and 3, the oscillation occurs when CPL is stepped from 0.32pu to 0.33pu. The PSCAD simulation results have shown good agreement to the eigenvalues analysis as discussed above.

To simplify the analysis, the stability degradation causes by the wind farm and the ESS is ignored and the DRF-CPL connected to grid via the transmission line is analyzed in the following section.

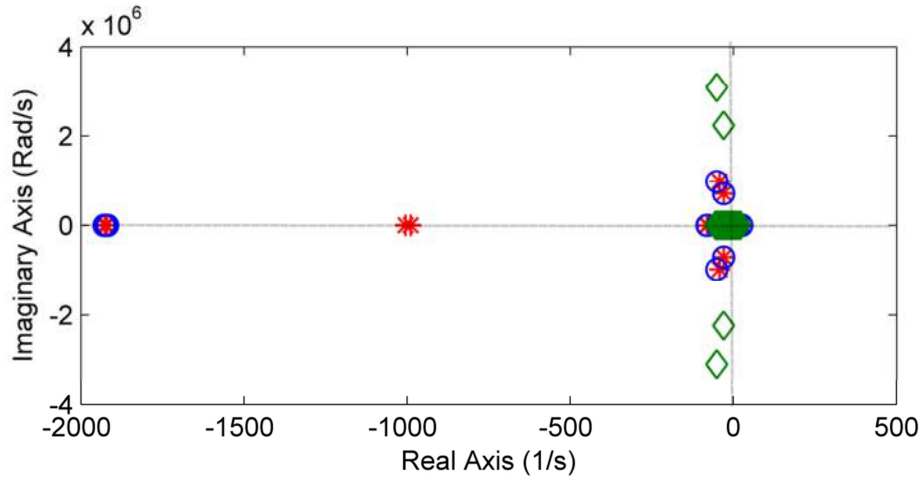


Figure 5.5: Eigenvalue plot when CPL varies from 0 to 0.5pu for three cases. (Legend: Case 1- Green diamond; Case 2-Blue circle; Case 3-Red star)

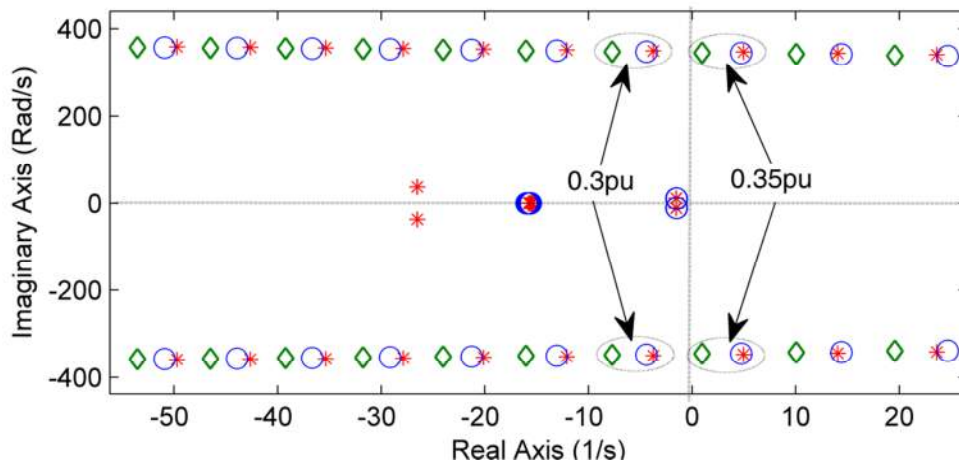


Figure 5.6: Zoomed for the area of interest from Figure 5.5 (Legend: Case 1- Green diamond; Case 2-Blue circle; Case 3-Red star)

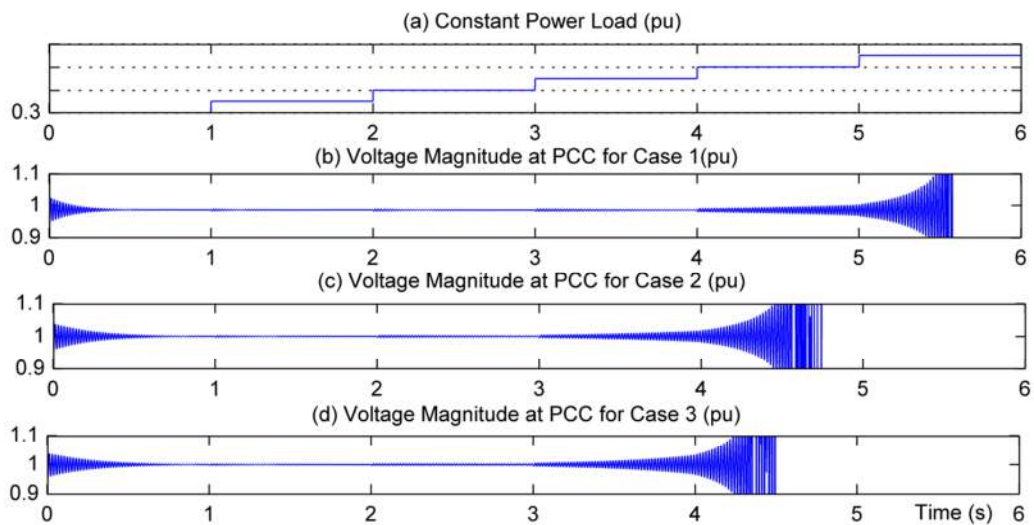


Figure 5.7: PSCAD simulation result for the three cases (a) CPL stepped by 0.01pu from 0.3 to 0.35pu; (b) V_{pcc} (pu) for Case 1; (c) V_{pcc} (pu) for Case 2; (d) V_{pcc} (pu) for Case 3

5.4 The CPL Connected to Local Grid

In the previous section, it is observed that the DRF-CPL is the main source of instability. Therefore, the DRF-CPL connected to the local grid as shown in Figure 5.8 is analyzed more closely in this section.

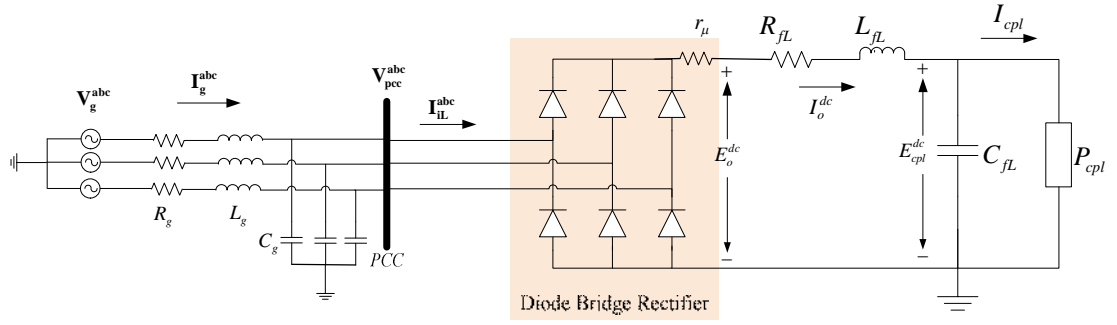


Figure 5.8: A block diagram of DRF-CPL connected to a local grid

Based on the modeling technique as discussed in 5.2.1, the system in Figure 5.8 can be simplified by an equivalent circuit as shown in Figure 5.9. In this modeling approach, the AC voltage source-rectifier subsystem is replaced by an equivalent non-ideal dc-voltage source supplying a CPL. The equivalent model is obtained by considering only the fundamental components on the AC side and by neglecting the ripples on the dc side. It should be noted that this reduced model provides reasonably good accuracy but cannot guarantee the stability of the system for the operating points very close to the stability margins.

The commutation effect of the diode bridge is taken into account and modeled as r_μ to represent the voltage drop at dc side [63], [101]. To simplify the model, C_t is assumed to be very small and ignored. The R_t and L_t are transformed to DC side by multiplying by $(S_d)^2 = (6 / (\pi\sqrt{2}))^2$:

$$\begin{aligned} R_{dc,t} &= R_t (S_d)^2 \\ L_{dc,t} &= L_t (S_d)^2 \\ V_{dc,t} &= S_d V_{d,t} \end{aligned} \quad (5.14)$$

where $V_{d,t}$ is the d -component of the grid voltage following the dq -transformation and S_d is the switching function.

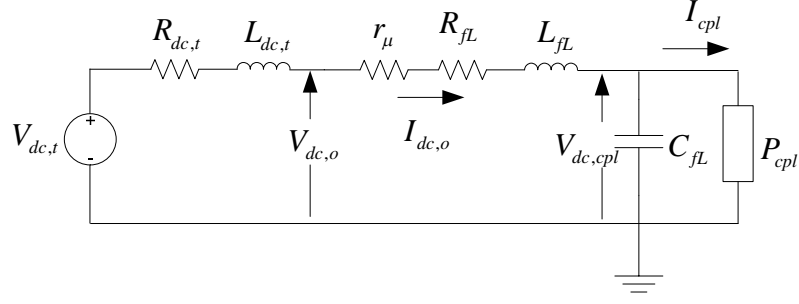


Figure 5.9: Simplified equivalent circuit of the system in Figure 5.8

For the equivalent circuit in Figure 5.9 and based on discussion in [65], the necessary condition for small-signal stability of the system can be determined by:

$$P_{cpl} < \frac{(R_{dc,t} + r_{\mu})C_{fL}}{L_{dc,t} + L_{fL}} (V_{dc,cpl})^2 \quad (5.15)$$

Analyzing(5.15), it is known that the small-signal stability of the DRF-CPL is influenced by the selection of LC filter values. Therefore, the following section discusses the effect of the LC filter value on the stability limit of the system.

5.4.1 The CPL DC Link Smoothing LC Filter and Stability Limit Characteristic

Typically, the DC-link LC filter is designed to filter with a particular resonance frequency. Referring to [102], the resonant frequency:

$$f_{res} = f_{ripple} \sqrt{\gamma_{filter}} \quad (5.16)$$

where f_{ripple} is the ripple frequency to be smoothed and γ_{filter} is the filter attenuation that is given by:

$$\gamma_{filter} = \frac{\gamma_{ripple}}{I_{Lripple} / I_{DC}} \quad (5.17)$$

where γ_{ripple} and I_{DC} are the maximum output current ripple and the maximum output DC current, respectively. The ripple current in the load is:

$$I_{Lripple} = V_{ripple} / |Z_L| \quad (5.18)$$

where V_{ripple} and Z_L are the maximum ripple voltage and nominal load impedance, respectively. Generally, f_{res} is less than f_{ripple} to be smoothed depending on a particular system requirement in term of γ_{ripple} and V_{ripple} . The curves in Figure 5.10 plot the value of inductance versus capacitance at three different resonance frequencies (shown by blue lines). It is seen that the inductance falls rapidly with the increase in capacitance for a fixed value of f_{res} . The relationship is given by:

$$2\pi f_{res} = \frac{1}{\sqrt{L_{fL} C_{fL}}} \quad (5.19)$$

As the resonance frequency increases, the inductance reduces for a given value of capacitance. For example, with $C_{fL}=0.01F$, L_{fL} is 0.395mH, 0.098mH and 0.043mH to produce resonance frequencies of 80 Hz, 160 Hz and 240 Hz respectively. This corresponds for typical filters for 6, 12 and 18 pulse, respectively.

Also shown in Figure 5.10 are the CPL stability limits of 0.2pu, 0.4pu and 0.6pu with respect to C_{fL} and L_{fL} values. The CPL stability limits are estimated values based on (5.15). For the estimation, the $V_{dc,cpl}$ is assumed constant for all CPL values. Transmission line parameters are as in Table 5.1. The CPL stability limit is increasing as the capacitance increases and decreases as the inductance increases.

To observe the trend of the CPL stability limit versus the capacitance, Figure 5.11 is prepared. The figure shows the CPL stability limit of the system in Figure 5.9 when C_{fL} is increased from 0.05F to 0.4F for $L_{fL}=0.05mH$, 0.1mH and 0.2mH. The plots are obtained using the analytical method based on (5.15) assuming $V_{dc,cpl}$ is constant and the transmission line parameters are the values in Table 5.1.

For a particular value of L_{fL} , an increase in C_{fL} raises the CPL stability limit as seen in Figure 5.11. For instance, at $L_{fL}=0.2mH$, the CPL stability limit increases from 0.08pu to 0.642MW as C_{fL} increases from 0.05F to 0.4F. For a lower L_{fL} the system hits the CPL stability limit at higher power level. Referring to Figure 5.11 for example, with C_{fL} of 0.02F, the CPL stability limit is 0.529pu, 0.435pu and 0.323pu for $L_{fL} = 0.05mH$, 0.1mH and 0.2mH, respectively.

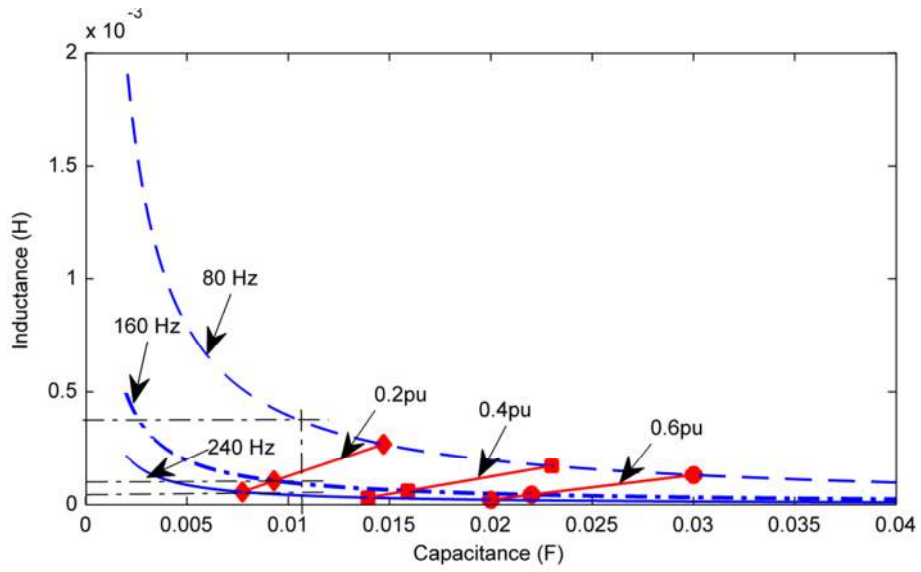


Figure 5.10: DC link capacitance versus inductance curve for 80, 160 and 240Hz (shown by blue lines) and CPL stability limits of 0.2,0.4 and 0.6pu (shown by red lines)

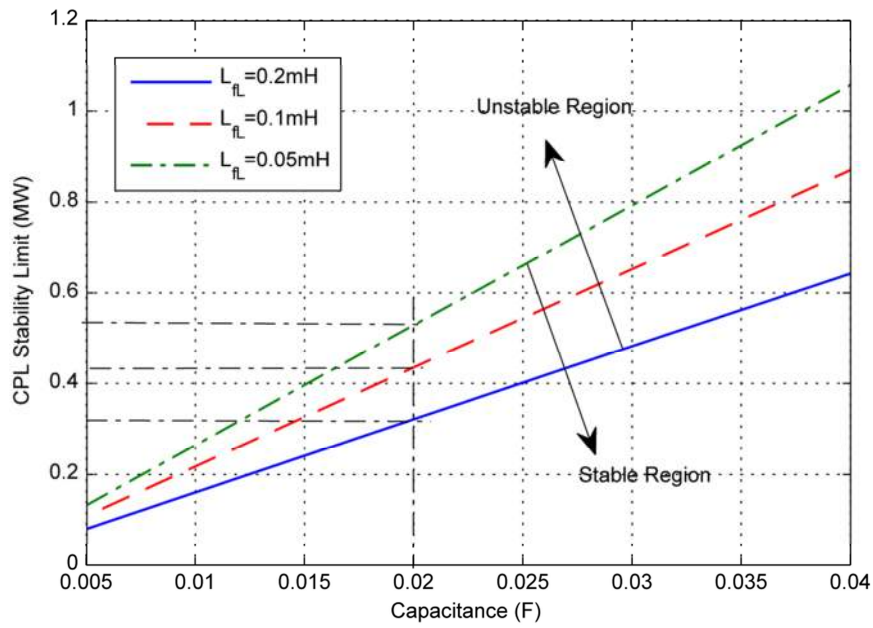


Figure 5.11: Capacitance versus CPL stability limit for $L_{fL} = 0.05\text{mH}$, 0.1mH and 0.2mH

Therefore, the system instability limit will be lower with a lower value of C_{fL} and a higher value of L_{fL} . A larger value of C_{fL} is preferable for better stability but it can result in a higher cost. A smaller value of L_{fL} is good for a better stability but results in higher ripple current. To compromise for a better system reliability and drive life time, a smaller C_{fL} at the expense of larger L_{fL} can be chosen in the LC filter but this will reduce the stability margin.

In practice, the selection of the DC-link capacitor for a diode rectifier is highly dependent on the manufacturer's specifications (i.e. the capability of the capacitor to handle a given amount of low frequency current ripple for a desired lifetime). It is also depends on the particularities of the circuit since multi-pulse rectifiers will typically produce less ripple and will therefore require smaller LC values. DC link capacitor selection also depends on the operating conditions as the design is always carried out to handle the worst case conditions i.e. the DC-link capacitor may have to deliver energy to the load during a power interruption. Because of the limitation of the capacitance value available from manufacturers, it is very likely that the capacitor will be oversized compared to that required from the basic DC-link voltage ripple condition. This explains why situations of unstable operation of diode rectifiers are not so often found in practice.

The conclusion is that the selection of L_{fL} and C_{fL} with a DRF-CPL will govern the small-signal stability limit of the constant power load. If the L_{fL} and C_{fL} values have been fixed, other actions have to be taken to increase the stability limit or margin imposed for those values. In this chapter, the L_{fL} and C_{fL} is chosen to be 0.2mH and 0.02F so that we can observe the instability occurring in the system studied within rated power. This allows for further analysis in order to improve the system stability.

5.5 Control System to Improve Stability

5.5.1 Participation Factor Analysis

The participation factor has been used widely for the analysis of small-signal stability [12], [103], [104]. A mode in the transient response corresponds to an eigenvalue or a pair of complex eigenvalues. If r_k^i and l_k^i are the right and left eigenvectors respectively, then, as defined in [103], the modal participation factor is:

$$p_{ki} = -l_k^i r_k^i \quad (5.20)$$

This is viewed as the degree of participation of the i^{th} mode in the k^{th} state. This corresponds to the concept of observability i.e. to what extent the mode is observed in a state. Meanwhile:

$$\pi_{ki} = \frac{(\text{Re}\{l_k^i\})^2}{\text{Re}\{l_k^i\}(\text{Re}\{l_k^i\})^T} \quad (5.21)$$

is regarded as the participation factor of the k^{th} state in the i^{th} mode. This corresponds to the concept of controllability i.e. the extent to which a state variation influences a mode.

The higher the p_{ki} value, the more the mode i participates in the transient response of the state k . On the other hand, a higher π_{ki} indicates that the state k participates more in determining the mode i .

In this thesis the participation factors of the unstable eigenvalues as discussed in section 5.3 is calculated as shown in Table 5.3 and Table 5.4 for the p_{ki} and π_{ki} , respectively. The Matlab code used for the calculation is given in Appendix E. The unstable modes are from the case with the CPL of 0.5pu using the parameters in Table 5.1, Table 5.2 and Appendix D with the wind farm disconnected (case 2 in section 5.3). Only participation factors of the unstable modes are presented because the aim is to find the influence of the unstable modes on the states and vice versa.

Table 5.3: Participation factor of the unstable modes in states, p_{ki}

Unstable Modes\State	$I_{d,t}$	$I_{q,t}$	$V_{d,pc}$	$V_{q,pc}$	$I_{d,e}$	$I_{q,e}$	$X_{v,e}$	$X_{d,e}$	$X_{q,e}$	$V_{dc,e}$	$I_{dc,o}$	$V_{dc,cpl}$
36.356±333.7i	0.2574	0	0	0	0	0.0017	0.0107	0	0.0006	0	0.2815	0.5416

Table 5.4: Participation factor of states in the unstable modes, π_{ki}

Unstable Modes\State	$I_{d,t}$	$I_{q,t}$	$V_{d,pc}$	$V_{q,pc}$	$I_{d,e}$	$I_{q,e}$	$X_{v,e}$	$X_{d,e}$	$X_{q,e}$	$V_{dc,e}$	$I_{dc,o}$	$V_{dc,cpl}$
36.356±333.7i	0	0	0	0	0	0	0.7178	0.2160	0.0630	0	0.0001	0

From Table 5.3, it is seen that the unstable modes highly influence the DC-link voltage in the CPL feed, $V_{dc,cpl}$, with a factor of 0.5416 followed by the DC link current, $I_{dc,o}$, and real power component of the AC line current, $I_{d,t}$, with factors of 0.2815 and 0.2574, respectively. The unstable modes have a very small effect on other states. From the participation factor values, we can detect instability by observing the states $V_{dc,cpl}$, $I_{dc,o}$ and $I_{d,t}$. The d -component of the AC side load current, $I_{d,iL}$ may be observed for the purpose. This is so because $I_{d,iL}$ is directly proportional to $I_{dc,o}$.

From Table 5.4, it is observed that the output of the voltage controller of the ES converter (actually the state $X_{v,e}$ -see Figure 5.12) has the highest participation factor in determining the unstable modes with a participation factor of 0.7178. The output of the d and q component of the current controller of the ES converter (actually the states $X_{d,e}$ and $X_{q,e}$, respectively – see Figure 5.12) have a factor of 0.2160 and 0.063, respectively. Therefore, it is possible to use the states $X_{v,e}$, $X_{d,e}$ and $X_{q,e}$ to shift the unstable modes towards the stable region and to increase stability margin.

5.5.2 Control Structure

From the participation factor analysis, $I_{d,iL}$ can be used to sense the changes in the dominant modes that have the tendency to cause instability and the states $X_{v,e}$, $X_{d,e}$ and $X_{q,e}$ can be employed to influence the modes in order to improve the stability margin. Based on this, two control schemes to improve the system stability are proposed and evaluated. The original energy storage unit front end converter controller as discussed in section 4.2.5 is modified. For convenience, the original controller is shown again in Figure 5.12.

The control scheme 1 modifies the original controller of the ESS as illustrated in Figure 5.13. The AC load current, I_{iL} (seen in Figure 5.1) is measured. The current is transformed to its equivalent d -component, $I_{d,iL}$, using the definition discussed in section 4.2.1. It is oriented on the voltage at the PCC. The current $I_{d,iL}$ is detected since it indicates changes in the dominant modes that may cause instability as discussed previously. The aim is to detect any sudden changes in $I_{d,iL}$ and then modify the ESS controller outputs to avoid instability following any transient. Hence a high pass filter (HPF) is applied to the d -component of the measured load current. The transfer function is:

$$\frac{k_1 s}{s\tau_r + 1} \quad (5.22)$$

It is employed to provide a feed forward reference current signal to the current controller. k_1 and τ_r in (5.22) are the HPF gain and time constant, respectively. A limiter is placed after the HPF to limit the current according to the ESS rating. The feed forward reference current, I_{fe}^* gradually reduces to zero following the sudden change. In this control scheme 1, I_{fe}^* is only fed to the reactive current controller, being added to the reactive current required for V_{pcc} control. Therefore, only reactive current will be injected to the system following rapid change in the load.

Control Scheme 2

In control scheme 2, I_{fe}^* is fed to both active and reactive current controller as shown in Figure 5.14. Hence, both active and reactive currents will be supplied responding to the load change.

5.5.3 PSCAD Simulation Results

The PSCAD simulation results are plotted in Figure 5.15, Figure 5.16 and Figure 5.17 for the system with original ESS controller, control scheme 1 and control scheme 2, respectively. For the simulation, $k_1 = k_2 = k_3 = 1$ and $\tau_r = 0.05$ has been used. These values are sufficient to illustrate the control principle. The study to properly determine the optimal values for the gains (k_1 , k_2 and k_3) and τ_r is a subject to be done in the future. It is shown that without the load current control feedback, the system becomes unstable when to CPL steps from 0.32pu to 0.33pu. The controller scheme 1 improves the stability margin to 0.66-0.67pu. As seen in Figure 5.16(c) and Figure 5.16(d), only reactive current is injected from the ESS when there is sudden change in the CPL. With the controller scheme 2, the active current is also injected on top of the reactive current. The stability margin is further improved to 0.72-0.73pu.

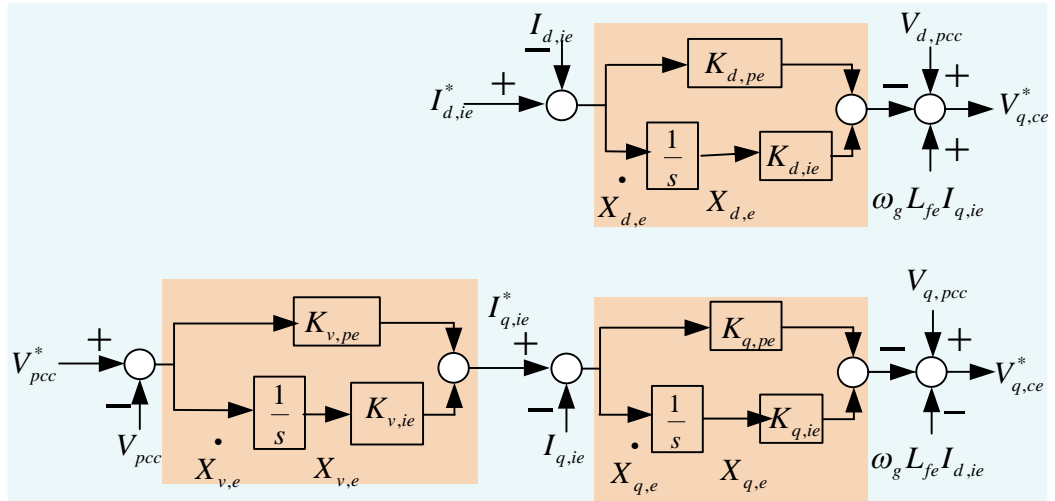


Figure 5.12: The original controller of ESS as described in section 4.2.5

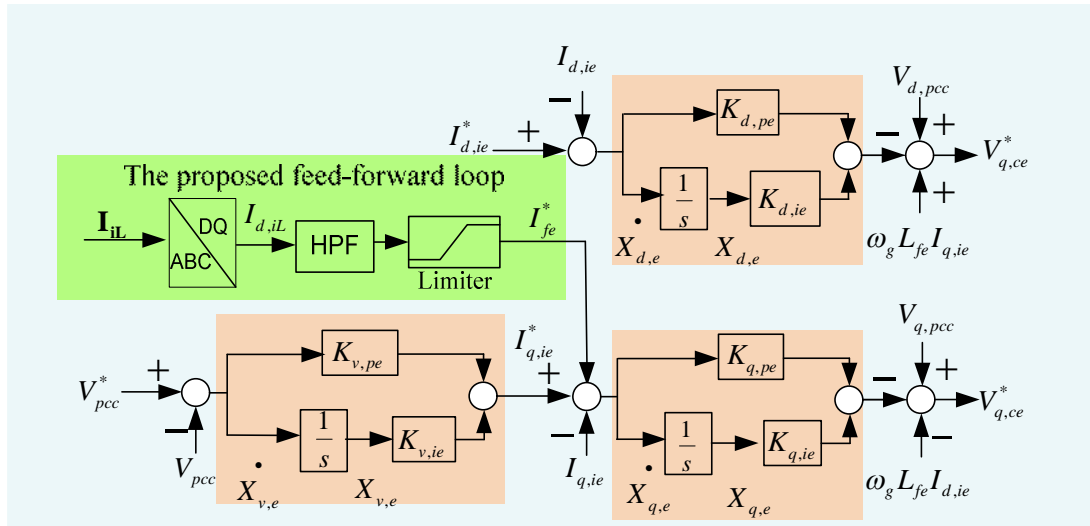


Figure 5.13: The control scheme 1

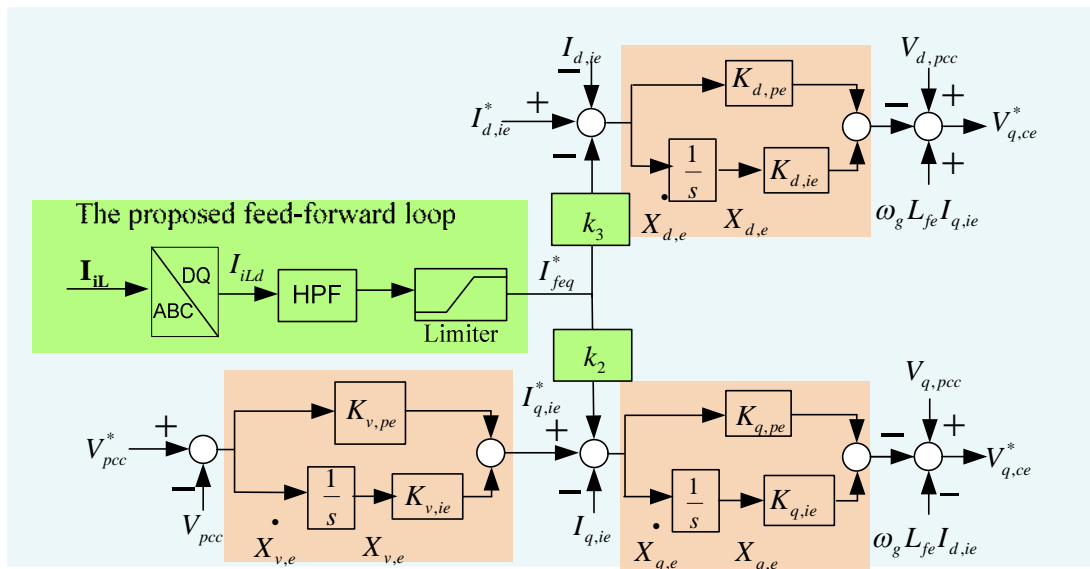


Figure 5.14: The control scheme 2

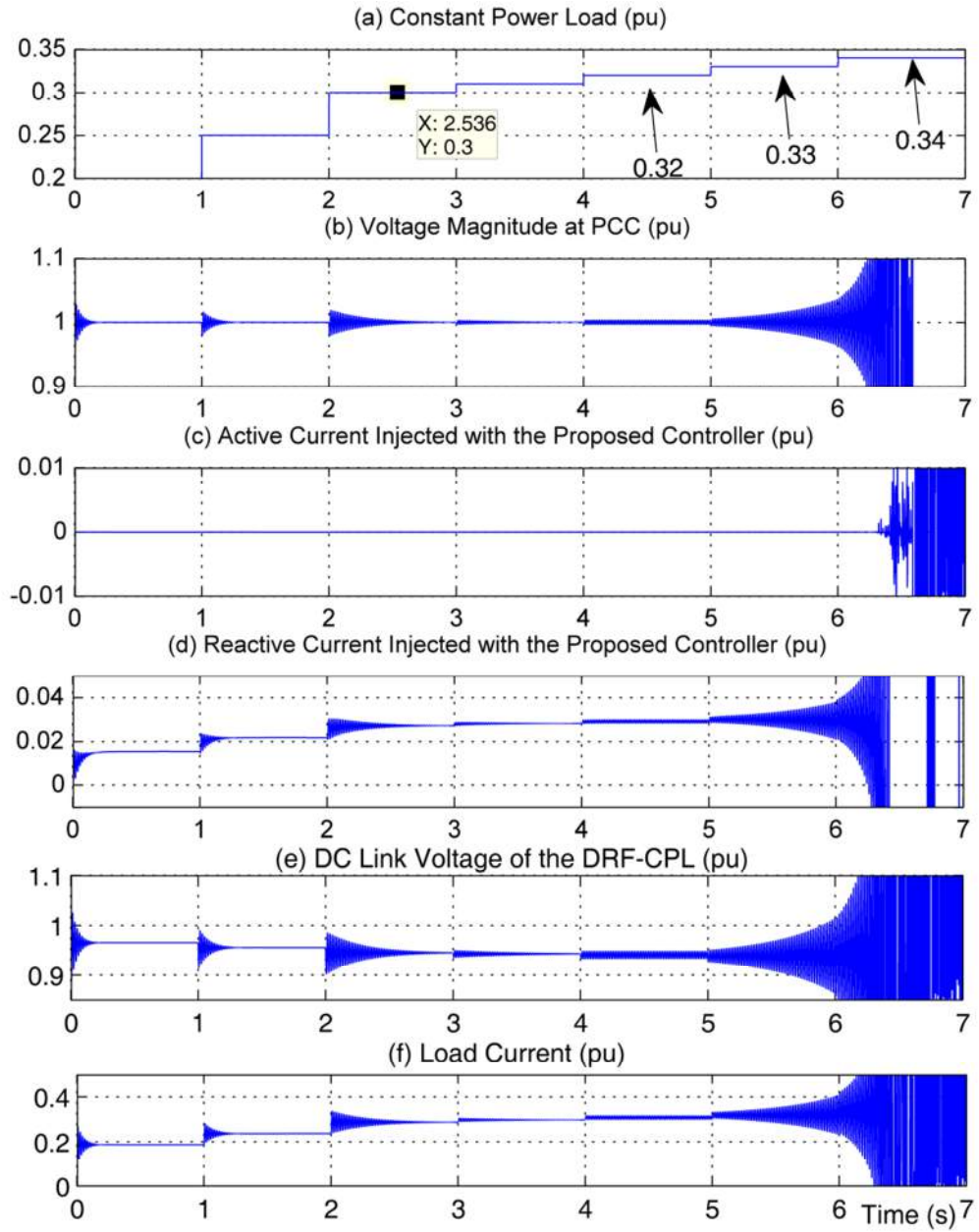


Figure 5.15: The simulation result for the system in Figure 5.1 with the original ESS controller; (a) CPL, P_{cpl} (pu); (b) Voltage magnitude at PCC, V_{pcc} (pu); (c) Active current injected by ESS, $I_{d,ie}$ (pu); (d) Reactive power injected by ESS, $I_{q,ie}$ (pu); (e) DC link voltage of the DRF-CPL, $V_{dc,cpl}$ (pu); (f) Load current, $I_{dc,o}$ (pu);

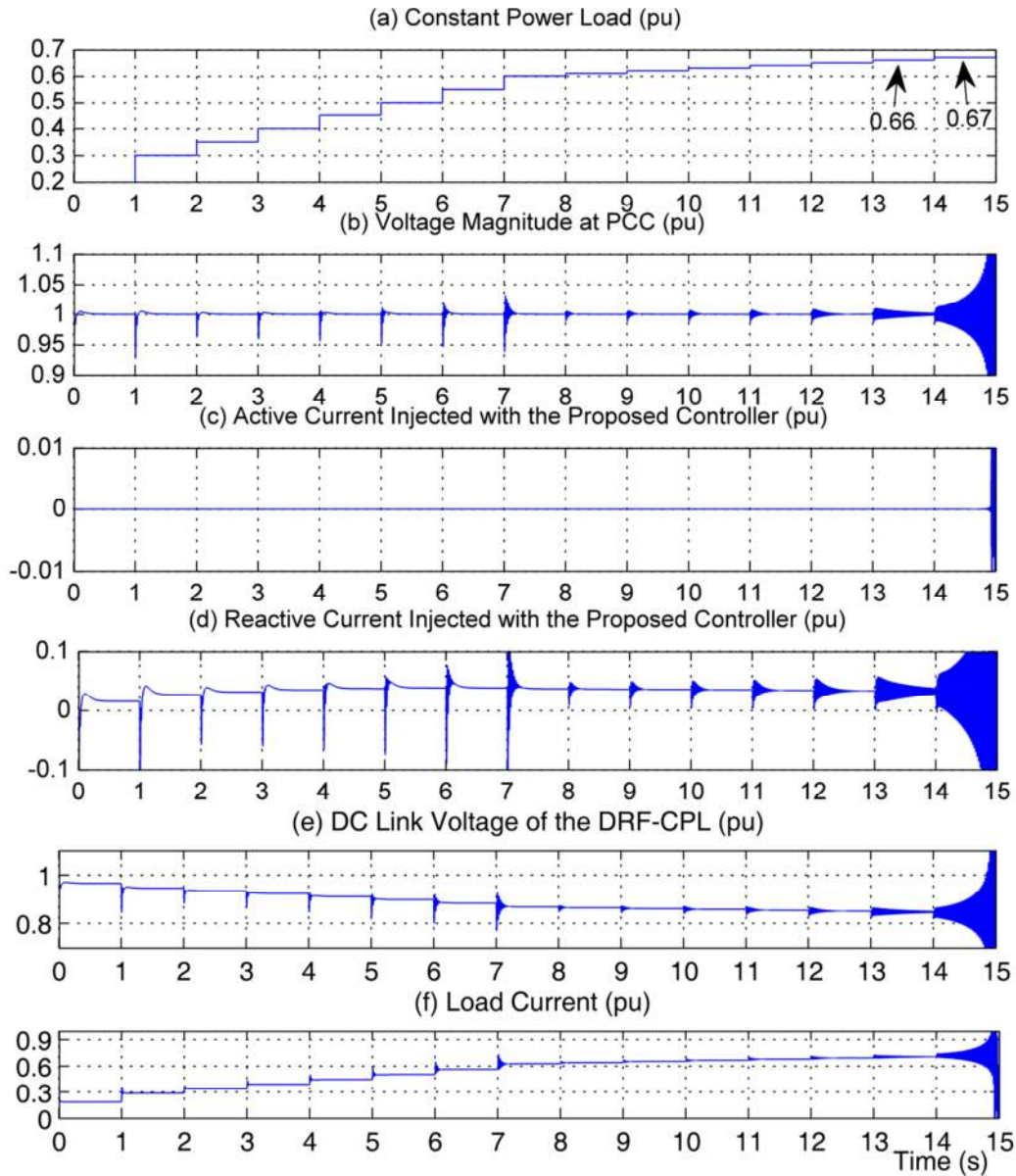


Figure 5.16: The simulation result for the system in Figure 5.1 with the ESS controller scheme 1; (a) CPL, P_{cpl} (pu); (b) Voltage magnitude at PCC, V_{pcc} (pu); (c) Active current injected by ESS, $I_{d,ie}$ (pu); (d) Reactive power injected by ESS, $I_{q,ie}$ (pu); (e) DC link voltage of the DRF-CPL, $V_{dc,cpl}$ (pu); (f) Load current, $I_{dc,o}$ (pu);

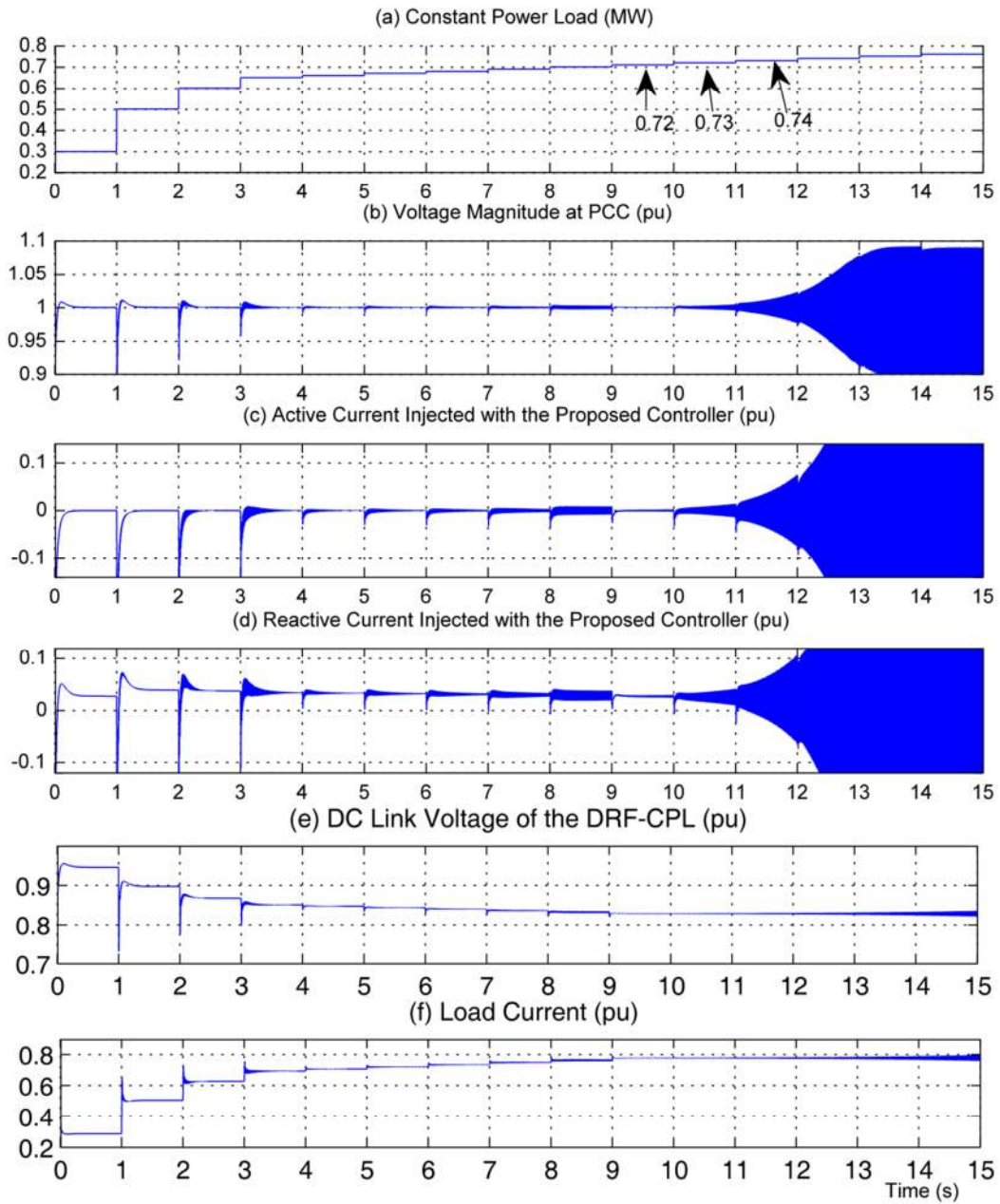


Figure 5.17: The simulation result for the system in Figure 5.1 with the ESS controller scheme 1; (a) CPL, P_{cpl} (pu); (b) Voltage magnitude at PCC, V_{pcc} (pu); (c) Active current injected by ESS, $I_{d,ie}$ (pu); (d) Reactive power injected by ESS, $I_{q,ie}$ (pu) (e) DC link voltage of the DRF-CPL, $V_{dc,cpl}$ (pu); (f) Load current, $I_{dc,o}$ (pu);

5.6 Chapter Summary

In chapter 4, the CPL is fed by PWM controlled rectifier and it is found that the system is always stable within the load capability limit. However, in this chapter a CPL is supplied by a diode-bridge rectifier. It is seen that the situation is different. The small-signal analysis is performed for the case where the CPL is fed by an uncontrolled diode bridge rectifier (DRF). The eigenvalues analysis of the system with the DRF-CPL, the wind farm and the ESS has shown that the system can become unstable under the transmission line load capability limit. It also established that the DRF-CPL contribute to the unstable modes. Further analysis using the mathematical model of the DRF-CPL connected to the grid has been developed and the stability analysis has identified that the instability depends on the selected value of the LC filter in the DC link. Therefore, by selecting a particular value for the LC filter, the CPL stability margin can be estimated. Participation factor analysis has been undertaken for the unstable modes to give an overview of the influence of the modes on the system states and vice versa. Based on the participation factors, two schemes for controlling the real and reactive currents fed by the ESS interface converter to extend the stability margin are proposed. In the first scheme, a control current is added to the ESS reactive current and has increased the stability margin by a factor of 2. The second scheme improves the stability by adding a control current to both the ESS real and reactive components. The results have demonstrated the possibility of using an energy storage system to increase the stability margin in a system with DRF-CPL. The control requires the feedback of the real component of current, or load current, drawn by the diode rectifier. While this will not increase the system measurements, it does assume the load current measurement can be transmitted to the ESS front end converter control. In practice, this means that the stability margin of a system with a DRF-CPL depends on the selected value of LC filter. If the capacitance is oversized which is typically the case, the stability margin is increased. However, economically, it is desirable to reduce the capacitance at the expense of increased inductance. For example, at 80Hz resonance frequency (see Figure 5.10), if we are to reduce the capacitance from 0.02F to 0.015F, we have to increase the inductor from 0.27mH to 0.17mH. The saving to decrease the capacitance by 0.005F is more than the cost to increase the inductance by 0.1mH

[105]. This reduces the stability margin from 0.4pu to 0.2pu. However by exploiting the improved stability margin using the energy storage system by injection of active and/or reactive currents, the use of decreased capacitance in such systems can be addressed. To investigate this, a cost analysis of per unit capacitance and inductance needs to be undertaken. This would be the subject of further work.

Chapter 6

Conclusion and Future Work

6.1 Conclusion

This thesis has investigated the Energy Storage System (ESS) benefits in terms of improving the overall system efficiency and increasing the power system stability for a remote local grid fed by a wind farm. For the case of stability investigation, we take the case of where the local grid feeds a large Constant Power Load (CPL). The main aims were to assess the system to determine the key parameters that are significant to improve the overall system efficiency and to investigate the possibility of benefiting the ESS to increase the system stability margin.

For the studies, a model of the DFIG wind turbine connected to a grid via a transmission line has been developed in PSCAD/EMTDC software. This is referred to as a detail model. The DFIG detail model and the control system are presented and simulated in PSCAD. The simulation results have shown that the detail model provides satisfactory results for the MPPT of the wind power system. However, the detail model takes a long time for the simulation. Therefore, a simplified model is proposed. The comparison has not been reported before. In the simplified model, some components have been removed in order to reduce the complexity and thus the simulation time by 5 times. It was assumed that the grid side converter is directly connected to the PCC and the grid voltage is constant, thus the machine flux is also constant. The stability region of the simplified model is considered the same as simplified model based on the study published in [50], [87]. The simplified model proposed is valid for wind turbine that is controlled for MPPT. It has been shown in the thesis that the simplified model gives acceptable results for low bandwidths as occurring with wind speed changes. Step change in output reactive power of the

simplified model can also give a good agreement with the detailed model. This simplified model may be very useful for the studies where simulation need to be repeated many times.

The thesis has clarified key parameters that are significant to make use of energy storage to improve the overall system efficiency. The mathematical analysis is undertaken for the simplified case of square wave variation and is consistent with the PSCAD simulation results as shown in Chapter 2. The analysis has suggested that the minimum mean variation in the wind power (represented by the minimum mean variation in transmitted current without ESS, $\Delta I_{t,pu\min}$), the average wind power (represented by $I_{t,o}$), the ESS round trip efficiency η_{rt} , and the line SCR and X/R ratio are the important parameters when considering the benefit of energy storage for overall system efficiency improvement. The relationship of (3.19) can be used to govern the selection and sizing of energy storage rating depending on a system η_{rt} , $I_{t,o}$, SCR and X/R ratio. From the simulation with the real wind speed waveform, it is shown that the relationship in (3.19) is also applicable where $\Delta I_{t,pu\min} = \sigma_{I_{t,\min}}$ - the minimum mean variation of the wind power. The analysis has examined for the case where the energy storage was used to keep the current delivered to the grid constant at an average constant value.

A mathematical model of a system consisting of a wind farm, a large CPL and an energy storage unit connected to the weak grid has been developed and presented. Each of the CPL, wind power and energy storage units is connected to the AC side via a PWM AC/DC converter. The mathematical model is validated by PSCAD simulation model. From the eigenvalue analysis, it is found that the system is generally stable if operated below the transmission line load-ability limit. However, the damping decreases as the transmission line has to carry more power. Therefore, more oscillation is observed when there is a sudden change in load at higher power carried by the line than that at lower power. The model is able to analyze the stability of the system for changes in the DC-link voltage controller values, the real and reactive current controller values and controller values for the V_{pcc} regulation. In practice, it is found that the system is stable under range of controller bandwidth and

that the main influence on stability arises always from the power capacity of transmission line. This is a consequence of the controlled nature of the PWM interface rectifier.

When a CPL is supplied by a diode-bridge rectifier, the situation is different. The small-signal analysis is performed for the case where the CPL is fed by an uncontrolled diode bridge rectifier (DRF). The eigenvalues analysis of the system with DRF-CPL, the wind farm and the ESS has shown that the system can become unstable under the transmission line load ability limit. It also established that unstable modes are contributed by the DRF-CPL. Further analysis using the mathematical model of the DRF-CPL connected to grid has been developed and the stability analysis has identified that such a system can be unstable depending on the selected value of the LC filter in the DC link. Therefore, by selecting a particular value for the LC filter, the CPL stability margin can be estimated. Participation factor analysis has been undertaken for the unstable modes to give an overview of the influence of the modes on the system states and vice versa. Based on the participation factors, two schemes for controlling the real and reactive currents fed by the ESS interface converter to extend the stability margin are proposed. In the first scheme, a control current is added to the ESS reactive current and has increased the stability margin by a factor of 2. The second scheme can be further improved the stability by adding a control current to both the ESS real and reactive components. The results have demonstrated the possibility of using energy storage system to increase the stability margin in a system with DRF-CPL. The control requires the feedback of the real component of current, or load current, drawn by the diode rectifier. While this will not increase the system measurements, it does assume the load current measurement can be transmitted to the ESS front end converter control.

6.2 Future work

Several subjects possible for future work are listed as follow:

- Establish a relationship between the actual wind speed profile and the wind power profile (or transmitted current profile) so the overall system efficiency increase with ESS can be calibrated in terms of wind speed variation. A wind

speed profile may be characterized with its standard deviation, σ_w and average speed, $\overline{V_w}$. A study based on the actual wind speed could then be done to obtain a relationship of σ_w and $\overline{V_w}$ with the SCR, X/R ratio and η_{rt} .

- To include the LCL filter in the system stability study. It is typically connected between a converter and PCC. The LCL filter causes oscillations at higher resonant frequencies. For the PWM front-end CPL load converter, the resonant frequencies are significantly higher than the unstable mode frequencies deriving from the transmission line limits. This justifies their exclusion. For the diode bridge rectifier it has been assumed that the line current smoothing has been undertaken by the DC-link filter. In practice however, AC-line filtering is included which will cause resonances related to the smoothing of the principle fundamental harmonics. These may not be so high and so that their effect would need to be included in the analysing the stability of the whole system.
- An experimental rig could be developed to validate the algorithm developed in this thesis for overall system efficiency improvement with an ESS. The experimental rig also shall be used to test the proposed controller to increase the stability margin.
- The thesis only illustrates the potential of the ESS control to increase stability margin. A thorough controller design needs to be undertaken. A control design would involve adding appropriate states for a HPF transfer functions feeding the control signals to the real and reactive current loops. The control to the two loops also requires different gains. A state variable feedback design can then be done by shifting the closed loop poles of the unstable modes. The thesis has shown that the significant improvement in stability margin can be obtained so that it is likely that the state feedback control gains will be practical to implement.
- Designing the controller for the stability margin improvement without the need to transmit the load current to the ESS controller. This may be done with active-impedance-based stabilization as discussed in [92].

- Using sensitivity analysis is possible to vary the parameters and determine the influence on the eigenvalues for each variation. One would have to recalculate the linearization point if the parameter variation affects the power flow. To do this sensitivity theory is required. This was not done since the stability criteria as a function of the DC-link filter parameter was addressed in this thesis and this gives a good indication of the main parameter affecting stability.

6.3 Publication

Conference papers arising from this thesis are:

1. M. F. Romlie, C. Klumpner, M. Rashed, M. Odavic, and G. Asher, “Analysis of stability aspects of a large constant power load in a local grid,” in *15th European Conference on Power Electronics and Applications (EPE)*, 2013.
2. M. F. Romlie, M. Rashed, C. Klumpner and G. Asher, “An Analysis of Efficiency Improvement with the Installation of Energy Storage in Power Systems,” in *International Conference on Power Electronics, Machines and Drives (PEMD)*, 2014”

Appendix A :

Matlab code to obtain a new set of wind profile at a different wind perturbation

```
%clc
clear
Vwo = csvread('windSTD_125.txt'); % Reading an available data from a
text file
STDO=std(Vwo); % Calculate standard deviation for the available wind
data
VA=mean(Vwo); %Calculate average

STDN=0.5; %Specify a new standard deviation
k=STDN/STDO; % Calculate constant

Vwn=k*(Vwo-VA)+VA; %Calculate new wind profile at the new
perturbation

figure
plot(Vwo)
hold on
plot(Vwn)
```

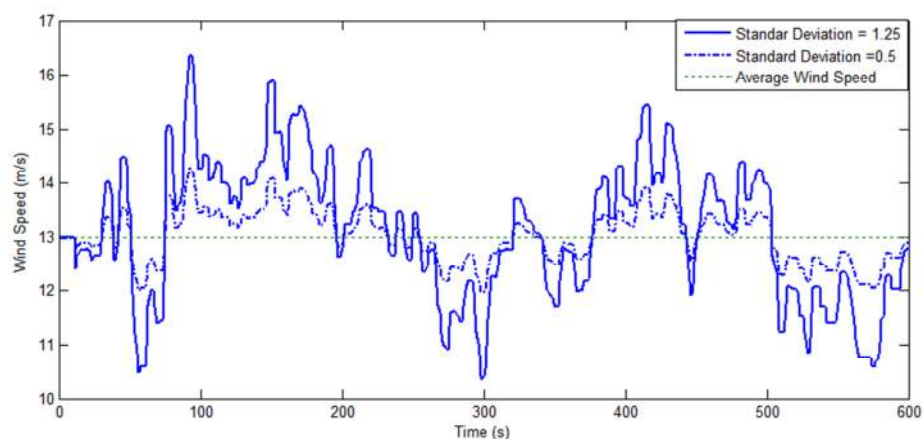


Figure A.1: Plot of wind profiles with standard deviation 0.5m/s and 1.25m/s. Both having average wind speed of 13 m/s.

Appendix B :

Average model of PWM AC/DC converter

Average model of a PWM AC/DC converter is used in the entire modeling and simulation in this thesis instead of a detailed PWM converter. For the detailed converter model, the power electronics components are switched on and off at a high frequency (few kHz or higher). It requires a small simulation time step. Therefore, it is comparatively slow. Because the study in this thesis is not focusing on the converter switches and average model without the switches is employed. This is very helpful to reduce computing time and hence speed up the simulation. The average model approximate the original system by averaging the effect of fast switching within a switching interval to provide continuous and fast respond system suitable for the simulation.

Assuming that the energy is conserved on the DC side and the AC side of the converter:

$$V_{dc}I_{dc} = V_a I_a + V_b I_b + V_c I_c \quad (\text{B.1})$$

where V_{dc} and I_{dc} are the DC voltage and current, V_a, V_b, V_c and I_a, I_b, I_c are the three phase AC voltage and current at AC side of the converter, respectively.

The average model assumes that the converter reproduce the reference voltages from the converter controller. Thus, the preferred voltages are directly applied without any switches. The converter is model in PSCAD and added to its library. The block diagram to realize the averaged model is shown in Figure B.1. The m_A, m_B, m_C in the

block diagram are the modulation signal obtained from the PWM converter controller.

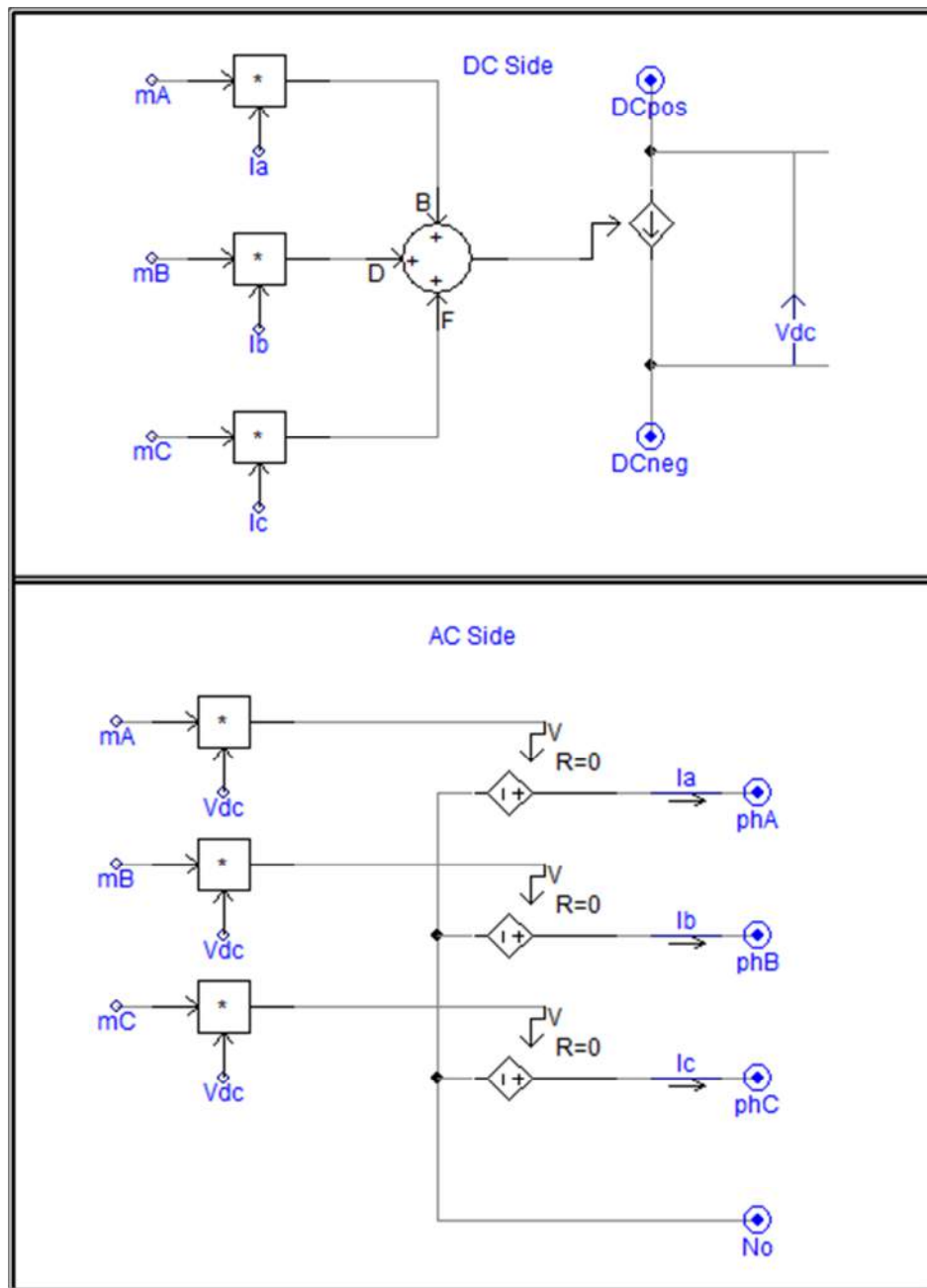


Figure B.1: Block diagram in PSCAD/EMTDC to realize the average model of a PWM AC/DC converter

Appendix C :

Parameters of Front End Converters

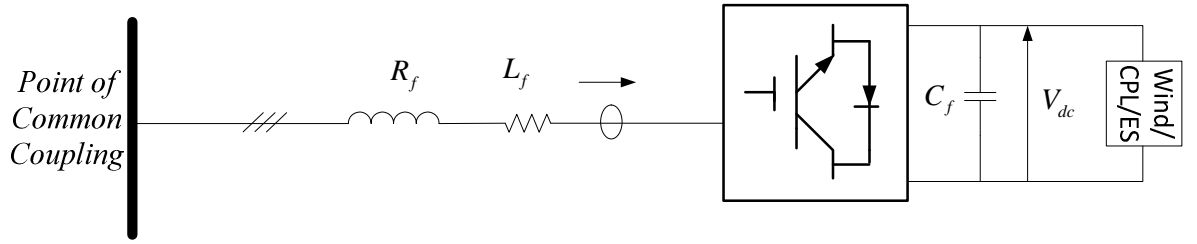


Figure C.1: Block diagram of a front end AC/DC converter connected to the PCC

This appendix provides detail of the front end converter parameters selection. In the thesis, the converters are either 10MVA or 1MVA at 1kV system. Therefore, two sets of parameters are calculated.

The AC filter inductor, L_f can be calculated for a particular voltage drop across the inductor, V_{drop} at nominal current. Therefore:

$$L_f = \frac{\sqrt{3}V_{drop}V_n}{\omega_n S_n} \quad (C.1)$$

Typical value of $V_{drop}=5\%$ is used [93].

The DC link capacitance, C_f is determine to handle certain value of ripple voltage, ΔV and ripple current, ΔI at a particular switching frequency, f_{sw} . Therefore:

$$C_f = \frac{\Delta I}{\Delta V f_{sw}} \quad (C.2)$$

Typical value of $\Delta V=5\%$, $\Delta I=2\%$ and $f_{sw}=1\text{kHz}$ are used [93].

The PI controller parameters of the current and voltage loop are determined using Matlab *pidtoolbox*. Current loop bandwidth and voltage loop bandwidth is 200Hz and 20Hz, respectively. The damping ratio for both loops is 0.8.

The parameters are given in Table C.1.

Table C.1: Parameters of 1MVA and 10MVA front end converter

Description	Value and unit	Value and unit
Nominal apparent power, S_n	1MVA	10MVA
Nominal AC voltage, V_n	1kV	1kV
Nominal current, I_n	577.35A	5773.5A
Nominal system frequency, ω_n	314.16rad/s	314.16 rad/s
DC link nominal voltage, V_{dc}	2kV	2kV
DC link nominal current, I_{dc}	500A	5000A
L_f	0.3mH or 0.09pu	0.03mH or 0.09pu
R_f	0.01ohm or 0.01pu	0.001ohm or 0.01pu
C_f	0.1mF or 0.125pu	1mF or 0.125pu
Current loop proportional gain	0.6	0.06
Current loop integral gain	475	47.5
Voltage loop proportional gain	0.02	0.2
Voltage loop integral gain	1.6	16

Appendix D :

Parameters of Energy Storage System

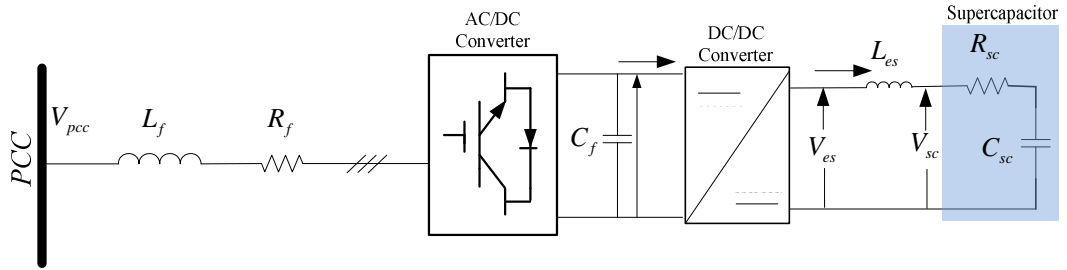


Figure D.1: Block diagram of Energy Storage System

The energy storage system is connected via a DC/DC converter and AC/DC converter to the point of common coupling. The parameters selection of the front end AC/DC converter is given in Appendix A. This appendix provides detail of the selection of DC/DC converter parameters.

As given in [93], the DC filter inductance, L_{es} can be determined by:

$$L_{es} = \frac{V_{sc,\min}}{\Delta I f_{sw}} \quad (\text{D.1})$$

where, $V_{sc,\min}$ is the minimum supercapacitor voltage, ΔI is the ripple current and f_{sw} is the switching frequency. Typical value of $\Delta I = 2\%$ and $f_{sw} = 1\text{kHz}$ is used.

The supercapacitor capacitance, C_{sc} can be determined by:

$$C_{sc} = \frac{I}{V_{sc,\max} - V_{sc,\min}} (T_{dis} + \tau) \quad (\text{D.2})$$

where, I is the average current, τ is time constant depending on type a particular type of supercapacitor, T_{dis} is the discharge time and $V_{sc,max}$ is the maximum supercapacitor voltage. A Maxwell supercapacitor with $\tau = 1.6$ is considered [106].

The controller gains of DC/DC converters are determined using using Matlab *pidtoolbox*. The inner loop bandwidth and outer loop bandwidth is 200Hz and 20Hz, respectively. The damping ratio for both loops is 0.8.

Table D.1: Parameters of energy storage system

Description	Value and unit
Maximum power, P_{max}	1MW
Maximum supercapacitor voltage, $V_{sc,max}$	2kV
Minumum supercapacitor voltage, $V_{sc,min}$	1kV
L_{es}	2mH
C_{es}	100F
DC/DC converter controller inner loop proportional gain	5
DC/DC converter controller inner loop integral gain	303
DC/DC converter controller outer loop proportional gain	20
DC/DC converter controller inner loop integral gain	303

Appendix E : Matlab code for the energy calculations in Chapter 3

```
clear
clc
m = csvread('Case32WES.txt'); % Obtain data for the case with ESS

t=m(:,1);
Isc=m(:,2);
PEss=m(:,3)*10;
E1=m(:,4);
Ploss=m(:,5);
Igsc2WES=m(:,7);

TT=2433; % determine from graph for a complete cycle
PC2=PEss(500:1500);
PD2=PEss(1500:TT);
EC2=trapz(PC2) %calculate energy charged from the ESS
ED2=trapz(PD2) %calculate energy discharge from the ESS
N2=-ED2/EC2*100 %calculate round trip efficiency

Ploss1=Ploss(500:TT);
ELossES=trapz(Ploss1) %Energy Loss in transmission line with the ESS

m = csvread('Case32WOES.txt'); %Obtain data for the case without ESS

t2=m(:,1);
PlossNES=m(:,5);
Igsc2WOES=m(:,7);

Ploss2=PlossNES(500:TT);
ELossNES=trapz(Ploss2) % Energy Loss in line without the ESS
ElossInES=-EC2-ED2 % Energy loss in ESS due to inefficiency of ESS
SavingTX=ElossNES-ELossES % Energy gain due to line loss reduction
Saving=ElossNES-ELossES-ElossInES %Overall energy gain from ESS
```

Appendix F :

Matlab code to obtain a Jacobian matrices

```

%Grid
%W=Wg+Kp11*Vpccq;
syms DIgd DIgq DVpccd DVpccq DLambda Igd Igq Vpccd Vpccq Lambda W Rg
Lg Cg Vg ITd ITq IiLd Iiwd Iied IiLq Iiwq Iieq Wg Kp11

W=Wg+Kp11*Vpccq;
ITd=IiLd+Iiwd+Iied;
ITq=IiLq+Iiwq+Iieq;

DIgd=-(Rg/Lg)*Igd+W*Igq-(1/Lg)*Vpccd+(1/Lg)*Vg*cos(Lambda);
DIgq=-W*Igd-(Rg/Lg)*Igq-(1/Lg)*Vpccq+(1/Lg)*Vg*sin(Lambda);

DVpccd=(1/Cg)*Igd+W*Vpccq-(1/Cg)*ITd;
DVpccq=(1/Cg)*Igq-W*Vpccd-(1/Cg)*ITq;
DLambda=Wg-W;

%CPL
syms VcLd VcLq DIiLd DIiLq DXLu DXLd DXLq DELdc
syms IiLd IiLq XLu XLd XLq ELdc
syms RfL LfL CfL
syms ELdcref IiLqref Pcp1
syms KpLu KiLu KpLd KiLd KpLq KiLq

VcLd=Vpccd-KpLu*KpLd*ELdcref+KpLu*KpLd*ELdc-KiLu*KpLd*XLu+KpLd*IiLd-
KiLd*XLd+W*LfL*IiLq;
VcLq=Vpccq-KpLq*IiLqref+KpLq*IiLq-KiLq*XLq-W*LfL*IiLd;

DIiLd=-(RfL/LfL)*IiLd-W*IiLq+Vpccd/LfL-VcLd/LfL;
DIiLq=-(RfL/LfL)*IiLq+W*IiLd+Vpccq/LfL-VcLq/LfL;
DXLu=-ELdc+ELdcref;
DXLd=-IiLd-KpLu*ELdc+KpLu*ELdcref+KiLu*XLu;
DXLq=-IiLq+IiLqref;
DELdc=3/(2*CfL*ELdc)*(VcLd*IiLd+VcLq*IiLq)-Pcp1/(CfL*ELdc);

%Wind
syms Vcwd Vcwq DIiwd DIiwq DXwu DXwd DXwq DEwdc
syms Iiwd Iiwq Xwu Xwd Xwq Ewdc
syms Rfw Lfw Cfw
syms Ewdcref Iiwqref Pwind

```

```

syms Kpwu Kiwu Kpwd Kiwd Kpwq Kiwq

Vcwd=Vpccd-Kpwu*Kpwd*Ewdcref+Kpwu*Kpwd*Ewdc-Kiwu*Kpwd*Xwu+Kpwd*Iiwd-
Kiwd*Xwd+W*Lfw*Iiwq;
Vcwq=Vpccq-Kpwq*Iiwqref+Kpwq*Iiwq-Kiwq*Xwq-W*Lfw*Iiwd;

DIiwd=-(Rfw/Lfw)*Iiwd-W*Iiwq+Vpccd/Lfw-Vcwd/Lfw;
DIiwq=-(Rfw/Lfw)*Iiwq+W*Iiwd+Vpccq/Lfw-Vcwq/Lfw;
DXwu=-Ewdc+Ewdcref;
DXwd=-Iiwd-Kpwu*Ewdc+Kpwu*Ewdcref+Kiwu*Xwu;
DXwq=-Iiwq+Iiwqref;
DEwdc=3/(2*Cfw*Ewdc)*(Vcwd*Iiwd+Vcwq*Iiwq)-Pwind/(Cfw*Ewdc);

%Energy Storage
syms Vpcc Ees D Ie Vced Vceq DIied DIieq DXed DXev DXeq DEedc DIES
DXs DXy
syms Iied Iieq Xed Xev Xeq Eedc Ies Xs Xy
syms Rfe Lfe Cfe Les Res
syms Vpccref Iiedref Eedcref Ves
syms Kped Kied Kpev Kiev Kpeq Kieq Kpy Kiy Kps Kis

Vpcc=sqrt(Vpccd^2+Vpccq^2);
Ees=-Kps*Kpy*Eedcref+Kps*Kpy*Eedc+Kps*Kiy*Xy-Kps*Ies+Kis*Xs;
D=Ees/Eedc;
Ie=D*Ies;

Vced=Vpccd-Kped*Iiedref+Kped*Iied-Kied*Xed+W*Lfe*Iieq;
Vceq=Vpccq-Kpev*Kpeq*Vpccref+Kpev*Kpeq*Vpcc-Kiev*Kpeq*Xev+Kpeq*Iieq-
Kieq*Xeq-W*Lfe*Iied;

DIied=-(Rfe/Lfe)*Iied+W*Iieq+Vpccd/Lfe-Vced/Lfe;
DIieq=-(Rfe/Lfe)*Iieq-W*Iied+Vpccq/Lfe-Vceq/Lfe;
DXed=-Iied+Iiedref;
DXev=-Vpcc+Vpccref;
DXeq=-Iieq+Kpev*Vpccref-Kpev*Vpcc+Kiev*Xev;
DEedc=3/(2*Cfe*Eedc)*(Vced*Iied+Vceq*Iieq)-3*Ie/(Cfe);
DXs=-Ies-Kpy*Eedcref+Kpy*Eedc+Kiy*Xy;
DXy=-Eedcref+Eedc;
DIES=Ees/Les-Ves/Les-Res*Ies/Les;

%Generating matrices A,B,C,D
f=[DIgd; DIgq; DVpccd; DVpccq; DLambda; DIiLd; DIiLq; DXLu; DXLd;
DXLq; DELdc; DIiwd; DIiwq; DXwu; DXwd; DXwq; DEwdc; DIied; DIieq;
DXed; DXev; DXeq; DEedc; DXs; DXy; DIES];

v=[Igd; Igq; Vpccd; Vpccq; Lambda; IiLd; IiLq; XLu; XLd; XLq; ELdc;
Iiwd; Iiwq; Xwu; Xwd; Xwq; Ewdc; Iied; Iieq; Xed; Xev; Xeq; Eedc;
Xs; Xy; Ies]

A=jacobian(f,v)

u=[ELdcref; IiLqref; Pcp1; Ewdcref; Iiwqref; Pwind; Vpccref;
Iiedref; Eedcref];
B=jacobian(f,u)
%
y=[Vpcc; ELdc; Ewdc]
C=jacobian(y,v)
%
D=jacobian(y,u)

```

Appendix G :

Matlab code to calculate participation factor

```
clc

A=A; % The Eigenvalues

[m,n]=size(A);
[V,D]=eig(A,'nobalance')
R=V; %right eigenvector

L=inv(V);%left eigenvector

k=1;
i=1;

for k=1:n
    for i=1:n
        p(k,i)=abs(L(i,k)*R(k,i));
    end
end
p=abs(p) %participation of the ith mode in the kth state
eig(A)

for k=1:n
    for i=1:n
        L1=L(:,i)'; ReL1=real(L1); ReL1Tr=real(L1)';
        pfn(k,i)=(real(L(k,i)))^2/(ReL1*ReL1Tr);
    end
end

pfn %participation factor of the kth state in the ith mode
```

References

- [1] Department of Energy & Climate Change, “UK Renewable Energy Roadmap,” 2011. [Online]. Available: https://www.gov.uk/government/uploads/system/uploads/attachment_data/file/48128/2167-uk-renewable-energy-roadmap.pdf.
- [2] US Energy Information Administration, “International Energy Statistics.” [Online]. Available: <http://www.eia.gov/cfapps/ipdbproject/IEDIndex3.cfm?tid=44&pid=44&aid=2>. [Accessed: 07-Nov-2013].
- [3] W. Jewell and Z. Hu, “The role of energy storage in transmission and distribution efficiency,” in Transmission and Distribution Conference and Exposition (T&D), 2012 IEEE PES, 2012, pp. 1–4.
- [4] D. Manz, R. Piwko, and N. Miller, “Look Before You Leap: The Role of Energy Storage in the Grid,” *Power Energy Mag. IEEE*, vol. 10, no. 4, pp. 75–84, 2012.
- [5] Q. Jiang and H. Wang, “Two-Time-Scale Coordination Control for a Battery Energy Storage System to Mitigate Wind Power Fluctuations,” *Energy Conversion, IEEE Trans.*, vol. 28, no. 1, pp. 52–61, 2013.
- [6] B. P. Roberts and C. Sandberg, “The Role of Energy Storage in Development of Smart Grids,” *Proc. IEEE*, vol. 99, no. 6, pp. 1139–1144, 2011.
- [7] A. Nourai, V. I. Kogan, and C. M. Schafer, “Load Leveling Reduces T&D Line Losses,” *Power Deliv. IEEE Trans.*, vol. 23, no. 4, pp. 2168–2173, 2008.
- [8] K. Areerak, S. V. Bozhko, G. M. Asher, L. De Lillo, and D. W. P. Thomas, “Stability Study for a Hybrid AC-DC More-Electric Aircraft Power System,” *Aerosp. Electron. Syst. IEEE Trans.*, vol. 48, no. 1, pp. 329–347, 2012.
- [9] D. Marx, P. Magne, B. Nahid-Mobarakeh, S. Pierfederici, and B. Davat, “Large Signal Stability Analysis Tools in DC Power Systems With Constant Power Loads and Variable Power Loads—A Review,” *Power Electron. IEEE Trans.*, vol. 27, no. 4, pp. 1773–1787, 2012.
- [10] M. Cespedes, L. Xing, and J. Sun, “Constant-Power Load System Stabilization by Passive Damping,” *Power Electron. IEEE Trans.*, vol. 26, no. 7, pp. 1832–1836, 2011.

- [11] N. Bottrell, M. Prodanovic, and T. Green, "Dynamic Stability of a Microgrid with an Active Load," *Power Electron. IEEE Trans.*, vol. PP, no. 99, p. 1, 2013.
- [12] N. Bottrell, M. Prodanovic, and T. C. Green, "Dynamic Stability of a Microgrid With an Active Load," *Power Electron. IEEE Trans.*, vol. 28, no. 11, pp. 5107–5119, 2013.
- [13] N. Pogaku, M. Prodanovic, and T. C. Green, "Modeling, Analysis and Testing of Autonomous Operation of an Inverter-Based Microgrid," *Power Electron. IEEE Trans.*, vol. 22, no. 2, pp. 613–625, 2007.
- [14] A. A. A. Radwan and Y. A. R. I. Mohamed, "Modeling, Analysis, and Stabilization of Converter-Fed AC Microgrids With High Penetration of Converter-Interfaced Loads," *Smart Grid, IEEE Trans.*, vol. 3, no. 3, pp. 1213–1225, 2012.
- [15] A. A. A. Radwan and Y. A.-R. I. Mohamed, "Analysis and Active-Impedance-Based Stabilization of Voltage-Source-Rectifier Loads in Grid-Connected and Isolated Microgrid Applications," *Sustain. Energy, IEEE Trans.*, vol. PP, no. 99, pp. 1–14, 2013.
- [16] E. A. A. Coelho, P. C. Cortizo, and P. F. D. Garcia, "Small-signal stability for parallel-connected inverters in stand-alone AC supply systems," *IEEE Trans. Ind. Appl.*, vol. 38, no. 2, pp. 533–542, 2002.
- [17] A. Kwasinski and C. N. Onwuchekwa, "Dynamic Behavior and Stabilization of DC Microgrids With Instantaneous Constant-Power Loads," *IEEE Trans. Power Electron.*, vol. 26, no. 3, pp. 822–834, Mar. 2011.
- [18] H. Polinder, "Overview of and trends in wind turbine generator systems," 2011 IEEE Power Energy Soc. Gen. Meet., pp. 1–8, Jul. 2011.
- [19] I. Hadjipaschalis, A. Poullikkas, and V. Efthimiou, "Overview of current and future energy storage technologies for electric power applications," *Renew. Sustain. Energy Rev.*, vol. 13, no. 6–7, pp. 1513–1522, 2009.
- [20] B. Roberts and J. McDowall, "Commercial successes in power storage," *Power Energy Mag. IEEE*, vol. 3, no. 2, pp. 24–30, 2005.
- [21] A. Ter-Gazarian, *Energy Storage for Power System*, vol. First Edit. London, United Kingdom: The Institute of Engineering and Technology, 1994.
- [22] D. Lindley, "Smart grids: The energy storage problem," *Nature*, vol. 463, no. 7277, pp. 18–20, 2010.
- [23] Electricity Storage Association, "Electricity Storage." [Online]. Available: <http://www.electricitystorage.org/>. [Accessed: 10-Jan-2011].

- [24] K. T. Mandle, "Dinorwig pumped-storage scheme," *Power Eng. J.*, vol. 2, no. 5, pp. 259–262, 1988.
- [25] P. A. EPRI CA, and the U.S. Department of Energy, "EPRI-DOE Handbook Supplement of Energy Storage for Grid Connected Wind Generation Applications," Washington, DC, 2004.
- [26] P. J. Hall and E. J. Bain, "Energy-storage technologies and electricity generation," *Energy Policy*, vol. 36, no. 12, pp. 4352–4355, Dec. 2008.
- [27] C. Klumpner, G. Asher, and G. Z. Chen, "Selecting the power electronic interface for a supercapattery based energy storage system," in *2009 IEEE Bucharest PowerTech: Innovative Ideas Toward the Electrical Grid of the Future*, 2009, vol. Bucharest.
- [28] A. M. Hemeida, "A fuzzy logic controlled superconducting magnetic energy storage, SMES frequency stabilizer," *Electr. Power Syst. Res.*, vol. 80, no. 6, pp. 651–656, 2010.
- [29] G. Zhang, X. Tang, and Z. Qi, "Research on battery supercapacitor hybrid storage and its application in MicroGrid," in *Asia-Pacific Power and Energy Engineering Conference, APPEEC 2010*, 2010, vol. Chengdu.
- [30] W. Li, G. Joos, and J. Belanger, "Real-Time Simulation of a Wind Turbine Generator Coupled With a Battery Supercapacitor Energy Storage System," *Ind. Electron. IEEE Trans.*, vol. 57, no. 4, pp. 1137–1145, 2010.
- [31] E. Sortomme and M. A. El-Sharkawi, "Optimal Power Flow for a System of Microgrids with Controllable Loads and Battery Storage," in *Power Systems Conference and Exposition, 2009. PSCE '09. IEEE/PES*, 2009, pp. 1–5.
- [32] J. Singh, R. Mittal, and D. K. Jain, "Improved performance of diesel driven permanent magnet synchronous generator using Battery Energy Storage System," in *Electrical Power & Energy Conference (EPEC)*, 2009 IEEE, 2009, pp. 1–6.
- [33] P. A. Taylor, "Update on the Puerto Rico electric power authority's spinning reserve battery system," in *Battery Conference on Applications and Advances*, 1996., Eleventh Annual, 1996, pp. 249–252.
- [34] A. Nourai and D. Kearns, "Batteries included: Realizing smart grid goals with intelligent energy storage," *IEEE Power Energy Mag.*, vol. 8, no. 2, pp. 49–54, 2010.
- [35] M. Tamaki, K. Takagi, K. Shimada, N. Kawakami, and Y. Iijima, "Development of PCS for battery system installed in megawatt photovoltaic system," in *2012 15th International Power Electronics and Motion Control Conference (EPE/PEMC)*, 2012, pp. LS1a–2.1–1–LS1a–2.1–4.

- [36] A. Price, S. Bartley, S. Male, and G. Cooley, "A novel approach to utility scale energy storage [regenerative fuel cells]," *Power Eng. J.*, vol. 13, no. 3, pp. 122–129, 1999.
- [37] P. Thounthong, S. Rael, and B. Davat, "Control Strategy of Fuel Cell and Supercapacitors Association for a Distributed Generation System," *Ind. Electron. IEEE Trans.*, vol. 54, no. 6, pp. 3225–3233, 2007.
- [38] A. Hajizadeh and M. A. Golkar, "Control of hybrid fuel cell/energy storage distributed generation system against voltage sag," *Int. J. Electr. Power Energy Syst.*, vol. 32, no. 5, pp. 488–497, Jun. 2010.
- [39] M. W. Ellis, M. R. Von Spakovsky, and D. J. Nelson, "Fuel cell systems: efficient, flexible energy conversion for the 21st century," *Proc. IEEE*, vol. 89, no. 12, pp. 1808–1818, 2001.
- [40] C. Abbey and G. Joos, "Supercapacitor Energy Storage for Wind Energy Applications," *IEEE Trans. Ind. Appl.*, vol. 43, no. 3, pp. 769–776, 2007.
- [41] P. Kulsangcharoen, C. Klumpner, X. H. Zhou, C. Peng, G. Z. Chen, M. Rashed, and G. Asher, "Efficiency Evaluation of a Novel Supercapattery Stack with a Power Electronic Interface for Energy Storage Systems," in *PCIM Europe*, 2010, no. May, pp. 398–403.
- [42] Z. Baharudin and N. Kamel, "Autoregressive method in short term load forecast," in *2008 IEEE 2nd International Power and Energy Conference, PECon 2008*, 2008, vol. Johor Baha, pp. 1603–1608.
- [43] E. E. Elattar, J. Y. Goulermas, and Q. H. Wu, "Generalized Locally Weighted GMDH for Short Term Load Forecasting," *Syst. Man, Cybern. Part C Appl. Rev. IEEE Trans.*, vol. PP, no. 99, pp. 1–12, 2011.
- [44] G. Gross and F. D. Galiana, "Short-Term Load Forecasting," *Proc. IEEE*, vol. 75, no. 12, pp. 1558–1573, 1987.
- [45] H. Farhangi, "The path of the smart grid," *IEEE Power Energy Mag.*, vol. 8, no. 1, pp. 18–28, 2010.
- [46] U. E.-I. Project, "Energy conservation and commercialization." [Online]. Available: <http://www.eco3.org/dsm/>. [Accessed: 11-Jan-2011].
- [47] G. Dupont and P. Baltus, "Dimensioning and grid integration of mega battery energy storage system for system load leveling," in *PowerTech, 2009 IEEE Bucharest*, 2009, pp. 1–6.
- [48] T. J. Lui, W. Stirling, and H. O. Marcy, "Get smart," *IEEE Power Energy Mag.*, vol. 8, no. 3, pp. 66–78, 2010.

- [49] X. Li, D. Hui, and X. Lai, "Battery Energy Storage Station (BESS)-Based Smoothing Control of Photovoltaic (PV) and Wind Power Generation Fluctuations," *Sustain. Energy, IEEE Trans.*, vol. 4, no. 2, pp. 464–473, 2013.
- [50] C. Luo, H. Banakar, B. Shen, and B.-T. Ooi, "Strategies to Smooth Wind Power Fluctuations of Wind Turbine Generator," *Energy Conversion, IEEE Trans.*, vol. 22, no. 2, pp. 341–349, 2007.
- [51] P. A. Ruiz and P. W. Sauer, "Spinning Contingency Reserve: Economic Value and Demand Functions," *IEEE Trans. Power Syst.*, vol. 23, no. 3, pp. 1071–1078, Aug. 2008.
- [52] T.-Y. Lee, "Optimal Spinning Reserve for a Wind-Thermal Power System Using EIPSO," *IEEE Trans. Power Syst.*, vol. 22, no. 4, pp. 1612–1621, Nov. 2007.
- [53] M. Bollen, *Understanding Power Quality Problems: Voltage Sags and Interruptions*. Wiley-IEEE Press, 1999.
- [54] A. Hajizadeh, L. Norum, and M. A. Golkar, "Robust power control of hybrid distributed power generation system during voltage sag," in *35th Annual Conference of the IEEE Industrial Electronics Society, IECON 2009, 2009*, vol. Porto, pp. 794–799.
- [55] F. Carastro, M. Sumner, and P. Zanchetta, "Mitigation of Voltage Dips and Voltage Harmonics within a Micro-grid, using a Single Shunt Active Filter with Energy Storage," in *IEEE Industrial Electronics, IECON 2006 - 32nd Annual Conference on, 2006*, pp. 2546–2551.
- [56] B. Singh, G. Kasal, A. Chandra, and Kamal-Al-Haddad, "Battery based voltage and frequency controller for parallel operated isolated asynchronous generators," in *2007 IEEE International Symposium on Industrial Electronics, ISIE 2007, 2007*, vol. Caixanova , pp. 883–888.
- [57] M. ud din Mufti, S. A. Lone, S. J. Iqbal, M. Ahmad, and M. Ismail, "Supercapacitor based energy storage system for improved load frequency control," *Electr. Power Syst. Res.*, vol. 79, no. 1, pp. 226–233, 2009.
- [58] B. Singh, J. Solanki, A. Chandra, and Kamal-Al-Haddad, "A Solid State Compensator with Energy Storage for Isolated Diesel Generator Set," in *Industrial Electronics, 2006 IEEE International Symposium on, 2006*, vol. 3, pp. 1774–1778.
- [59] H. Karimi, A. Yazdani, and R. Iravani, "Robust Control of an Autonomous Four-Wire Electronically-Coupled Distributed Generation Unit," *Power Deliv. IEEE Trans.*, vol. PP, no. 99, p. 1, 2010.

- [60] H. Polinder, J. A. Ferreira, B. B. Jensen, A. B. Abrahamsen, K. Atallah, and R. A. McMahon, "Trends in Wind Turbine Generator Systems," *IEEE J. Emerg. Sel. Top. Power Electron.*, vol. 1, no. 3, pp. 174–185, Sep. 2013.
- [61] R. Cardenas, R. Pena, S. Alepuz, and G. Asher, "Overview of Control Systems for the Operation of DFIGs in Wind Energy Applications," *IEEE Trans. Ind. Electron.*, vol. 60, no. 7, pp. 2776–2798, Jul. 2013.
- [62] L. Wang and D.-N. Truong, "Stability Enhancement of DFIG-Based Offshore Wind Farm Fed to a Multi-Machine System Using a STATCOM," *IEEE Trans. Power Syst.*, vol. 28, no. 3, pp. 2882–2889, Aug. 2013.
- [63] K. Areerak, "Modelling and Stability Analysis of Aircraft Power Systems," PhD Thesis, University of Nottingham, 2009.
- [64] A. Emadi, S. Member, A. Khaligh, S. Member, C. H. Rivetta, and G. A. Williamson, "Constant Power Loads and Negative Impedance Instability in Automotive Systems : Definition , Modeling , Stability , and Control of Power Electronic Converters and Motor Drives," vol. 55, no. 4, pp. 1112–1125, 2006.
- [65] A. Emadi, "Modeling of Power Electronic Loads in AC Distribution Systems Using the Generalized State-Space Averaging Method," *IEEE Trans. Ind. Electron.*, vol. 51, no. 5, pp. 992–1000, Oct. 2004.
- [66] A. Baghranian, "Averaged-value models of twelve-pulse rectifiers for aerospace applications," in *Second IEE International Conference on Power Electronics, Machines and Drives*, 2004, vol. 2004, pp. v1–220–v1–220.
- [67] K.-N. Areerak, S. V. Bozhko, G. M. Asher, and D. W. P. Thomas, "DQ-transformation approach for modelling and stability analysis of AC-DC power system with controlled PWM rectifier and constant power loads," in *2008 13th International Power Electronics and Motion Control Conference*, 2008, pp. 2049–2054.
- [68] K. Areerak, S. V. Bozhko, G. M. Asher, L. De Lillo, and D. W. P. Thomas, "Stability Study for a Hybrid AC-DC More-Electric Aircraft Power System," *IEEE Trans. Aerosp. Electron. Syst.*, vol. 48, no. 1, pp. 329–347, Jan. 2012.
- [69] IEEE Power Engineering Society, *IEEE Guide for Planning DC Links Terminating at AC Locations Having Low Short-Circuit Capacities*. IEEE Std 1204-1997, 1997.
- [70] IEEE Power & Energy Society, "IEEE Application Guide for AC High-Voltage Circuit Breakers Rated on a Symmetrical Current Basis." IEEE Std C37.010-1999 (R2005), 2000.
- [71] L. J. Gary, *Wind Energy System*, Electronic. 2006.

- [72] P. M. Anderson and A. Bose, "Stability Simulation Of Wind Turbine Systems," *Power Appar. Syst. IEEE Trans.*, vol. PAS-102, no. 12, pp. 3791–3795, 1983.
- [73] S. K. Salman and A. L. J. Teo, "Windmill modeling consideration and factors influencing the stability of a grid-connected wind power-based embedded generator," *Power Syst. IEEE Trans.*, vol. 18, no. 2, pp. 793–802, 2003.
- [74] B.-A. Chen, T.-K. Lu, Y.-Y. Hsu, W.-L. Chen, and Z.-C. Lee, "An Analytical Approach to Maximum Power Tracking and Loss Minimization of a Doubly Fed Induction Generator Considering Core Loss," *IEEE Trans. Energy Convers.*, vol. 27, no. 2, pp. 449–456, Jun. 2012.
- [75] S. M. Barakati, M. Kazerani, and J. D. Aplevich, "Maximum Power Tracking Control for a Wind Turbine System Including a Matrix Converter," *IEEE Trans. Energy Convers.*, vol. 24, no. 3, pp. 705–713, Sep. 2009.
- [76] B. Kou, Y. Bai, and L. Li, "A Novel Wind Power Generator System with Automatic Maximum Power Tracking Capability," *IEEE Trans. Energy Convers.*, vol. 28, no. 3, pp. 632–642, Sep. 2013.
- [77] M. Fazeli, "Wind Generator-Energy Storage Control Schemes for Autonomous Grid," University of Nottingham, University of Nottingham, 2010.
- [78] Y. El-Tous, "Pitch Angle Control of Variable Speed Wind Turbine," *Am. J. Eng. Appl. Sci.*, vol. 1, no. 2, pp. 118–120, Feb. 2008.
- [79] L. Lin, J. Zhang, and Y. Yang, "Comparison of pitch angle control models of wind farm for power system analysis," in *Power & Energy Society General Meeting, 2009. PES '09. IEEE, 2009*, pp. 1–7.
- [80] T. Sun, "Power Quality of Wind Connected Wind Turbines with DFIG and their Interaction with the Grid," University of Illinois at Urbana-Champaign, University of Illinois at Urbana-Champaign, 2004.
- [81] P. Sørensen, A. D. Hansen, and P. A. C. Rosas, "Wind models for simulation of power fluctuations from wind farms," *Fifth Asia-Pacific Conf. Wind Eng.*, vol. 90, no. 12–15, pp. 1381–1402, 2002.
- [82] R. Pena, J. C. Clare, and G. M. Asher, "A Doubly Fed Induction Generator using Back-to-back PWM Converters Supplying an Isolated Load from a Variable Speed Wind Turbine," *IEE Proc. - Electr. Power Appl.*, vol. 143, no. 5, p. 380, 1996.
- [83] H. M. el-helw and S. B. Tennakoon, "Vector Control of a Doubly Fed Induction Generator for Standalone Wind Energy Application," in *2008 Wind Power to the Grid - EPE Wind Energy Chapter 1st Seminar, 2008*, pp. 1–6.

- [84] L. Wang, J.-Y. Yu, and Y.-T. Chen, "Dynamic stability improvement of an integrated offshore wind and marine-current farm using a flywheel energy-storage system," *IET Renew. Power Gener.*, vol. 5, no. 5, p. 387, 2011.
- [85] N. R. Ullah and T. Thiringer, "Variable Speed Wind Turbines for Power System Stability Enhancement," *IEEE Trans. Energy Convers.*, vol. 22, no. 1, pp. 52–60, Mar. 2007.
- [86] A. Petersson, "Analysis , Modeling and Control of Doubly-Fed Induction Generators for Wind Turbines," PhD Thesis, Chalmers University Technology, 2005.
- [87] H. Banakar, C. Luo, and B. T. Ooi, "Steady-state stability analysis of doubly-fed induction generators under decoupled P–Q control," *IEE Proc. - Electr. Power Appl.*, vol. 153, no. 2, p. 300, 2006.
- [88] H. Lee, B. Y. Shin, S. Han, S. Jung, B. Park, and G. Jang, "Compensation for the Power Fluctuation of the Large Scale Wind Farm Using Hybrid Energy Storage Applications," *Appl. Supercond. IEEE Trans.*, vol. 22, no. 3, p. 5701904, 2012.
- [89] A. A. A. Radwan and Y. A. I. Mohamed, "Assessment and Mitigation of Interaction Dynamics in Hybrid AC/DC Distribution Generation Systems," *Smart Grid, IEEE Trans.*, vol. 3, no. 3, pp. 1382–1393, 2012.
- [90] M. A. Golkar and A. Hajizadeh, "Control strategy of hybrid fuel cell/battery distributed generation system for grid-connected operation," *J. Zhejiang Univ. Sci. A*, vol. 10, no. 4, pp. 488–496, 2009.
- [91] M. S. Joseph, *Wind Energy Conversion Systems*. 1973.
- [92] A. A. A. Radwan, S. Member, Y. A. I. Mohamed, and S. Member, "Analysis and Active-Impedance-Based Stabilization of Voltage-Source-Rectifier Loads in Grid-Connected and Isolated Microgrid Applications," pp. 1–14, 2013.
- [93] P. Srithorn, "Control of STATCOM with Supercapacitor Energy Storage," PhD Thesis, University of Nottingham, 2009.
- [94] R. Pena, J. C. Clare, and G. M. Asher, "Doubly fed induction generator using back-to-back PWM converters and its application to variable-speed wind-energy generation," *Electr. Power Appl. IEE Proc. -*, vol. 143, no. 3, pp. 231–241, 1996.
- [95] N. Pogaku, M. Prodanovic, and T. C. Green, "Inverter-based microgrids: Small-signal modelling and testing," in *Power Electronics, Machines and Drives*, 2006. The 3rd IET International Conference on, 2006, pp. 499–504.

- [96] R. Gutman, P. P. Marchenko, and R. D. Dunlop, "Analytical Development of Loadability Characteristics for EHV and UHV Transmission Lines," *Power Appar. Syst. IEEE Trans.*, vol. PAS-98, no. 2, pp. 606–617, 1979.
- [97] J. Hao and W. Xu, "Extended transmission line loadability curve by including voltage stability constrains," in *Electric Power Conference, 2008. EPEC 2008. IEEE Canada, 2008*, pp. 1–5.
- [98] J. D. Glover, M. S. Sarma, and T. J. Overbye, *Power System Analysis and Design*, vol. 4th Ed. Thomson, 2008.
- [99] X. Liu, Y. Zhou, W. Zhang, and S. Ma, "Stability Criteria for Constant Power Loads With Multistage LC Filters," *IEEE Trans. Veh. Technol.*, vol. 60, no. 5, pp. 2042–2049, 2011.
- [100] K. Honghai and W. Zhengqiu, "Research of super capacitor energy storage system based on DG connected to power grid," *2009 Int. Conf. Sustain. Power Gener. Supply*, pp. 1–6, Apr. 2009.
- [101] N. Mohan, T. M. Undeland, and W. P. Robbins, *Power Electronics: Converters, Applications, and Design*. John Wiley & Sons, 2002, p. 824.
- [102] B. M. Bird, K. G. King, and D. A. G. Pedder, *An Introduction to Power Electronics*. Wiley-Blackwell, 1992, p. 392.
- [103] W. A. Hashlamoun, M. A. Hassouneh, and E. H. Abed, "New Results on Modal Participation Factors: Revealing a Previously Unknown Dichotomy," *Autom. Control. IEEE Trans.*, vol. 54, no. 7, pp. 1439–1449, 2009.
- [104] F. Barruel, N. Retiere, J.-L. Schanen, and A. Caisley, "Stability Approach for Vehicles DC Power Network: Application to Aircraft On-board System," in *Power Electronics Specialists Conference, 2005. PESC '05. IEEE 36th, 2005*, pp. 1163–1169.
- [105] "Vishay - manufacturer of discrete semiconductors and passive components." [Online]. Available: <http://www.vishay.com/>. [Accessed: 03-May-2014].
- [106] S. X. Chen, S. Member, H. B. Gooi, S. Member, and M. Q. Wang, "Sizing of Energy Storage for Microgrids," *IEEE Trans. on Smart Grid*, pp. 1–10, 2011.